



**UNIVERSITÀ
DEGLI STUDI
DI TRIESTE**



Università
Ca' Foscari
Venezia

UNIVERSITÀ DEGLI STUDI DI TRIESTE

e

UNIVERSITÀ CA' FOSCARI DI VENEZIA

**XXXIV CICLO DEL DOTTORATO DI RICERCA IN
CHIMICA**

**SELF-ASSEMBLY OF MINIMALISTIC PHENYLALANINE
DERIVATIVES INTO SUPRAMOLECULAR HYDROGELS**

Settore scientifico-disciplinare: CHIM/06

DOTTORANDA

OTTAVIA BELLOTTO

COORDINATORE

PROF. ENZO ALESSIO

SUPERVISORE DI TESI

PROF. SILVIA MARCHESAN

ANNO ACCADEMICO 2020/2021

Table of Contents

List of abbreviations	1
Abstract	3
Riassunto	4
Chapter 1. General introduction	6
1.1. Bioinspiration for self-assembling nanomaterials.....	6
1.2. From natural self-assembling proteins to peptides	7
1.3. Minimalistic peptides as building blocks for supramolecular biomaterials.....	9
1.4. Peptide self-assembly.....	12
1.4.1. Non-proteogenic D-amino acids (D-aa).....	14
1.4.2. Effect of D-amino acids on self-assembly.....	15
1.5. Biomedical applications of peptide-based materials.....	18
1.5.1. Drug delivery and regenerative medicine	18
1.5.2. Antimicrobial agents	20
1.5.3. Water-channels in biomedicine and other applications	21
References.....	22
Chapter 2. Aim of the Thesis	25
References.....	28
Chapter 3. Self-assembly of <i>N</i>-(4-nitrobenzoyl)-L-Phe into a hydrogel	29
3.1. Introduction.....	29
3.2. Self-assembly of <i>N</i> -(4-nitrobenzoyl)-L-Phe into a nanostructured hydrogel.....	30
3.3. Secondary structure analysis	32
3.4. Single-crystal XRD analysis	35
3.5. MicroRaman analysis.....	36
3.6. pH titrations to evaluate apparent pKa shift with self-assembly	37
3.7. Biocompatibility assessment for wound healing applications	38
3.8. Conclusions.....	41
References.....	42
Chapter 4. Halogenation effect on Phe-Phe heterochiral dipeptides	45
4.1. N-terminal halogenation effect on D-Phe-L-Phe.....	45
4.1.1. Introduction.....	45
4.1.2. Results and discussion	47
4.1.2.1. Peptide self-assembly into nanostructured hydrogels.....	47
4.1.2.2. Peptides' conformation analysis	52
4.1.2.3. Chirality effects on interactions responsible for hierarchical bundling	55
4.1.2.4. Fluorination effects on nanotube hierarchical assembly.....	57

4.1.2.5. Hydrogels' biocompatibility assessment in cell culture	60
4.1.3. Conclusions of <i>Manuscript 2</i>	64
4.2. C-terminal halogenation effect on D-Phe-L-Phe	65
4.2.1. Introduction	65
4.2.2. Results and discussion	66
4.2.2.1. Synthesis and molecular characterization	66
4.2.2.2. Self-assembly in phosphate buffer	68
4.2.2.3. Single-crystal X-ray diffraction (XRD)	71
4.2.2.4. Visible Raman spectroscopy	73
4.2.2.5. UV Resonance Raman (UVR) spectroscopy	74
4.2.3. Conclusions of <i>Manuscript 3</i>	76
References	77
Chapter 5. Self-assembly of Leu-Phe and Phe-Leu dipeptides	81
5.1. Introduction	81
5.2. Dipeptides synthesis and self-assembly into hydrogels	82
5.3. Nanomorphologies of dipeptides' assemblies	86
5.4. Single-crystal X-ray diffraction analysis	87
5.5. Peptides' conformational analysis	89
5.6. Biocompatibility assessment of dipeptides' hydrogels	92
5.7. Conclusions	95
References	96
Chapter 6. Self-assembly of Ile-Phe and Phe-Ile dipeptides	100
6.1. Introduction	100
6.2. Dipeptides synthesis and molecular characterization	101
6.3. Self-assembly into hydrogel or crystals and optical microscopic investigation	103
6.4. Oscillatory rheology and thermoreversibility test for the hydrogelator D-Phe-L-Ile	107
6.5. Nanomorphologies of dipeptides' assembly	108
6.6 Spectroscopic analysis of peptide conformations	110
6.6. Single-crystal X-ray diffraction analysis	112
6.7. Biocompatibility assays of D-Phe-L-Ile hydrogel	114
6.8. Conclusions	116
References	117
Chapter 7. Self-assembly of Val-Phe and Phe-Val dipeptides	120
7.1. Introduction	120
7.2. D-Phe-L-Val and D-Val-L-Phe conformation analysis in solution	121
7.3. Self-assembly and hydrogelation of D-Phe-L-Val and D-Val-L-Phe	122
7.4. D-Phe-L-Val and D-Val-L-Phe conformational analysis in the assembled state	123

7.5. Raman microspectroscopy of D-Phe-L-Val and D-Val-L-Phe assemblies	125
7.6. Single-crystal X-ray diffraction analysis of D-Phe-L-Val and D-Val-L-Phe.....	126
7.7. Oscillatory rheology and thermoreversibility of D-Phe-L-Val and D-Val-L-Phe assembly..	130
7.8. Biocompatibility assessment of D-Phe-L-Val	132
7.9. Conclusions.....	134
References.....	135
Chapter 8. Conclusions.....	137
Chapter 9. Materials & Methods.....	140
Manuscript 1. “Self-assembly of an amino acid derivative into an antimicrobial hydrogel biomaterial” described in Chapter 3.....	140
1.1. Peptide self-assembly.....	140
1.2. Cytotoxicity assay	140
1.2.1. Trypan blue test for cell viability and cell count.....	140
1.2.2. Live/Dead assay	142
Manuscript 2. “Heterochirality and Halogenation Control Phe-Phe Hierarchical Assembly” described in Chapter 4.....	143
2.1. D-Phe-L-Phe synthesis.....	143
2.1.1. Loading of the first amino acid on the resin	143
2.1.2. N-terminal Fmoc group deprotection.....	144
2.1.3. Colorimetric tests	144
2.1.3.1. Bromophenol blue test	144
2.1.3.2. Acetaldehyde/chloranil test.....	145
2.1.4. Coupling of the second amino acid.....	145
2.1.5. Cleavage of the dipeptide from the resin	146
2.2. Peptide purification and characterization.....	146
2.3. Peptide self-assembly.....	147
2.4. Cytotoxicity assay	147
2.4.1. Trypan blue test for cell viability and cell count	147
2.4.2. Live/Dead assay	147
2.4.3. MTT Assay	147
Manuscript 3. “Single-atom substitution enables supramolecular diversity from dipeptide building blocks” described in Chapter 4	148
3.1. Peptide self-assembly into hydrogels or crystals	148
3.2. Oscillatory rheology.....	148
3.3. Transmission Electron Microscopy (TEM)	148
3.4. Circular dichroism (CD) spectroscopy	148
3.5. Attenuated Total Reflectance (ATR) Infrared Spectroscopy.....	149
3.6. Single-crystal XRD data	149

Manuscript 4. “Supramolecular hydrogels from unprotected dipeptides: a comparative study on stereoisomers and structural isomers” described in Chapter 5.	149
4.1. Peptide synthesis	149
4.2. Peptide purification	149
4.3. Peptide characterization	149
4.4. Peptide self-assembly	150
4.5. Oscillatory rheology	150
4.6. Transmission Electron Microscopy (TEM)	150
4.7. Circular dichroism (CD) spectroscopy	150
4.8. Attenuated Total Reflectance (ATR) Infrared Spectroscopy	151
4.9. Single-crystal XRD data	151
4.10. Cytotoxicity assays	151
4.10.1. Trypan blue test for cell viability and cell count	151
4.10.2. Live/Dead assay	151
4.10.3. MTT assay	152
Manuscript 5. “Self-Assembly of Unprotected Dipeptides into Hydrogels: Water-Channels Make the Difference” described in Chapter 6.....	152
5.1. Peptide synthesis	152
5.2. Peptide purification	152
5.3. Peptide characterization	153
5.4. Self-assembly	153
5.5. ¹⁹ F-NMR, TFA removal and self-assembly with chloride counterion.....	153
5.6. Oscillatory rheology	153
5.7. Transmission electron microscopy (TEM) and optical microscopy	154
5.8. Circular Dichroism (CD) spectroscopy.....	154
5.9. Attenuated total reflectance (ATR) infrared spectroscopy	154
5.10. Single-crystal X-ray diffraction (XRD)	154
5.11. Cytotoxicity assays	155
5.11.1. Trypan blue test for cell viability and cell count	155
5.11.2. Live/Dead assay	155
5.11.3. MTT assay.....	155
Manuscript 6. “Dipeptide self-assembly into water-channels and gel biomaterial” described in Chapter 7.	156
6.1. Peptide synthesis	156
6.2. Peptide purification	156
6.3. Peptide characterization	156
6.4. Self-assembly into hydrogels or crystals	157
6.5. Oscillatory rheology	157
6.6. Transmission electron microscopy (TEM) and optical microscopy	157

6.7. Circular dichroism (CD) spectroscopy	157
6.8. Attenuated Total Reflectance (ATR) Infrared Spectroscopy.....	157
6.9. Thioflavin T fluorescence assay	157
6.10. Single-crystal X-ray diffraction (XRD).....	158
6.11. Cytotoxicity assays	158
6.11.1. Trypan blue test for cell viability and cell count	158
6.11.2. Live/Dead assay	158
6.11.3. MTT assay.....	158
References.....	159
Chapter 10. Appendix.....	160

List of abbreviations

<i>Abbreviations</i>	<i>Name</i>
Ala, A	Alanine
AMPs	Antimicrobial peptides
AO	Acridine Orange
AP	Aquaporin
Arg, R	Arginine
Asn, N	Asparagine
Asp, D	Aspartic Acid
ATR-IR	Attenuated Total Reflectance Infrared Spectroscopy
c.a.c.	Critical aggregation concentration
CD	Circular Dichroism
CHC	Central hydrophobic cluster
DCM	Dichloromethane
DKPs	2,5-diketopiperazines
DIPEA	Diisopropylethylamine
DMF	Dimethylformamide
DMEM	Dulbecco's modified Eagle's medium
DMSO-<i>d</i>₆	Deuterated Dimethyl Sulfoxide
ECM	Extracellular matrix
ESI-MS	Electrospray Ionization Mass Spectrometry
FBS	Fetal bovine serum
Fmoc	Fluorenylmethyloxycarbonyl
FT-IR	Fourier Transform Infrared Spectroscopy
GAGs	Glycosaminoglycans
G'	Elastic or storage modulus
G''	Viscous or loss modulus
Gln, Q	Glutamine
Gly, G	Glycine
Glu, E	Glutamic Acid
HBTU	<i>N,N,N',N'</i> -Tetramethyl- <i>O</i> -(1 <i>H</i> -benzotriazol-1-yl)uronium
HOAt	1-Hydroxy-7-azabenzotriazole
IR	Infrared

Ile, I	Isoleucine
LC-MS	Liquid Chromatography-Mass Spectrometry
Leu, L	Leucine
Lys, K	Lysine
m.g.c.	Minimum gelling concentration
MD	Molecular Dynamics
MeCN	Acetonitrile
Met	Methionine
MIC	Minimum Inhibitory Concentration
MTT	3-(4,5-dimethylthiazol-2-yl)-2,5-diphenyl tetrazolium bromide
Nap	Naphthalene
NMR	Nuclear Magnetic Resonance
PBS	Phosphate Buffered Saline
PG	Peptidoglycan
Phe, F	Phenylalanine
PI	Propidium Iodide
Pro, P	Proline
RP-HPLC	Reverse Phase-High Performance Liquid Chromatography
Rt	Retention time
SD	Standard Deviation
SEM	Scanning electron microscopy
Ser, S	Serine
SOCl₂	Thionyl chloride
SPPS	Solid Phase Peptide Synthesis
TEM	Transmission Electron Microscopy
TFA	Trifluoroacetic Acid
TMS	Tetramethylsilane
ThT	Thioflavin T
TIPS	Triisopropylsilane
Tm	Melting Temperature
Tyr, Y	Tyrosine
UVRR	UV Resonance Raman
Val, V	Valine
XRD	X-Ray Diffraction

Abstract

Biodegradable nanomaterials based on short-peptide building blocks have raised an increasing interest in research over the years. They present several advantages (*i.e.*, biocompatibility, chemical diversity, low cost) relative to other types of materials, and there is a large scope to study minimalistic short sequences as active building blocks for biomaterials, with single amino acids and dipeptides standing out as ideal candidates, although prediction of their supramolecular behaviour is very challenging.

This PhD thesis aims to fill this gap firstly describing the self-assembly of a N-capped phenylalanine (Phe) derivative into a transparent gel under physiological conditions with promising antimicrobial activity and biocompatibility *in vitro*. Next, the substitution of the N-cap with another hydrophobic amino acid (*i.e.*, Phe, Leu, Ile, or Val) has been explored as a preferable strategy towards biocompatible self-assembling dipeptides, and effects of amino acid chirality over gelation has been studied. Heterochirality revealed to be a successful strategy to control the hierarchical assembly of dipeptides, especially in the case of Phe-Phe, and to promote self-assembly in water through increased peptide hydrophobicity. As self-assembly is a cooperative process, small structural sequence differences (*i.e.*, branching of the aliphatic amino acid side chain for the regioisomers Leu and Ile) can be amplified and lead to significant supramolecular differences. Furthermore, halogenation was studied for its influence on the supramolecular organization of D-Phe-L-Phe.

Peptides were synthesized by Fmoc-based solid-phase peptide synthesis, purified by reverse-phase HPLC and characterized by ¹H-NMR, ¹³C-NMR and ESI-MS. Self-assembly was probed under physiological conditions (*i.e.*, phosphate buffered solutions) and the supramolecular behaviour was investigated by means of rheology, circular dichroism (CD), fourier-transformed infrared spectroscopy (FT-IR), thioflavin T fluorescence, optical imaging, transmission electron microscopy (TEM), powder and single-crystal X-ray diffraction (XRD), visible and UV-resonant Raman spectroscopy. Finally, biocompatibility was assayed qualitatively (live/dead) and quantitatively (MTT, 3-(4,5-dimethylthiazol-2-yl)-2,5-diphenyl tetrazolium bromide).

Overall, this PhD thesis allows to delineate design rules for the self-assembly of very simple building blocks based on 1-2 amino acids into biocompatible biomaterials and outlines several examples of supramolecular water-channels and hydrogels with potential applications in medicine.

Riassunto

Nel corso degli anni, i materiali nanostrutturati costituiti da piccoli peptidi e con una buona biodegradabilità hanno suscitato un notevole interesse nella ricerca. Grazie ai numerosi vantaggi che presentano rispetto ad altri tipi di materiali (ad es. biocompatibilità, versatilità chimica di composizione e semplicità di preparazione con bassi costi e su grande scala), si è assistito ad un crescente ed attivo interesse verso lo sviluppo di biomateriali di natura peptidica a partire da sequenze il più semplici e brevi possibili, quali singoli amminoacidi o dipeptidi, secondo un approccio di tipo minimalista.

Questa tesi di dottorato, per prima cosa, descrive la capacità di un derivato dell'amminoacido fenilalanina, protetta all'N-terminale in posizione para con un gruppo nitrobenzoile, di auto-assemblarsi in condizioni fisiologiche per formare un idrogel trasparente. Studi preliminari *in vitro*, hanno rivelato per questo composto una promettente attività antimicrobica ed una buona biocompatibilità verso colture cellulari di mammifero. Successivamente, è stato investigato l'effetto della sostituzione del gruppo N-terminale della fenilalanina con un altro amminoacido di natura idrofobica, quale fenilalanina, leucina, isoleucina o valina, considerando questa sostituzione come una strategia promettente per ottenere biomateriali a partire da dipeptidi capaci di auto-organizzarsi. È stata inoltre esplorata l'influenza della chiralità nei singoli amino acidi, sulla capacità di questi dipeptidi di formare idrogeli. L'eterochiralità si è rivelata una promettente strategia sia per guidare l'organizzazione gerarchica di piccole molecole quali i dipeptidi, specialmente nel caso della difenilalanina, sia per favorirne la loro auto-organizzazione in acqua, aumentando l'idrofobicità della sequenza peptidica. Poiché il fenomeno di auto-organizzazione è un processo cooperativo, anche minime differenze strutturali nella sequenza peptidica, quali la diversa ramificazione della catena alifatica nei due regioisomeri leucina ed isoleucina, può essere amplificata e portare a significative differenze a livello sopramolecolare. In questa tesi, infine, è stata investigata anche la possibile influenza dell'alogeneazione sull'organizzazione sopramolecolare della difenilalanina eterochirale.

I peptidi sono stati sintetizzati in fase solida, purificati mediante HPLC in fase inversa e caratterizzati a livello molecolare tramite $^1\text{H-NMR}$, $^{13}\text{C-NMR}$ e studi di massa ESI-MS. La capacità di ogni dipeptide sintetizzato di auto-organizzarsi e formare degli idrogeli è stata testata in condizioni fisiologiche (es. soluzioni di tampone fosfato) ed il comportamento sopramolecolare è stato investigato tramite l'utilizzo di diverse tecniche, quali analisi di reologia, dicroismo circolare (CD), spettroscopia infrarossa (FT-IR), saggi di fluorescenza (Th-T) amiloide, microscopia ottica ed a trasmissione elettronica (TEM), diffrazione a raggi X (XRD) su singolo cristallo e su polvere e spettroscopia visibile ed UV-Raman. Infine, la biocompatibilità di questi composti è stata testata *in*

in vitro attraverso saggi di citotossicità sia di tipo qualitativo (live/dead) che quantitativo (MTT, 3-(4,5-dimethylthiazol-2-yl)-2,5-diphenyl tetrazolium bromide) su colture cellulari di mammifero.

Complessivamente, questa tesi di dottorato consente di definire le regole chiave che guidano l'auto-organizzazione di semplici e piccole molecole, costituite da 1 o 2 amminoacidi, per ottenere biomateriali con ideali caratteristiche di biodegradabilità e biocompatibilità. Inoltre, molti dei sistemi studiati in questa tesi dimostrano la loro capacità di organizzarsi in maniera ordinata a formare interessanti strutture a canale ed idrogel, con promettenti e potenziali applicazioni future nel campo della biomedicina.

Chapter 1. General introduction

1.1. Bioinspiration for self-assembling nanomaterials

Nowadays, there is a great interest in small molecules, such as organic molecules, nucleic-acid motifs, oligosaccharides, and short peptides, able to self-assemble into distinct nanostructures and supramolecular architectures with diverse properties [1]. In Nature, the inherent propensity of metabolites/biomacromolecules or their mimics to naturally self-organize into complex structures is widespread [2]. The resulting supramolecular metabolite structures can play an active role in several metabolic disorders, for instance by forming amyloids involved in neurodegenerative diseases or through the acid-uric accumulation around the joints responsible of gout disorders.

At the same time, their physiological and functional role in biological systems is well-known. For instance, natural structural colours usually rely on a multiscale hierarchical organization of biological building blocks able to interact with light efficiently (**Figure 1.1**). A suitable management of light is of vital importance for living systems enabling them to adopt different strategies, such as photoprotection, photosynthesis, camouflage, regulation of circadian rhythms, and detection of light, to survive [3]. Other examples of functional supramolecular structures comprise viruses, whereby nucleic acids are encased by a capsid self-assembled from proteins, which can be further enclosed in a cell membrane derived from the viral host [4]. Furthermore, cell organelles and membranes are rich of functional examples of biomolecules that self-organise into diverse nanostructures that ensure compartmentalization and organization of cellular processes [5].

Nature has widely used self-assembly of proteins and peptides to build a vast array of structures like silk, corals, shells as well as collagen and keratin into ligaments and hair, respectively. Besides, the individual chaperone proteins assembly into a sophisticated ring structures to sort out, fold and refold proteins [6]. Nature is certainly a generous source of bioinspiration for the design of functional supramolecular nanocomposites [7].

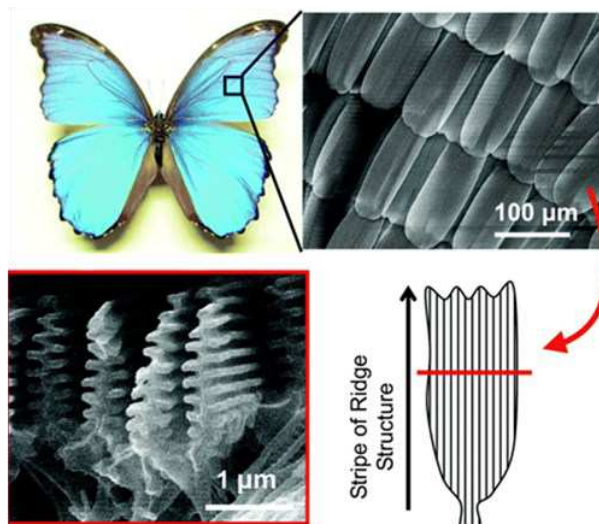


Figure 1.1. Typical *Morpho* butterfly (*Morpho didius*) and SEM images of the scale, each covered with ridges whose lateral profile has the typical “Christmas tree” shape. Reproduced from ref. [8] with permission from © 2016 Royal Society of Chemistry.

Therefore, self-organization has recently emerged as an attractive approach in chemical synthesis, polymer and materials science, and engineering by providing a means for the bottom-up fabrication of various materials to tailor novel physicochemical and functional properties. Supramolecular assembly is a dynamic and versatile process, which is driven by non-covalent interactions that can be weak when considered individually. However, their synergism and cooperativity once they are combined together can give rise to highly stable architectures that display advantageous features, such as reversibility, responsiveness and tunable characteristics [9].

1.2. From natural self-assembling proteins to peptides

(Adapted from: Bellotto, O; Marchesan, S. Peptide nanostructured materials as drug delivery carriers. *Peptide Bionanomaterials: From Design to Application*, 2022, in press)

In nature, proteins play an elective role as building blocks to attain functional structures and materials, thanks to their large chemical diversity. Through years of intense research, several functions have been decoded into corresponding short motifs that can consist of simple sequences of just a few amino acids, exerting specific functions ranging from targeting to bioactivity, and belonging to several peptide classes (**Figure 1.2**) [10]. It is thus not surprising that peptides have since enjoyed popularity as building blocks of supramolecular materials, thanks to their great diversity, inherent biocompatibility and biodegradability, and the possibility to attain structural and functional complexity from very simple building blocks [11]. Their ability to deliver powerful and selective biological messages to cells is very important for possible biological applications. Likewise, their

inherent biocompatibility and biodegradability means the possibility to work in environmentally friendly conditions, thus facilitating the use of green solvents, such as water, with consequent lower impact on the environment [12].

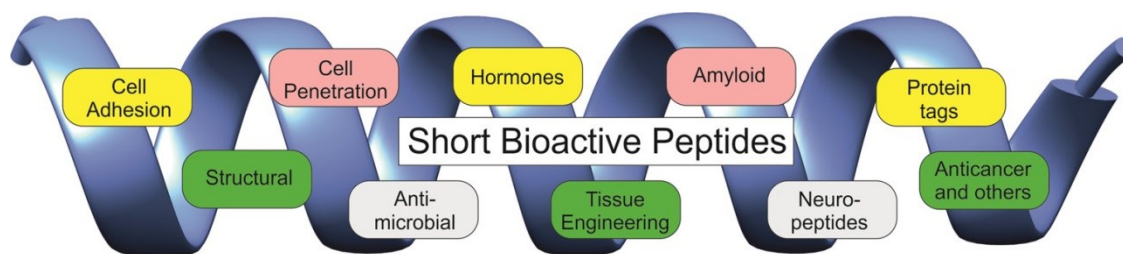


Figure 1.2. Bioactive short motifs belonging to several classes have been recently reviewed. Reprinted with permission from [10], Copyright © 2017 American Chemical Society.

Peptides can be attained through the very easy and modular solid-phase synthesis, although costs can rise exponentially as the number of amino acids in the desired product increases, and especially for the scale-up on large amounts. However, short motifs can be obtained also through liquid-phase methods, which are significantly cheaper, and whose chemistry is also well-established. Depending on the amino acid sequence, they can present a great chemical diversity, which can be further amplified through the introduction of non-proteogenic amino acids [13]. Although peptide and proteins are weakly resistant to enzymatic activity, a higher degree of proteolytic protection can be pursued through several chemical approaches aimed at the modification of the original chemical structure. Some examples are cyclization, introduction of D-residues, methylation of the α -C, methylation of the amidic N, and introduction of β^3 residues. Among them, a change in chirality has been shown to be a very efficient strategy for this purpose [14].

Overall, the versatility of peptides and proteins, alongside notable physicochemical properties, offer an ideal playground to employ them in the design of new technological tools, bulk nanomaterials, or adaptive nanostructures. Peptides are able to gather into diverse nanomorphologies, including fibrillar structures (nanotubes, fibrils) and vesicles supported by their device and self-assembly conditions. **(Figure 1.3)** [15,16].

Different hydrogen-bonding pattern interactions stabilize the secondary structures elements, among which, α -helices and β -sheets have been predominantly used in peptide materials [17]. Combination of multiple peptide components into the assemblies allows to further expand the versatility of these

systems [18]. One of the main challenges is the identification of the smallest and cheapest components with enhanced performance to allow for their self-assembly into complex structures in a controlled manner. Within the peptide landscape, reductionist approaches became popular towards the identification of the shortest self-assembling peptides for biomaterials [19]. Indeed, this interesting strategy allows to minimize the synthesis and purification steps and to reduce the costs of production for practical applications.

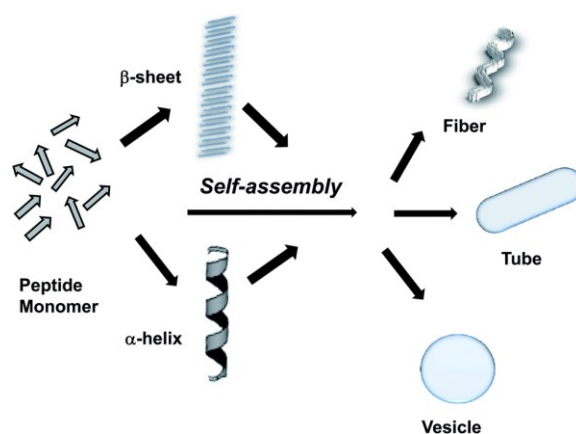


Figure 1.3. Self-assembly of peptides into different types of nanostructures. Reproduced from ref. [16] with permission from © 2014 Royal Society of Chemistry.

1.3. Minimalistic peptides as building blocks for supramolecular biomaterials

Already in 2003, Reches and Gazit identified the dipeptide diphenylalanine (Phe-Phe) as a powerful minimalistic self-assembling motif belonging to the Amyloid Beta ($A\beta$) peptide sequence [20], corresponding precisely to the 19th and 20th residues of the central hydrophobic cluster (CHC) in the sequence (**Figure 1.4**).

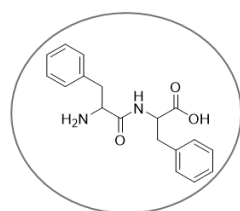


Figure 1.4. Amyloid Beta ($A\beta$) peptide sequence and the molecular recognition motif Phe-Phe, corresponding to the the 19th and 20th residues of the sequence, respectively [20].

Nowadays, there is a large scope to study minimalistic short sequences (especially di- and tripeptides) as bioactive building blocks for soft biomaterials, and the presence of a large aromatic N-capping groups (*i.e.*, Fmoc, Nap, Cbz, Azo...) reported in **Figure 1.5**, [21] that drive self-assembly in water is usually required. Both hydrophobic and non-covalent π - π interactions have demonstrated a special role and engagement in the peptide supramolecular organization, for which the presence of an aromatic moiety appears critical.

For instance, Ulijn's group investigated the supramolecular behaviour of short sequences such as aromatic dipeptides and tripeptides, considering the introduction of a rigid template, such as Nap, Fmoc or Cbz and the differences due to the aromatic ligand used [22,23]. Further studies showed that the presence of the fluorenylmethoxycarbonyl (Fmoc) moiety at the N-terminus of the diphenylalanine favoured the hydrogelation *via* a π - π interlocked β -sheets interactions [24]. Among them, the fluorenyl methoxycarbonyl (Fmoc) group, easily available and commonly used in peptide chemistry, and naphthalene (Nap) derivatives are the most common moieties employed to this aim.

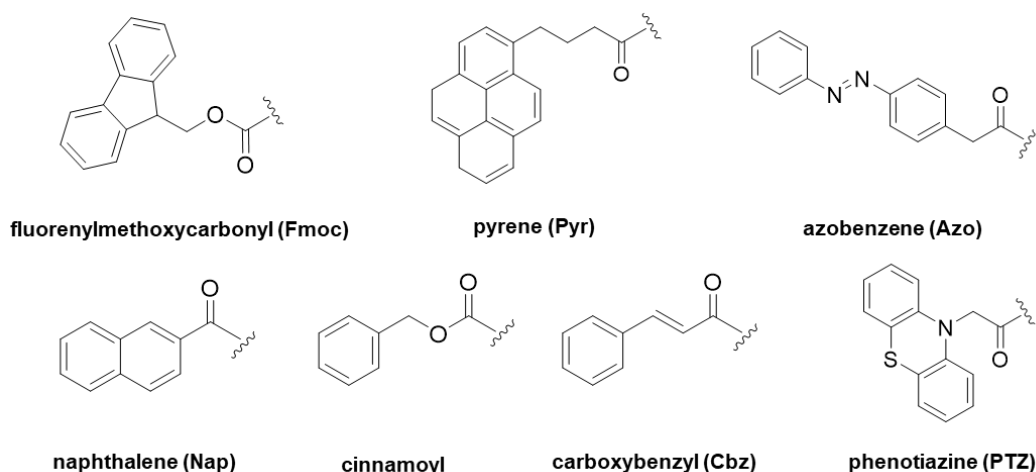


Figure 1.5. N-capping aromatic groups used to facilitate the self-assembly of ultrashort peptide sequences [21].

However, to date safety concerns exist on the biological fate of such rigid N-caps *in vivo*, such as those due to the degradation products of the Fmoc group [25]. Furthermore, such aromatic templates often require small amount of organic solvents to assist with the peptide dissolution [26,27].

For such reasons, simpler aromatic analogues whose nature can assist hydrophobically driven self-organization with desirable biocompatibility *in vivo* or *in vitro* would be preferable alternatives [28]. The amino acid Phe was shown to self-assemble on its own into ordered fibrillar structures with amyloid-like properties [29]. Hence, it is not too surprising that Phe is a recurrent building block also in other self-assembling peptides sequences. The replacement of traditional N-capping groups with

long alkyl chains in Phe-containing short peptides has been reported as a useful strategy to obtain supramolecular aggregates and hydrogels in aqueous environments. Changes in the number of Phe residues and in the alkyl chain length provided a vast array of nanostructural morphologies, such as nanosheets or fiber networks [30]. Features such as hydrophobicity and aromaticity were preserved to drive the self-assembly.

In 2006, Görbitz focused his studies on the aromatic homochiral dipeptide Phe-Phe by confirming its peculiar arrangement into stiff nanotubes through X-ray crystallography. The aromatic side chains, oriented on the same side against the backbone plane, were able to interact through π - π stackings [31]. Later, he also extended his investigation to other homochiral hydrophobic dipeptides, considering their ability to adopt a packing structure with nanopores in the supramolecular assembly. He noticed that different families of hydrophobic dipeptides led to channels with different properties in terms of nature of the pores (hydrophilic or hydrophobic) and the dimensionality of the H-bonding patterns (three- or one-dimensional) [32] (**Figure 1.6**).

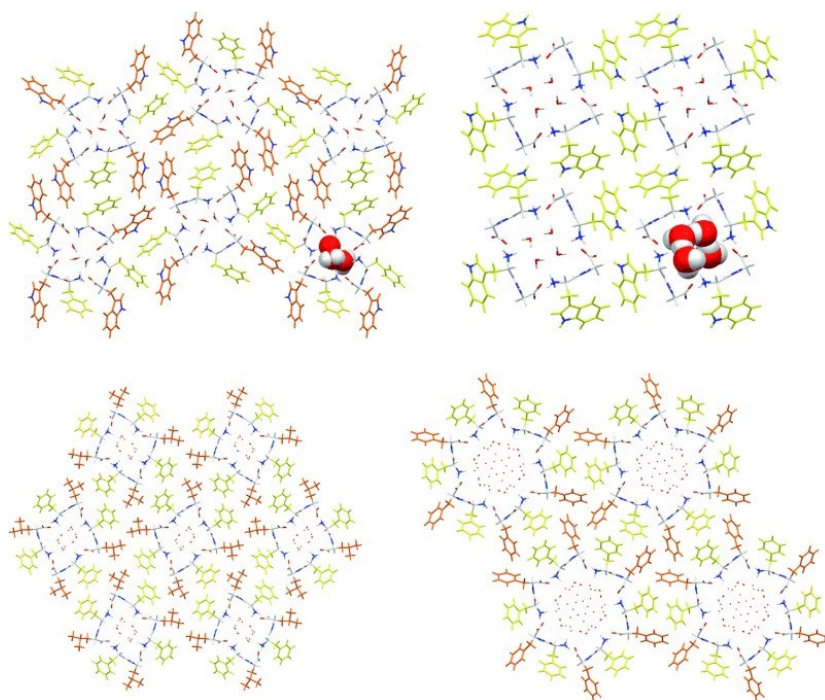


Figure 1.6. Structural variability within the Phe-Phe class of structures: Phe-Trp [33] (top left), Trp-Gly [34,35] (top right), Phe-Leu [36] (bottom left), and Phe-Phe [36] (bottom right). In the top images ordered molecules in one column have been depicted in space-fill representation. Small spheres in the bottom images represent disordered solvent positions. Reproduced with permission from ref. [32], © 2007 John Wiley and Sons.

It is thus not surprising that there is active research towards the design of short peptides and their derivatives, containing structural motifs required to enable self-assembly and bottom-up fabrication of nanostructures with specific properties. So far, these peptide-based supramolecular materials offer unique advantages over other classes of molecules and have exhibited a great potential for a wide range of biomedical applications, ranging from immunotherapy and biosensing, to the development of scaffolds for tissue engineering and theranostic tools, and drug delivery vehicles [37].

1.4. Peptide self-assembly

Molecular self-assembly is commonly found in nature and it is defined as a spontaneous process where single molecular building blocks arrange themselves into organized supramolecular architectures. Typically, the driving forces involved in the self-assembly consist of intermolecular non-covalent interactions (*i.e.*, *H-bonds*, *electrostatic interactions*, *van der Waals forces*, *π - π interactions*, *halogen bonds* and *hydrophobic interactions*) [38], which are rather weak if alone, but also they are able to produce stable structures through a synergistic effect [39]. For instance, the well-defined directionality and specificity of *hydrogen bonds* provide stability to the peptides' secondary structure and protein folding. Typically, the amides of the peptide backbone and the amino and carboxylic terminal groups are involved in such interactions. *Electrostatic interactions* are based on Coulombic attractions between opposite charges and the use of charged residues can also be used to provide ionic interactions. The ionic bond displays a strength that is higher (~ 500 kJ/mol) than the H-bond. By contrast, the energy of a typical *van der Waals* bond is lower in comparison to a hydrogen one. The van der Waals forces can be considered as a kind of instantaneous electrostatic interactions. *Halogenation* can be also exploited as an advantageous tool to fine-tune the peptide self-assembly, especially whenever used as substitution on the aromatic group in the sequence. The type of the halogen substituent (Cl, F, Br, I) and its position on the aromatic side chain (ortho, meta, para) can dramatically affect the rate of self-assembly by means of a fine balance between steric and electronic effects [40–42]. *π - π interactions* arise from the stacking of aromatic groups containing *π orbitals*. They can be classified on the base of the aromatic ring orientation into edge-to-face T shape, parallel-displaced and parallel stacked geometries, represented in **Figure 1.7** [43], and potentially influenced by the presence of substituents [44].

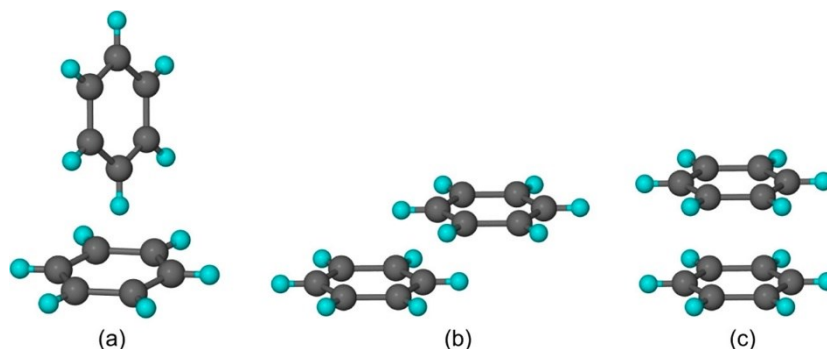


Figure 1.7. (a) Edge-to-face T-shape, (b) parallel displaced, and (c) cofacial parallel stacked geometries of π - π interactions between aromatic systems. Reprinted with permission from ref. [43] Copyright © 2019, American Chemical Society.

The aromatic moieties in a peptide system may be involved in either π - π or in *hydrophobic interactions*. *Hydrophobicity* stands out as a key factor for molecular self-assembly in water since it limits the peptide solubility and favours the aggregation. This effect is due to the tendency of hydrophobic groups, either aliphatic or aromatic, to aggregate and to limit their surface area in contact with water [45].

Interestingly, the presence of salts, especially in relatively high concentrations, may also affect the peptide self-assembly in aqueous solution since they influence the hydrophobic interactions between peptide molecules. It is assumed that the highly hydrate anions in water (*kosmotropes*), such as phosphate and sulphate, are able to organize the water molecules around themselves, subtracting water from protein molecules and enhancing hydrophobic interactions. Therefore, a decrease in protein solubility provokes its precipitation or so called “salting-out” from aqueous solutions. By contrast, some weakly hydrate ions (*chaotropes*) such as iodide, can induce protein solubilization by means of facilitating their hydration and by reducing the hydrophobic effect [46]. This is defined as the so called “Hofmeister effect”, which is well-known in protein science and beyond [47].

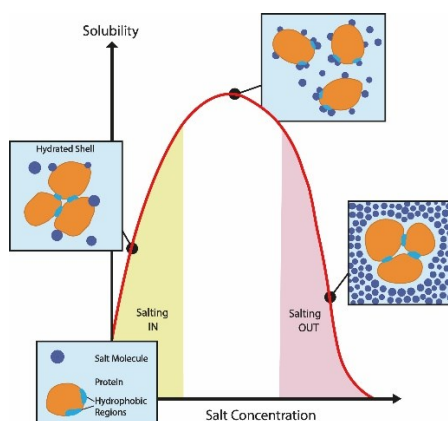


Figure 1.8. Mechanism of salting out

Over the last two decades, peptide self-assembly stood out as a convenient strategy to achieve supramolecular smart materials [48]. The numerous interactions between amino acids can provide complex self-assembled nanostructures. The varying properties of amino acids can therefore be manipulated in the design of peptides for self-assembly to achieve novel functional biomaterial. A great diversity from natural, non-natural, and D- or L-enantiomers means enormous space to chemical sequence combinations. Single amino acid can influence the properties of the final product (*e.g.*, gel or not). Finally, the functionalization of the side chains and of the sequence termini allows for the formation of different self-assembled products [9]. Depending on the amino acid sequence, peptides can present a great chemical diversity, which can be amplified through the introduction of non-proteogenic amino acids [13].

1.4.1. Non-proteogenic D-amino acids (D-aa)

Except for glycine (Gly), all natural amino acids exist in two enantiomeric forms (L and D) and the L-form is predominant in nature. However, D-amino acids (D-aa) or non-proteogenic amino acids have been found in many living systems too, as free form or as a part of bioactive proteins. In humans, D-Ser and D-Asp have been found to have neuroendocrine and neuromodulation activity. The former has been detected in β -amyloid proteins of Alzheimer's patients [49]. Meanwhile, an accumulation of the latter in some specific tissues (*i.e.*, bone, eye lenses and tooth) is associated to the aging process. D-Phe provides an enhancement in the antimicrobial efficacy of some antibiotics such as gramicidin S and polymyxin B [13]. From a medicinal point of view, the presence of D-amino acids may provide interesting features for bioactivity of peptide-based molecules. For instance, D-Ala in the natural opioid pentapeptide dermorphin (Tyr-^DAla-Phe-Gly-Tyr-Pro-Ser-NH₂) has been shown to play a crucial role in binding to opioid receptors [50] while D-Phe in cyclic RGD-peptides can increase their affinity with cellular integrin receptors [51,52]. The presence of D-amino acids is necessary in bacteria to protect them from proteolysis. Among them, D-Ala and D-Glu are the most common to be incorporated in the peptidoglycan (PG) bacterial cell walls. Bacteria have also shown to generate other D-amino acids as well, such as D-Met, D-Leu, D-Phe and D-Tyr, to downregulate the PG synthesis and slow down metabolic activities to adapt to changes in the surrounding environment [53]. Interestingly, D-aa fluorescent derivatives have been proposed as *in situ* probes to study the PG synthesis and modification in live bacterial cells [54] while the incorporation of D-aa in antimicrobial peptides (AMPs) is attracting increasing interest as a well-known strategy to achieve high proteolytic resistance (haemolytic and proteases hydrolysis) and effectiveness against pathogenic bacteria [55].

From structural studies, D-aa residues have shown to determine an inversion of the peptides' spatial orientation compared to the L-peptides (**Figure 1.9**) by breaking the secondary structures of the peptides, thus providing enzymatic resistance and, *in vitro* and *vivo* bioavailability [56].

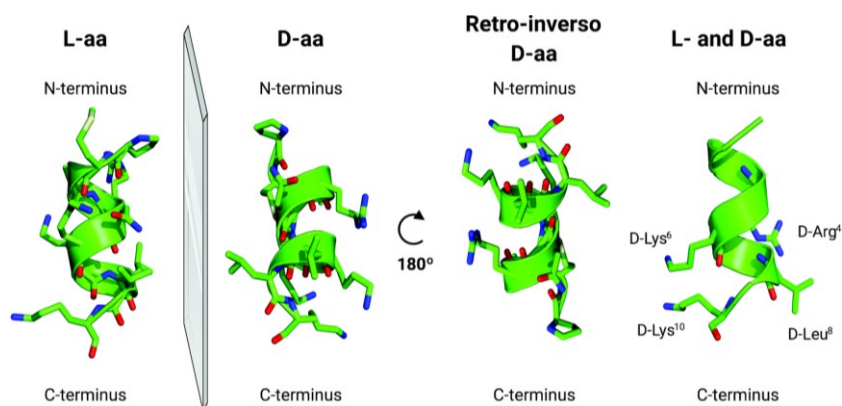


Figure 1.9. Insertion of D-amino acids into AMP sequences. An all-L-amino acid AMP can be submitted to a complete chirality change (mirror image), thus generating an all-D-amino acid AMP with an inverted spatial orientation and structural topology. AMPs can also be synthesized as the reverse sequence of their all-D-amino acid counterparts, thus generating retro-inverse AMPs. The incorporation of D-aa in all-L-amino acid AMPs generates diastereomeric AMPs [57]. Reproduced from ref [57] with permission from © 2021 Royal Society of Chemistry.

1.4.2. Effect of D-amino acids on self-assembly

From a functional point of view, the use of D-aa therapeutics is attractive due to their resistance to enzymatic degradation, leading to its application in medical devices. However, how the incorporation of D-aa (s) can affect the peptide sequence in terms of conformations, therapeutic effect and at supramolecular level is not always trivial to predict *a priori*, especially for short sequences such as dipeptides. In synthetic peptides, the introduction of one or more D-amino acids may induce significant changes in the secondary structure due to the different interactions between amino acids at supramolecular level. When present in a defined position in the backbone, D-residues may favour turn conformations, giving stability to the self-assembled short peptides [58]. By replacing each L-amino acid of a peptide sequence with its relative D-enantiomer, it is possible to investigate the importance rate of a particular amino acid, in the folding as well as in providing certain conformations with biological activity [59].

The substitution of block chirality motif in the primary sequence may also influence the level of molecular packing and the supramolecular arrangement of self-assembling peptides. For instance, *Rudra et al.* used the homochiral amphipathic peptide KFE8 (Ac-FKF₂FEFKFE-NH₂) as a model and

studied its block heterochiral analogues, composed of two repeat motifs (FKFE) with an opposite chirality (LD or DL). They showed that such block heterochiral peptides were able to self-assemble into helical nanotapes, unlike the fibril-forming homochiral counterparts (LL or DD), confirmed also by molecular dynamic (MD) modelling that elucidated the intermolecular interactions involved. Significant differences were observed in terms of average diameters across the homochiral and heterochiral samples by transmission electron microscopy (TEM). Compared to the homochiral peptides that formed fibers with a median diameter of ~ 8 nm, the dimension of the nanotapes were significantly higher (90% of samples 50-150 nm wide) with a broad width distribution. Furthermore, hydrogels derived from the self-assembly of heterochiral peptides maintained some viscoelastic properties observed in homochiral hydrogels, such as a shear-thinning behaviour and mechanical recovery, while the storage moduli (G') decreased. Hence, chirality changes in the primary sequence may significantly influence the supramolecular behaviour of self-assembling peptides in terms of packing, morphology and rheological properties [60].

The L/D isomerization even of a single amino acid is reported to alter the physicochemical properties of a peptide [61]. For instance, in 2012, *Marchesan et al.*, reported the first case of a small system based on unprotected hydrophobic tripeptides, containing both L- and D-amino acids able to self-assemble into a hydrogel under physiological conditions. A difference in chirality of the N-terminally amino acid, favoured the hydrogelation of the heterochiral (D-L-L) tripeptide into a self-supporting hydrogel whilst the L-analogue (L-L-L) did not self-assemble [62]. The key role of chirality to drive the self-assembly of different short hydrophobic tripeptides was elucidated by further investigations. Such studies demonstrated that the variable amino acid stereo configuration along the peptide sequence can direct the self-assembly into different supramolecular morphologies (*i.e.*, nanotapes, nanoparticles, aggregates,..) and the increased hydrophobicity due to the heterochirality may be a convenient strategy to promote hydrophobically-driven self-organization into nanomaterials [63,64]. A different spatial orientation of the side chains between the heterochiral tripeptides and homochiral analogue as well as the different supramolecular behaviour has recently been reported. The heterochirality promoted the orientation of the side chains on the same side of the peptide backbone, contrarily to the L-analogues. The result is that only heterochiral tripeptides displayed an amphipathic conformation due to a net segregation between hydrophilic and hydrophobic regions that allowed to achieve the self-organization into hydrogels [65,66] (**Figure 1.10**).

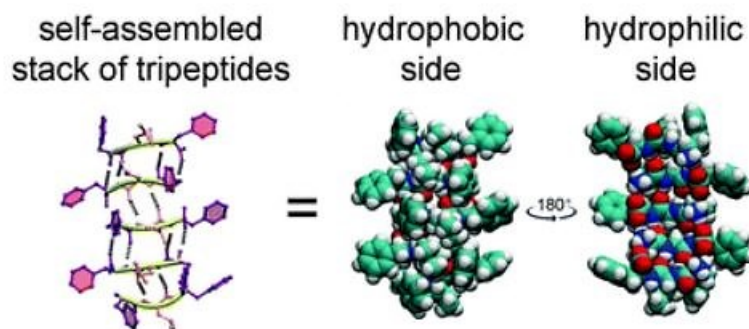


Figure 1.10. Antiparallel β -sheets of Phe^DLeu-Phe display a hydrophobic and a hydrophilic surface. Reproduced from ref with permission from © 2016 Royal Society of Chemistry.

Another noteworthy aspect to consider is that heterochirality allows also to modulate the enzymatic degradation rate of a peptide. This is due to not only to the strategical position of the D- and L- amino acids along the sequence but also to the level of supramolecular packing that can hinder some specific enzymatic molecular sites and prevent their enzymatic hydrolysis [63,67]. As a result, the presence of one or more unnatural D-aa increases the enzymatic proteolytic resistance of supramolecular hydrogelators derived from small peptides and such findings generate motivation for employing biomaterials bearing D-amino acids as simple building blocks. To test the enzymatic processing of a peptide *in vitro*, several enzymes can be chosen (*i.e.*, matrix metalloproteinases (MMP), chymotrypsin, collagenase or cathepsin B). Among them, Proteinase K, a serine protease isolated from *Tritirachium album*, is the most frequently used for this purpose due to its hydrolytic activity on a broad spectrum of peptide substrates [68,69]. However, the potential ability of some enzymes to act beyond their physiological reactions and their natural substrates, the so called “enzymatic promiscuity”, allows to further broad the application of such enzymes in chemistry [70]. For instance, it is possible to use hydrolase enzymes in reverse, such as lipases, under thermodynamic control to synthesize peptides consisting of both D- and L- amino acids as building blocks for molecular self-assembly [71,72]. The choice to introduce one or more non proteogenic D-amino acids inside the peptide sequence aims at increasing the peptide resistance to enzymatic degradation; the presence of both D- and L- amino acids is also interesting because it is a feature important to have self-assembling peptides and gelation. It is true that a dynamic equilibrium is present but even if a little amount of product is able to self-assemble, it will be able to push up the equilibrium towards its formation [73]. The presence of one or more unproteogenic D-amino acids inside a peptide may unfavour the hydrolysis of unnatural peptide bonds by the enzyme that will be more inclined to work in the opposite direction. Incorporation of D-amino acids inside the sequence can be convenient to broad terms of

stability, potency, permeability, bioavailability of peptide-based therapeutics. Conversely, undesired effects such as toxicity or immunogenicity should also be considered.

1.5. Biomedical applications of peptide-based materials

To date, the use of peptides for drugs and bioactive molecules has gained an increasing importance as alternative to protein therapeutics because of their advantages such as simplicity of synthesis and low cost. New structural and functional properties, such as self-healing, shape-memory, mechanical strength and bioactivity, can be easily introduced in peptide-based materials through chemical modifications, by further broadening their scope for biomedicine [74]. Furthermore, the unexpected advantages of peptides containing D-amino acids, in terms of enhanced proteolytic stability and improved lifetime and function in biological environment, make them ideal candidates for use in biomedical fields [14].

1.5.1. Drug delivery and regenerative medicine

Nowadays, drug delivery is probably one of the main fields in which short peptide-based systems have found promising applications, especially in place of other types of nanomaterials (*i.e.*, inorganic nanoparticles, liposomes, polymers, etc.) that may be difficult to functionalize or that may arise safety concerns in living systems [16]. Among the well-defined peptide-based assemblies, nanostructured hydrogels have a great importance as soft materials to be used as drug-delivery vehicles. Thanks to their three-dimensional (3D) network, they are able to swell and retain a large amount of water and acquire physicochemical properties similar to the natural soft tissues. The porous structure of the hydrogel thus allows drug loading into the matrix, and they can be designed for on-demand cargo release using specific triggering factors (*i.e.*, temperature, pH, ionic strength, etc.) at the target site [16]. This allows for a precise control over the amount of drug and its release rate in a site-specific way. In general, this could have numerous advantages over conventional therapeutics' release, such as enhanced bioavailability of the drug and decreased systemic side effects in the body, thus improving the patient's well-being [75]. The incorporation of the drug into the peptide-based self-assembled system can be carried out through three different pathways, classified according to the type of interactions involved between the cargo molecule and the delivery system. They are divided as follows: *i*) physical entrapment of the drug inside the matrix, *ii*) peptide-hydrogel drug non covalent interactions *iii*) drug covalent binding into the carrier. The therapeutic outcome usually depends on the drug release mechanism [76]. In recent years, great progress has also been made in the conjugation

of peptide and nanoparticles for biomedical use, including drug delivery, especially to solve many drawbacks related to the stability and suitable lifetime of therapeutic nanoparticles [77].

Self-assembled peptide systems have also been found applications in the field of immunotherapy, as carrier agents of antigens constituting vaccines [78] with benefits coming also from their ability to induce body immune response without additional immunological adjuvants [79,80]. The ability of short peptide to self-assemble into hydrogels with an outstanding biocompatibility, biodegradability, and soft tissue mimicry, place them in a prominent position for tissue engineering and regenerative medicine applications. Inspired by the biological extracellular matrix (ECM) that sustains individual cells and facilitates communications between them within a 3D network, self-assembly peptides are designed to produce engineered-tissue scaffolds mimicking the natural nanofibrous network of the extracellular matrix. Such peptide biomimetic scaffolds used in 3D cell culture, enable cell attachment and viability and provide mechanical support for cell proliferation by featuring a cell-adhesion peptide, a short amino-acid motif that promotes interactions between cells and the matrix [81]. These synthetic peptide fibrillar networks may be able to mimic the fibrillar assemblies and their relative properties of glycosaminoglycans (GAGs) and collagens, the main protein components of ECM (**Figure 1.11**).

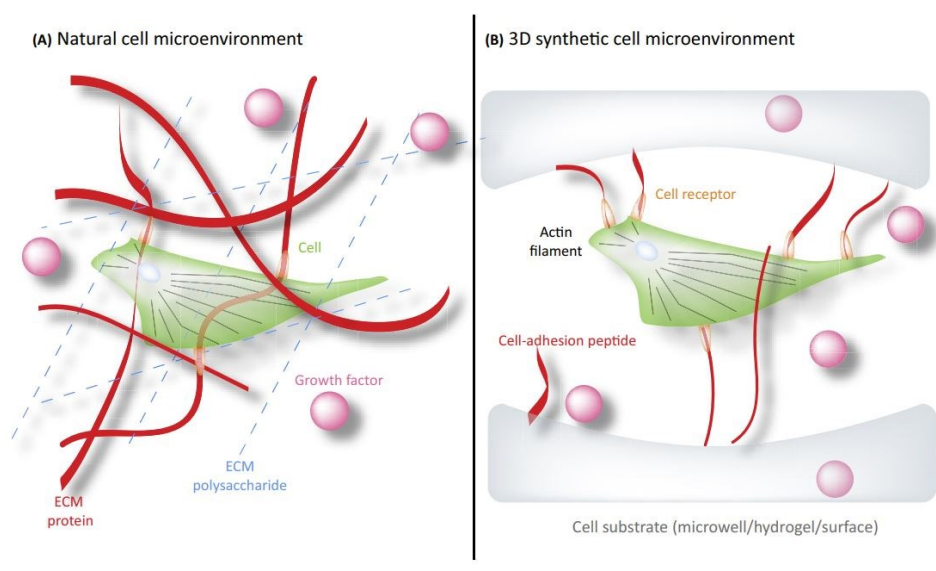


Figure 1.11. Comparison between Natural Tissue and Synthetic Cell Microenvironment. (A) In the native extracellular matrix, cells attach through cell receptors to polysaccharides and proteins. (B) 3D synthetic cell microenvironment made of a substrate with defined mechanical properties functionalized with peptide sequences able to bind to cell receptors. Reprinted from [81], Copyright © 2018 with permission from Elsevier.

Nowadays, developing hierarchically organized functional collagen structures such as bone tissue or corneal is still challenging, despite of the widespread use of collagen as structural scaffold in tissue engineering. For this reason, collagen-like peptide amphiphiles have been extensively studied and

appeared promising collagen substitutes. For instance, the system formed by a collagen-like peptide (12-mer peptide) coupled to a hydrophobic fatty acid chain (C16), was shown to self-assemble into hierarchically organized nanofibrous structures. Such biomimetic scaffold showed its potential to mimic the bioactive function of collagen. Indeed, the resulting material can serve as soft- and hard-tissue guiding scaffolds, by directing and sustaining the growth of both hydroxyapatite biominerals and bone cells [82]. The possibility to incorporate different functional components into self-assemble peptide network, gives them ample scope for specific applications [83] and different biomimetic scaffolds derived from the assembly of several short-peptides, can offer optimal microenvironment for a variety of mammalian cell cultures, including fibroblast and keratinocytes [84]. Further advantages such as the enzymatic resistance to proteases secreted by cells and an increase durability of the scaffold, can be achieved introducing D-residues into the self-assembling peptide sequence [85].

1.5.2. Antimicrobial agents

Antimicrobial peptides (AMPs) represent a powerful strategy to combat the current crisis due to the spreading of multidrug-resistant bacteria [86]. The design of self-assembled peptide into supramolecular structures able to destabilize interfaces or surfaces, including those forming biological membranes, has been explored as a strategy to develop novel antimicrobial agents. Peptide-based systems have attracted great interest because of their biodegradability and their benign fate in the environment. Inspirations for their design can be found in endogenous AMPs, well-known to be the first line of defence against pathogenic microorganisms [87]. Nanostructures and even macroscopic hydrogels derived from the ultrashort peptides (*i.e.*, 2-3 amino acids) hold great potential as novel antimicrobial materials, envisaged to work alone or in combination with other antibiotics or antibacterial drugs [88,89]. In comparison to proteins or other macromolecular systems, ultrashort peptide sequence display lots of advantages such as low-cost of production, ease of preparation and lower immunogenicity. Based on weak and non-covalent interactions, supramolecular hydrogels derived from self-assembling small molecules can be disrupted and reformed with a small energy requirement allowing fine control over their formation and disassembly. This could pave the way for the development of smart systems, whose antimicrobial activity can be switched on/off *on demand*, by releasing biodegradable molecules in the environment to address concerns over drug-pollution and antimicrobial resistance [90,91]. Both the stability and the activity of a peptide can be generally improved due to the presence of D-amino acid (s) inside the sequence. The peptide receptor recognition can be enhanced as well [92]. In literature, amyloids structures derived from the amyloid beta (A β) peptide have been showed to display antimicrobial activity against bacteria and even viruses

[93,94] for instance, by forming amphipathic peptide channels able to disrupt pathogens membranes through specific interactions. Thus, a link between amyloid beta (A β) peptide and self-assembled amyloid peptide sequences has been deeply investigated for the development of innovative peptide-based antimicrobial agents such as in the case of Phe-Phe [95] and Fmoc-Phe [96]. The latter, has shown to display antibacterial activity both in the gel and solution phases, due to the release of the soluble molecule (from the hydrogel network) that alters bacteria membrane permeabilization and integrity by exhibiting a surfactant-like behaviour [96]. The comprehension of the relationship between chemical structure and antimicrobial activity for short peptide sequences remains always challenging.

1.5.3. Water-channels in biomedicine and other applications

Nowadays, water-filled peptide nanotubes have found great attention especially as antimicrobial agents as they could potentially insert into bacteria membranes, alter cell permeability and lead to cell death. In this context, Phe-Phe can be far considered the shortest peptide based antimicrobial agents for its ability to self-assemble into supramolecular nanostructures with specific membrane interaction and disrupting activity [95]. Nanotubes formed also by stacks of cyclic peptides, beyond linear short peptide sequences, were studied for the discovery of novel therapeutic agents, aiming to discover the relationship between their structure and mechanism of action [97]. Besides the aim to treat infections, peptide-based water channels have attracted great interest for the design of new therapies to treat serious diseases such as channelopathies, due to a down regulation of ion channels and transporters that usually regulate the ion homeostasis [98]. Taking inspiration from natural water translocating channels, well-known as aquaporin (AP), several attempts have been reported to design water-channels that also mimic such natural structures for several purposes, ranging from the treatment of AQP-related diseases (such as congenital cataracts and nephrogenic diabetes insipidus) to desalination [99]. Furthermore, water-filled nanotubes can find application as green devices for energy storage and conversion that do not persist in the environment by showing proton conductivity [100]. For short peptides, the rules to understand 1) which sequences can assemble into macroscopic hydrogels through the formation of water-channels 2) which are the structural rules behind this spatial rearrangement and 3) if the peptide sequence can influence the number of molecules that define the inner cavity, are still a challenge and one of the purposes of such thesis will be shed light on these points.

References

- [1] X. Du, J. Zhou, J. Shi, B. Xu, *Chem. Rev.* **2015**, *115*, 13165–13307.
- [2] R. Aizen, K. Tao, S. Rencus-Lazar, E. Gazit, *J. Nanopart. Res.* **2018**, *20*, 125.
- [3] S. Tadepalli, J. M. Slocik, M. K. Gupta, R. R. Naik, S. Singamaneni, *Chem. Rev.* **2017**, *117*, 12705–12763.
- [4] J. D. Perlmutter, M. F. Hagan, *Annu. Rev. Phys. Chem.* **2015**, *66*, 217–239.
- [5] R. A. J. F. Oerlemans, S. B. P. E. Timmermans, J. C. M. van Hest, *ChemBioChem* **2021**, *22*, 2051–2078.
- [6] S. Zhang, *Biotechnol. Adv.* **2002**, *20*, 321–339.
- [7] F. Lossada, D. Hoenders, J. Guo, D. Jiao, A. Walther, *Acc. Chem. Res.* **2020**, *53*, 2622–2635.
- [8] A. G. Dumanli, T. Savin, *Chem. Soc. Rev.* **2016**, *45*, 6698–6724.
- [9] J. Zhou, J. Li, X. Du, B. Xu, *Biomaterials* **2017**, *129*, 1–27.
- [10] I. W. Hamley, *Chem. Rev.* **2017**, *117*, 14015–14041.
- [11] A. Levin, T. A. Hakala, L. Schnaider, G. J. L. Bernardes, E. Gazit, T. P. J. Knowles, *Nat. Rev. Chem.* **2020**, *4*, 615–634.
- [12] C. M. Rubert Pérez, N. Stephanopoulos, S. Sur, S. S. Lee, C. Newcomb, S. I. Stupp, *Ann. Biomed. Eng.* **2015**, *43*, 501–514.
- [13] Y. Ding, J. P. Ting, J. Liu, S. Al-Azzam, P. Pandya, S. Afshar, *Amino Acids* **2020**, *52*, 1207–1226.
- [14] H. M. Werner, C. C. Cabalteja, W. S. Horne, *ChemBioChem* **2016**, *17*, 712–718.
- [15] S. Marchesan, A. V. Vargiu, K. E. Styan, *Molecules* **2015**, *20*, 19775–19788.
- [16] J. J. Panda, V. S. Chauhan, *Polym. Chem.* **2014**, *5*, 4418–4436.
- [17] J. Wang, K. Liu, R. Xing, X. Yan, *Chem. Soc. Rev.* **2016**, *45*, 5589–5604.
- [18] D. M. Raymond, B. L. Nilsson, *Chem. Soc. Rev.* **2018**, *47*, 3659–3720.
- [19] E. Gazit, **2019**, *87*, 533–553.
- [20] M. Reches, E. Gazit, *Science* **2003**, *300*, 625–627.
- [21] G. Fichman, E. Gazit, *Acta Biomater.* **2014**, *10*, 1671–1682.

- [22] V. Jayawarna, A. Smith, J. E. Gough, R. V Ulijn, *Biochem. Soc. Trans.* **2007**, *35*, 535–537.
- [23] S. Toledano, R. J. Williams, V. Jayawarna, R. V. Ulijn, *J. Am. Chem. Soc.* **2006**, *128*, 1070–1071.
- [24] A. M. Smith, R. J. Williams, C. Tang, P. Coppo, R. F. Collins, M. L. Turner, A. Saiani, R. V. Ulijn, *Adv. Mater.* **2008**, *20*, 37–41.
- [25] W. T. Truong, Y. Su, D. Gloria, F. Braet, P. Thordarson, *Biomater. Sci.* **2015**, *3*, 298–307.
- [26] J. J. Panda, R. Dua, A. Mishra, B. Mitra, V. S. Chauhan, *ACS Appl. Mater. Interfaces* **2010**, *2*, 2839–2848.
- [27] R. Orbach, L. Adler-Abramovich, S. Zigerson, I. Mironi-Harpaz, D. Seliktar, E. Gazit, *Biomacromolecules* **2009**, *10*, 2646–2651.
- [28] A. D. Martin, P. Thordarson, *J. Mater. Chem. B* **2020**, *8*, 863–877.
- [29] L. Adler-Abramovich, L. Vaks, O. Carny, D. Trudler, A. Magno, A. Caflisch, D. Frenkel, E. Gazit, *Nat. Chem. Biol.* **2012**, *8*, 701–706.
- [30] R. Martí-Centelles, B. Escuder, *ChemNanoMat* **2018**, *4*, 796–800.
- [31] C. H. Görbitz, *Chem. Commun.* **2006**, *22*, 2332–2334.
- [32] C. H. Görbitz, *Chem. - A Eur. J.* **2007**, *13*, 1022–1031.
- [33] C. H. Görbitz, *Acta Crystallogr. Sect. C* **2006**, *62*, o328-o330.
- [34] H. Birkedal, D. Schwarzenbach, P. Pattison, *Angew. Chemie* **2002**, *114*, 780–782.
- [35] T. J. Emge, A. Agrawal, J. P. Dalessio, G. Dukovic, J. A. Inghrim, K. Janjua, M. Macaluso, L. L. Robertson, T. J. Stiglic, Y. Volovik, M. M. Georgiadis, *Acta Crystallogr. Sect. C* **2000**, *56*, e469-e471.
- [36] C. H. Görbitz, *Chem. – A Eur. J.* **2001**, *7*, 5153–5159.
- [37] N. Yadav, M. K. Chauhan, V. S. Chauhan, *Biomater. Sci.* **2020**, *8*, 84–100.
- [38] X. Hu, M. Liao, H. Gong, L. Zhang, H. Cox, T. A. Waigh, J. R. Lu, *Curr. Opin. Colloid Interface Sci.* **2020**, *45*, 1–13.
- [39] A. S. Mahadevi, G. N. Sastry, *Chem. Rev.* **2016**, *116*, 2775–2825.
- [40] C. Wu, Z. Zheng, Y. Guo, C. Tian, Q. Xue, G. Liang, *Nanoscale* **2017**, *9*, 11429–11433.

- [41] D. M. Ryan, S. B. Anderson, B. L. Nilsson, *Soft Matter* **2010**, *6*, 3220–3231.
- [42] D. M. Ryan, S. B. Anderson, F. T. Senguen, R. E. Youngman, B. L. Nilsson, *Soft Matter* **2010**, *6*, 475–479.
- [43] R. Thakuria, N. K. Nath, B. K. Saha, *Cryst. Growth Des.* **2019**, *19*, 523–528.
- [44] C. A. Hunter, J. K. M. Sanders, *J. Am. Chem. Soc.* **1990**, *112*, 5525–5534.
- [45] P. W. J. M. Frederix, G. G. Scott, Y. M. Abul-Haija, D. Kalafatovic, C. G. Pappas, N. Javid, N. T. Hunt, R. V. Ulijn, T. Tuttle, *Nat. Chem.* **2015**, *7*, 30–37.
- [46] N. Singh, M. Kumar, J. F. Miravet, R. V. Ulijn, B. Escuder, *Chem. - A Eur. J.* **2017**, *23*, 981–993.
- [47] J. Paterová, K. B. Rembert, J. Heyda, Y. Kurra, H. I. Okur, W. R. Liu, C. Hilty, P. S. Cremer, P. Jungwirth, *J. Phys. Chem. B* **2013**, *117*, 8150–8158.
- [48] R. V. Ulijn, A. M. Smith, *Chem. Soc. Rev.* **2008**, *37*, 664–675.
- [49] I. Kaneko, N. Yamada, Y. Sakuraba, M. Kamenosono, S. Tutumi, *J. Neurochem.* **1995**, *65*, 2585–2593.
- [50] M. Amiche, A. Delfour, P. Nicolas, *Int. J. Pept. Protein Res.* **1988**, *32*, 28–34.
- [51] R. Haubner, R. Gratias, B. Diefenbach, S. L. Goodman, A. Jonczyk, H. Kessler, *J. Am. Chem. Soc.* **1996**, *118*, 7461–7472.
- [52] H. Vilaça, P. M. T. Ferreira, N. M. Micaelo, *Tetrahedron* **2014**, *70*, 5420–5427.
- [53] H. Lam, D.-C. Oh, Cava, Felipe, C. N. Takacs, C. Jon, M. a. de Pedro, M. K. Waldor, *Science* **2009**, *325*, 1552–1555.
- [54] Y. P. Hsu, G. Booher, A. Egan, W. Vollmer, M. S. Vannieuwenhze, *Acc. Chem. Res.* **2019**, *52*, 2713–2722.
- [55] S. Kapil, V. Sharma, *Can. J. Microbiol.* **2021**, *67*, 119–137.
- [56] S. B. Rezende, K. G. N. Oshiro, N. G. O. Júnior, O. L. Franco, M. H. Cardoso, *Chem. Commun.* **2021**, *57*, 11578–11590.
- [57] S. B. Rezende, K. G. N. Oshiro, N. G. O. Júnior, O. L. Franco, M. H. Cardoso, *Chem. Commun.* **2021**, *57*, 11578–11590.
- [58] Y. Ozawa, H. Sato, Y. Kayano, N. Yamaki, Y. I. Izato, A. Miyake, A. Naito, I. Kawamura,

Phys. Chem. Chem. Phys. **2019**, *21*, 10879–10883.

- [59] V. J. Hruby, *Nat. Rev. Drug Discov.* **2002**, *1*, 847–858.
- [60] T. M. Clover, C. L. O'Neill, R. Appavu, G. Lokhande, A. K. Gaharwar, A. E. Posey, M. A. White, J. S. Rudra, *J. Am. Chem. Soc.* **2020**, *142*, 19809–19813.
- [61] D. H. Mast, J. W. Checco, J. V. Sweedler, *Biochim. Biophys. Acta - Proteins Proteomics* **2021**, *1869*, 140553.
- [62] S. Marchesan, C. D. Easton, F. Kushkaki, L. Waddington, P. G. Hartley, *Chem. Commun.* **2012**, *48*, 2195–2197.
- [63] S. Marchesan, K. E. Styan, C. D. Easton, L. Waddington, A. V. Vargiu, *J. Mater. Chem. B* **2015**, *3*, 8123–8132.
- [64] A. M. Garcia, M. Melchionna, O. Bellotto, S. Kralj, S. Semeraro, E. Parisi, D. Iglesias, P. D'Andrea, R. De Zorzi, A. V. Vargiu, S. Marchesan, *ACS Nano* **2021**, *15*, 3015–3025.
- [65] A. V. Vargiu, D. Iglesias, K. E. Styan, L. J. Waddington, C. D. Easton, S. Marchesan, *Chem. Commun.* **2016**, *52*, 5912–5915.
- [66] A. M. Garcia, D. Iglesias, E. Parisi, K. E. Styan, L. J. Waddington, C. Deganutti, R. De Zorzi, M. Grassi, M. Melchionna, A. V. Vargiu, S. Marchesan, *Chem* **2018**, *4*, 1862–1876.
- [67] M. Melchionna, K. E. Styan, S. Marchesan, **2016**, *16*, 2009–2018.
- [68] G. Liang, Z. Yang, R. Zhang, L. Li, Y. Fan, Y. Kuang, Y. Gao, T. Wang, W. W. Lu, B. Xu, *Langmuir* **2009**, *25*, 8419–8422.
- [69] D. Brömme, K. Peters, S. Fink, S. Fittkau, *Arch. Biochem. Biophys.* **1986**, *244*, 439–446.
- [70] O. K. and D. S. Tawfik, *Annu. Rev. Biochem.* **2010**, *79*, 471–505.
- [71] L. Chronopoulou, S. Lorenzoni, G. Masci, M. Dentini, A. R. Togna, G. Togna, F. Bordi, C. Palocci, *Soft Matter* **2010**, *6*, 2525–2532.
- [72] L. Chronopoulou, A. R. Togna, G. Guarguaglini, G. Masci, F. Giammaruco, G. I. Togna, C. Palocci, *Soft Matter* **2012**, *8*, 5784–5790.
- [73] C. G. Pappas, R. Shafi, I. R. Sasselli, H. Siccardi, T. Wang, V. Narang, R. Abzalimov, N. Wijerathne, R. V. Ulijn, *Nat. Nanotechnol.* **2016**, *11*, 960–967.
- [74] J. Chen, X. Zou, *Bioact. Mater.* **2019**, *4*, 120–131.

- [75] J. Mayr, C. Saldías, D. Díaz Díaz, *Chem. Soc. Rev.* **2018**, *47*, 1484–1515.
- [76] D. Iglesias, S. Marchesan, *Short Peptide Self-Assembled Nanostructures for Therapeutics Innovative Delivery*, Elsevier Inc., **2017**.
- [77] C. D. Spicer, C. Jumeaux, B. Gupta, M. M. Stevens, *Chem. Soc. Rev.* **2018**, *47*, 3574–3620.
- [78] D. F. Zeigler, E. Gage, R. Roque, C. H. Clegg, *npj Vaccines* **2019**, *4*, 1-8.
- [79] G. A. Hudalla, T. Sun, J. Z. Gasiorowski, H. Han, Y. F. Tian, A. S. Chong, J. H. Collier, *Nat. Mater.* **2014**, *13*, 829–836.
- [80] H. Wang, Z. Luo, Y. Wang, T. He, C. Yang, C. Ren, L. Ma, C. Gong, X. Li, Z. Yang, *Adv. Funct. Mater.* **2016**, *26*, 1822–1829.
- [81] N. Huettner, T. R. Dargaville, A. Forget, *Trends Biotechnol.* **2018**, *36*, 372–383.
- [82] H. E. Jin, J. Jang, J. Chung, H. J. Lee, E. Wang, S. W. Lee, W. J. Chung, *Nano Lett.* **2015**, *15*, 7138–7145.
- [83] J. H. Collier, J. S. Rudra, J. Z. Gasiorowski, J. P. Jung, *Chem. Soc. Rev.* **2010**, *39*, 3413–3424.
- [84] S. Zhang, T. C. Holmes, C. M. DiPersio, R. O. Hynes, X. Su, A. Rich, *Biomaterials* **1995**, *16*, 1385–1393.
- [85] Z. Luo, Y. Yue, Y. Zhang, X. Yuan, J. Gong, L. Wang, B. He, Z. Liu, Y. Sun, J. Liu, M. Hu, J. Zheng, *Biomaterials* **2013**, *34*, 4902–4913.
- [86] B. P. Lazzaro, M. Zasloff, J. Rolff, *Science* **2020**, *368*, aau5480.
- [87] M. Erdem Büyükkiraz, Z. Kesmen, *J. Appl. Microbiol.* **2022**, *132*, 1573–1596.
- [88] L. Lombardi, A. Falanga, V. Del Genio, S. Galdiero, *Pharmaceutics* **2019**, *11*, 166.
- [89] J. Mayr, C. Saldías, D. Díaz Díaz, *Chem. Soc. Rev.* **2018**, *47*, 1484–1515.
- [90] S. Marchesan, Y. Qu, L. J. Waddington, C. D. Easton, V. Glattauer, T. J. Lithgow, K. M. McLean, J. S. Forsythe, P. G. Hartley, *Biomaterials* **2013**, *34*, 3678–3687.
- [91] M. Kurbasic, E. Parisi, A. M. Garcia, S. Marchesan, *Curr. Top. Med. Chem.* **2020**, *20*, 1300–1309.
- [92] H. Li, N. Anuwongcharoen, A. A. Malik, V. Prachayasittikul, J. E. S. Wikberg, C. Nantasenamat, *Int. J. Mol. Sci.* **2016**, *17*, 1–27.

- [93] B. L. Kagan, H. Jang, R. Capone, F. Teran Arce, S. Ramachandran, R. Lal, R. Nussinov, *Mol. Pharm.* **2012**, *9*, 708–717.
- [94] K. Bourgade, G. Dupuis, E. H. Frost, T. Fülöp, *J. Alzheimer's Dis.* **2016**, *54*, 859–878.
- [95] L. Schnaider, S. Brahmachari, N. W. Schmidt, B. Mensa, S. Shaham-Niv, D. Bychenko, L. Adler-Abramovich, L. J. W. Shimon, S. Kolusheva, W. F. Degrado, E. Gazit, *Nat. Commun.* **2017**, *8*, 1365.
- [96] A. Y. Gahane, P. Ranjan, V. Singh, R. K. Sharma, N. Sinha, M. Sharma, R. Chaudhry, A. K. Thakur, *Soft Matter* **2018**, *14*, 2234–2244.
- [97] B. Claro, E. González-Freire, M. Calvelo, L. J. Bessa, E. Goormaghtigh, M. Amorín, J. R. Granja, R. Garcia-Fandiño, M. Bastos, *Colloids Surfaces B Biointerfaces* **2020**, *196*, 111349.
- [98] G. Picci, S. Marchesan, C. Caltagirone, *Biomedicines* **2022**, *10*, 885.
- [99] L. B. Huang, M. Di Vincenzo, Y. Li, M. Barboiu, *Chem. - A Eur. J.* **2021**, *27*, 2224–2239.
- [100] J. Lerner Yardeni, M. Amit, G. Ashkenasy, N. Ashkenasy, *Nanoscale* **2016**, *8*, 2358–2366.

Chapter 2. Aim of the Thesis

Self-assembling amino acid derivatives and dipeptides have been raising researchers' interest as simple and low-cost building blocks for functional nanostructures and supramolecular soft matter. Applications are diverse and range from mimicry of the extracellular matrix for regenerative medicine and wound healing, to controlled release of therapeutics, selective entrapment of pollutants for environmental remediation, and more. In particular, inclusion of D-amino acids is an attractive strategy to modulate self-assembly and enable higher resistance against enzymatic hydrolysis to prolong their lifetime in biological environments. However, the design of such minimalistic self-assembling units is quite challenging, in light of the variety of molecular conformations they can adopt, in contrast with polyaromatic rigid molecules with very defined geometries.

Therefore, the aim of this project is to shed light and clearly identify molecular design rules for minimalistic dipeptides containing Phe that self-assemble into water-channels and biocompatible gels, for the future development of supramolecular biomaterials with fine control over nanomorphological features. In particular, this thesis firstly describes the self-assembling behaviour, in physiological conditions, of an N-capped Phe derivative, *i.e.*, *N*-(4-nitrobenzoyl)-Phe, (**Figure 2.1**), described in *Manuscript 1*, for applications as antimicrobial hydrogel.

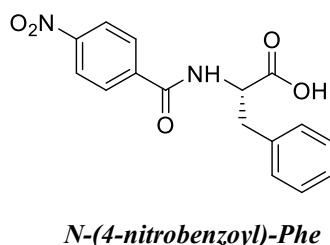


Figure 2.1. Chemical structure of the *N*-(4-nitrobenzoyl)-Phe. (*Manuscript 1*)

Next, the N-cap will be substituted with D-Phe, and heterochirality of D-Phe-L-Phe (**Figure 2.2**) will be studied for its effects on the hierarchical self-assembly to overcome the cytotoxicity of L-Phe-L-Phe, as described in *Manuscript 2*.

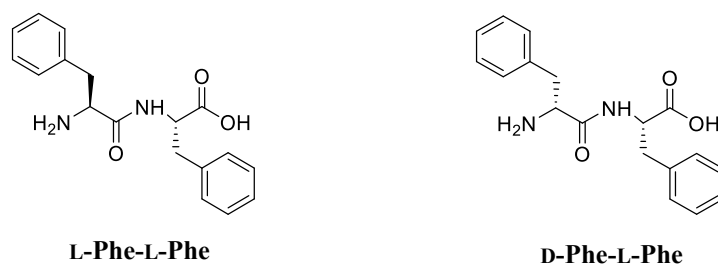


Figure 2.2. Chemical structures of the diphenylalanine, homochiral (left) and heterochiral (right) (*Manuscript 2*)

Then, halogenation on various positions (*i.e.*, *ortho*, *meta*, or *para*) of the aromatic ring of Phe will be studied for its effects on self-assembly and hydrogelation. In particular, halogenation on either the N-terminus (**Figure 2.3**) or the C-terminus (**Figure 2.4**) will be investigated, as described in *Manuscripts 2 and 3*.

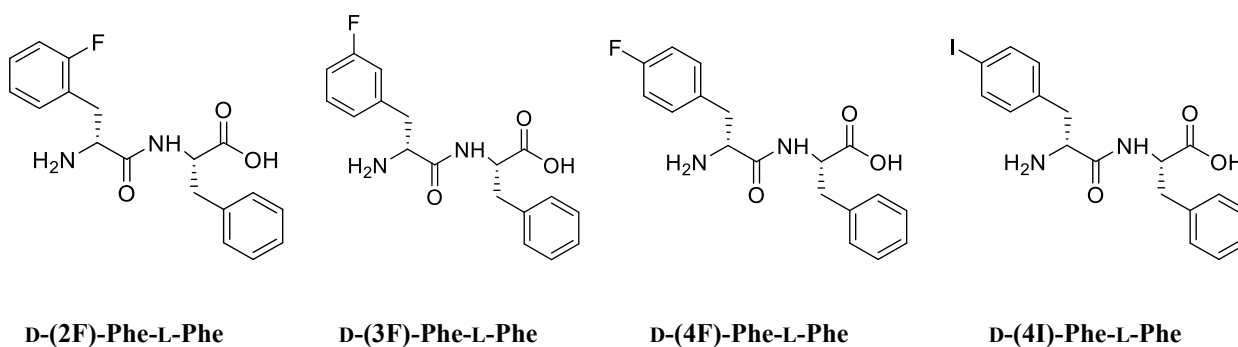


Figure 2.3. Chemical structures of the halogenated N-terminus of D-Phe-L-Phe (*Manuscript 2*).

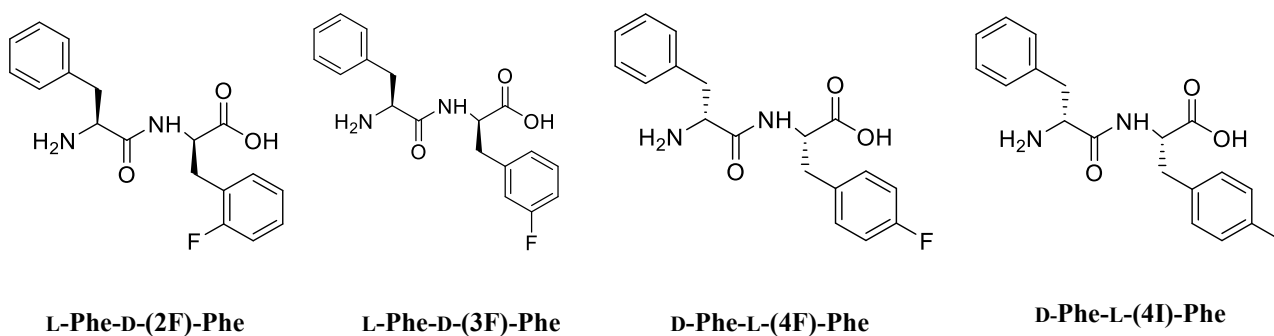


Figure 2.4. Chemical structures of the halogenated C-terminus of D-Phe-L-Phe. (*Manuscript 3*).

As the use of another aliphatic hydrophobic amino acid (*i.e.*, Leu, Ile or Val) in place of an aromatic group in the sequence could be considered an interesting alternative to achieve biomaterials from unprotected dipeptides, the supramolecular behaviour of different dipeptides' libraries will be explored as well as their potential cytotoxicity (**Figures 2.5-2.7**), as described in *Manuscripts 4-6*, respectively. In particular, the position of both D- and L-amino acids along the peptide sequence as well as the different sidechain of each amino acid will be studied for their influence in the self-assembly process. Considering that all possible stereoconfigurations of dipeptides lead to 8 stereoisomers, consisting of 4 enantiomeric couples, we will focus our studies solely on the non-enantiomeric compounds, since enantiomers have the same physicochemical properties, thus analogous self-assembling behaviour in achiral environments.

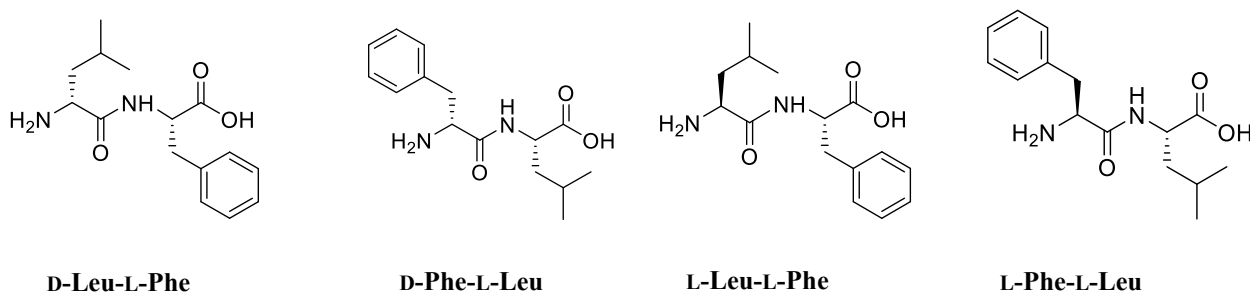


Figure 2.5. Chemical structures of dipeptides bearing Phe and Leucine as building blocks. (*Manuscript 4*)

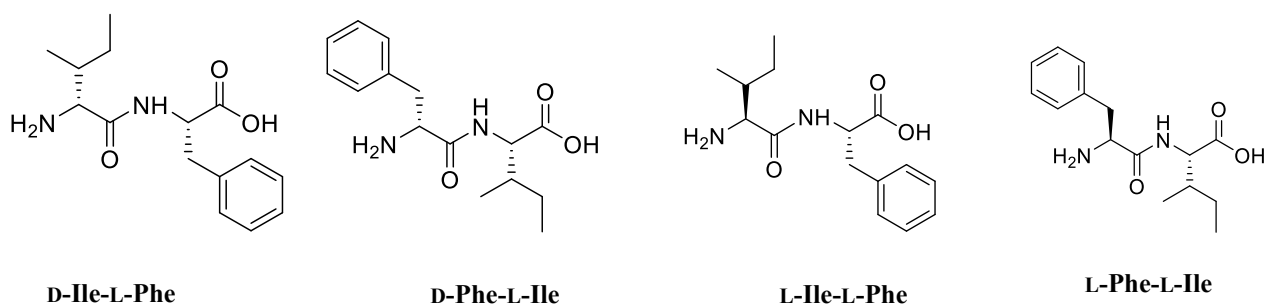


Figure 2.6. Chemical structures of dipeptides bearing Phe and Isoleucine as building blocks. (*Manuscript 5*)

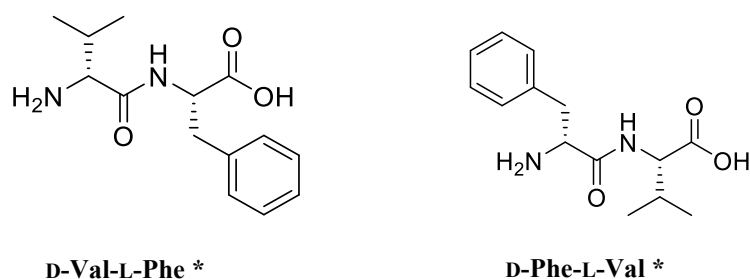


Fig 2.7. Chemical structures of the heterochiral dipeptides bearing Phe and Valine as building blocks (*Manuscript 6*)
*Homochiral sequences already reported in literature, Val-Phe^[1] and Phe-Val^[2] respectively.

The experimental plan includes solid-phase peptide synthesis (SPPS), reverse-phase high-performance liquid chromatography (RP-HPLC) purification, freeze-drying, ¹H- and ¹³C-NMR spectroscopy and electrospray ionization-mass spectrometry (ESI-MS) characterization to verify peptide identity and purity. Self-assembly will be probed in phosphate-buffered solutions, and the supramolecular behaviour will be probed by circular dichroism spectroscopy (CD), attenuated total reflectance infrared spectroscopy (ATR-IR), amyloid fluorescence assays, single-crystal, and powder X-ray diffraction (XRD), optical microscopy, and transmission electron microscopy (TEM). Finally, cytotoxicity assays (live/dead and MTT assays) will be performed on mammalian cells lines (*i.e.*, fibroblast, keratinocytes) to identify the best hydrogel candidates for future biomedical applications.

References

- [1] N. S. De Groot, T. Parella, F. X. Aviles, J. Vendrell, S. Ventura, *Biophys. J.* **2007**, *92*, 1732–1741.
- [2] M. Kurbasic, S. Semeraro, A. M. Garcia, S. Kralj, E. Parisi, C. Deganutti, R. De Zorzi, S. Marchesan, *Synthesis (Stuttg)*. **2019**, *51*, 2829–2838.

Chapter 3. Self-assembly of *N*-(4-nitrobenzoyl)-L-Phe into a hydrogel

This chapter describes the work of *Manuscript 1*, entitled “*Self-assembly of an amino acid derivative into an antimicrobial hydrogel biomaterial*” [1].

3.1. Introduction

Supramolecular hydrogels formed by protected amino acids or short peptides have become popular biomaterials, by virtue of their simple and low-cost preparation in comparison with longer peptides, as well as their inherent compatibility with biological systems [2–5]. In the case of single amino acids, examples of self-assembly have been reported thus far, with phenylalanine (Phe) being in a privileged position due to its aromatic and hydrophobic nature [6–9]. In this case, even the unprotected amino acid self-assembles at very high concentrations in environments as complex as whole cells [8]. In water, Phe was first reported to form polymorphic systems that featured a mixture of crystals and a gel phase [10]. Simple inclusion of non-gelling additives, such as other amino acids, was a successful strategy to tailor the physical properties of the supramolecular hydrophobic system [11]. In aqueous environments, aromatic interactions and hydrogen bonding play a key role for the self-assembly of low-molecular-weight gelators, and also of their derivatives with polymers [12,13]. Hydrogelation of molecules as simple as amino acids can be favored with rigid and aromatic N-capping groups, which reduce the solubility in aqueous media and facilitate hydrophobic interactions that drive self-assembly. Different examples have been described to date, with fluorenylmethyloxycarbonyl (Fmoc) being the most popular appendage, followed by naphthalene [9][14,15]. In particular, use of a naphthaleneimide N-cap led to fluorescent fibrils that could be used for imaging purposes [16]. Alternatively, pyrene was successfully applied to obtain a tryptophan-based gel in phosphate buffer at neutral pH for encapsulation of biomolecules [17]. Alkyl-chain N-acylations have also been explored, although prediction of the supramolecular behavior of these derivatives is far from trivial [18]. For instance, in the case of *N*-lauroyl-Phe, self-assembly into the unusual morphology of 2D sheets led to a weak hydrogel [18]; by contrast *N*-palmitoyl-Phe self-assembled into fibrils that yield a viscous solution [18]. Small-peptide hydrogels could find useful applications in the area of drug delivery and bioactive biomaterials, for instance in wound healing for burns or diabetic patients [19,20]. The shorter is the peptide (even a single amino acid), the lower will be the cost of production, and the ease of its scale-up. Additionally, concerns exist over the potential toxicity of polyaromatic cycles, which should be carefully evaluated since cell viability was negatively affected by Fmoc-derivatives [21,22]. Therefore, simpler analogues, which would still allow for gelation of small molecules to occur, would be preferable alternatives [9].

3.2. Self-assembly of *N*-(4-nitrobenzoyl)-L-Phe into a nanostructured hydrogel

N-(4-nitrobenzoyl)-Phe self-assembled into a nanostructured hydrogel in phosphate buffer saline, PBS, (**Figure 3.1 A**), without the aid of organic solvents. The minimum gelling concentration (MGC) corresponds to 20 mM, *i.e.*, 0.63 wt.%. TEM imaging (**Figure 3.1 B**) revealed low-contrast bundles of fibrils as thin as 5.0 ± 1.1 nm ($n = 100$). The hydrogel is thermoreversible with a gel-to-sol transition corresponding to 39-42 °C (**Figure 3.1 C**), giving scope to its use for therapeutic applications. If left to cool down to room temperature, the gel reformed within 10 minutes. Increasing the gelator concentration to 30 mM allowed to increase the gel-to-sol transition to 54-57 °C, thus confirming that the thermal behavior can be fine-tuned by varying the gelator concentration.

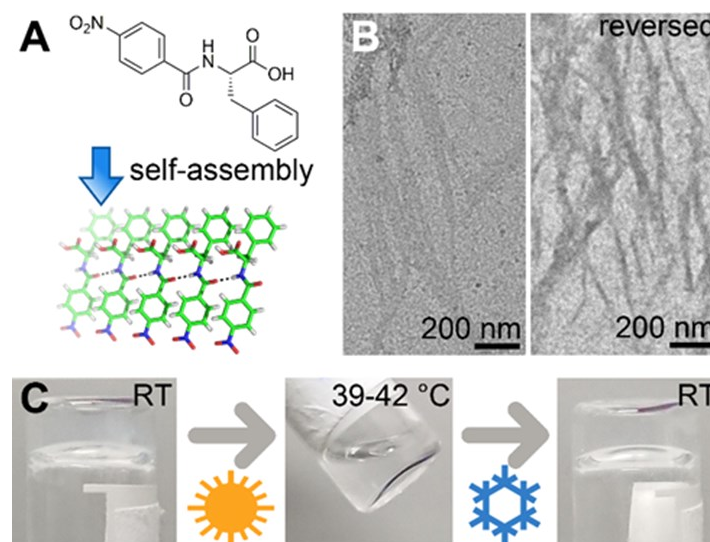


Figure 3.1. A) *N*-(4-nitrobenzoyl)-Phe self-assembles into parallel displaced stacks held together by hydrogen bonding ($d = 3.1$ Å) between the amide groups, as revealed by single-crystal XRD data. B) TEM images reveal low-contrast bundles of fibrils as thin as 5 nm, which are present also in the thermoreversed gel (right). C) The 20 mM hydrogel is transparent and thermoreversible within a range compatible with physiological conditions. Reproduced with permission from ref. [1] © 2020 John Wiley and Sons.

Oscillatory rheometry confirmed rapid gelation reaching a plateau within an hour (**Figure 3.2 A**) corresponding to an elastic or storage modulus G' of 2.0 kPa and a viscous or loss modulus G'' of 0.2 kPa. The hydrogel also displayed a high resistance [8] [12] to applied stress, with a linear viscoelastic regime maintained up to 40 Pa and a gel-to-sol transition occurring at nearly 100 Pa (**Figure 3.2 B**).

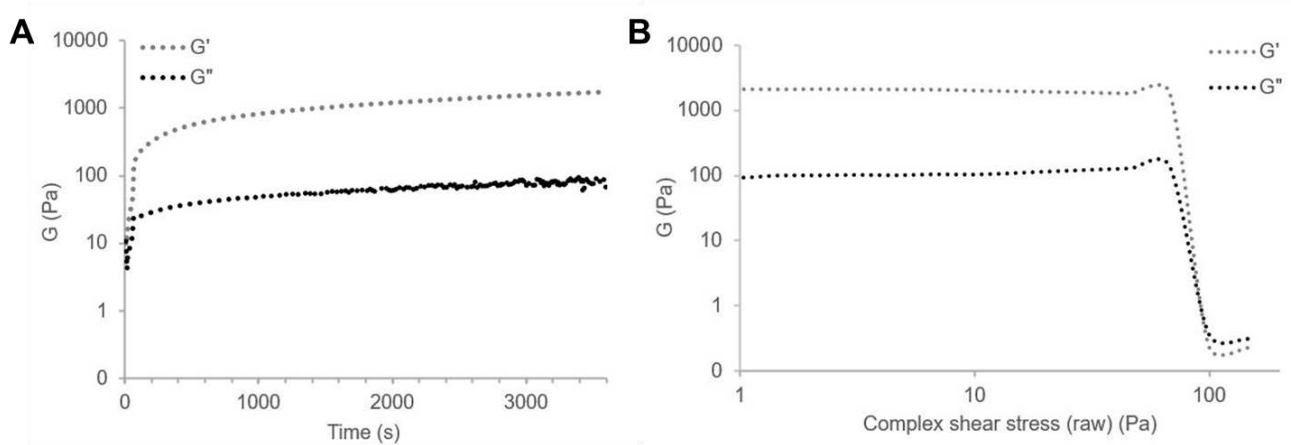


Figure 3.2. Rheology time (A) and stress (B) sweeps show rapid gelation kinetics with plateau reached within 1 hour and high resistance of the gel with failure occurring at nearly 100 Pa. Reproduced with permission from ref. [1] © 2020 John Wiley and Sons.

Frequency sweep analysis confirmed the gel state, with G' and G'' being independent from the applied frequency, and $G' > G''$ (**Figure 3.3**).

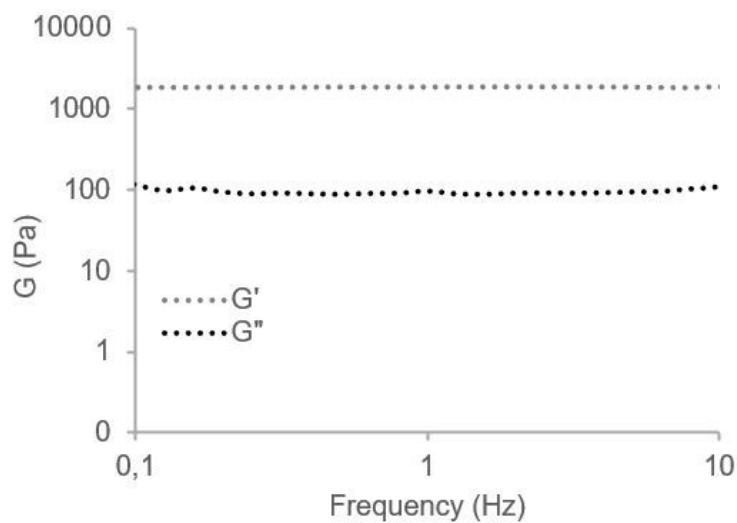


Figure 3.3. Frequency sweep data at 1 Pa after 1 h of self-assembly shows that a stable hydrogel was formed. Reproduced with permission from ref. [1] © 2020 John Wiley and Sons.

Temperature sweep analysis in the linear viscoelastic regime confirmed gel-to-sol transition occurred at ca. 40 °C (**Figure 3.4**).

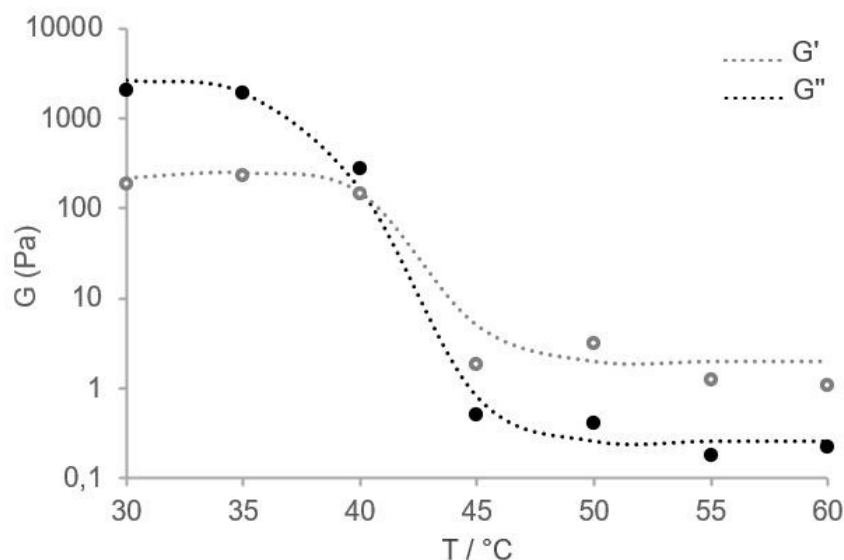


Figure 3.4. Temperature sweep data after 1 h of self-assembly at 1 Pa and 1 Hz. Reproduced with permission from ref. [1] © 2020 John Wiley and Sons.

3.3. Secondary structure analysis

The secondary structure can be analyzed by several techniques, such as circular dichroism (CD), Fourier-transformed Infrared (FT-IR) spectroscopy, and Thioflavin T fluorescence. It should be noted, however, that it is rather controversial to use traditional peptide conformational assignments in this case where there is only one amide bond. The purpose is purely for a comparison between spectral data of this work and the literature to shed light on the hydrogen bonding and packing organization. In the far-UV region of circular dichroism (CD) spectra (**Figure 3.5**), the minima at 220 and 240 nm are dominated by the $n-\pi^*$ transition characteristic of interactions between Phe side chains, thus impeding elucidation of the amide bond environment. The maximum at 280 nm can be attributed to the offset face-to-face stacking of the nitro-phenyl rings [23]. Unfortunately, the experimental conditions for self-assembly in PBS impede CD analysis below 220 nm.

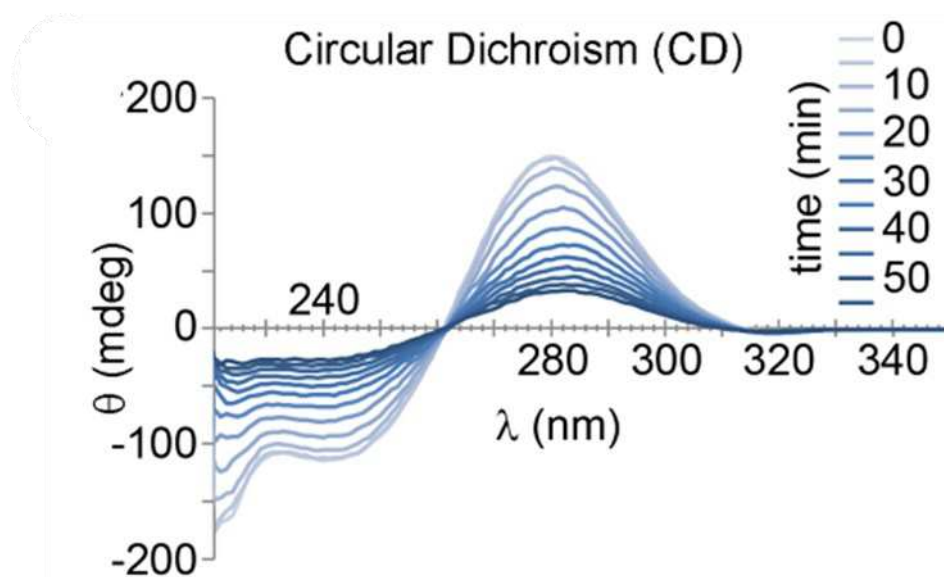


Figure 3.5. CD spectra evolution over 1 h of self-assembly. Reproduced with permission from ref. [1] © 2020 John Wiley and Sons.

The amide I band region of the FT-IR spectrum (**Figure 3.6**) reveals secondary structure signatures due to the hydrogen bonding network in compounds containing even a single amide group that can be used as peptide models [24,25]. The amide I region is dominated by a peak at 1645 cm^{-1} , which is compatible with disordered structures, and indeed is present also in the FT-IR spectrum of the compound in its non-assembled state (**Figure 3.7**) [26,27]. A minor peak at 1700 cm^{-1} can be assigned to the protonated COOH [28]; this peak is more intense in the powder form, and we inferred this is due to partial deprotonation in the gel state. By contrast, the shoulder at 1623 cm^{-1} arises in the self-assembled state and corresponds to the traditional signature of amyloid fibrils [26,29]. The signal at 1600 cm^{-1} was already reported for Phe-derived supramolecular xerogels, however, it is present also in the FT-IR spectrum of *N*-(4-nitrobenzoyl)-Phe in its non-assembled state and could be due to the aromatic C=C stretching [27,30]. Finally, the amide III region is dominated by a broad signal centered at 1460 cm^{-1} that arises with self-assembly. Interpretation of this region is more challenging relative to the amide I, however, the N-H bending signal has been reported to shift down to 1450 cm^{-1} as a result of extended hydrogen bonding and in the presence of inorganic salts [24].

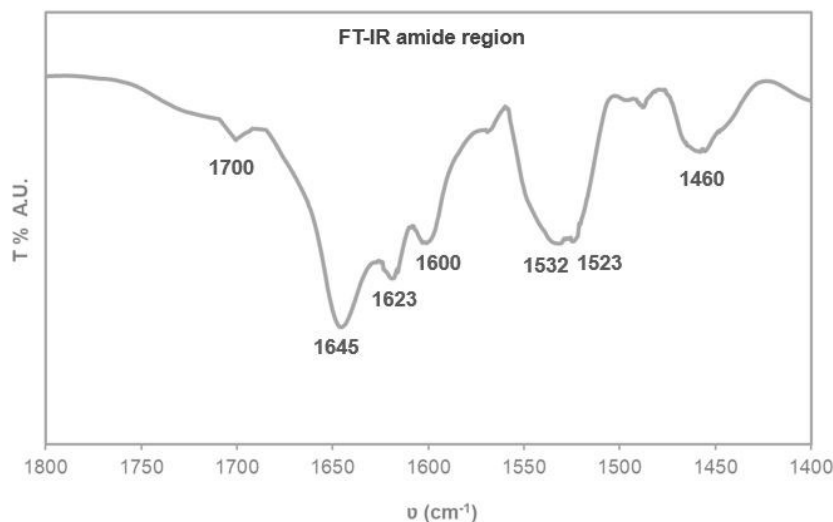


Figure 3.6. FT-IR spectrum (amide I-III region) of the xerogel. Reproduced with permission from ref. [1] © 2020 John Wiley and Sons.

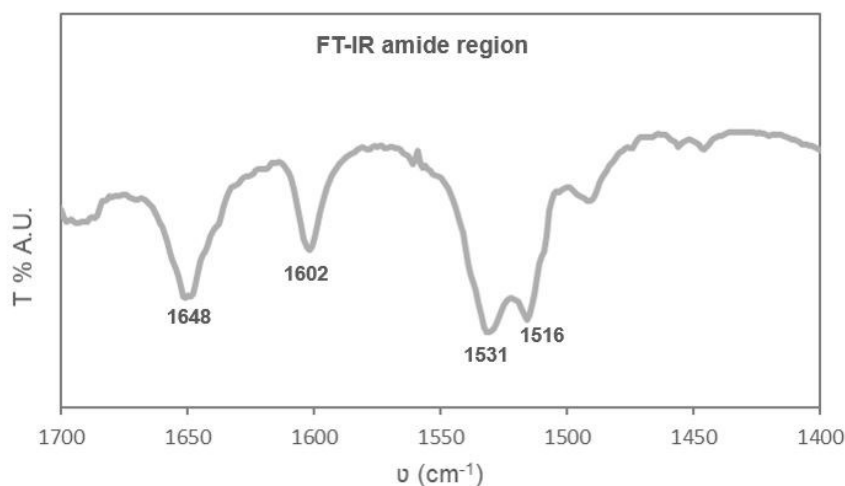


Figure 3.7. Amide region of the FT-IR spectrum of the gelator in the powder form. Reproduced with permission from ref. [1] © 2020 John Wiley and Sons.

A very popular approach to confirm the amyloid-like nature of Phe-derived assemblies is the Thioflavin T fluorescence assay (**Figure 3.8**) [8]. The rotation between the two aromatic rings of this dye is limited when it binds laterally to amyloid fibrils, resulting in fluorescence [31]. *In silico* investigations have shown that the dye binds to aromatic and hydrophobic grooves formed by at least four consecutive β -strands in a linear β -sheet [32]. Interestingly, the dye does not bind to highly charged surfaces, as the binding is not mediated by electrostatic interactions, being instead favored onto neutral species [33]. When performed at different gelator concentrations, the assay results in mild fluorescence only when the MGC is reached (**Figure 3.8**). This data supports the amyloid nature

of assemblies, although it also suggests the lack of extended stacks ordered in a similar fashion as peptide β -sheets, in agreement with the considerable amount of disorder noted by FT-IR.

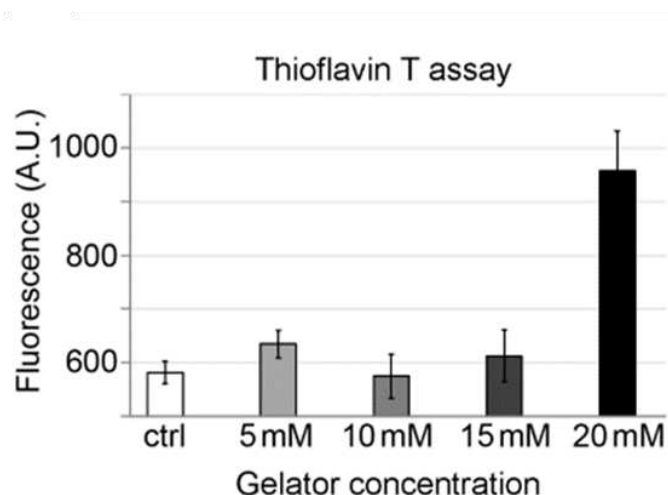


Figure 3.8. Thioflavin T fluorescence at various compound concentrations. Reproduced with permission from ref. [1] © 2020 John Wiley and Sons.

3.4. Single-crystal XRD analysis

Single-crystal XRD analysis (**Figure 3.9 A**) confirmed presence of a hydrogen bond between amides of adjacent molecules, which stack similarly to peptides in β -sheets. Two main hydrophobic interactions are visible in the crystal structure, namely a π - π stacking interaction between the phenyl ring and the nitro-phenyl ring of a symmetry-related molecule (located at a distance of 4.7 Å), and a CH- π interaction between two phenyl rings at a distance of 3.1 Å (**Figure 3.9 B**). The carboxylic acid terminus appears protonated as it engages in strong hydrogen bonding with two other carboxylic acid moieties with an inter-oxygen atomic distance as short as 2.7 Å (**Figure 3.9 A**). Indeed, stacks of carboxylate anions not only would be disfavored due to charge repulsion, but also would not be expected to bind Thioflavin T and lead to fluorescence [33].

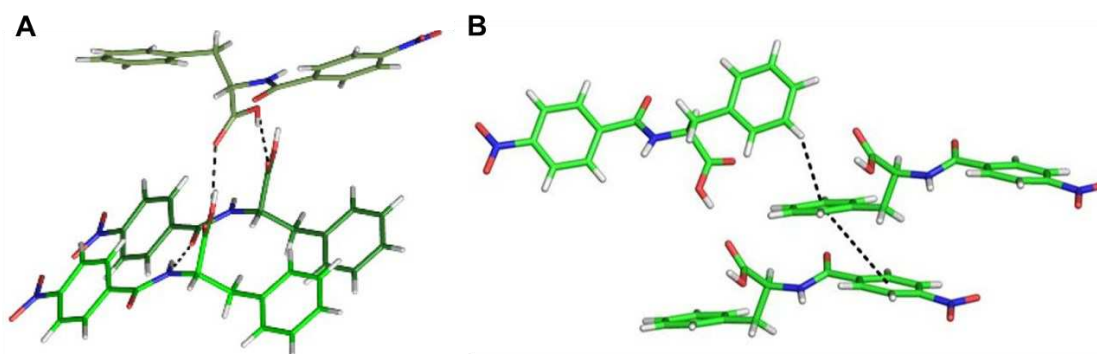


Figure 3.9. A) Single-crystal XRD structure showing hydrogen bonds (dashed lines). CCDC 1919220; B) Hydrophobic interactions visible in the crystal structure of *N*-(4-nitrobenzoyl)-Phe, namely a π - π stacking interaction between the phenyl ring and the nitro-phenyl ring of a symmetry-related molecule, at a distance 4.7 Å between the centres of the aromatic rings, and a CH- π interaction between two phenyl rings, at a distance of 3.1 Å between the hydrogen atom and the centre of the aromatic ring. Reproduced with permission from ref. [1] © 2020 John Wiley and Sons.

3.5. MicroRaman analysis

In the field of supramolecular systems based on amino acid and peptide derivatives, there is an ongoing debate as to whether the packing arrangement observed in the crystal form is analogous to the one observed in the hydrogel state, since clearly the two solid forms are different, and certainly so both at the macro- and microscopic level. Hierarchical organization of this class of small molecules into supramolecular hydrogels and crystals, as well as the interconversion between the two, indeed is the focus of intense investigations [34,35]. It is generally accepted that the hydrogel is a kinetic product, while the crystal form is the thermodynamic product [36]. To shed light as to whether the packing arrangement observed in the crystal form by XRD is relevant to that observed in the hydrogel state, we performed microRaman analysis on both (**Figure 3.10**). The very same signals dominated both spectra, with the most dominant ones being at 1355 cm^{-1} (symmetric stretching of the nitro group)[37], and 1607 cm^{-1} (stretching of C-C bond of the aromatic ring) [38]. The signal at 1003 cm^{-1} is also present in both spectra and it is assigned to the breathing mode of the aromatic ring, typically a dominant peak in Raman spectra of Phe derivatives [38]. The signal at 1113 cm^{-1} is not present in the Phe Raman spectra, while it has been observed for the 4-nitrobenzoyl moiety [39]. The signal at 884 cm^{-1} is absent in the spectra of 4-nitrobenzoyl chloride [39] and underivatized Phe yet present as weak signal in those of Phe-containing peptides, [38] and in amino acid *N*-benzoyl derivatives, [40] thus we infer it can be assigned to the amide N-H bending [41]. Unfortunately, the other amide signals that have been reported to shift based on the hydrogen bonding pattern are extremely weak in both spectra. In particular, the amide I C=O stretch centered at 1645 cm^{-1} was present in both spectra, as was the amide III at ca. 1260 cm^{-1} . Overall, the main difference between the Raman spectra of the gel

and the crystals lies in the signal's intensities, which are significantly higher in the latter. No significant shifts, which are known to occur as result of different non-covalent interactions or supramolecular environments, are noted. We thus infer that the packing arrangement between the two states is not dramatically different, although it is possible that minor differences related to more disorder in the hydrogel state are not clearly visible as the signals may simply be too weak to be assigned unambiguously.

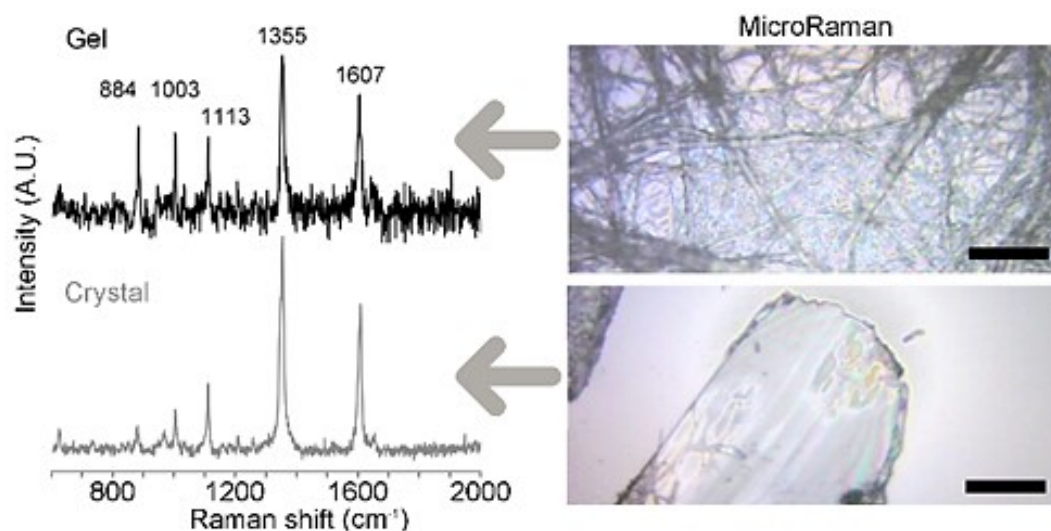


Figure 3.10. MicroRaman analysis of both the gel and crystal states. Scale bar = 20 microns. Reproduced with permission from ref. [1] © 2020 John Wiley and Sons.

3.6. pH titrations to evaluate apparent pKa shift with self-assembly

The unexpected protonation of the carboxylic acid at neutral pH would appear plausible in the hydrogel, only if accompanied by a pKa shift of the carboxylic group, due to the self-assembled state interactions. This phenomenon has been previously described for protein and peptides when self-assembled in hydrophobic environments, as well as peptide-derived gelators in their self-assembled state [42–46]. It can easily be envisaged how otherwise adjacent carboxylate moieties in the supramolecular stacks would result in electrostatic repulsion that would disfavor self-assembly [46]. The apparent pKa shift of carboxylic acids was indeed noted with adjacent Phe residues, whereby the highly cooperative competition for hydration between apolar and polar species creates repulsive free energy. As a net result, a protonated and neutral state for the carboxylic acid moiety is favored [47]. Indeed, pH titrations at increasing gelator concentrations under mgc confirm a pKa increase also in the case of *N*-(4-nitrobenzoyl)-Phe from 3.5 at 5 mM to 4.3 at 12.5 mM (**Figure 3.11 A**); when the solubility limit is surpassed, the heterogeneous system leads to unstable pH readings and considerable noise. Nevertheless, tedious titration experiments with extremely diluted NaOH solutions ultimately

showed a pKa shift up to 6.8 at mgc in PBS (**Figure 3.11 B**). While apparent pKa shifts for COOH groups in N-capped short peptide gelators have been reported, [42,43,45,48,49] often these do not exceed a pKa of 6, thus allowing the formation of the corresponding hydrogels only at acidic pH [42][48].

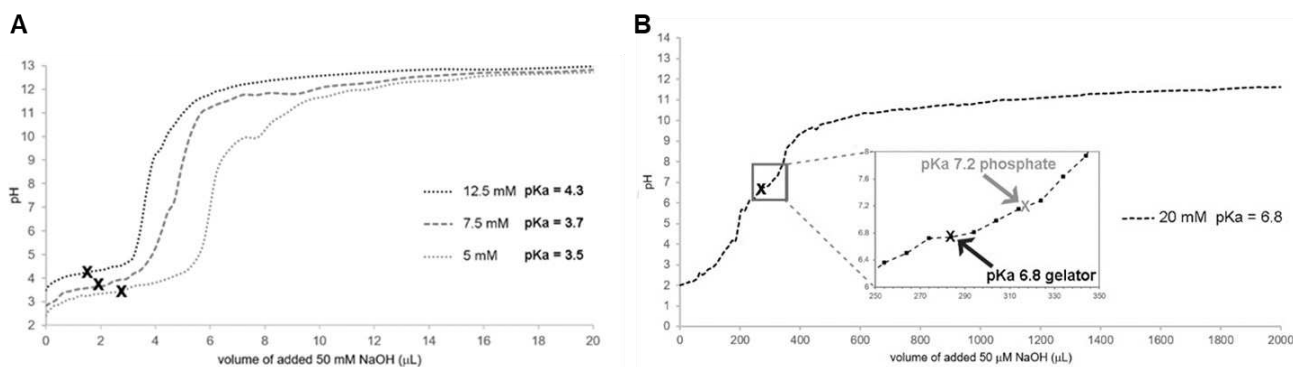


Figure 3.11. A) pH titrations in milliQ water with NaOH at different gelator concentrations under the mgc. B) pH titrations in PBS buffer with 50 μM NaOH at mgc. Reproduced with permission from ref. [1] © 2020 John Wiley and Sons.

Overall, the spectroscopic data suggest that the hydrogel shares common features of intermolecular packing with the crystalline state, such as a certain number of parallel stacks with aromatic rings in an offset position. Crystals can arise from the hydrogel over a several-week period, confirming the hypothesis that they constitute the thermodynamic and kinetic product, respectively [36]. However, FT-IR and fluorescence data suggest that the hydrogel displays a significantly higher level of disordered structures relative to the crystalline state. We infer that the hydrogel contains both protonated and non-protonated carboxyl groups, the latter being bridged by water molecules. It is plausible that, during crystallization, a water molecule gives way to a more stable hydrogen bonding network due to the intervention of the proton of the COOH group, resulting in the packing shown in **Figure 3.9 A**.

3.7. Biocompatibility assessment for wound healing applications

In terms of potential applications, *N*-(4-nitrobenzoyl)-Phe was reported to have antimicrobial activity of the same order of magnitude as reference sulphonamides against *S.aureus*, *E.coli*, and *S.enteritidis* when tested in a disk-diffusion assay [27]. Additionally, intraperitoneal injection in mice revealed an LD₅₀ of 6 g/kg on a 7-day period average [27]. Encouraged by this data, we reasoned that if the supramolecular hydrogel retained such properties, it would be an attractive candidate for wound healing applications.

To this end, *in vitro* studies were performed to investigate the biocompatibility of the hydrogel on two different types of mammalian cells. Usually, the most common and appropriate cell model for such preliminary studies about the toxicity of a material in contact with living cells, are fibroblasts and keratinocytes. Their choice is directly correlated to their noteworthy role in the physiological process of skin regeneration [50] and their ease of handling and identification of their relative condition even for a novice operator. Furthermore, a rapid growth rate and their ability to be adherently cultured on a favourable material, give them further scope for their use for such investigations. Particularly, NIH/3T3 (embryonic mouse fibroblast) and HaCaT (human keratinocytes) were the cell lines chosen for this work. To assess cell viability, we used a well-in-well microscopy slide as shown in **Figure 3.12**, whereby the hydrogel is formed *in situ* in the inner well, and then cells and media are added in the outer well.

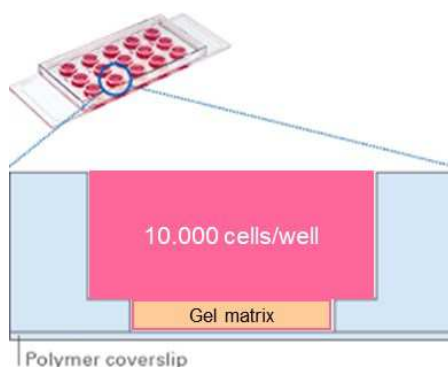


Figure 3.12. Well-in-well microscopy slide used to assess biocompatibility of the hydrogel. Image modified from www.ibidi.com.

Both types of cells were left to grow on the hydrogel for 24 hours in a humidified incubator at 37 °C, 5% CO₂ for 24 h, by handling the slides according to the manufacturers' instructions, before performing the live/dead assay. Such test was performed by using two fluorescent colour dyes, the acridine orange (AO) and the propidium iodide (PI) (**Figure 3.13**) that allow the detection under a fluorescence microscope of live and dead cells, respectively, in the same experiment [51,52].

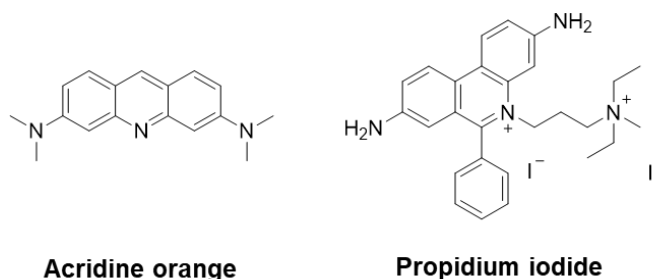


Figure 3.13. Structure of the two fluorescent colour dyes used for live/dead assay

The fluorescence observed during the cytotoxicity assay is due to the ability of the two dyes to interact and bind nucleic acids with some differences between them. AO is able to permeate viable cells, and binding to dsDNA produces the green fluorescence. Binding of the ssDNA or RNA may produce red fluorescence. Propidium iodide is not able to permeate intact cell membranes but it can be taken up by cells with a compromised membrane (dead or almost dead cells) and bind nucleic acids with a red fluorescence as result. Because of the FRET (Förster resonance energy transfer) effect, the PI signal is able to absorb the AO signal in the dead cells avoiding a double positive result [53].

From live/dead assay we were pleased to see high viability for relevant cell types [54] grown on the hydrogel, *i.e.*, fibroblasts (NIH/3T3) and keratinocytes (HaCaT) (**Figure 3.14**). Both cell lines were able to spread consistently on the hydrogel surface, maintaining a normal and physiological morphology without any sign of apoptotic process.

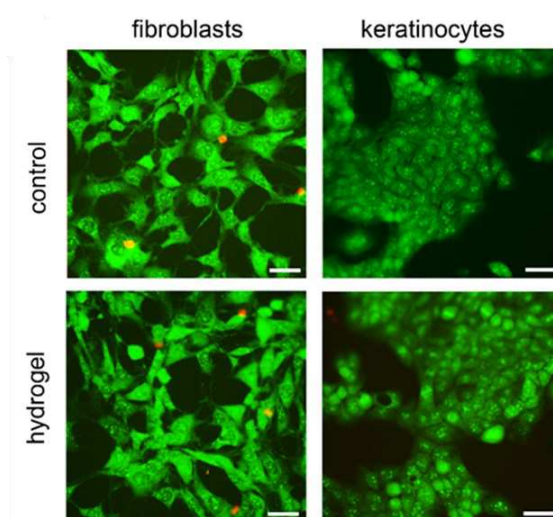


Figure 3.14. Live(green)/dead(red) fluorescence microscopy on mammalian cells (fibroblast and keratinocytes). Cells are simply grown on tissue culture plastic surface as a control. Scale bar = 20 microns. Reproduced with permission from ref. [1] © 2020 John Wiley and Sons.

In the case of *E. coli*, the hydrogel displays antimicrobial activity, although to a minor extent than the compound in solution at 0.5 mM (**Figure 3.15 A**), which we established as the minimum inhibitory concentration (MIC) (**Figure 3.15 B**), [55] suggesting that fibrillization is not required to exert the bioactivity. We inferred that the antibacterial effect is thus due to the amount of *N*-(4-nitrobenzoyl)-Phe that is released from the gel. This finding is in agreement with observations that Fmoc-Phe also displays antibacterial activity both in the gel and solution phases, thanks to the release of the soluble molecule (from the gel) that exhibits a surfactant-like behavior, as it alters membrane permeabilization and integrity, thus ultimately leading to the death of bacteria [56].

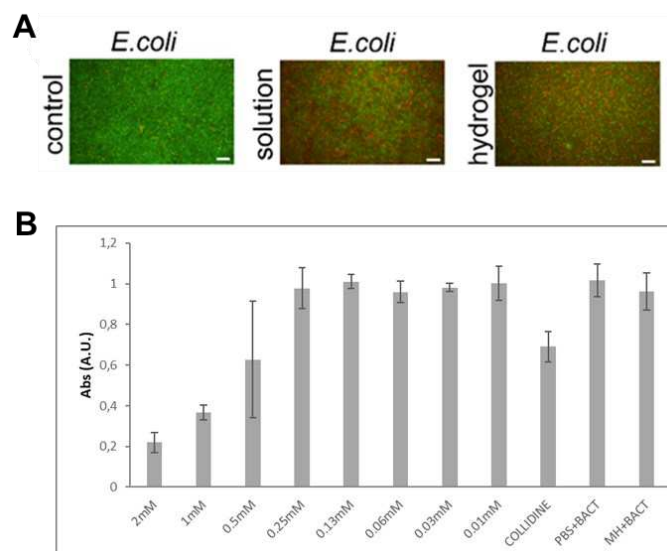


Figure 3.15. Live(green)/dead(red) fluorescence microscopy on (A) bacteria. Scale bar = 20 microns. Cells are simply grown on tissue culture plastic surface as a control (B) MIC assay average data with standard deviation as error bars. Reproduced with permission from ref. [1] © 2020 John Wiley and Sons.

3.8. Conclusions

In conclusion, this work reports the self-assembly into hydrogels of the amino acid derivative *N*-(4-nitrobenzoyl)-Phe, which has been characterized by several spectroscopic techniques, as well as single-crystal XRD and microscopy. A pKa shift in the self-assembled state is compatible with the presence of protonated carboxylic moieties as revealed by XRD data. Importantly, the hydrogel displayed mild antimicrobial activity against *E. coli*, whilst allowing high viability of fibroblasts and keratinocytes. Since the gel-to-sol transition can occur at the physiologically relevant temperature of 39-42 °C and the antimicrobial activity is maintained by the compound in solution, we think this material constitutes an interesting starting point for the development of cost-effective, antimicrobial hydrogels for wound healing applications.

References

- [1] A. M. Garcia, R. Lavendomme, S. Kralj, M. Kurbasic, O. Bellotto, M. C. Cringoli, S. Semeraro, A. Bandiera, R. De Zorzi, S. Marchesan, *Chem. - A Eur. J.* **2020**, *26*, 1880–1886.
- [2] M. A. Sequeira, M. G. Herrera, V. I. Doderó, *Phys. Chem. Chem. Phys.* **2019**, *21*, 11916–11923.
- [3] M. Amit, S. Yuran, E. Gazit, M. Reches, N. Ashkenasy, *Adv. Mater.* **2018**, *30*, 1707083.
- [4] G. Deidda, S. V. R. Jonnalagadda, J. W. Spies, A. Ranella, E. Mossou, V. T. Forsyth, E. P. Mitchell, M. W. Bowler, P. Tamamis, A. Mitraki, *ACS Biomater. Sci. Eng.* **2017**, *3*, 1404–1416.
- [5] P. D'Andrea, D. Scaini, L. U. Severino, V. Borelli, S. Passamonti, P. Lorenzon, A. Bandiera, *Biomaterials* **2015**, *67*, 240–253.
- [6] S. Bera, S. Mondal, S. Rencus-Lazar, E. Gazit, *Acc. Chem. Res.* **2018**, *51*, 2187–2197.
- [7] M. Mba, D. Mazzier, S. Silvestrini, C. Toniolo, P. Fatás, A. I. Jiménez, C. Cativiela, A. Moretto, *Chem. – A Eur. J.* **2013**, *19*, 15841–15846.
- [8] L. Adler-Abramovich, L. Vaks, O. Carny, D. Trudler, A. Magno, A. Caflisch, D. Frenkel, E. Gazit, *Nat. Chem. Biol.* **2012**, *8*, 701–706.
- [9] B. L. Abraham, W. Liyanage, B. L. Nilsson, *Langmuir* **2019**, *35*, 14939–14948.
- [10] W.-P. Hsu, K.-K. Koo, A. Myerson, *Chem. Eng. Commun.* **2002**, *189*, 1079–1090.
- [11] S. M. Ramalhete, K. P. Nartowski, N. Sarathchandra, J. S. Foster, A. N. Round, J. Angulo, G. O. Lloyd, Y. Z. Khimyak, *Chem. – Eur. J.* **2017**, *23*, 8014–8024.
- [12] R. Otter, N. A. Henke, C. Berac, T. Bauer, M. Barz, S. Seiffert, P. Besenius, *Macromol. Rapid Commun.* **2018**, *39*, e1800459.
- [13] W. E. M. Noteborn, D. N. H. Zwagerman, V. S. Talens, C. Maity, L. van der Mee, J. M. Poolman, S. Mytnyk, J. H. van Esch, A. Kros, R. Eelkema, R. E. Kieltyka, *Adv. Mater.* **2017**, *29*, 1603769.
- [14] V. Singh, K. Snigdha, C. Singh, N. Sinha, A. K. Thakur, *Soft Matter* **2015**, *11*, 5353–5364.
- [15] J. Shi, Y. Gao, Z. Yang, B. Xu, *Beilstein J. Org. Chem.* **2011**, *7*, 167–172.
- [16] S.-M. Hsu, F.-Y. Wu, H. Cheng, Y.-T. Huang, Y.-R. Hsieh, D. T.-H. Tseng, M.-Y. Yeh, S.-C. Hung, H.-C. Lin, *Adv. Healthc. Mater.* **2016**, *5*, 2406–2412.
- [17] J. Nanda, A. Biswas, A. Banerjee, *Soft Matter* **2013**, *9*, 4198–4208.
- [18] R. Martí-Centelles, B. Escuder, *ChemNanoMat* **2018**, *4*, 796–800.
- [19] N. C. Carrejo, A. N. Moore, T. L. Lopez Silva, D. G. Leach, I.-C. Li, D. R. Walker, J. D. Hartgerink, *ACS Biomater. Sci. Eng.* **2018**, *4*, 1386–1396.

- [20] Y. Loo, Y.-C. Wong, E. Z. Cai, C.-H. Ang, A. Raju, A. Lakshmanan, A. G. Koh, H. J. Zhou, T.-C. Lim, S. M. Moochhala, C. A. E. Hauser, *Biomaterials* **2014**, *35*, 4805–4814.
- [21] J. P. Wojciechowski, A. D. Martin, A. F. Mason, C. M. Fife, S. M. Sagnella, M. Kavallaris, P. Thordarson, *ChemPlusChem* **2017**, *82*, 383–389.
- [22] W. T. Truong, Y. Su, D. Gloria, F. Braet, P. Thordarson, *Biomater. Sci.* **2015**, *3*, 298–307.
- [23] W. Liyanage, W. W. Brennessel, B. L. Nilsson, *Langmuir* **2015**, *31*, 9933–9942.
- [24] J. Zhao, J. Wang, *J. Phys. Chem. B* **2016**, *120*, 9590–9598.
- [25] N. S. De Groot, T. Parella, F. X. Aviles, J. Vendrell, S. Ventura, *Biophys. J.* **2007**, *92*, 1732–1741.
- [26] J. Seo, W. Hoffmann, S. Warnke, X. Huang, S. Gewinner, W. Schöllkopf, M. T. Bowers, G. von Helden, K. Pagel, *Nat. Chem.* **2017**, *9*, 39–44.
- [27] C. Rosca, A. C. Benchea, V. Sunel, D. Sutiman, D. O. Dorohoi, C. B. Zelinschi, C. Stan, C. Cheptea, *Rev. Chim.* **2016**, *67*, 1062–1067.
- [28] J. G. Mesu, T. Visser, F. Soulimani, B. M. Weckhuysen, *Vib. Spectrosc.* **2005**, *39*, 114–125.
- [29] J. P. Lomont, K. L. Rich, M. Maj, J.-J. Ho, J. S. Ostrander, M. T. Zanni, *J. Phys. Chem. B* **2018**, *122*, 144–153.
- [30] Y. Yu, N. Chu, Q. Pan, M. Zhou, S. Qiao, Y. Zhao, C. Wang, X. Li, *Materials* **2019**, *12*, 1890.
- [31] N. Amdursky, Y. Erez, D. Huppert, *Acc. Chem. Res.* **2012**, *45*, 1548–1557.
- [32] M. Biancalana, K. Makabe, A. Koide, S. Koide, *J. Mol. Biol.* **2009**, *385*, 1052–1063.
- [33] C. Wu, M. T. Bowers, J.-E. Shea, *Biophys. J.* **2011**, *100*, 1316–1324.
- [34] C. Yuan, W. Ji, R. Xing, J. Li, E. Gazit, X. Yan, *Nat. Rev. Chem.* **2019**, *3*, 567–588.
- [35] A. D. Martin, J. P. Wojciechowski, M. M. Bhadbhade, P. Thordarson, *Langmuir* **2016**, *32*, 2245–2250.
- [36] J. Wang, K. Liu, R. Xing, X. Yan, *Chem. Soc. Rev.* **2016**, *45*, 5589–5604.
- [37] C. Passingham, P. J. Hendra, C. Hodges, H. A. Willis, *Spectrochim. Acta Part A Mol. Spectrosc.* **1991**, *47*, 1235–1245.
- [38] D. Iglesias, M. Melle-Franco, M. Kurbasic, M. Melchionna, M. Abrami, M. Grassi, M. Prato, S. Marchesan, *ACS Nano* **2018**, *12*, 5530–5538.
- [39] SDBSWeb: <https://sdb.sdb.aist.go.jp> (*National Inst. Adv. Ind. Sci. Technol.* accessed 15/12/2019).
- [40] R. H. Angus, P. R. Carey, H. Lee, A. C. Storer, K. I. Varughese, *Can. J. Chem.* **1985**, *63*, 2169–2175.
- [41] C. Westley, Y. Xu, B. Thilaganathan, A. J. Carnell, N. J. Turner, R. Goodacre, *Anal. Chem.* **2017**, *89*, 2472–2477.

- [42] E. R. Cross, D. J. Adams, *Soft Matter* **2019**, *15*, 1522–1528.
- [43] M. Tena-Solsona, J. Nanda, S. Díaz-Oltra, A. Chotera, G. Ashkenasy, B. Escuder, *Chem. – Eur. J.* **2016**, *22*, 6687–6694.
- [44] L. Chen, S. Revel, K. Morris, L. C. Serpell, D. J. Adams, *Langmuir* **2010**, *26*, 13466–13471.
- [45] F. Rodríguez-Llansola, B. Escuder, J. F. Miravet, *J. Am. Chem. Soc.* **2009**, *131*, 11478–11484.
- [46] C. Tang, A. M. Smith, R. F. Collins, R. V Ulijn, A. Saiani, *Langmuir* **2009**, *25*, 9447–9453.
- [47] D. W. Urry, D. C. Gowda, S. Peng, T. M. Parker, N. Jing, R. D. Harris, *Biopolymers* **1994**, *34*, 889–896.
- [48] L. Chen, K. Morris, A. Laybourn, D. Elias, M. R. Hicks, A. Rodger, L. Serpell, D. J. Adams, *Langmuir* **2010**, *26*, 5232–5242.
- [49] A. M. Smith, R. J. Williams, C. Tang, P. Coppo, R. F. Collins, M. L. Turner, A. Saiani, R. V. Ulijn, *Adv. Mater.* **2008**, *20*, 37–41.
- [50] A. M. Wojtowicz, S. Oliveira, M. W. Carlson, A. Zawadzka, C. F. Rousseau, D. Baksh, *Wound Repair Regen.* **2014**, *22*, 246–255.
- [51] K. Mascotti, J. McCullough, S. R. Burger, *Transfusion* **2000**, *40*, 693–696.
- [52] C. G. Yedjou, S. S. Tchounwou, K. Williams, P. B. Tchounwou, *Int. J. Eng. Sci. Res. Technol.* **2018**, *7*, 552–556.
- [53] www.LogosBios.com, **2018**, *33*, 59650.
- [54] E. Y. X. Loh, N. Mohamad, M. B. Fauzi, M. H. Ng, S. F. Ng, M. C. I. Mohd Amin, *Sci. Rep.* **2018**, *8*, 2875.
- [55] European Committee for Antimicrobial Susceptibility Testing (EUCAST) of the European Society of Clinical Microbiology and Infectious Diseases, *Clin. Microbiol. Infect.* **2003**, *9*, ix–xv.
- [56] A. Y. Gahane, P. Ranjan, V. Singh, R. K. Sharma, N. Sinha, M. Sharma, R. Chaudhry, A. K. Thakur, *Soft Matter* **2018**, *14*, 2234–2244.

Chapter 4. Halogenation effect on Phe-Phe heterochiral dipeptides

This chapter contains the work of both *Manuscript 2*, entitled “*Heterochirality and Halogenation Control Phe-Phe Hierarchical Assembly*” [1] and *Manuscript 3*, entitled “*Single-atom substitution enables supramolecular diversity from dipeptide building blocks*”[2].

First, heterochirality has been studied as a tool to control the hierarchical assembly of diphenylalanine into hydrogel biomaterials. Then, the influence of halogenation and its position (*i.e.*, *ortho*, *meta*, or *para*) on the supramolecular behaviour of D-Phe-L-Phe was investigated. The effects of halogenation at the N-terminus and the C-terminus of the Phe aromatic ring were both considered, and they are described in the following **sections 4.1 and 4.2**, respectively.

4.1. N-terminal halogenation effect on D-Phe-L-Phe

4.1.1. Introduction

Phenylalanine (Phe) stands out among the 20 natural amino acids for its unmatched propensity toward self-assembly, and indeed it was reported to form toxic fibrils on its own at high concentrations [3]. Phe-Phe is possibly the most versatile self-assembling motif in minimalistic gelators, and subtle chemical variations led to a variety of nanomorphologies [4–8]. Studies continue to emerge describing its useful properties, ranging from piezoelectricity to ferroelectricity, for applications that span printing to semiconductors [9–13]. At the base of these features are the electronic properties that arise from the peculiar supramolecular arrangement of Phe-Phe in nanotubes [14]. Clearly, there is ample scope to tailor derivatives of this compound toward the development of cost-effective supramolecular materials.

In particular, halogenation was reported to favor self-organization and hydrogelation of Fmoc-Phe derivatives [15,16]. Iodination can be advantageous through the establishment of halogen-bonding, as reported in a pentapeptide [17]. However, the design of halogenated peptides that self-organizes into supramolecular hydrogels is not trivial since the formation of macroscopic and stable hydrogels is the result of a fine balance between many steric and electronic factors. Phe-Phe gave rise to metastable hydrogels that underwent syneresis over time [18,19] and N-terminal halogenation was shown to affect self-assembly, so that the poorly water-soluble L-(4-I)-Phe-L-Phe and L-(4-I)-Phe-L-(4-I)-Phe were reported to form crystals [20].

Inspired by these works, we chose diphenylalanine (**1**) as a model compound and studied the self-organization of heterochiral D-Phe-L-Phe (**2**), as well as its halogenated derivatives D-(2-F)-Phe-L-Phe (**3**), D-(3-F)-Phe-L-Phe (**4**), D-(4-F)-Phe-L-Phe (**5**), and D-(4-I)-Phe-L-Phe (**6**), as shown in

Figure 4.1. Iodination in the *ortho*- or *meta*-positions of Phe was not studied as it was envisaged to likely disrupt assembly due to iodine's bulky nature and ability to engage in halogen bonding with carbonyl groups [21].

Our choice of heterochiral sequences was dictated by the observation that introducing D-amino acids at selected positions has proven successful as a strategy to achieve hydrogels from uncapped tripeptides [22,23]. In this manner, it is possible to orient favorably the side chains of hydrophobic sequences to access amphiphilic gelling structures, as was recently reviewed [24]. Heterochirality is gaining momentum as a strategy to tailor peptide self-assembly [25–27]. Uncapped dipeptides are very attractive building blocks due to their chemical simplicity. Furthermore, enantiomers are expected to display the same self-assembly behaviour in achiral environments, therefore, investigation of compounds **2–6** will shed light also on the self-assembly of their mirror-image L-D dipeptide isomers.

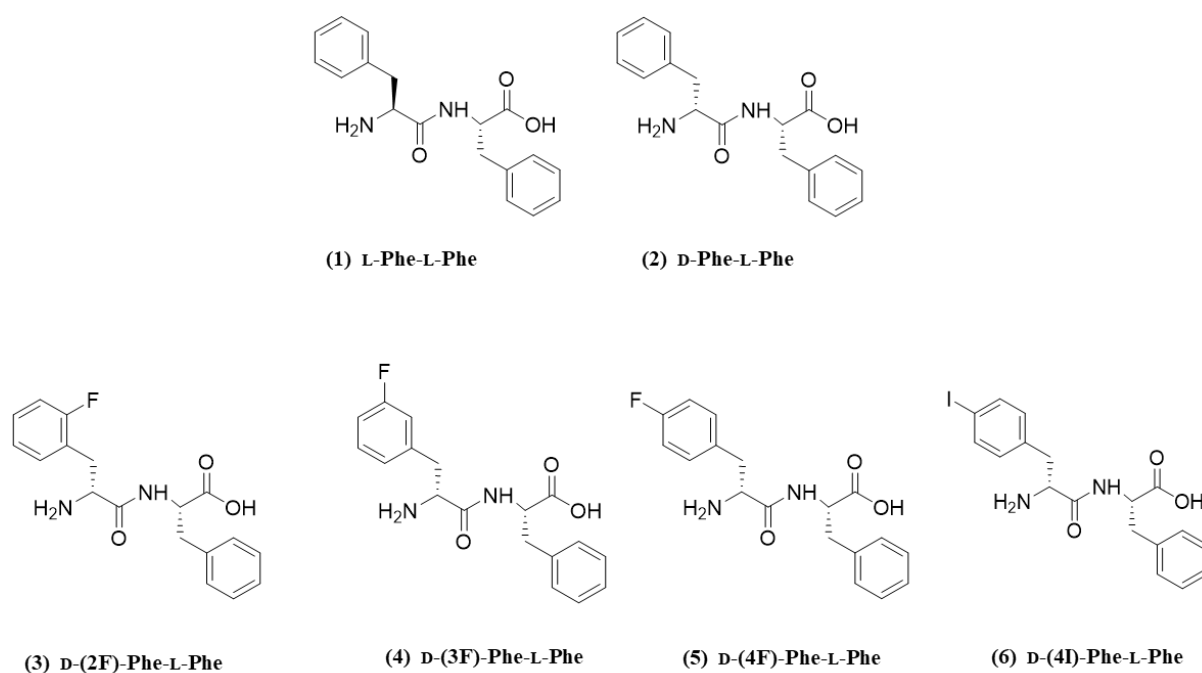


Figure 4.1. Chemical structures of Phe-Phe compounds studied in *Manuscript 2* for self-assembly. Diphenylalanine peptide, homochiral **(1)** and heterochiral **(2)**. Halogenated N-terminus Phe-Phe compounds **(3-6)**. Modified from Chart 1 of the *Manuscript 2*. Reproduced from ref [1] under a Creative Commons Licence.

4.1.2. Results and discussion

4.1.2.1. Peptide self-assembly into nanostructured hydrogels

Each compound shown in **Figure 4.1.** was synthesized and purified by reverse-phase HPLC, which revealed increasing retention times from **1** to **6**, with only minor differences among fluorinated regioisomers (**Table 4.1**).

compound	HPLC Rt (min)	log P	mgc (mM)
1	6.0	2.3 ± 0.5	20
2	7.1	2.3 ± 0.5	20
3	7.1	2.4 ± 0.5	15
4	7.2	2.4 ± 0.5	10
5	7.3	2.4 ± 0.5	7
6	7.9	3.6 ± 0.5	4

Table 4.1. Hydrophobicity and Minimum Gelling Concentration (mgc) of dipeptides **1–6**. Reproduced from ref [1] under a Creative Commons Licence.

All compounds were dissolved in aqueous sodium phosphate at pH ~12, since at alkaline pH the repulsion between the negative charges of the peptide anions impedes self-assembly. Subsequent dilution with an equal volume of mildly acidic phosphate buffer led to a final pH of 7.3. Under these conditions, peptide zwitterions formed salt bridges between their charged termini, triggering self-assembly. All compounds **1–6** formed supramolecular hydrogels as confirmed by oscillatory rheology. In all cases, gelation kinetics were fast, with gels forming within 500 seconds, as shown in **Figure 4.2**. The average values of G' and G'' are reported in **Table 4.2**.

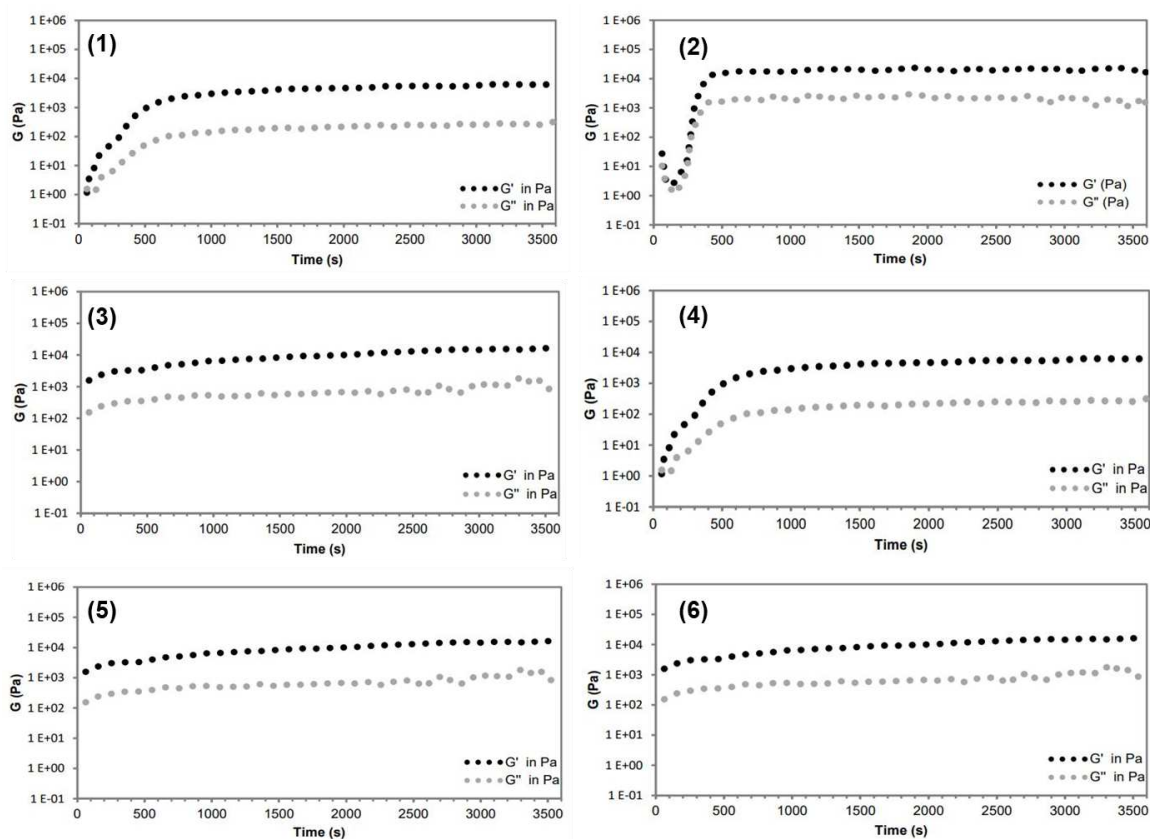


Figure 4.2. Time sweep analyses of supramolecular hydrogels obtained by the self-assembly of the Phe-Phe compounds from **1** to **6**. Reproduced from ref [1] under a Creative Commons Licence.

Compound	G' (Pa)	G'' (Pa)
1	22.0 ± 3.0	3.7 ± 0.5
2	22.9 ± 3.5	1.5 ± 0.3
3	8.0 ± 1.9	0.5 ± 0.1
4	6.1 ± 0.5	0.3 ± 0.1
5	20.7 ± 2.3	1.2 ± 0.4
6	17.7 ± 1.7	1.3 ± 0.6

Table 4.2. Average of storage (G') and loss (G'') moduli of the hydrogels at their mgc after 1 hour of gelation at room temperature at 1 Pa. Reproduced from ref [1] under a Creative Commons Licence.

The minimum gelling concentration (mgc) was inversely proportional to the HPLC retention time, which is an experimental measure of hydrophobicity [28], as shown in **Table 4.1**. However, not all hydrogels were stable over time (**Figure 4.3**). Compounds **1** and **4** displayed syneresis, as already reported for **1** [18,19]. This feature, which consists of the gel contraction with concomitant release of liquid, may be attractive for the capture and release of small molecules [29,30] such as pollutants or

drugs, provided that release kinetics are controlled. Compounds **2**, **3**, and **6** yielded stable and homogeneous hydrogels; in particular, compounds **2** and **3** formed materials of high transparency, which is a desirable feature for optical applications. Compound **5** crystallized over days, suggesting a low energetic barrier and high structural similarity between the two states, gel and crystal [31].

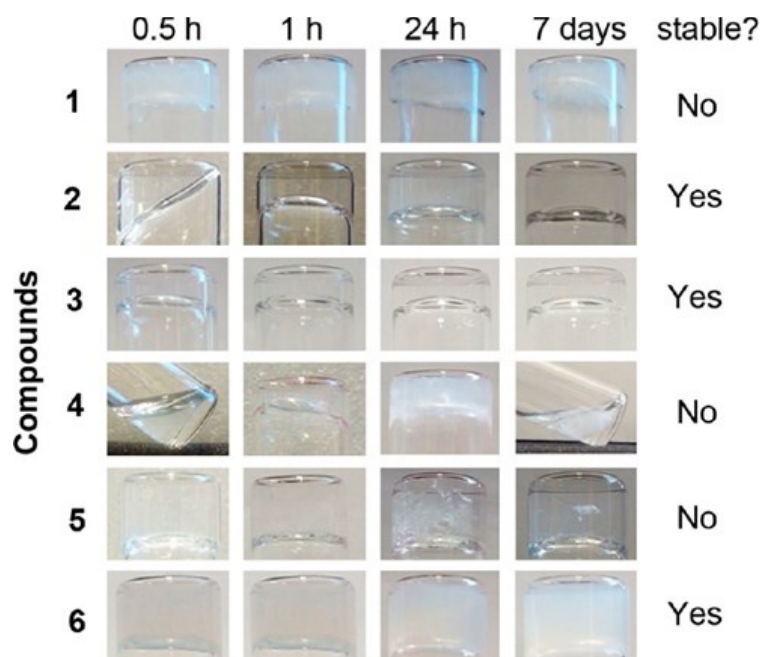


Figure 4.3. Photographs of supramolecular hydrogels of compounds **1–6** at their mgc and hydrogel stability over 7 days (*i.e.*, no transition to other phases). Reproduced from ref [1] under a Creative Commons Licence.

Hydrogel resistance to applied stress increased with heterochirality and halogenation as reported in **Figure 4.4**. Compound **1** displayed a gel-to-sol transition at just 0.02 kPa, whereas its diastereomer **2** transitioned at 0.15 kPa, similarly, to halogenated **4–6** (0.11 kPa) despite their lower mgc. Ortho-fluorination in **3** led to an intermediate stress resistance (0.07 kPa).

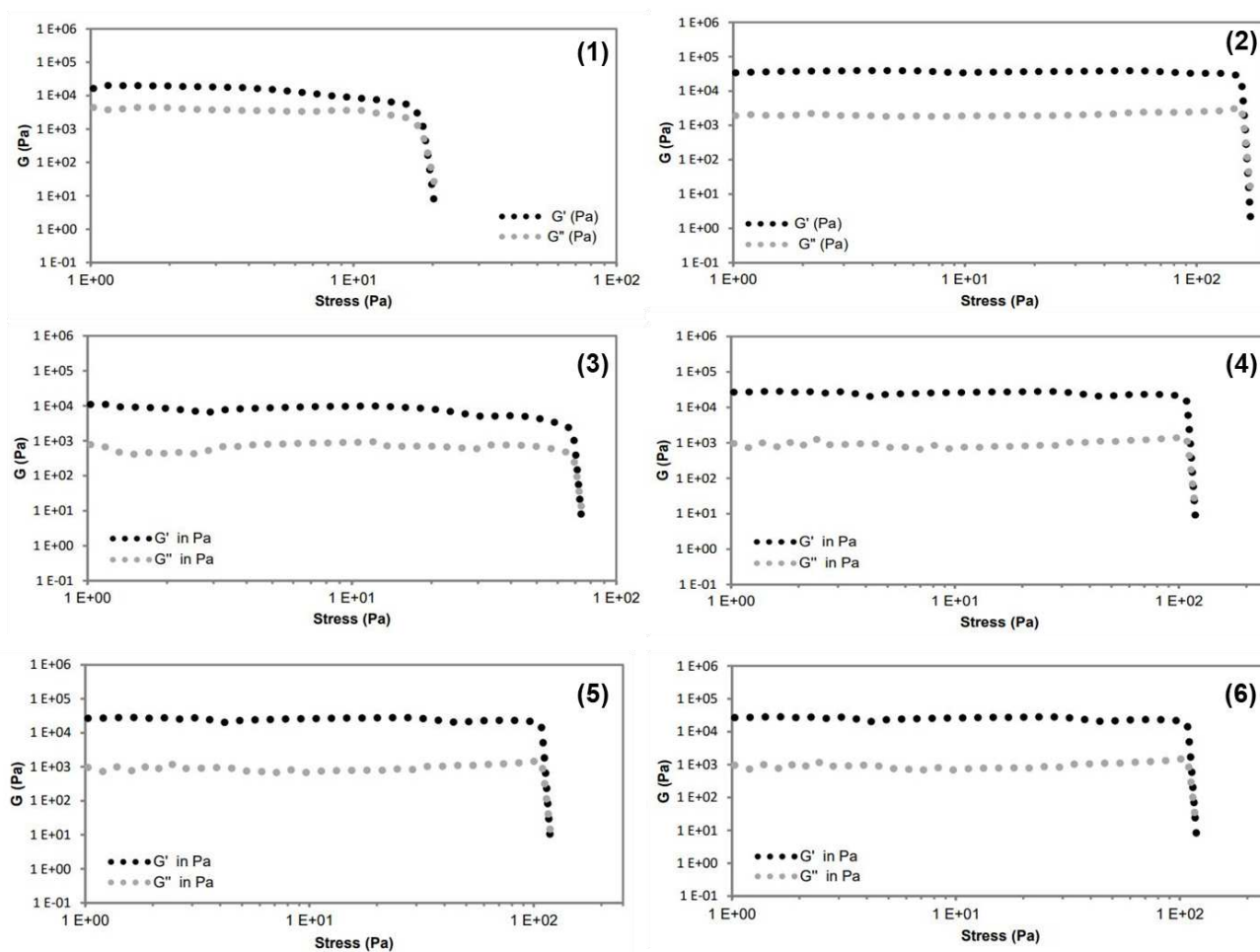


Figure 4.4. Stress sweep analyses of supramolecular hydrogels obtained by the self-assembly of the Phe-Phe compounds from **1** to **6**. Reproduced from ref [1] under a Creative Commons Licence.

After 1 h of self-assembly, gels were tested for thermoreversibility in a hot-bath, with a heating ramp of 5 °C/min, and results are reported in **Table 4.3**. Compounds **1–5** started to disassemble at 42–47 °C, whereas iodinated **6** showed higher thermal stability until 74 °C. Interestingly, homochiral **1** did not recover after melting, whereas all heterochiral dipeptides **2–6** recovered within a few minutes with iodinated **6** showing the fastest recovery.

Compound	T_{onset} (°C)	T_{offset} (°C)	Recovery time (min)
1	46	67	NO
2	44	66	8
3	44	56	13
4	47	59	10
5	42	51	7
6	74	83	4

Table 4.3. Thermoreversibility test of supramolecular hydrogels of compounds **1–6** at their mgc. Reproduced from ref [1] under a Creative Commons Licence.

TEM micrographs revealed anisotropic morphologies in all cases (**Figure 4.5**). Homochiral **1** formed rigid microtubes, as reported previously, with heterogeneous diameters in the range of several hundreds of nanometers. After thermoreversion, sample **1** was heterogeneous with liquid separation from the solid; TEM micrographs revealed larger microtubes, thus with reduced surface area to interact with water, and this feature could explain its inability to gel. In contrast, heterochiral **2** assembled in homogeneously sized fibrils with an average diameter of 4.3 ± 0.6 nm ($n = 100$). An analogous size distribution was observed also for **3** (4.4 ± 0.7 nm) and **4** (3.9 ± 0.6 nm) after thermoreversion, suggesting a similar supramolecular packing. Compounds **5** and **6** formed thicker fibers, which was not too surprising given the opacity of their corresponding hydrogels.

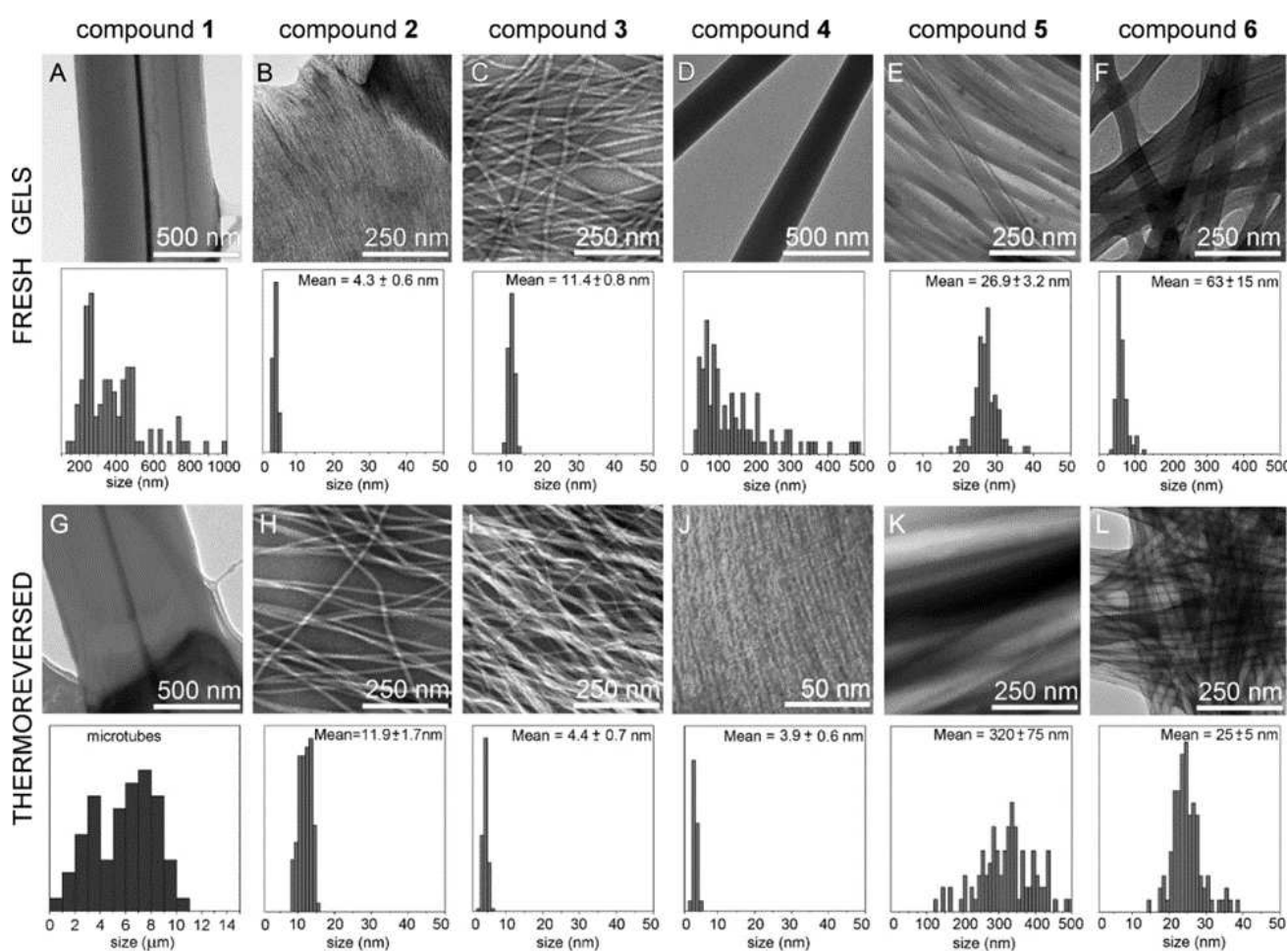


Figure 4.5. TEM micrographs with, underneath, the corresponding fibril diameter distribution ($n = 100$) of self-assembled **1–6** at their mcg before (A–F) and after (G–L) thermoreversion. Reproduced from ref [1] under a Creative Commons Licence.

4.1.2.2. Peptides' conformation analysis

To gain a deeper understanding of the self-assembly mechanisms of these dipeptides, their conformations were investigated spectroscopically. The circular dichroism (CD) spectrum for homochiral **1** was in agreement with the literature (**Figure 4.6 A**) [19]. Heterochiral dipeptides **2–6** displayed diverse CD signatures in the UV region. The complex signals for the supramolecular hydrogels (**Figure 4.6 A**) were the result of the self-assembly process and were challenging to interpret. However, it is worth noting that the CD spectrum of the gel of compound **6** was significantly different compared to all the others, being the only one displaying an unusual maximum at 243 nm. The spectrum suggested a different packing mode relative to compounds **1–5**. It was reminiscent of the CD signature of Asp-Phe-Asn-Lys-(4-I)-Phe, an amyloidogenic gelator that did not establish halogen bonding, characterized by a cross- β -sheet structure, whereby the peptides stacked in layers with the backbones perpendicular to the long axis of the fibrils [17]. Heating ramps confirmed a similar trend in melting temperatures as observed macroscopically, that is, 38–50 °C for compounds **1–5**, and a significantly higher T_m of 60 °C for iodinated **6** (**Figure 4.7**). In the disassembled state (*i.e.*, at 70–80 °C), all compounds **1–6** displayed similar spectra (**Figure 4.6 B**), analogous to **1** in the assembled state (**Figure 4.6 A**). We inferred that all peptides adopted analogous conformations in the solution state, and the different details of their structures were amplified during the assembly process. The CD signature in the 200–220 nm range has been recently assigned to a distribution of conformations in solution with the most stable ones populating the top left quadrant of the Ramachandran plot (*i.e.*, β -structures and turns) [32].

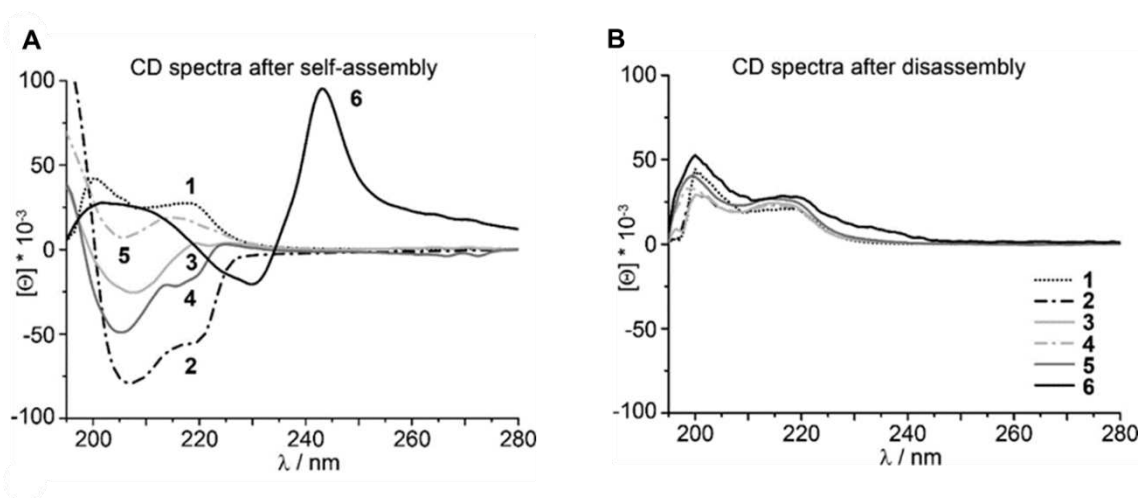


Figure 4.6. CD spectra for **1–6** hydrogels in the assembled state (A) and upon heating-induced disassembly at 70–80 °C (B). Reproduced from ref [1] under a Creative Commons Licence.

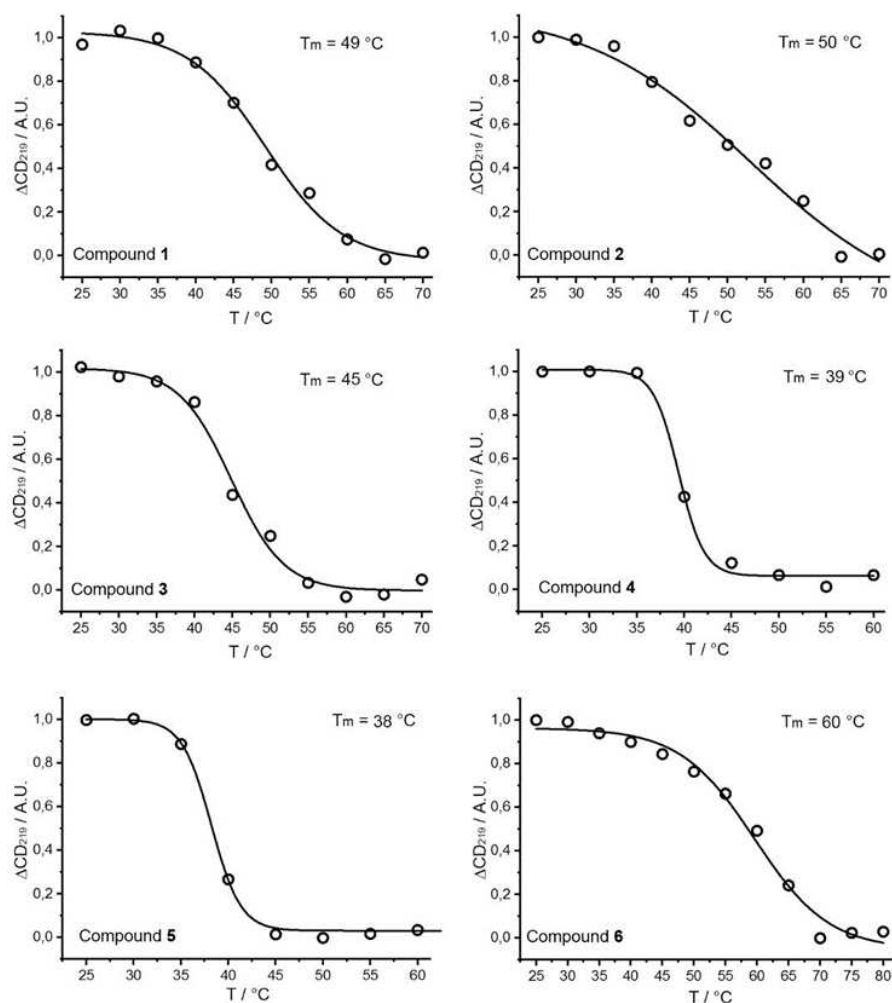


Figure 4.7. Circular dichroism data for the compounds **1-6** over a heating ramp. Reproduced from ref [1] under a Creative Commons Licence.

The amide I-II region ($\sim 1400-1800\text{ cm}^{-1}$) of ATR-IR spectra and positive response to the Thioflavin T fluorescence amyloid assay showed a behaviour similar to β -structures (**Figures 4.8-4.9**), although dipeptides have just one amide bond that is insufficient to satisfy the requirement of the hydrogen bonding network that defines β -sheets [33].

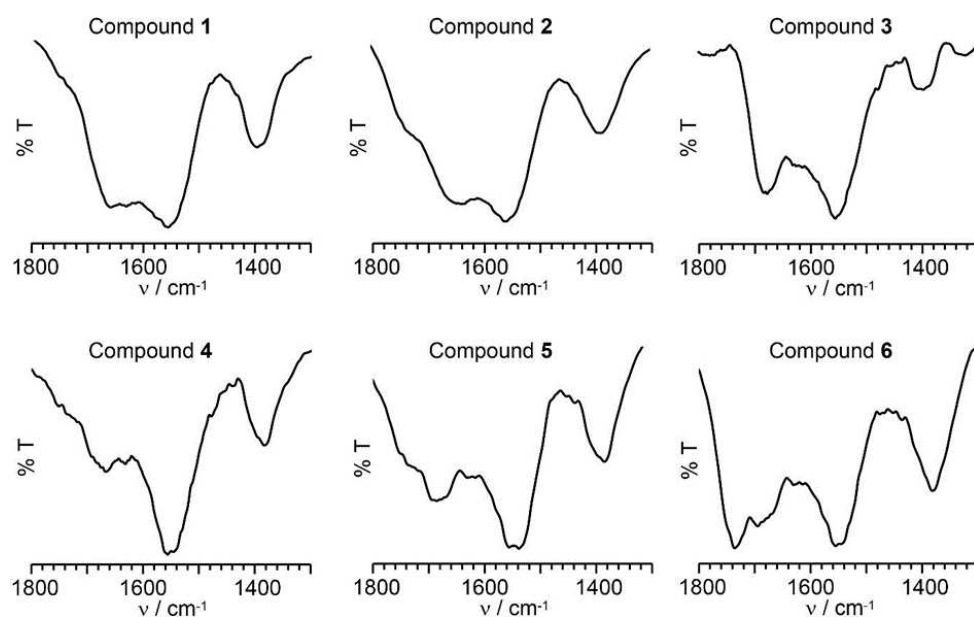


Figure 4.8. Amide region of the ATR-IR spectra for compounds 1-6. Reproduced from ref [1] under a Creative Commons Licence.

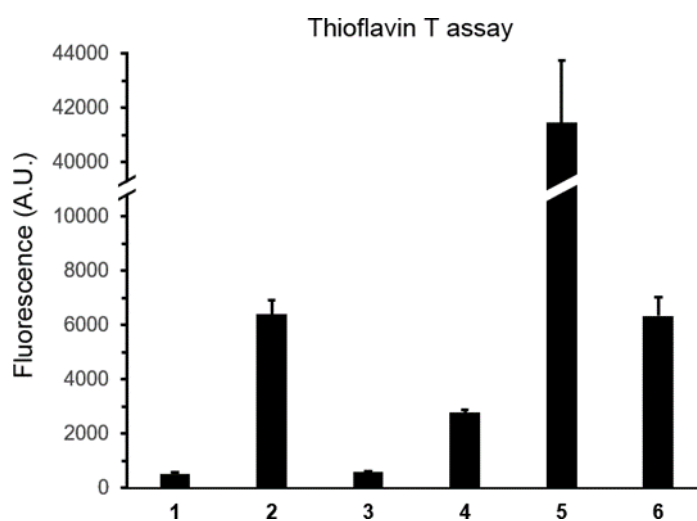


Figure 4.9. Thioflavin T fluorescence assay for compounds 1-6. Reproduced from ref [1] under a Creative Commons Licence.

4.1.2.3. Chirality effects on interactions responsible for hierarchical bundling

Single-crystal XRD structures revealed that despite the different stereoconfigurations of **1** [34] and **2** they displayed a strikingly similar supramolecular packing (**Figure 4.10**). In both cases, peptides stacked to form nanotubes, whereby the hydrogen-bond and salt-bridge patterns were conserved with similar interatomic distances. The chirality of the N-terminal residue dictated the direction of the peptide helical arrangement along the tube, which was thus left-handed for the L-dipeptide **1** (silver in **Figure 4.10 A**) and right-handed for D-L-heterochiral **2** (cyan in **Figure 4.10 A**). A key difference between the two stereoisomers was the orientation of Phe aromatic side chains (**Figure 4.10 B**, top) with only heterochiral **2** (cyan) displaying the Phe side chains engaged in intramolecular face-to-face interactions. The nanotube inner cavity (**Figure 4.10 B**, bottom) was defined by a tubular single layer of peptide molecules arranged head-to-tail with a 6-fold helical symmetry in both **1** and **2** crystals, thus forming an amphipathic water-channel with hydrophilic interior and hydrophobic exterior. Hydrophobic interactions involving molecules forming the water-channel further identified a tubular double layer of peptides with a total of 18 molecules visible in the top-view projection for both **1** and **2** (**Figure 4.10 C**, top). However, as a result of the different spatial orientation of Phe side chains between stereoisomers **1** and **2**, only in the case of homochiral **1** was the outer surface of the tubular double layer of peptides rugged with significant interdigitation between aromatic rings in steric zippers, which are an amyloid stabilizing feature [35] that secured hierarchical assembly into bundles (**Figure 4.10 C**, silver). By contrast, in the case of heterochiral **2**, the tubular double layer of peptides displayed a smoother outer surface, thanks to a higher level of intramolecular aromatic interactions, with an outer diameter of 4.2 nm (cyan in **Figure 4.10 C**) which matched well the average fibril size of 4.3 nm observed by TEM (see **Figure 4.5**). The heterochirality of **2** oriented Phe side chains to avoid hierarchical bundling and instead stabilize double layers of peptides constituting 4 nm-wide fibrils. In light of the well-known challenges to control the growth of hierarchical assemblies of flexible simple molecules, such as unprotected dipeptides, this dataset revealed a promising yet very simple strategy to control self-organization to yield a highly homogeneous population of nanofibrils.

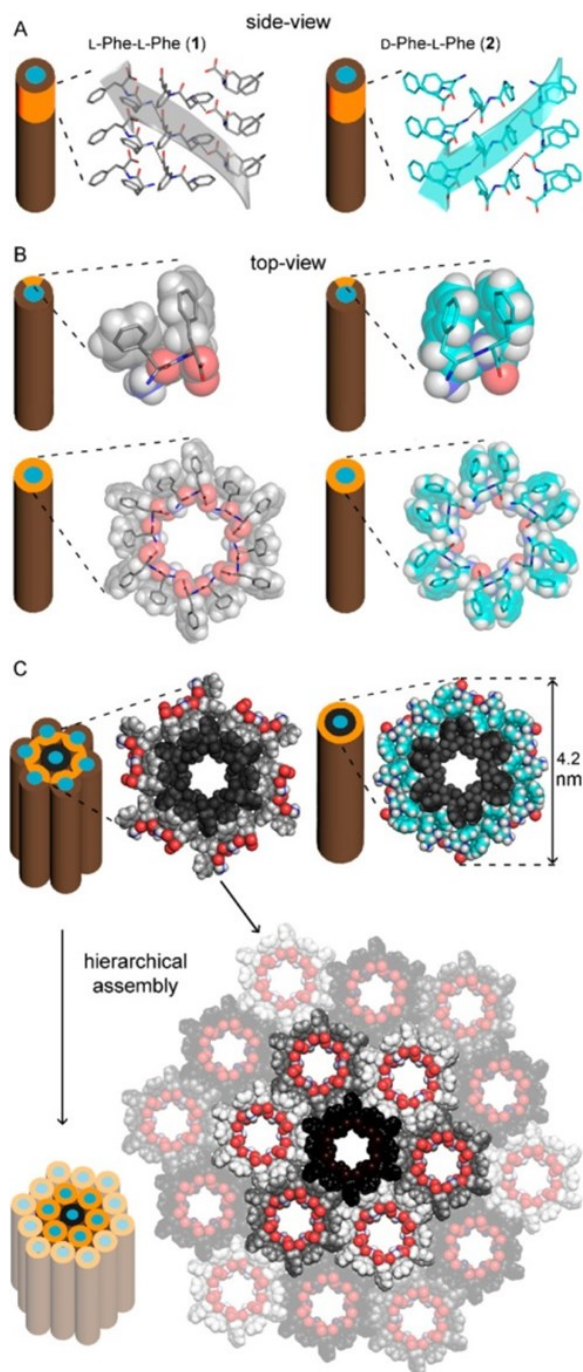


Figure 4.10. Single-crystal XRD structures of homochiral **1**[34] (silver) and heterochiral **2** (cyan, CCDC 2016375) peptide nanotubes. (A) Side-view of stacked peptides revealed opposite screw-sense for **1** (silver) and **2** (cyan), dictated by the chirality of the N-terminal amino acids. (B) Top-view of nanotube inner cavities defined by the projection six peptide molecules arranged head-to-tail for both **1** (silver) and **2** (cyan), but only in **2** do the two Phe side chains interact face to face intramolecularly. (C) Top-view of the nanotubes identified by the projection of 18 peptide molecules for **1** (silver) showed hierarchical bundling stabilized by aromatic zippers; instead, a space-fill view of heterochiral **2** (cyan) revealed the outer diameter of a double layer of peptide molecules to agree with the diameter of fibrils measured by TEM. Reproduced from ref [1] under a Creative Commons Licence.

4.1.2.4. Fluorination effects on nanotube hierarchical assembly

Single-crystal structures of halogenated heterochiral dipeptides confirmed that the zwitterionic state was essential but not sufficient for their self-assembly into water-channels. In particular, ionic interactions between termini observed in the head-to-tail packing shown in **Figure 4.10 A-B** could not be established in the crystal structure of the cationic form of fluorinated **4**, $4^+ \cdot \text{CF}_3\text{COO}^-$, (CCDC 2016372) see **Figure 4.11**.

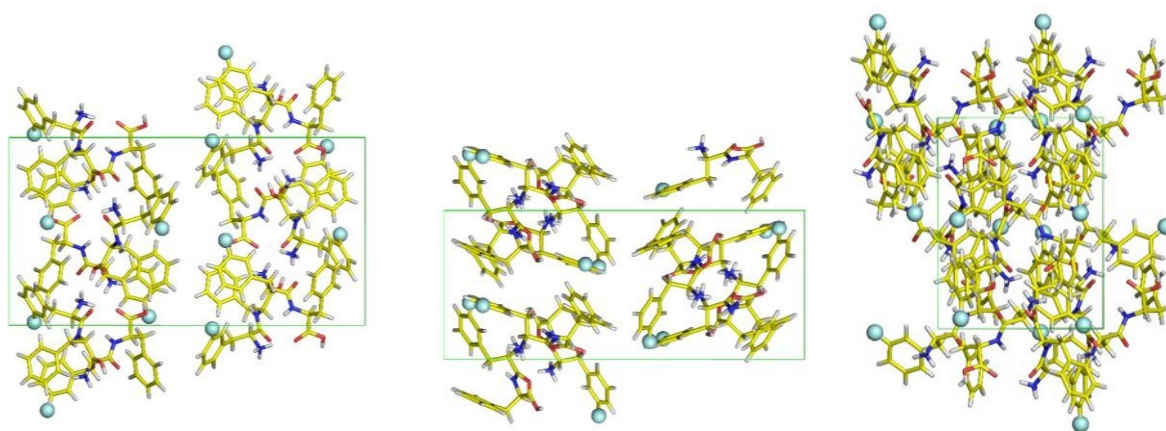


Figure 4.11. Unit cell of crystals of compound **4** as a TFA salt. Views along the a (left), b (center), and c (right) crystallographic axes. Hydrogens, solvent, and TFA counterions are not shown for clarity. F atoms are displayed as spheres. Reproduced from ref [1] under a Creative Commons Licence.

In contrast, the zwitterionic states of fluorinated heterochiral dipeptides could engage in interactions and packing analogous to those described above for heterochiral **2**, as confirmed by the crystal structure of fluorinated **5** (**Figure 4.12 A**), as well as powder-XRD diffraction analysis of aged gels, whose patterns matched well those generated from the single-crystal structures of the corresponding zwitterions (not shown).

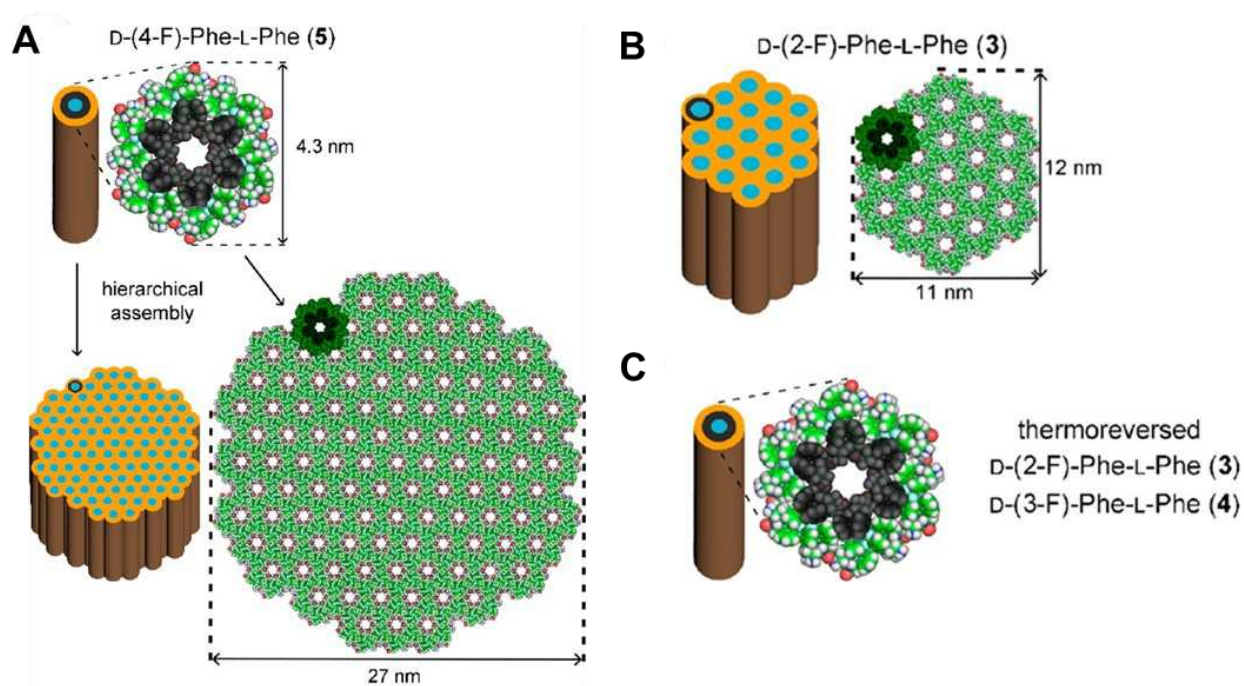


Figure 4.12. (A) Single-crystal XRD structure (CCDC 2016373) of fluorinated heterochiral **5** revealed analogous packing to heterochiral **2** (compare with **Figure 4.10.C**) with an intermediate level of bundling to generate 27 nm-wide fibrils as observed by TEM. (B, C). Powder XRD on microcrystals grown on hydrogels of **3–4** confirmed packing analogous to **5**. (B) Fibrils of **3** had a diameter of 11–12 nm by TEM, corresponding to the packing of 19 water-channels. (C) Thermoreversion stabilized 4 nm wide fibrils for both **3** and **4**, corresponding to a double-layer of peptides around a water channel as revealed by the single-crystal XRD of **5**. Reproduced from ref [1] under a Creative Commons Licence.

Iodine appeared too bulky to fit in the supramolecular water-channel organization identified by XRD for compounds **1–5** (shown in **Figures 4.10–4.12**). Indeed, iodinated **6** displayed a different mode of packing with layers (**Figure 4.13 A**) of stacks of peptides (**Figure 4.13 B**). The aromatic side chains of facing dipeptides defined hydrophobic regions that were occupied by the iodine atoms, similarly, to iodinated L-diphenylalanines [20]. The stabilizing effect of the interdigitation of the iodinated aromatic rings (**Figure 4.13 C**) was likely the reason for the superior gelling ability of iodinated **6** relative to the other compounds **1–5**. Surprisingly, no evidence for halogen-bonding was observed, as no atoms were located within van der Waals radius of iodine, and no Lewis partner was oriented in the surroundings at a suitable angle [36]. This is in marked contrast with L-(4-I)-Phe-L-Phe and L-(4-I)-Phe-L-(4-I)-Phe crystal structure, where iodine atoms engaged in halogen bonding, yet no gel was formed [20]. However, examples of amyloidogenic short peptides with (4-I)-Phe not engaging in halogen bonding were also described, whereby peptides stacked with their backbones perpendicular to the long axis of the assembly's growth, similarly, to compound **6** (**Figure 4.13 D**) [17][21]. There is an ongoing debate as to the relevance of the packing observed in the crystalline state relative to the hydrogel, as the two forms are clearly different at the macroscopic and

microscopic level. Depending on the nature of the solvent and the solute, in some cases both the crystal state and the hydrogel state can act as thermodynamic systems [37]. In other cases, the hydrogel is the kinetic product, and the crystal is the thermodynamic one [38].

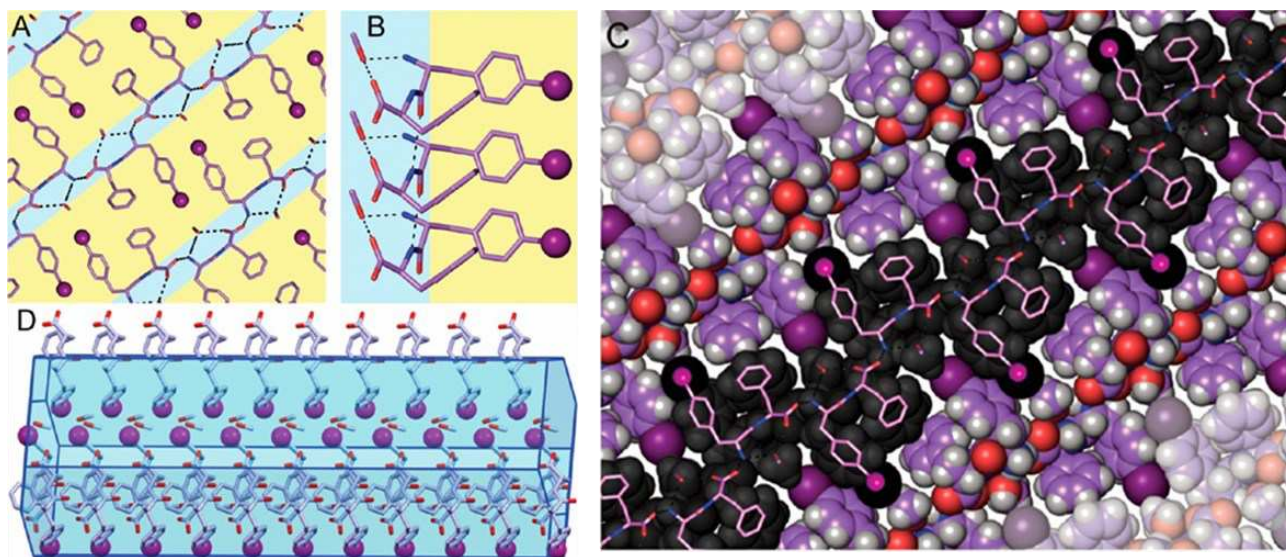


Figure 4.13. Single-crystal XRD structure of iodinated **6** (CCDC 2016374). (A) Hydrogen bonding and ionic interactions (dotted lines) defined hydrophilic layers (light blue), whereas iodine (purple sphere) allowed interdigitation of Phe side chains in hydrophobic layers (yellow). (B) Side-view of amphiphilic peptide stacks. Iodine atoms are located 4.9 Å from each other. (C) Space-fill view of peptide layers shown in panel A to show the tight supramolecular packing. (D) Side-view of peptide stacks reveals peptide backbones perpendicular to the preferential growth direction of the crystals. Reproduced from ref [1] under a Creative Commons Licence.

To shed light on the presence of halogen bonding in the gel state, we thus performed micro-Raman analysis (**Figure 4.14**). Raman spectra of **6** in the crystal and gel states were nearly identical, suggesting analogous packing. By contrast, diagnostic differences were noted with the powder (signals marked with * in **Figure 4.14**). The presence of iodine in **6** resulted in three additional bands relative to **2**, due to the C–I stretching (246 cm^{-1}), ring asymmetric torsion (630 cm^{-1}) and ring vibration (1062 cm^{-1}) of the iodinated benzene ring (**Figure 4.14 B**) [39,40]. The former of the three bands displayed a 6 cm^{-1} red shift in the gel and crystal, relative to the powder form. Because no halogen bond was observed in the crystal, and because Raman spectra of the crystal and the gel state displayed analogous signature, we inferred that the red shift was simply a manifestation of the hydrophobic environment surrounding the iodine atom as a result of self-assembly [41,42]. In the amide I region, the signal at 1664 cm^{-1} in the powder was shifted to 1685 cm^{-1} in the gel and crystal states, as a result of the extended hydrogen-bonding pattern between amides [43,44]. Similarly, the signal at 1250 cm^{-1} in the amide III region, resembling the β -sheet signature, was clearly visible in

the gel and crystal states [43,44]. Analysis of the other gels confirmed presence of the diagnostic signals due to supramolecular organization (**Figure 4.14 B**).

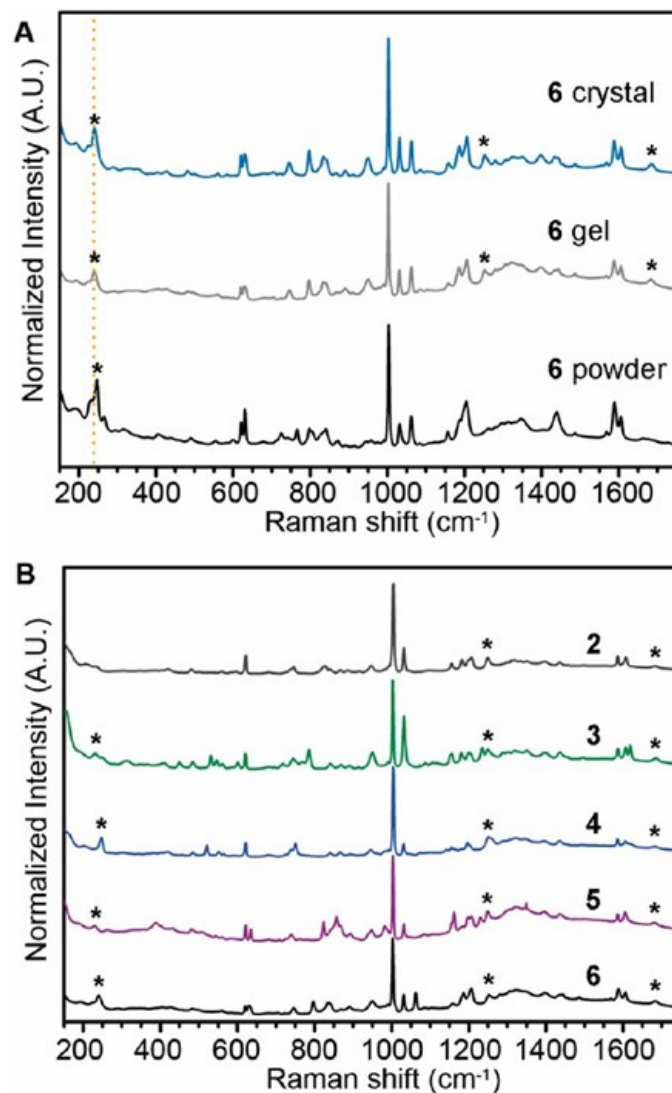


Figure 4.14. (A) Raman spectra of iodinated **6** in the crystal, gel, and powder forms. The dotted orange line marks the C–I stretch. (B) Raman spectra of compounds **2–6** in the gel form. * Denotes significant differences that were inferred to arise from supramolecular organization. Reproduced from ref [1] under a Creative Commons Licence.

4.1.2.5. Hydrogels' biocompatibility assessment in cell culture

The hydrogels were tested for cytotoxicity in cell culture (**Figure 4.15**). Heterochirality was confirmed to stabilize self-assembly into hydrogels. The metastable gel of L-Phe-L-Phe **1** did not last for 24 h in cell culture, and the characteristic microtubes with a few round cells were observed at the high concentration of 35 mM (**Figure 4.15**), whereas at 25 mM microtubes were not observed by the end of the experiment. By contrast, heterochiral **2** formed a homogeneous hydrogel sheet that detached from the plastic dish, and onto which cells densely grew with high viability and integrated into the matrix as in a tissue, both at 25 and 35 mM (**Figures 4.15–4.16**). Fibroblasts preferred to

grow in the hydrogel **2** as opposed to the tissue-culture plastic surface, showing promise for the future development of this scaffold as a biomaterial (**Figure 4.15 right**).

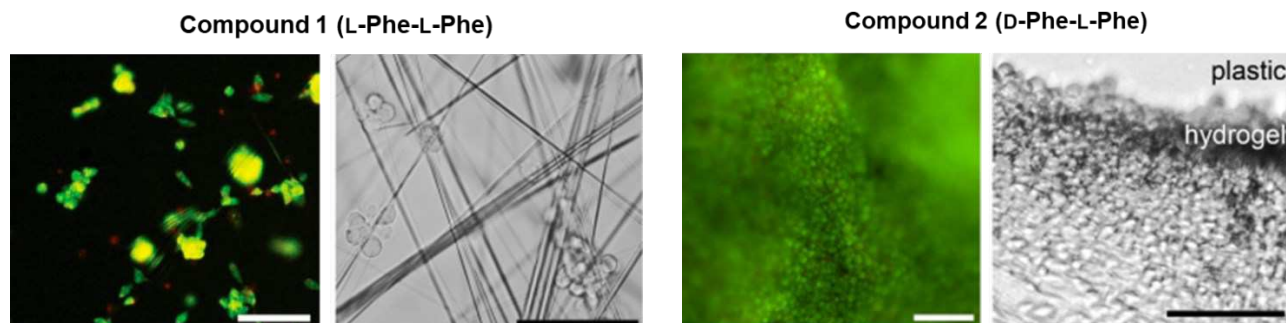


Figure 4.15. Live (green)/dead (red) fluorescence (left,) and bright-field (right) microscopy images of fibroblasts cultured on hydrogels **1-2** as scaffold support. Scale bars = 100 μm . 10x objective for fluorescence green filter and 40x for bright-field filter. Reproduced from ref [1] under a Creative Commons Licence.

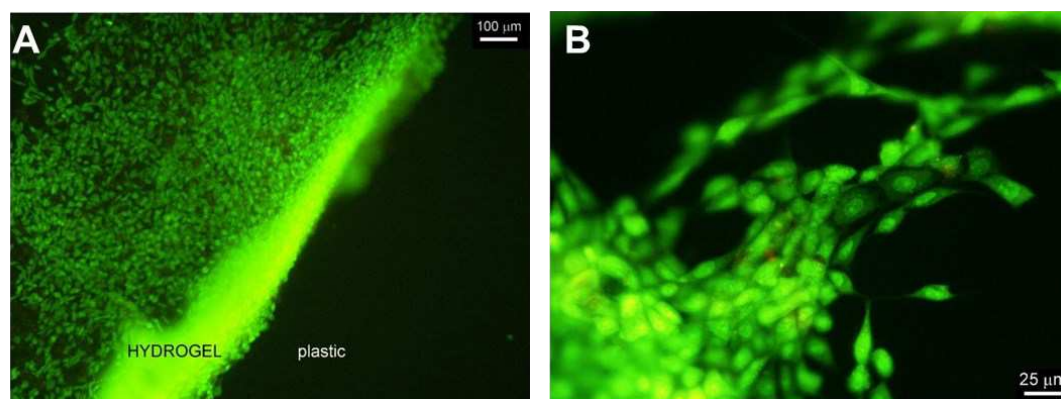


Figure 4.16. Fluorescence microscopy of cells cultured on compound **2** hydrogel at 25 mM (**A**) and 35 mM (**B**) for 24 h. Reproduced from ref [1] under a Creative Commons Licence.

Among the halogenated analogues, fluorinated **3-5** did not persist as hydrogels in cell culture, and cell viability was negatively affected with cell debris clearly visible in all cases (**Figure 4.17**). Finally, fibroblasts grew in the hydrogel of iodinated **6**, although with suboptimal viability. This scaffold was the most durable as it was intact and attached to the plastic bottom after 24 h of cell culture, yet its translucent nature somewhat impeded bright-field visualization of cells (**Figure 4.17**).

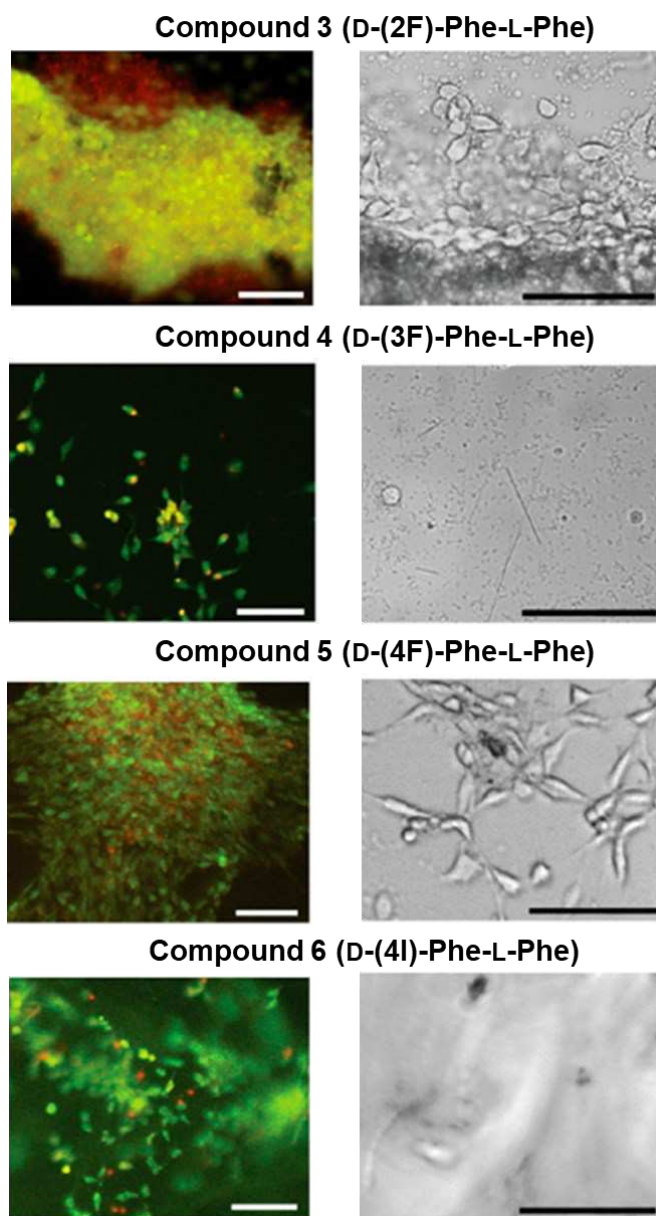


Figure 4.17. Live (green)/dead (red) fluorescence (left,) and bright-field (right) microscopy images of fibroblasts cultured on hydrogels **3–6**. Scale bars = 100 μm . 10x objective for fluorescence green filter and 40x for bright- field filter.

From live/dead assays, compound **2**, the heterochiral D-Phe-L-Phe, appeared to be the most promising biomaterial scaffold among all the dipeptides tested. This result was also confirmed by the quantitative MTT (3-[4,5-dimethylthiazole-2-yl]-2,5-diphenyltetrazolium bromide) assay performed in solution on a second cell line, the keratinocytes (HaCaT).

MTT (3-[4,5-dimethylthiazole-2-yl]-2,5-diphenyltetrazolium bromide) cell proliferation assay is a colorimetric test used to determine the number of viable cells by assessing cell metabolic activity. The method is based on the conversion of the water-soluble yellow dye MTT (tetrazolium inner salt) into a purple-coloured insoluble formazan product by living cells through the action of a mitochondrial reductase. Then, formazan crystals are dissolved in a specific organic solvent for

homogeneous measurements of its concentration determined spectrometrically using a multiwell scanning spectrophotometer. As the mitochondrial activity in the most of living cells is constant, either a decrease or an increase in the number of viable cells is linearly related to mitochondrial activity. The mitochondrial activity of the cells is reflected by the conversion of the dye MTT into formazan precipitates [53].

The mechanism of the MTT assay involves a conversion of the tetrazolium salt MTT carried out by NAD (P)H-dependent dehydrogenase enzymes in metabolically active cells. (**Figure 4.17**).

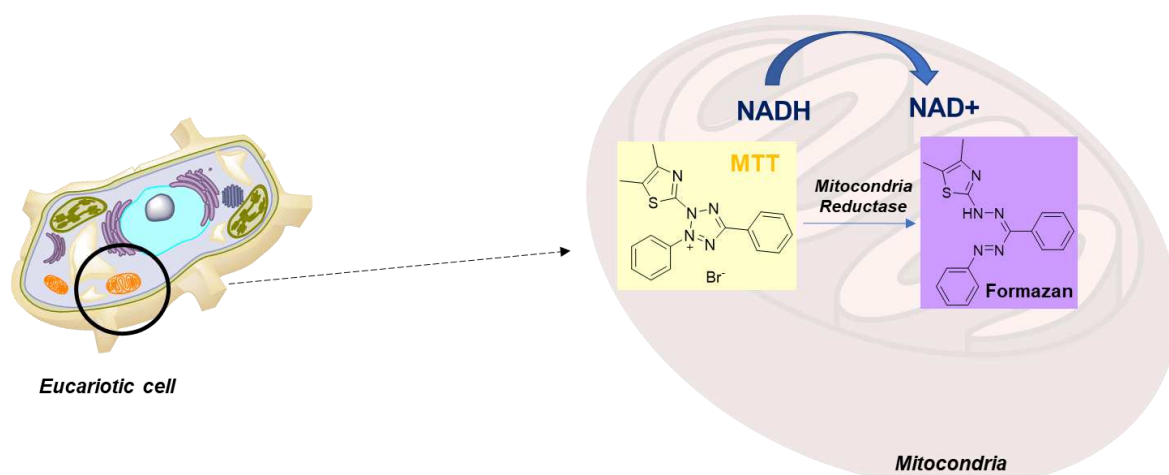


Figure 4.17. Metabolization of tetrazolium salt MTT (yellow) to formazan (purple) crystals by viable mammalian cells such as keratinocytes or fibroblast.

HaCat (keratinocytes) cells were cultured in the presence of increasing concentrations of each compound (**1-6**) in solution for 24 hours to assess the cytocompatibility of each dipeptide in contact with mammalian cells (**Figure 4.18**). Even at the highest concentration tested, the compound **2** displayed a good cytocompatibility compared to the other compounds (**2-6**). The compound **6** appeared the worst performer of the series with a low biocompatibility versus mammalian cells.

After a visual observation for the complete purple formazan crystals solubilization, the absorbance of the resulting-coloured solution was read at 570 nm (with the reference wavelengths at 690 nm) using a scanning multiwell spectrophotometer.

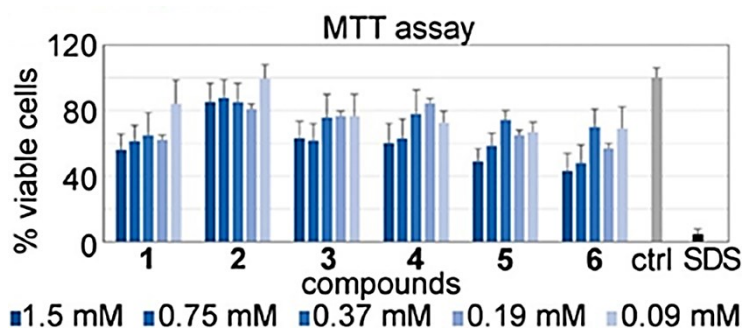


Figure 4.18. Quantitative MTT assay on keratinocytes (HaCaT cell line) incubated with peptides **1-6** in solution, in presence of different concentrations of each compound.

Overall, among all the compounds tested in *Manuscript 2*, D-Phe-L-Phe has been shown to have an encouraging biocompatibility on mammalian cells and future studies may focus on its optimization and enrichment with bioactive cues to direct cell behaviour.

4.1.3. Conclusions of *Manuscript 2*

This work focused on a building block as simple as the unprotected dipeptide D-Phe-L-Phe (compound **2**) and deciphered how and why heterochirality of dipeptides works as an effective design strategy to generate hydrogel biomaterials. Our studies revealed key insights that allowed control over hierarchical assembly into microstructures. Single crystal XRD studies revealed that despite having the opposite stereoconfiguration at one stereocenter, **2** self-organized into nanotubes with the same overall supramolecular arrangement as L-Phe-L-Phe (**1**), although the N-terminal amino acid stereoconfiguration dictated the screw-sense handedness from N- to C-terminus to be left-handed for **1** and right-handed for **2**. Relative to **1**, heterochiral **2** displayed increased intramolecular hydrophobic contact area between Phe side chains at the expense of the interchannel hydrophobic contact and of the consequent fibril bundling. The net result was that while L-Phe-L-Phe (**1**) is notorious for forming heterogeneously sized microtubes, heterochiral **2** self-organized into homogeneous and transparent hydrogels composed by 4 nm wide fibrils, arising from a double layer of peptides around a water-filled channel. Importantly, heterochirality resulted in thermoreversibility and complete alleviation of the well-known cytotoxicity of diphenylalanine, as observed in fibroblast and keratinocyte cell culture.

Halogenation likewise proved an effective strategy to influence supramolecular organization. In particular, fluorination preserved dipeptide packing into water channels as observed for non-halogenated **1** and **2** and provided an intermediate level of intra- versus inter-molecular hydrophobic interactions, thus resulting in an intermediate level of bundling into fibrils, and hence influencing

hydrogel viscoelastic properties, depending on the positioning of the fluorine atom. XRD analyses confirmed that the zwitterionic state was necessary but not sufficient for self-organization of the unprotected dipeptides into nanotubes. Interestingly, *p*-iodination of D-Phe-L-Phe completely altered the packing from water channels to amphipathic layers, yet it promoted self-assembly and zipping and yielded overall higher stability for hydrogel **6**, in agreement with the literature on iodinated peptides [26,29]. We note, however, that the previously reported iodinated homochiral dipeptide analogs displayed limited solubility as a result of iodination and were not reported to form gels [29]. Counterintuitively, single-crystal XRD and microRaman analyses revealed no halogen bonding occurring in the present case, suggesting a mere increase in hydrophobicity and steric hindrance that stabilized the interdigitation of Phe zippers at the basis of hydrogel stability for **6**. When tested in cell culture, fluorinated compounds **3–5** were unstable and displayed limited cytocompatibility as evidenced by reduced cell numbers, presence of dead cells, and evident cell debris. Iodinated **6** was the most stable hydrogel also in cell culture conditions, yet its translucent nature and limited cytocompatibility indicated it is not promising as a biomaterial scaffold. In contrast, hydrogels of D-Phe-L-Phe (**2**) formed a continuous sheet that detached from the bottom of the wells and was of preference for cells to proliferate in high numbers over the plastic found underneath. Future studies will focus on the optimization of scaffold **2** toward the inclusion of bioactive motifs to direct cell fates, thus preparing advanced, yet low-cost, biomaterials.

4.2. C-terminal halogenation effect on D-Phe-L-Phe

4.2.1. Introduction

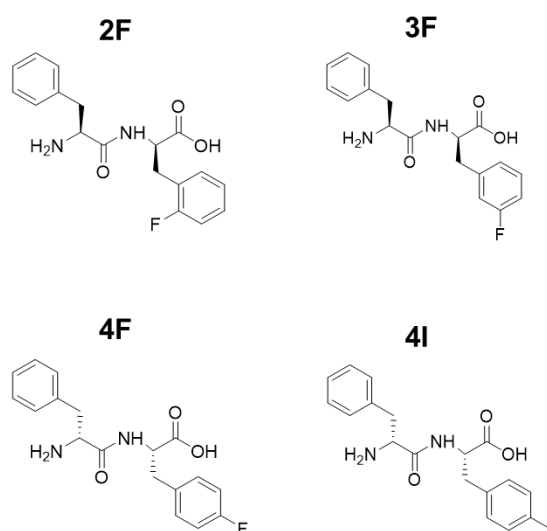
We have seen in the previous section that D-Phe-L-Phe surprisingly maintained the ability of homochiral L-Phe-L-Phe to self-assemble into nanotubes through stacking of dipeptides arranged head-to-tail to enclose a hydrophilic inner core [1]. As a result of the different stereoconfiguration, however, only the heterochiral Phe-Phe displayed the two aromatic rings face-to-face, enabling intramolecular interactions at the expense of intermolecular ones. Interestingly, the net result is the stabilization of a double-layer of peptides into 4-nm wide nanotubes, which formed a stable hydrogel, with suppression of the bundling tendency noted for the homochiral Phe-Phe. Monohalogenation of the N-terminal Phe into the corresponding **2-F**, **3-F**, **4-F**, and **4-I** derivatives maintained the ability to gel, with the advantage of a lower minimum gelling concentration (mgc). To extend the toolbox of self-assembling Phe-Phe derivatives, in this work, we show that when this approach is applied to the C-terminus, very different outcomes result from the supramolecular behaviour. Detailed investigation

using several techniques, including synchrotron-based UV Resonance Raman (UVRR) spectroscopy, sheds light on key differences in the Phe hydrophobic environment.

4.2.2. Results and discussion

4.2.2.1. Synthesis and molecular characterization

The four dipeptides shown in **Scheme 4.1**. were synthesized by solid-phase reaction, purified by reversed-phase HPLC and analysed for the purity and identity by LC-MS, ^1H -NMR spectroscopy and ^{13}C -NMR spectroscopy.



Scheme 4.1. Chemical structures of the four heterochiral Phe–Phe dipeptides. Reproduced from ref [2] with permission from © 2022 Royal Society of Chemistry.

All dipeptides are heterochiral, and since enantiomers display the same supramolecular behaviour in achiral environments, they are representatives of the four enantiomeric pairs D–L and L–D. All the fluorinated compounds displayed almost identical retention times (R_t) to their halogenated analogues at the N-terminus [1]. The R_t were all similar, with only **4-I** being slightly more hydrophobic (**Table 4.1**).

Halogen Substitution	Retention time (min) for C-terminal substitution (<i>Manuscript 3</i>)	Retention time (min) for N-terminal substitution (<i>Manuscript 2</i>)
2-F	14.2	14.1
3-F	14.4	14.4
4-F	14.4	14.4
4-I	15.5	15.5

Table 4.1. Retention time of heterochiral Phe-Phe dipeptides from Hplc analysis and their comparison with their gelling analogues halogenated at the N-terminal position (described in *ACS Nano* **2020**, 14, 16951). The HPLC method, which was run on an analytical C-18 column (Luna, Phenomenex), with a flux of 0.3 ml/min, consisted of a mixture MeCN/water with a gradient from 5% to 95% MeCN (with 0.05% TFA) over 20 minutes. Reproduced from ref [2] with permission from © 2022 Royal Society of Chemistry.

In diluted solutions, the CD spectra were reminiscent of their analogues halogenated at the N-terminus [1], with the D-L dipeptides displaying a positive signal above 200 nm, and the two L-D dipeptides displaying a negative signal (Figure 4.1 A). Previous studies showed that this type of CD signature can be a representative of a population of conformations, which can also be found for non-assembling analogues [32].

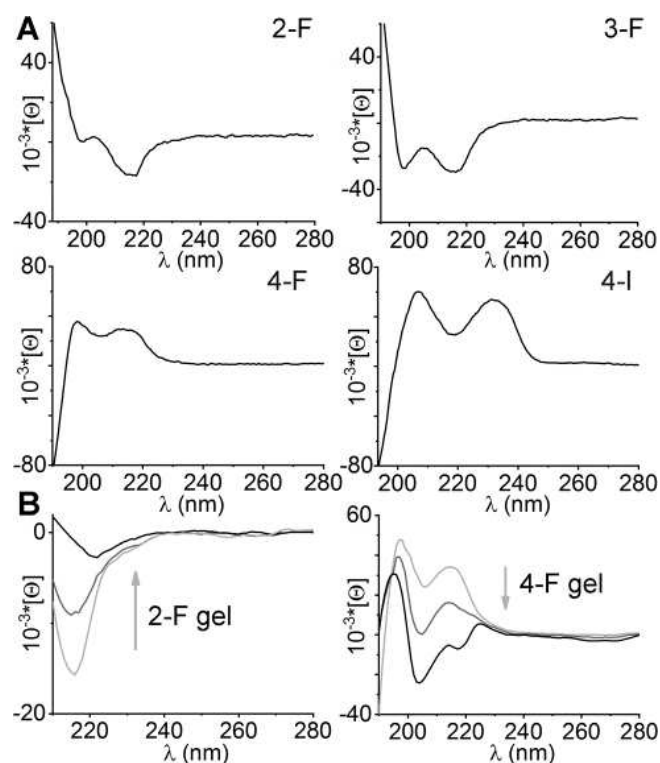


Figure 4.1. CD spectra of the dipeptides in solution (A) and in the gel state (B). The grey arrow indicates signal evolution over time. Reproduced from ref [2] with permission from © 2022 Royal Society of Chemistry.

4.2.2.2. Self-assembly in phosphate buffer

When subjected to a pH trigger from alkaline to neutral (**Figure 4.2**), only **2-F** and **4-F** gelled with mgc values of 15 and 7 mM, respectively. The gels were thermoreversible (**Figure 4.3**). Conversely, **3-F** and **4-I** consistently crystallized, allowing for XRD analysis (*vide infra*).

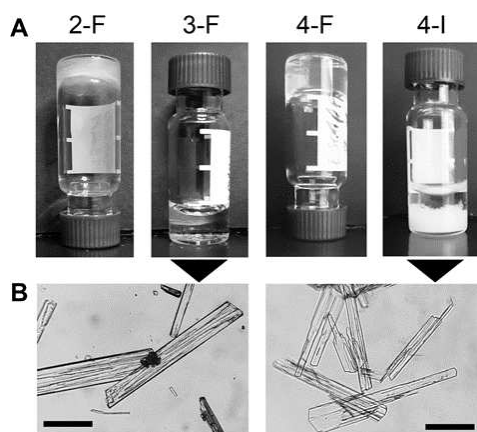


Figure 4.2. (A) Photographs of the four compounds in phosphate buffer (pH 7.3) above their solubility limit. (B) Optical microscopy image (10 \times) of the crystals formed by the **3-F** (left) and **4-I** (right) dipeptides. Scale bar = 200 μm . Reproduced from ref [2] with permission from © 2022 Royal Society of Chemistry.

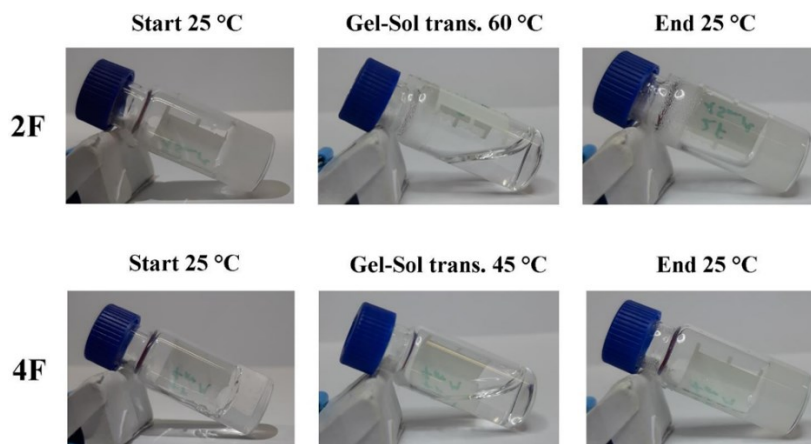


Figure 4.3. Gel thermoreversibility tests for **2-F** and **4-F** at their mgc.

Above the mgc, the CD signal rapidly evolved for **2-F** and **4-F** (**Figure 4.1 B**). Considering the similar HPLC retention times (**Table 4.1**), molecular hydrophobicity is not a discriminating parameter for gelation within this series.

The amide I and III regions of the FT-IR spectra were dominated in all cases by signals at 1680, 1210 and 1255 cm^{-1} , with an additional peak at 1228 cm^{-1} for **2-F**, which were all compatible with β -sheet-like hydrogen-bonding networks [33]. Other signals in the amide I region included a peak at 1639

cm^{-1} , compatible with β -sheet-like stacks, for the two gelators **2-F** and **4-F**, which was not evident in the case of **3-F** and **4-I** analogues. The amide II band, which is of more difficult interpretation, was also similar for the two gelators (1534 and 1572 cm^{-1}), and with blue-shifted signals for the other two compounds (1551 and 1585 cm^{-1}), in agreement with the more extended H-bonding network for the latter. The signal at 1570 cm^{-1} was already reported for fibrillating dipeptides, and it had been attributed to the strong association between the charged N- and C-termini in the supramolecular state [45][46]. The formation of β -sheet-like stacks was confirmed by thioflavin T fluorescence for the two gelators that formed homogeneous systems, enabling quantitative analysis (**Figure 4.4**).

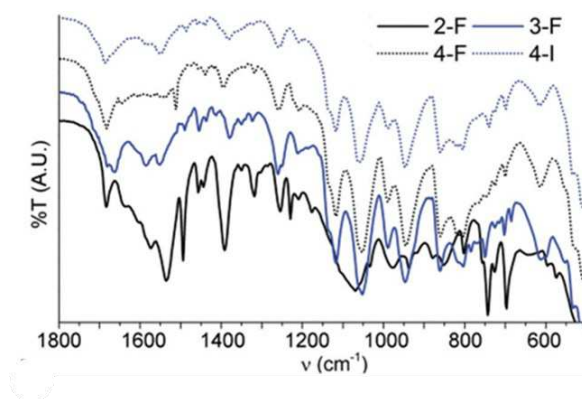


Figure 4.4. ATR FT-IR spectra of the four dipeptides upon application of the pH trigger. Reproduced from ref [2] with permission from © 2022 Royal Society of Chemistry.

In both cases, amyloid-associated fluorescence allowed the corresponding critical aggregation concentration (cac) [47] to be estimated as 13 and 4 mM for **2-F** and **4-F**, respectively (**Figure 4.5**).

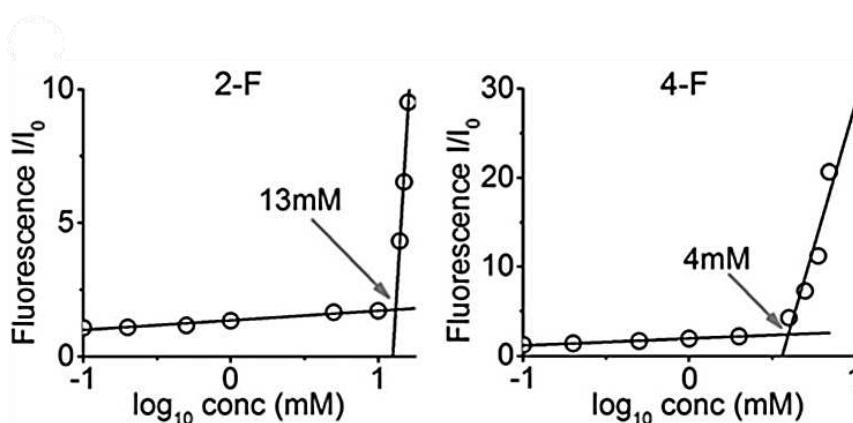


Figure 4.5. Thioflavin T fluorescence for the two gelators allowed the corresponding critical aggregation concentration to be calculated (cac, see the grey arrow). Reproduced from ref [2] with permission from © 2022 Royal Society of Chemistry.

Transmission electron microscopy (TEM) confirmed the presence of microcrystals for **3-F** and **4-I** and of fibrils for the gelling **2-F** and **4-F** (**Figure 4.6**). In particular, the fibrils of the **2-F** dipeptide displayed an average diameter of 17.5 ± 5.8 nm ($n = 200$) but also a marked tendency to bundle into fibres as thick as 100 nm, with many instances of fibres branching into fibrils and interconnecting points between the latter. This type of nanostructure is in agreement with the opaque appearance of the corresponding hydrogel and denotes a marked difference in the supramolecular behaviour relative to D-Phe-L-Phe that does not bundle [1]. Conversely, the **4-F** dipeptide formed a highly homogenous population of fibrils with an average diameter of 11.9 ± 1.8 nm ($n = 100$) that could run parallel for some lengths but without fusing into fibres, which was in agreement with the translucent appearance of the hydrogel.

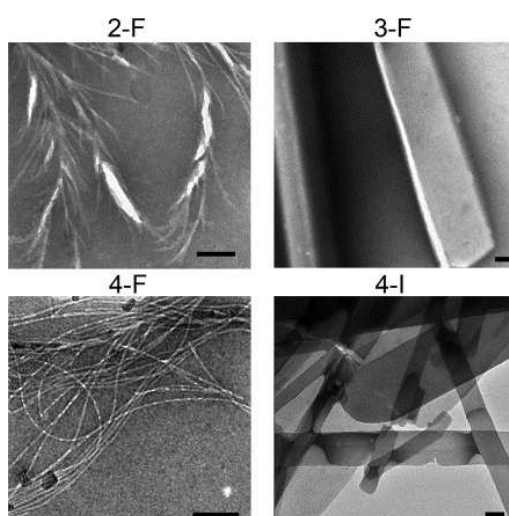


Figure 4.6. Transmission electron microscopy (TEM) images of the four dipeptides under self-assembly conditions. Scale bar = 200 μ m. Reproduced from ref [2] with permission from © 2022 Royal Society of Chemistry.

Previous studies on protein complexes suggested that fluorination in the *ortho* position can lead to stronger intermolecular stacking interactions, relative to the *para* position, and they could take part in fibril bundling observed only for **2-F**, but not **4-F** [48]. Local and direct positive effects of electron withdrawing substitutions on aromatic stacking interactions are established [49].

Oscillatory rheology confirmed the gel nature of the **2-F** and **4-F** compounds, whose gelation reached a plateau within 15 minutes, with elastic modulus G' values of 18 kPa and 8 kPa, respectively, at their corresponding mgc (**Figures 4.7-4.8**). Unsurprisingly, the gelation kinetics for **2-F** were slower than for **4-F**, as only the fibrils of the former bundled during the process, as confirmed by TEM (**Figure 4.6**). Similarly, the decrease in viscoelastic moduli accompanying the gel-to-sol transition in the stress sweeps (**Figure 4.7**) was wider for the former, whose gel is composed of a heterogeneous population of fibrils and fibers.

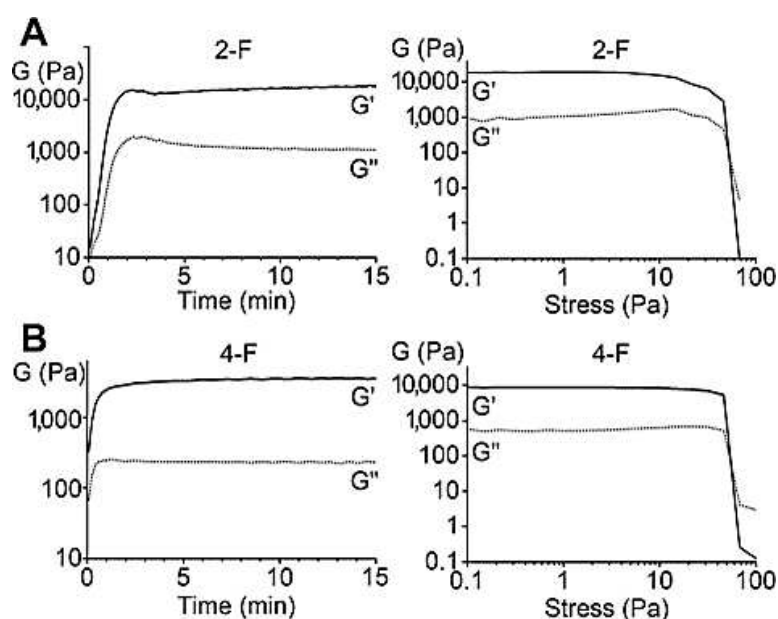


Figure 4.7. Oscillatory rheology time sweeps (left) and stress sweeps (right) for the two gelators 2-F (A) and 4-F (B) at their mcg. Reproduced from ref [2] with permission from © 2022 Royal Society of Chemistry.

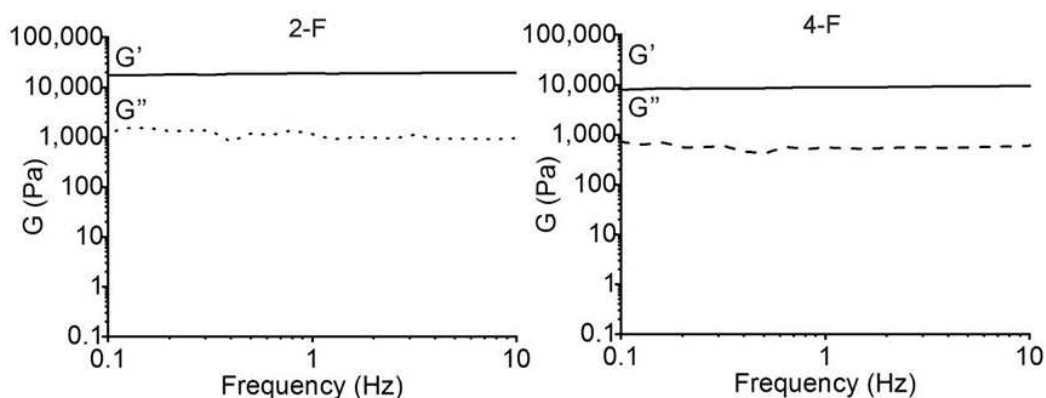


Figure 4.8. Frequency sweeps for 2-F and 4-F at their mcg.

4.2.2.3. Single-crystal X-ray diffraction (XRD)

The two compounds **3-F** and **4-I** consistently crystallized when subjected to the pH trigger (**Figure 4.2**), thus allowing for their study by X-ray diffraction (XRD, **Figure 4.9**). In both cases, the asymmetric unit contains a molecule of the peptide in its zwitterionic form and three molecules of water. Despite the notable differences between the iodine and fluorine radii, there is a striking similarity between the two structures, as evident from the superimposition of the peptide backbones of D-Phe-L-(**3-F**)-Phe and D-Phe-L-(**4-I**)-Phe, that adopt the same conformation (**Figure 4.9 A**). Furthermore, both peptides interact in the same way with their polar groups within the hydrophilic layer, although minor differences are noted in the hydrophobic layer where the halogen atoms reside.

In both cases, crystal packing shows a separation between the hydrophobic layers (shown in yellow in **Figure 4.9 C-D**) with the prevalence of phenyl groups and hydrophilic layers (shown in cyan in **Figure 4.9 C-D**) with the peptide backbones and water molecules. In particular, in hydrophilic layers, peptides form piles in the crystallographic direction *b*, held together by hydrophilic interactions, most of which are mediated by solvent molecules (**Figure 4.9 B**), which is a recurring feature of fibrillating dipeptides that do not gel [45,50]. (See *Manuscripts 4 and 5* of this Thesis). The iodine atoms are equally spaced along a crystallographic direction, with an average distance of 4.6 Å and no evidence of halogen bonding.

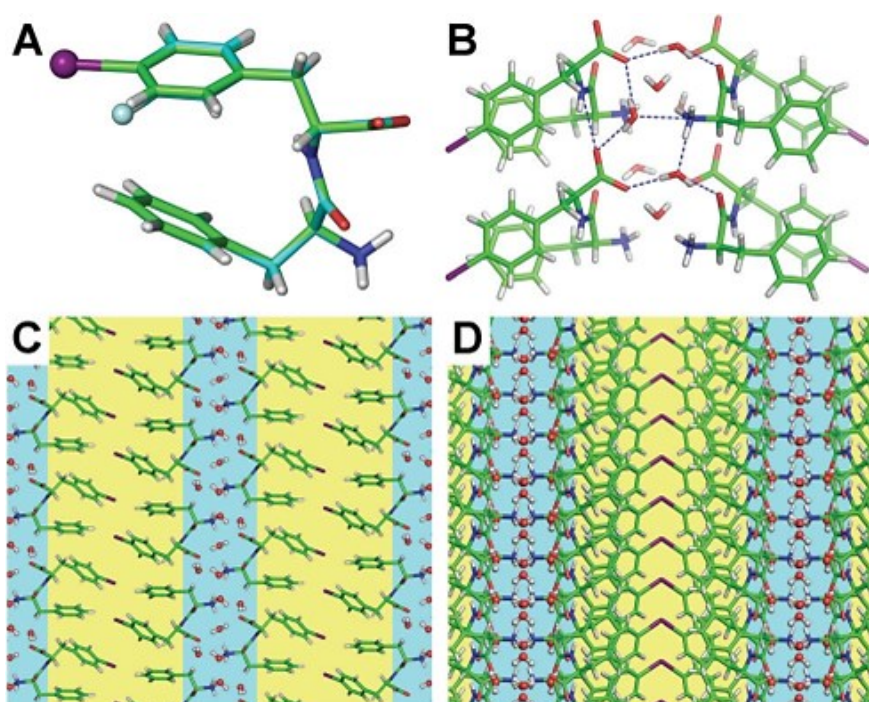


Figure 4.9. Single-crystal XRD data. (A) Superimposition of D-Phe-L-(**3-F**)-Phe (CCDC 2130532, carbon atoms in cyan) and D-Phe-L-(**4-I**)-Phe (carbon atoms in green). (B) Hydrophilic interactions of 4-I (CCDC 2130533). (C and D) Supramolecular packing of 4-I into hydrophobic (yellow) and hydrophilic (cyan) regions. (C) Top-view and (D) side-view of the peptide stacks. Reproduced from ref [2] with permission from © 2022 Royal Society of Chemistry.

This type of packing for **4-I** is not too surprising since a similar situation was found for the analogue D-(**4-I**)-Phe-L-Phe. Conversely, the fact that **3-F** shows the same type of layered packing is unexpected, since all the analogues that were fluorinated at the N-terminus formed, instead, supramolecular water channels [1].

Molecular models of the four dipeptides did not reveal clearcut trends in the orientation or magnitude of the dipole moment that could explain the higher propensity towards the crystallization of **3-F** and **4-I**, relative to **2-F** and **4-F**. This finding is in agreement with previous studies on fluorination at different positions of benzene and its effects on intermolecular interactions involved in protein complexes [48]. Other studies have also shown that electron density dispersion has a major contribution relative to electrostatics, in stabilizing stacking interactions between aromatic rings, of which one is fluorinated [51]. However, the minimized conformations of gelling **2-F** and **4-F** were very different relative to those found in the crystal structures of the former two. In particular, the dipeptide molecules were more extended with the phenyl rings further apart in a position that appears to be unfavourable for the establishment of intramolecular interactions (**Figure 4.10 A-C**) and the exclusion of water from hydrophobic layers as seen in **Figure 4.9 C-D**. The gels were tested for powder XRD, but no diffraction was observed. Thus, Raman spectroscopy was used to shed further light on the packing of the four compounds.

4.2.2.4. Visible Raman spectroscopy

Recently, we applied Raman spectroscopy to analyse the self-assembling behavior of short peptides based on the Phe–Phe motif [44]. In particular, this technique proved useful to assess the presence of halogen bonding and identify differences due to the supramolecular packing, in the crystal and gel phases, compared with the powder form [1][31]. Visible Raman spectra of the dipeptides in their powder form and gel or crystal states are shown in **Figure 4.11**. Due to the Raman interfering signal of water in the spectral region of interest, spectra were collected on dry samples. The most intense Raman signals are assigned to Phe, hereafter referred to as F1 ($\sim 1004\text{ cm}^{-1}$) and F2 ($\sim 1034\text{ cm}^{-1}$). Both these modes are due to side-chain vibrational motions of the Phe ring; in particular, the F1 band is due to the benzene breathing mode, while the F2 signal is associated with the in-plane CH bending [39][52]. Interestingly, the F2 band displays a blue shift of $4\text{--}5\text{ cm}^{-1}$ only for **3-F** and **4-I** in the crystals (insets in **Figure 4.11** for these two compounds). Conversely, no significant spectral changes for F1 and F2 were detected upon assembly of **2-F** and **4-F** into gels. This distinct behaviour may be related to the different packing of the Phe rings in the crystal or gel state, in agreement with molecular models. Furthermore, new signals (denoted with * in **Figure 4.11**) arose with assembly in all cases, of which those at 1256 cm^{-1} and 1687 cm^{-1} were evident only for **2-F** and **4-F** gels, respectively. These peaks were attributed to the amide III and amide I bands related to the formation of extended H-bond networks in β -sheet-like stacks of dipeptide gels [50]. However in this region, both aromatic and amide signals overlapped, and for this reason, UVRR spectroscopy was needed. Finally, no shifts due to halogen bonding were noted [1] in agreement with XRD.

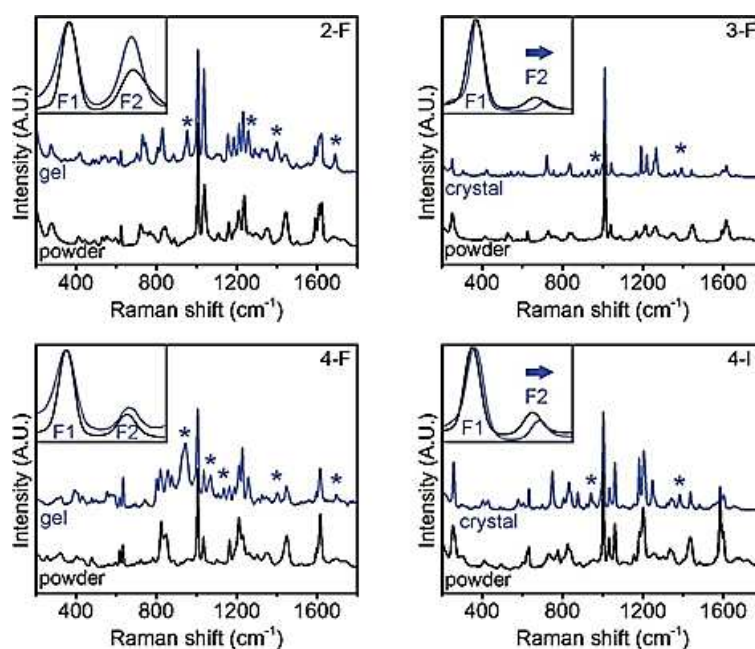


Figure 4.11. Visible Raman spectra of the four dipeptides. Reproduced from ref [2] with permission from © 2022 Royal Society of Chemistry.

4.2.2.5. UV Resonance Raman (UVRR) spectroscopy

Thanks to the resonance effect, UV Resonance Raman (UVRR) spectroscopy offers several advantages with respect to the conventional visible Raman technique, such as the significant increment of the detection limit and the selectivity needed to incisively monitor specific chromophores within the sample. The fine tunability of the synchrotron radiation source allows an accurate choosing of UVRR excitation wavelengths to efficiently disentangle the Raman bands associated with specific chemical groups. These conditions determine the usefulness of UVRR spectroscopy as a highly sensitive and selective spectral probe for exploring peptides under very diluted or concentrated conditions in water. UVRR spectra of peptides usually contain many vibrational fingerprints that can be related to the conformation and intermolecular interactions. In particular, the excitation wavelength at 226 nm is the most suitable for investigating the aromatic signals of Phe due to the close resonance of this excitation energy with their electronic transitions. [53,54]. This results in a strong enhancement of the UV Raman cross-section of some vibrational modes of Phe whose Raman signal dominates the UVRR spectrum, as confirmed by analysis of amino acid precursors devoid of the amide bond (**Figure 4.12**). The prominent Raman band observed between 1580 and 1620 cm^{-1} in the spectra of **Figure 4.13** is attributable to the in-plane ring stretching mode ν_{8a} of Phe [55] and is very sensitive to ring substituents [56]. In unsubstituted Phe, it appears at

1609 cm^{-1} [55,56] while *p*-substitution in **4-F** and **4-I** causes red shifts to 1604 and 1584 cm^{-1} , respectively. Conversely, a red shift to 1614 cm^{-1} is found for **2-F** and **3-F** (**Figures 4.12-4.13**).

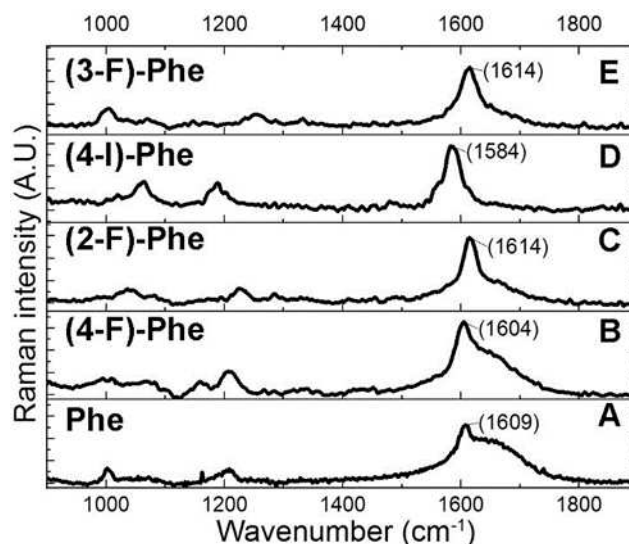


Figure 4.12. UVRR spectra (excitation wavelength at 226 nm) of the halogenated amino acid precursors (devoid of the amide bond) allows unambiguous assignment of the vibrational mode of the aromatic signal in the region of interest. Samples were dissolved (1 mg/ml) in the alkaline sodium phosphate buffer (pH 11.8, 0.1 M) and measured at 298 K. (A) L-Phe (B) L-(4-F)-Phe (C) D-(2-F)-Phe (D) L-(4-I)-Phe (E) D-(3-F)-Phe. Reproduced from ref [2] with permission from © 2022 Royal Society of Chemistry.

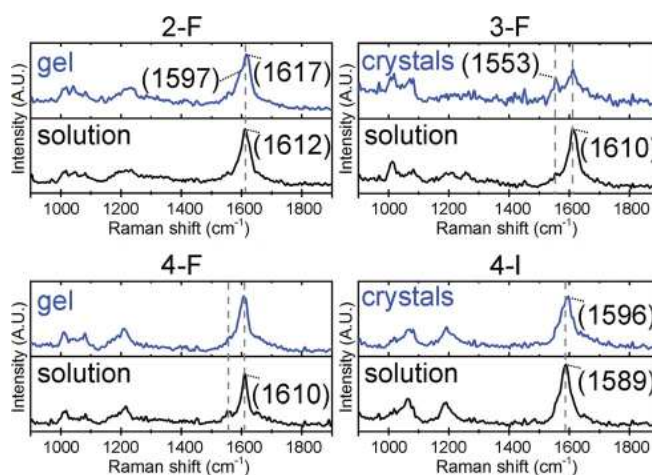


Figure 4.13. UVRR spectra of the four dipeptides in their precursor solutions (black traces) and after the pH trigger to neutral (blue traces) that yielded hydrogels (2-F and 4-F) or crystal suspensions (3-F and 4-I). Reproduced from ref [2] with permission from © 2022 Royal Society of Chemistry.

Phe can be involved in hydrophobic, cation- π and H-bond interactions with nearby residues or surrounding molecules of a solvent [57]. Both the wavenumber position and intensity of the Raman band assigned to the ring-stretching mode n8a were reported to be very sensitive to the local environment in peptide self-assembly [58]. In the case of **2-F**, the Raman signal corresponding to the ring-stretching mode of Phe is detected at $\sim 1612\text{ cm}^{-1}$ in solution (**Figure 4.13**). Gelation causes a 5 cm^{-1} red shift to 1617 cm^{-1} and the appearance of a shoulder at 1597 cm^{-1} . The blue shift is indicative of aromatic interactions arising from fibrillization, whilst splitting of the Raman signal could arise from interlayer interactions on the stacking order in the **2-F** gel, which is formed by fibrils and fibres of various diameters.

In the case of **4-F**, only a broadening of the n8a signal at 1610 cm^{-1} occurred upon assembly. The Raman cross section of these bands has been demonstrated to markedly depend on the exposure to water of the aromatic ring [59]. This finding could suggest a minor strength of the stacking interactions among Phe rings in **4-F** hydrogels, which indeed arise from fibrils that do not further bundle into fibers and are thus more exposed to the solvent relative to the **2-F** hydrogel. UVRR is thus consistent with TEM. Crystals of **3-F** and **4-I** were more difficult to analyze due to the heterogeneity of their dispersions in the liquid buffer. Indeed, the UVRR signal is collected from a spot size of several mm^2 ; thus, homogeneous gels of **2-F** and **4-F** allow for higher quality data relative to crystal dispersions of **3-F** and **4-I**. In the case of **4-I**, after several measurements, good-quality spectra were obtained that allowed a 7 cm^{-1} blue shift arising from the hydrophobic interactions of the Phe rings to be discerned, which was in agreement with the XRD data (see **Figure 4.9**). Unfortunately, in the case of **3-F**, the partial loss of the UV-resonant aromatic signals was noted, with the appearance of the non-resonant amide II signal at 1553 cm^{-1} , and no Phe-associated shifts could be unambiguously seen. However, since **3-F** and **4-I** display analogous packing, superimposable peptide backbones, and positions of water molecules (**Figure 4.9**), we expect a similar situation to **4-I**. Overall, UVRR allowed the amide and Phe aromatic signals to be disentangled and the inherent shifts due to halogen substitution to be unambiguously assigned. Secondly, UVRR enabled the monitoring of variations in the Phe environment arising from the assembly of the different peptides.

4.2.3. Conclusions of Manuscript 3

In this work, we report on the differing effects of Phe halogenation at the C-terminus, as opposed to the N-terminus, of heterochiral Phe-Phe, which provides gelators in all cases [1]. In particular, the peptides **3-F** and **4-I** demonstrate a strong propensity towards crystallization, with analogous supramolecular packing into amphipathic layers, and the absence of iodine-mediated halogen bonding. Conversely, **2-F** and **4-F** self-assemble into thermoreversible hydrogels, albeit with

differing amyloid nanostructures, cac, mgc, and viscoelastic properties. Remarkably, the presence of fluorine in the paraposition at the C-terminus maintained the suppression of hierarchical bundling noted for heterochiral Phe–Phe [1], whilst the opposite was true for the ortho position. Molecular models and visible and UV Resonance Raman spectroscopy indicate that the diverging behaviour is not due to molecular dipoles, but to the tendency of the Phe rings to adopt differing spatial orientations, which ultimately affect the peptides' ability to establish more or less hydrophobic regions that exclude water and stabilize gelling fibrils. In the future, it would be interesting to expand the application of UVRR to monitor diagnostic amyloid signals to other assembling peptides in an attempt to better identify more general rules for their self-assembly in physiologically relevant conditions.

References

- [1] S. Kralj, O. Bellotto, E. Parisi, A. M. Garcia, D. Iglesias, S. Semeraro, C. Deganutti, P. D'Andrea, A. V. Vargiu, S. Geremia, R. De Zorzi, S. Marchesan, *ACS Nano* **2020**, *14*, 16951–16961.
- [2] E. Scarel, O. Bellotto, P. Rozhin, S. Kralj, M. Tortora, A. V. Vargiu, R. De Zorzi, B. Rossi, S. Marchesan, *Soft Matter* **2022**, *18*, 2129–2136.
- [3] L. Adler-Abramovich, L. Vaks, O. Carny, D. Trudler, A. Magno, A. Caflisch, D. Frenkel, E. Gazit, *Nat. Chem. Biol.* **2012**, *8*, 701–706.
- [4] Y. Wang, W. Qi, R. Huang, X. Yang, M. Wang, R. Su, Z. He, *J. Am. Chem. Soc.* **2015**, *137*, 7869–7880.
- [5] Q. Xiong, Y. Jiang, X. Cai, F. Yang, Z. Li, W. Han, *ACS Nano* **2019**, *13*, 4455–4468.
- [6] N. Cheng, Y. Chen, J. Yu, J. Li, Y. Liu, *ACS Appl. Mater. Interfaces* **2018**, *10*, 6810–6814.
- [7] H.-L. Sun, Y. Chen, X. Han, Y. Liu, *Angew. Chemie Int. Ed.* **2017**, *56*, 7062–7065.
- [8] J. Chen, S. Qin, X. Wu, and P. K. Chu, *ACS Nano* **2016**, *10*, 832–838.
- [9] T. Kai, M. Pandeewar, A. Ruth, G. EHUD, *Science* **2017**, *358*, eaam9756.
- [10] Z. Gan, X. Wu, X. Zhu, J. Shen, *Angew. Chemie Int. Ed.* **2013**, *52*, 2055–2059.
- [11] V. Nguyen, R. Zhu, K. Jenkins, R. Yang, *Nat. Commun.* **2016**, *7*, 13566.
- [12] J.-H. Lee, K. Heo, K. Schulz-Schönhagen, J. H. Lee, M. S. Desai, H.-E. Jin, S.-W. Lee, *ACS Nano* **2018**, *12*, 8138–8144.

- [13] S. Safaryan, V. Slabov, S. Kopyl, K. Romanyuk, I. Bdikin, S. Vasilev, P. Zelenovskiy, V. Y. Shur, E. A. Uslamin, E. A. Pidko, A. V Vinogradov, A. L. Kholkin, *ACS Appl. Mater. Interfaces* **2018**, *10*, 10543–10551.
- [14] M. Reches, E. Gazit, *Science* **2003**, *300*, 625–627.
- [15] D. M. Ryan, S. B. Anderson, F. T. Senguen, R. E. Youngman, B. L. Nilsson, *Soft Matter* **2010**, *6*, 475–479.
- [16] D. M. Ryan, S. B. Anderson, B. L. Nilsson, *Soft Matter* **2010**, *6*, 3220–3231.
- [17] A. Bertolani, L. Pirrie, L. Stefan, N. Houbenov, J. S. Haataja, L. Catalano, G. Terraneo, G. Giancane, L. Valli, R. Milani, O. Ikkala, G. Resnati, P. Metrangolo, *Nat. Commun.* **2015**, *6*, 7574.
- [18] M. P. Conte, N. Singh, I. R. Sasselli, B. Escuder, R. V Ulijn, *Chem. Commun.* **2016**, *52*, 13889–13892.
- [19] M. Kurbasic, S. Semeraro, A. M. Garcia, S. Kralj, E. Parisi, C. Deganutti, R. De Zorzi, S. Marchesan, *Synthesis (Stuttg)*. **2019**, *51*, 2839–2844.
- [20] A. Pizzi, L. Catalano, N. Demitri, V. Dichiarante, G. Terraneo, P. Metrangolo, *Pept. Sci.* **2020**, *112*, e24127.
- [21] A. Pizzi, V. Dichiarante, G. Terraneo, P. Metrangolo, *Pept. Sci.* **2018**, *110*, e23088.
- [22] A. V. Vargiu, D. Iglesias, K. E. Styan, L. J. Waddington, C. D. Easton, S. Marchesan, *Chem. Commun.* **2016**, *52*, 5912–5915.
- [23] A. M. Garcia, M. Kurbasic, S. Kralj, M. Melchionna, S. Marchesan, *Chem. Commun.* **2017**, *53*, 8110–8113.
- [24] M. Melchionna, K. E. Styan, S. Marchesan, **2016**, *16*, 2009–2018.
- [25] T. M. Clover, C. L. O'Neill, R. Appavu, G. Lokhande, A. K. Gaharwar, A. E. Posey, M. A. White, J. S. Rudra, *J. Am. Chem. Soc.* **2020**, *142*, 19809–19813.
- [26] M. Li, M. Liu, Y. Shang, C. Ren, J. Liu, H. Jin, Z. Wang, *RSC Adv.* **2020**, *10*, 13900–13906.
- [27] I. Insua, J. Montenegro, *J. Am. Chem. Soc.* **2020**, *142*, 300–307.
- [28] H. L. Bolt, C. E. J. Williams, R. V Brooks, R. N. Zuckermann, S. L. Cobb, E. H. C. Bromley, *Pept. Sci.* **2017**, *108*, e23014.

- [29] B. K. Das, B. Pramanik, S. Chowdhuri, O. A. Scherman, D. Das, *Chem. Commun.* **2020**, *56*, 3393–3396.
- [30] V. Castelletto, I. W. Hamley, C. Stain, C. Connon, *Langmuir* **2012**, *28*, 12575–12580.
- [31] A. D. Martin, J. P. Wojciechowski, M. M. Bhadbhade, P. Thordarson, *Langmuir* **2016**, *32*, 2245–2250.
- [32] A. M. Garcia, D. Iglesias, E. Parisi, K. E. Styan, L. J. Waddington, C. Deganutti, R. De Zorzi, M. Grassi, M. Melchionna, A. V. Vargiu, S. Marchesan, *Chem* **2018**, *4*, 1862–1876.
- [33] N. Amdursky, Y. Erez, D. Huppert, *Acc. Chem. Res.* **2012**, *45*, 1548–1557.
- [34] C. H. Görbitz, *Chem. - A Eur. J.* **2001**, *7*, 5153–5159.
- [35] M. R. Sawaya, S. Sambashivan, R. Nelson, M. I. Ivanova, S. A. Sievers, M. I. Apostol, M. J. Thompson, M. Balbirnie, J. J. W. Wiltzius, H. T. McFarlane, A. Ø. Madsen, C. Riek, D. Eisenberg, *Nature* **2007**, *447*, 453–457.
- [36] G. Cavallo, P. Metrangolo, R. Milani, T. Pilati, A. Priimagi, G. Resnati, G. Terraneo, *Chem. Rev.* **2016**, *116*, 2478–2601.
- [37] I. Ramos Sasselli, P. J. Halling, R. V. Ulijn, T. Tuttle, *ACS Nano* **2016**, *10*, 2661–2668.
- [38] J. Wang, K. Liu, R. Xing, X. Yan, *Chem. Soc. Rev.* **2016**, *45*, 5589–5604.
- [39] B. Hernández, F. Pflüger, S. G. Kruglik, M. Ghomi, *J. Raman Spectrosc.* **2013**, *44*, 827–833.
- [40] M. T. Messina, P. Metrangolo, W. Navarrini, S. Radice, G. Resnati, G. Zerbi, *J. Mol. Struct.* **2000**, *524*, 87–94.
- [41] H. Li, R. Lantz, D. Du, *Molecules* **2019**, *24*, 186.
- [42] Q. Wang, Y. Wang, H. P. Lu, *J. Raman Spectrosc.* **2013**, *44*, 670–674.
- [43] B. Lekprasert, V. Korolkov, A. Falamas, V. Chis, C. J. Roberts, S. J. B. Tandler, I. Notingher, *Biomacromolecules* **2012**, *13*, 2181–2187.
- [44] D. Iglesias, M. Melle-Franco, M. Kurbasic, M. Melchionna, M. Abrami, M. Grassi, M. Prato, S. Marchesan, *ACS Nano* **2018**, *12*, 5530–5538.
- [45] O. Bellotto, S. Kralj, M. Melchionna, P. Pengo, M. Kisovec, M. Podobnik, R. De Zorzi, S. Marchesan, *ChemBioChem* **2022**, *23*, e202100518.
- [46] N. S. De Groot, T. Parella, F. X. Aviles, J. Vendrell, S. Ventura, *Biophys. J.* **2007**, *92*, 1732–

1741.

- [47] V. Castelletto, P. Ryumin, R. Cramer, I. W. Hamley, M. Taylor, D. Allsop, M. Reza, J. Ruokolainen, T. Arnold, D. Hermida-Merino, C. I. Garcia, M. C. Leal, E. Castaño, *Sci. Rep.* **2017**, *7*, 43637.
- [48] Y. Benitex, A. M. Baranger, *J. Am. Chem. Soc.* **2011**, *133*, 3687–3689.
- [49] S. E. Wheeler, *J. Am. Chem. Soc.* **2011**, *133*, 10262–10274.
- [50] O. Bellotto, S. Kralj, R. De Zorzi, S. Geremia, S. Marchesan, *Soft Matter* **2020**, *16*, 10151–10157.
- [51] M. O. Sinnokrot, C. D. Sherrill, *J. Am. Chem. Soc.* **2004**, *126*, 7690–7697.
- [52] W. B. Fischer, H. H. Eysel, *Spectrochim. Acta Part A Mol. Spectrosc.* **1992**, *48*, 725–732.
- [53] S. A. Oladepo, K. Xiong, Z. Hong, S. A. Asher, J. Handen, I. K. Lednev, *Chem. Rev.* **2012**, *112*, 2604–2628.
- [54] Z. Chi, S. A. Asher, *Biochemistry* **1998**, *37*, 2865–2872.
- [55] S. A. Asher, M. Ludwig, C. R. Johnson, *J. Am. Chem. Soc.* **1986**, *108*, 3186–3197.
- [56] S. P. A. Fodor, R. A. Copeland, C. A. Grygon, T. G. Spiro, *J. Am. Chem. Soc.* **1989**, *111*, 5509–5518.
- [57] H. Takeuchi, *Anal. Sci. Int. J. Japan Soc. Anal. Chem.* **2011**, *27*, 1077–1086.
- [58] A. A. Profit, V. Felsen, J. Chinwong, E.-R. E. Mojica, R. Z. B. Desamero, *Proteins* **2013**, *81*, 690–703.
- [59] N. Kuhar, S. Sil, S. Umapathy, *Spectrochim. Acta. A. Mol. Biomol. Spectrosc.* **2021**, *258*, 119712.

Chapter 5. Self-assembly of Leu-Phe and Phe-Leu dipeptides

This chapter describes the work of *Manuscript 4* entitled “*Supramolecular hydrogels from unprotected dipeptides: a comparative study on stereoisomers and structural isomers*”[1].

5.1. Introduction

In the previous chapters, we have described the self-assembly and hydrogelation of Phe derivatives, *i.e.*, *N*-(4-nitrobenzoyl)-L-Phe (**Chapter 2**), and D-Phe-L-Phe and its halogenated derivatives (**Chapter 3**). We have discussed their applications as biomaterials, however, what is less known is that dipeptides can exert some biological effect too, and they are very relevant for instance to the food industry [2]. They could find application to improve taste in drug formulations, and they have been long studied as food supplements [3-6]. New biological activities continue to emerge, *e.g.*, Phe-Leu was shown to act as antidepressant [7], anxiolytic [8], and, to a higher extent relative to its structural isomer Leu-Phe, to be an angiotensin I-converting enzyme (ACE) inhibitor [9]. Short repeats of Leu and Phe can activate neutrophils [10], and the activity is maintained, or even boosted, when the sequence alternates D- and L-amino acids [11,12] giving scope to study heterochiral short peptides. Dipeptides containing Leu and Phe thus appeared as interesting candidates for self-assembly into soft matter. To the best of our knowledge, Ile-Phe is the only unprotected dipeptide reported to form a stable hydrogel, while Phe-Phe hydrogels were reported to be metastable [13,14], unless the dipeptide was cyclised to the corresponding 2,5-diketopiperazine, or further modified, *e.g.*, by adding a p-nitro substitution on the Phe benzene ring [14]. The removal of just one methylene unit from the gelling Ile-Phe to give Val-Phe was sufficient to disrupt self-assembling ability in water [14], and the same applied to Phe-Val that was too hydrophilic to gel unless it was cyclised to the corresponding 2,5-piperazinedione [14]. Indeed, the design of linear unprotected dipeptide gelators is a challenging aim, whilst their cyclic derivatives have been more widely applied, for instance for enzyme mimicry, drug release, and photo responsive systems [15-18]. In addition, amino acid chirality is an interesting tool to fine tune self-assembly, as it was reported to have dramatic effects in the case of unprotected tripeptide stereoisomers. For instance, in the case of Leu-Phe-Phe and Phe-Leu-Phe, at high concentration the homochiral L-peptides precipitated into amorphous aggregates, while heterochiral isomers self-organised into stable, nanostructured hydrogels [19-22]. However, the effects of combining D- and L-amino acids on dipeptides is still unknown, hence for this work the ability to form supramolecular hydrogels was tested for the unprotected dipeptides reported in **Table 5.1**. The mirror-images D-Leu-D-Phe, L-Leu-D-Phe, D-Phe-D-Leu, and L-Phe-D-Leu were not included, because enantiomers display the same supramolecular behaviour in an achiral environment. Thus, the

current investigation aims to cover the self-organisation ability of all possible sequence and stereoconfiguration combinations of Leu and Phe in an unprotected dipeptide.

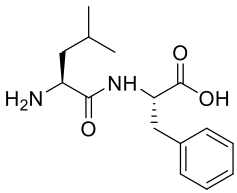
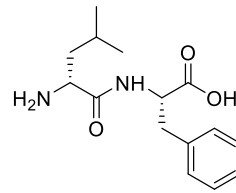
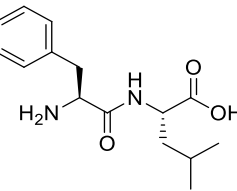
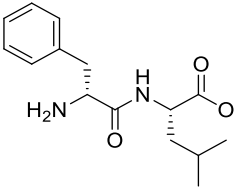
Homochiral peptides	Heterochiral peptides
<p data-bbox="448 510 660 539">L-Leu-L-Phe (LF)</p> 	<p data-bbox="890 510 1102 539">D-Leu-L-Phe (IF)</p> 
<p data-bbox="448 824 660 853">L-Phe-L-Leu (FL)</p> 	<p data-bbox="890 824 1102 853">D-Phe-L-Leu (fL)</p> 

Table 5.1. Set of the four unprotected dipeptide sequences investigated in the *Manuscript 4*

5.2. Dipeptides synthesis and self-assembly into hydrogels

All dipeptides were synthesised according to standard protocols on solid-phase and purified by reverse-phase HPLC. Their purity and identity were confirmed by $^1\text{H-NMR}$, $^{13}\text{C-NMR}$, and ESI-MS (see **Materials and Methods** and **Appendix**). They were dissolved in phosphate-buffered saline (PBS) with the aid of sonication and heating, then they were left to cool down to room temperature. Hydrogelation was first probed by the inversion tube test, next it was confirmed by oscillatory rheology measurements. As can be seen from **Table 5.2**, all dipeptides, except for L-Phe-L-Leu, gelled. Among the three hydrogels, the heterochiral dipeptide D-Phe-L-Leu formed a metastable hydrogel that gave rise to crystals over time. However, the effects of changing amino acid chirality were less dramatic on dipeptides than what reported for unprotected tripeptides [19,20].









Sequence	Hplc Rt (min)	Gel?	Time (min)	mgc (mM)	Stable Gel?
L-Leu-L-Phe	11.7	Yes 	24	40	Yes 
D-Leu-L-Phe	13.0	Yes 	12	40	Yes 
L-Phe-L-Leu	11.6	No 	n.a	n.a.	n.a. 
D-Phe-L-Leu	13.1	Yes 	<1	20	No 

Table 5.2. Dipeptides investigated in this work for self-assembly into hydrogels.

The viscoelastic properties of each sample were probed by oscillatory rheometry, starting with time sweeps (**Figure 5.1**). In the case of Leu-Phe, gelation time doubled going from the D, L heterochiral to the L-homochiral sequence (**Figure 5.1 A-B**). Higher peptide concentrations (50 mM) led to faster kinetics and higher moduli (**Figure 5.2**). In the case of Phe-Leu, the D, L-heterochiral peptide formed a metastable hydrogel, while the L-homochiral did not gel at all (**Figure 5.1 C-D**).

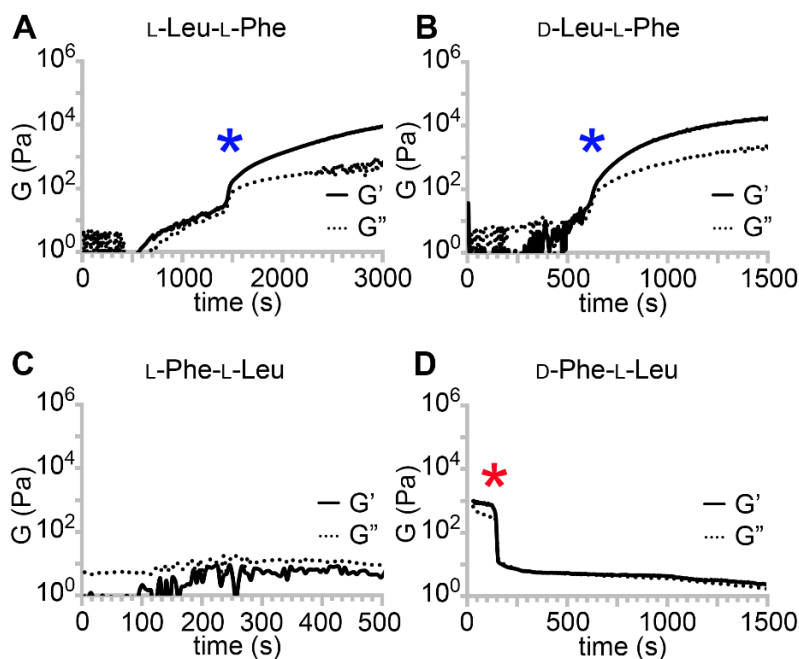


Figure 5.1. Oscillatory rheology time sweeps for the four dipeptides at 40 mM. Blue stars mark sol-to-gel transitions for the two gelators L-Leu-L-Phe and D-Leu-L-Phe; the red star in (D) marks gel-to-sol transition for the metastable gel formed by D-Phe-L-Leu. Reproduced from Ref. [1] with permission from © 2020 Royal Society of Chemistry.

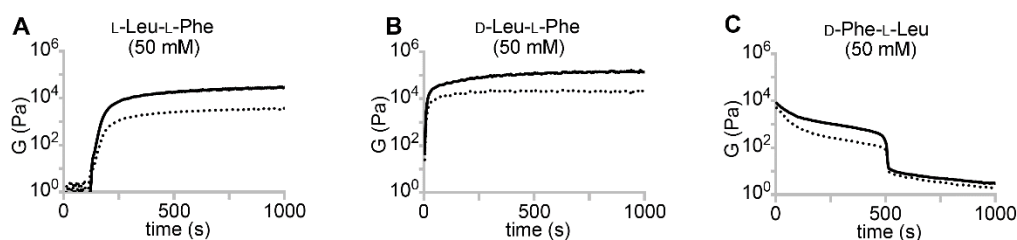


Figure 5.2. Time sweeps for (A) L-Leu-L-Phe, (B) D-Leu-L-Phe, and (C) D-Phe-L-Leu at 50 mM. . Reproduced from Ref. [1] with permission from © 2020 Royal Society of Chemistry.

Stress sweeps (**Figure 5.3**) revealed no significant differences between Leu-Phe stereoisomers (**Figure 5.3 A-B**), while the metastable hydrogel formed by D-Phe-L-Leu disassembled during the test (**Figure 5.3 D**), thus not allowing for an accurate analysis. The same issue affected the frequency sweeps, while in the case of Leu-Phe stereoisomers, both the elastic modulus G' and the viscous modulus G'' were independent from the applied frequency, with $G' > G''$, as expected for stable hydrogels (**Figure 5.4**).

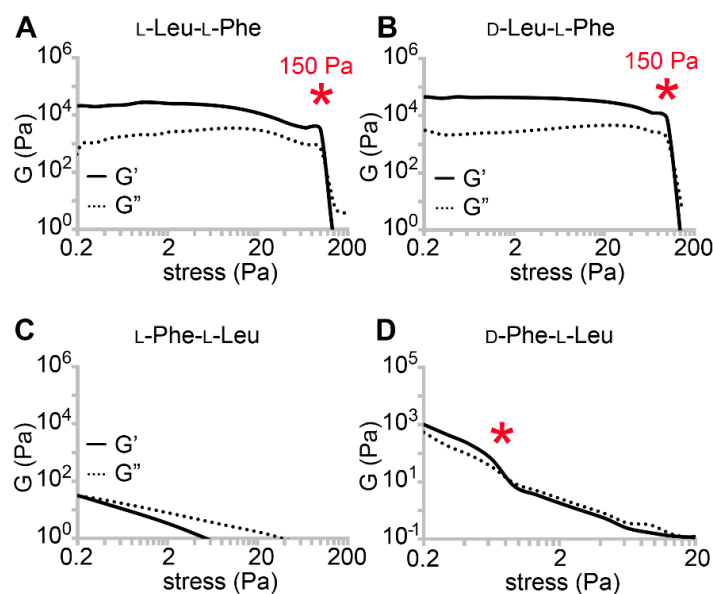


Figure 5.3. Oscillatory rheology stress sweeps for the four dipeptides. Red stars mark gel to-sol transitions. . Reproduced from Ref. [1] with permission from © 2020 Royal Society of Chemistry.

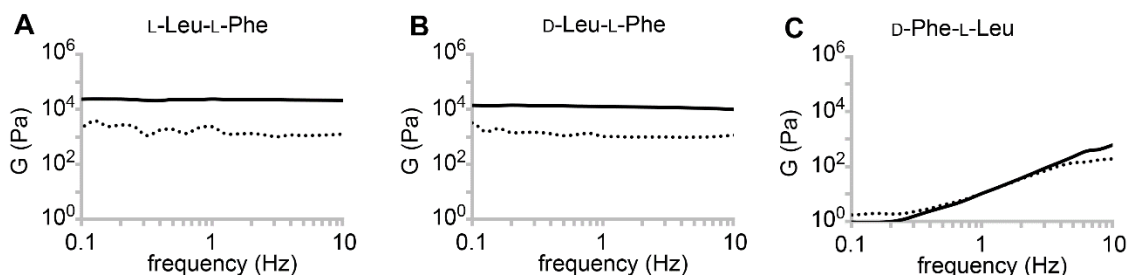


Figure 5.4. Frequency sweeps for L-Leu-L-Phe (A), D-Leu-L-Phe (B) and D-Phe-L-Leu (C) at 40 mM. . Reproduced from Ref. [1] with permission from © 2020 Royal Society of Chemistry.

Overall, from the rheological analysis, we inferred that heterochirality promoted hydrogelation, since in the case of Leu-Phe, it reduced gelation time, while in the case of Phe-Leu, it yielded a gel in contrast to the non-gelling L-isomer. The reasons behind this phenomenon could lie in the hydrophobicity increase, as supported by HPLC retention times (R_t) [23], which were higher for heterochiral than homochiral isomers (**Table 5.2**). It was recently demonstrated on hydrophobic tripeptides that heterochirality oriented the side chains on the same side of the peptide backbone, contrarily to the L-isomers. As a result, an amphipathic conformation arose only for heterochiral tripeptides, with net segregation between hydrophilic and hydrophobic regions that allowed for the successful self-organization into stable superstructures.

The thermoreversibility of both D-Leu-L-Phe and L-Leu-L-Phe hydrogels was verified with the “water-bath test”. After 1 h of self-assembly, each hydrogel was heated in a water bath by increasing the temperature from 25 °C to 85 °C with a ramp of ~ 5 °C/min. After cooling down each hydrogel at

room temperature, only the heterochiral hydrogel exhibited thermoreversibility verified through visual observations reported in **Table 5.3**. Conversely, for L-Leu-L-Phe only aggregates were observed even after overnight. Unfortunately, it was not possible to determine the melting temperature (T_m) by using CD spectroscopy with a temperature ramp, due to the scattering related to the high concentration of the sample (40 mM) and the presence of salts.




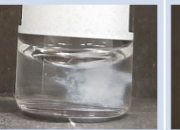
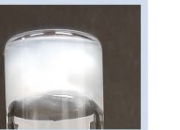



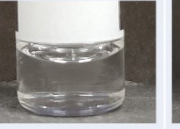

Sequence	MGC	RT	60°C	75-80 °C	RT after 1h	RT after O/N
D-Leu-L-Phe	40 mM					
L-Leu-L-Phe	40 mM					

Table 5.3. Pictures of both D-Leu-L-Phe and L-Leu-L-Phe hydrogels before and after the water-bath test at 40 mM.

5.3. Nanomorphologies of dipeptides' assemblies

Transmission electron microscopy (TEM) micrographs (**Figure 5.5**) confirmed a network of anisotropic structures for L-Leu-L-Phe, D-Leu-L-Phe, and D-Phe-L-Leu. The amorphous aggregates formed by L-Phe-L-Leu did not have nanoscale features that could be seen by TEM. Rigid fibers with heterogeneous size were noted for L-Leu-L-Phe (**Figure 5.5 A**), which arose from the association of thinner fibrils (**Figure 5.5 B**) that were difficult to distinguish individually. Similar was the case of D-Leu-L-Phe (**Figure 5.5 C**), although in this case 12 ± 2 nm wide ($n = 100$) individual fibrils were clearly visible (**Figure 5.5 D**). Finally, for the metastable hydrogel formed by D-Phe-L-Leu, instances of crystal nucleation and clusters of short fibrils were seen (**Figures 5.5 E-F**), in agreement with its transient nature confirmed by the rheological analysis. Hydrogels are often the kinetic product of peptide self-assembly, while crystals are the thermodynamic product [24] Indeed, within an hour, single crystals arose from the disassembly of the metastable gel, giving the opportunity for XRD investigation. Although a crystal and a gel are clearly two different phases, it was recently shown for a similar Phe-derived gelator that they share key intermolecular interactions [25] while differing mainly in the long-range order and hydration level.

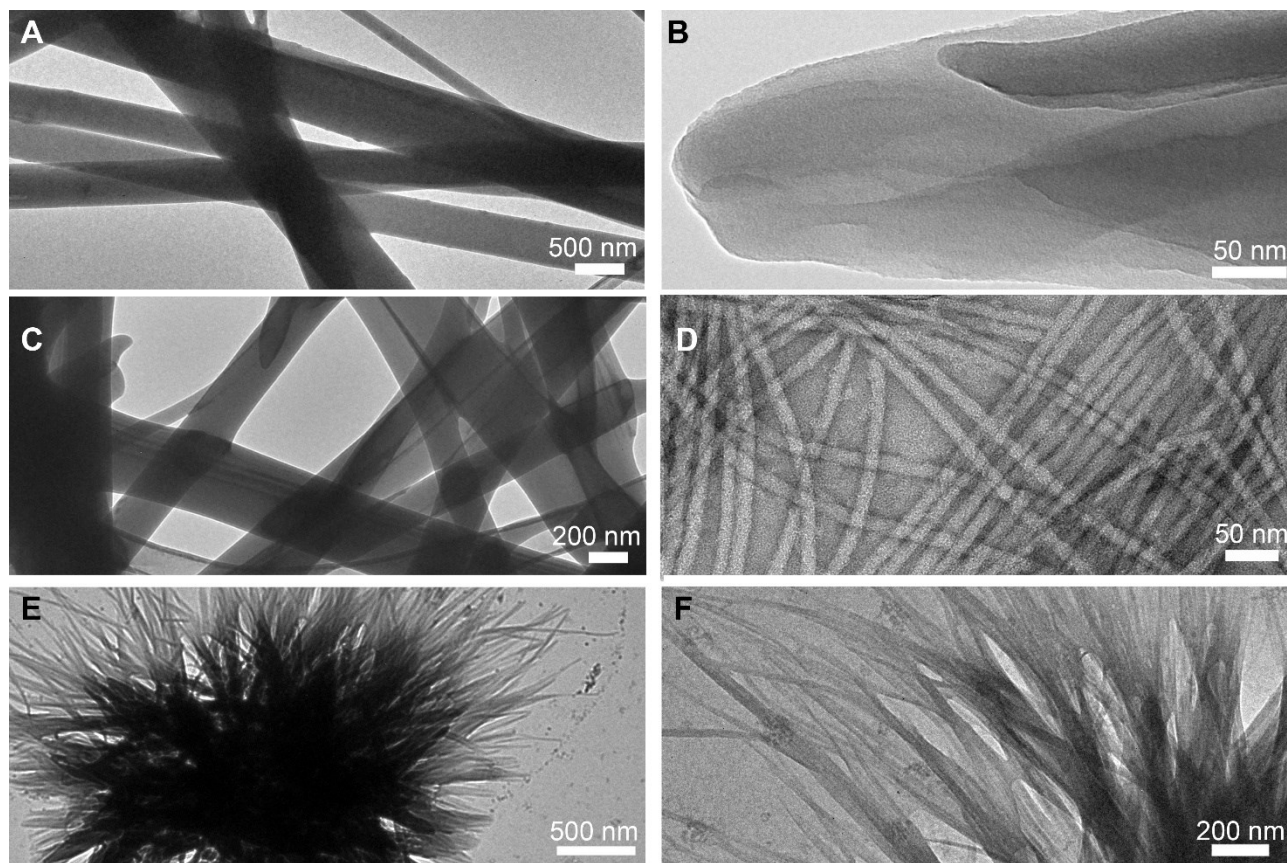


Figure 5.5. TEM micrographs of self-organised dipeptides at lower (left) and higher (right) magnification. A-B) L-Leu-L-Phe; C-D) D-Leu-L-Phe; E-F) D-Phe-L-Leu. Reproduced from Ref. [1] with permission from © 2020 Royal Society of Chemistry.

5.4. Single-crystal X-ray diffraction analysis

The crystal structures of homochiral L-Leu-L-Phe and L-Phe-L-Leu were reported by Görbitz [26] as part of a series of studies on hydrophobic dipeptides (**Figure 5.6 A-B**) [27,28]. Both compounds displayed a remarkably similar packing into hydrophilic nanotubes, thanks to their amphipathic conformation. The inner, water-filled, cavity featured the amide-rich peptide backbone, while the hydrophobic side-chains were displayed on the outer surface, where they faced those of the other channels, and, only in the case of gelling L-Leu-L-Phe, they interdigitated with each other into zippers (**Figure 5.7**). On the contrary, D-Phe-L-Leu – reported in the present work for the first time – assembled into alternating hydrophilic and hydrophobic layers devoid of interactions between the latter (**Figure 5.6 C**). Interestingly, the interdigitation of the aromatic side chains of Phe into dry zippers that exclude solvent is a common feature of the unprotected dipeptides that form stable hydrogels, *i.e.*, Ile-Phe [29,30] and Leu-Phe [26] (**Figure 5.7**), while it is absent in the non-gelling Phe-Leu [26], Val-Phe [31] and Phe-Val [32]. This feature is very common for amyloid structures [33] and may play a role in providing stability to the hydrogels [20]. In terms of hydrogen bonding pattern, surprisingly, gelling L-Leu-L-Phe and non-gelling L-Phe-L-Leu displayed analogous head-to-

tail extended interactions. It is possible, though, that the latter successfully established such network of interactions only in the crystal phase, while gelation may have been hampered by its inability to effectively establish Phe zippers. By contrast, D-Phe-L-Leu featured water molecules bridging between N-termini and engaging in hydrogen bonding also with the amide carbonyl moiety; the amide N-H atoms were hydrogen-bonded to the C-termini, which also interacted through hydrogen-bonding through water as a bridging element (**Figure 5.6 D**).

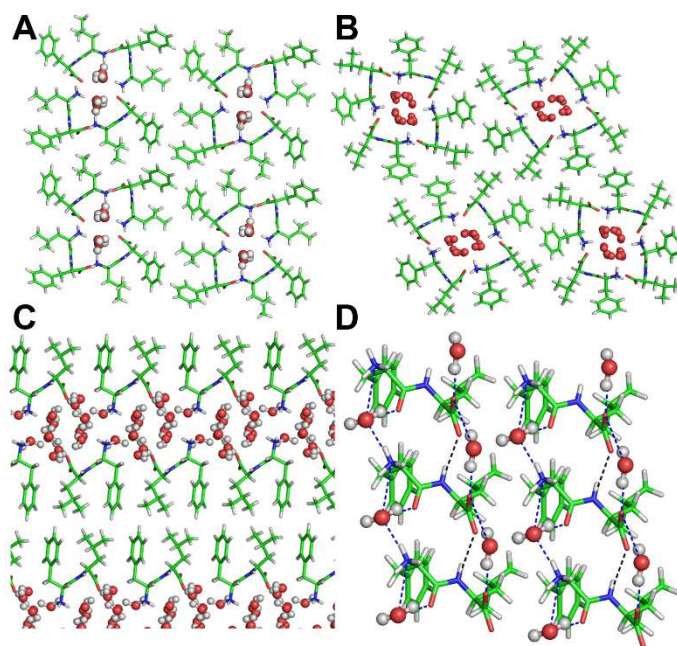


Figure 5.6. Single-crystal XRD structures of (A) L-Leu-L-Phe, (36) (B) L-Phe-L-Leu, (36) and (C-D) D-Phe-L-Leu (CCDC 2012848), highlighting the alternation of hydrophobic and hydrophilic layers (C) and the hydrogen bonding pattern (D), hydrogen bonding involving only peptide molecules as black dashes, hydrogen bonding involving both peptide and water molecules in blue dashes). Reproduced from Ref. [1] with permission from © 2020 Royal Society of Chemistry.

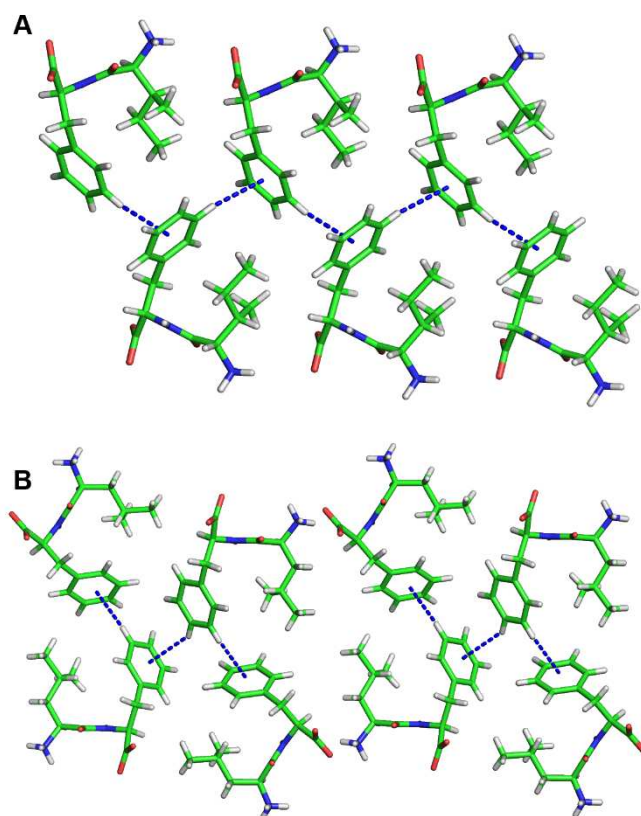


Figure 5.7. Phe zipper for for L-Leu-L-Phe (A) and L-Ile-L-Phe (B), from C. H. Görbitz, *Chem. Eur. J.* 2001, 7 (23), 5153 and C. H. Görbitz, *Acta Crystallogr. C*, 2004, 60, o371. Reproduced from Ref. [1] with permission from © 2020 Royal Society of Chemistry .

We inferred that the presence of localised interactions, as opposed to extended networks of hydrogen bonding, and the absence of Phe zippers, may be key to the metastability of the hydrogel formed by D-Phe-L-Leu.

5.5. Peptides' conformational analysis

Circular dichroism (CD) is a useful technique to probe the spatial arrangement of chiral molecules. In the case of longer sequences, it is widely applied to determine conformation thanks to the vast literature on well-established signatures that can be ascribed to α -helices, β -sheets, and so on. What is less known is that also single amino acids display CD spectra, which are positive in the 200-250 nm UV region for the L-stereo configuration [34]. While their D-mirror images are expected to display negative mirror-image spectra, the case of heterochiral sequences is more complex and difficult to predict. It has been reported that the stereoconfiguration of the N-terminal [35] central [36], or C-terminal [37,38] amino acid dictates the sign of the CD spectrum, but clearly other factors come into play, and the observed trends appear to be sequence-specific [39,40].

CD spectra of the four dipeptides are reported in **Figure 5.8**. In this study, there was only one CD spectrum that was negative in the 200-230 nm region for D-Phe-L-Leu (**Figure 5.8 D**), with two minima at 200 and 219 nm. A similar case, but opposite in sign, was displayed by the other two gelling peptides L-Leu-L-Phe and D-Leu-L-Phe (**Figure 5.8 A-B**). The CD signature was very similar to what reported for gelling D-Phe-L-Phe-L-Leu [41], and for L-Phe-D-Leu-L-Phe, for which a combination of experimental and molecular dynamics revealed it corresponded to a population of conformations in the non-assembled state, whereby the most visited displayed dihedral angles typical of β -structures (sheets and turns) [19]. The non-assembling L-Phe-L-Leu peptide was the only one displaying the maximum at 219 nm of higher intensity than that at 200 nm (**Figure 5.8 C**). We inferred that the distribution of conformations populated by this non-gelling sequence was different relative to the gelators. CD spectra were also acquired in the hydrogel state, however, due to the presence of salts and high peptide concentration, it was not possible to acquire meaningful data in the far UV range.

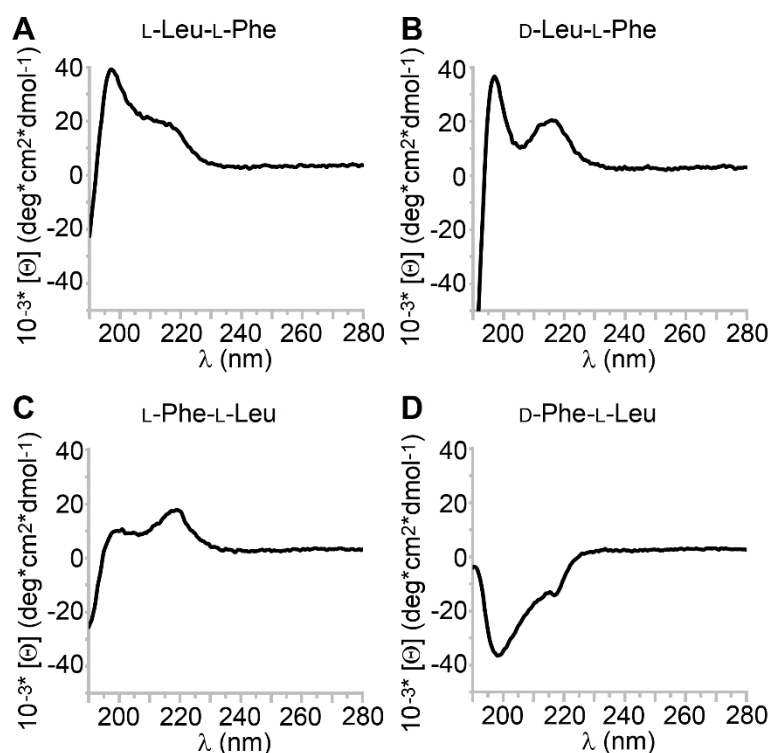


Figure 5.8. Circular dichroism spectra of the four dipeptides in solution (1 mM). Reproduced from Ref. [1] with permission from © 2020 Royal Society of Chemistry.

Interestingly, the CD spectra above 220 nm were all positive, including D-Phe-L-Leu, for which a sign inversion occurred with assembly (**Figure 5.9**).

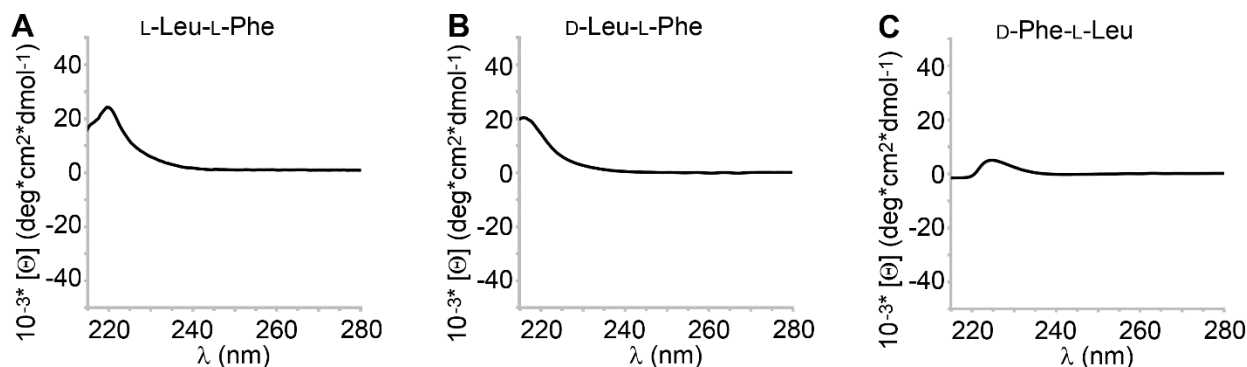


Figure 5.9. CD spectra for the hydrogels at 40 mM, except for L-Leu-L-Phe that was at the mgc of 45 mM. . Reproduced from Ref. [1] with permission from © 2020 Royal Society of Chemistry.

Peptide conformation was also investigated by Attenuated Total Reflectance (ATR) FT-IR on gel samples. **Figure 5.10** shows the amide region for the three dipeptides in the gel state (**Figure 5.10 A, B, D**) and for the non-gelling L-Phe-L-Leu (**Figure 5.10 C**) in the precipitate obtained at the same concentration. While it would be rather controversial to assign typical peptide conformations to a dipeptide, the canonical signatures can provide a useful reference for the hydrogen bonding pattern that arises in the supramolecular assemblies. In all cases, a signal was clearly visible in the 1670-1680 cm^{-1} range, where β -turns are located for longer peptides [42]. A second peak in the amide I region was clearly visible in all samples, and it occurred in the β -structure region (1600-1625 cm^{-1}). The metastable gel formed by D-Phe-L-Leu was the only sample to display an amide signal in the disordered region at 1641 cm^{-1} , which could explain its instability. In the amide II region, all gelling samples displayed two maxima (≈ 1525 and 1560 cm^{-1}), which were both downshifted of 5-10 cm^{-1} for the non-gelling peptide. For comparison, the reported L-Ile-L-Phe gelator IR signal at 1570 cm^{-1} arose from strong association between the carboxylate and ammonium charged termini in the supramolecular state and was absent for non-assembling L-Val-L-Phe [29]. In addition, the lack of such extended interactions resulted in a signal for the carboxylate group to 1598 cm^{-1} for the non-assembling L-Val-L-Phe, as noticed in this work for the metastable D-Phe-L-Leu [29]. This is in agreement with the interactions noticed in the crystal structure (**Figure 5.6 D**). By contrast, the other heterochiral dipeptide, the gelling D-Leu-L-Phe, was the only sample to display a signal at 1717 cm^{-1} that is typically ascribed to carboxylic functionalities that are strongly engaged in hydrogen bonding in the protonated form [43]. Overall, we inferred from the ATR-IR and the XRD analyses that the

stable gelators had two distinctive features; 1) they engaged in Phe zippers; 2) they displayed an extended network of hydrogen bonds between N- and C-termini, while the metastable gel displayed more disorder and only localised hydrogen-bond networks.

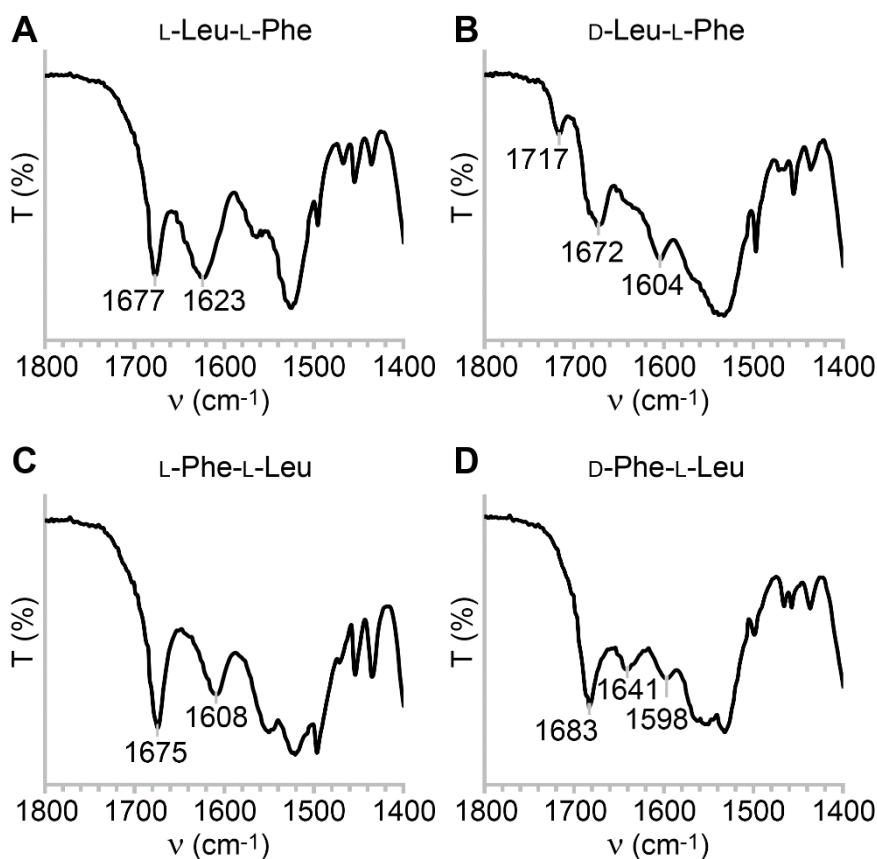


Figure 5.10. Amide region of the ATR-IR spectra of the four dipeptides in the gel (A, B, D) or precipitate (C) form. Reproduced from Ref. [1] with permission from © 2020 Royal Society of Chemistry.

5.6. Biocompatibility assessment of dipeptides' hydrogels

To assess the biocompatibility of the two stable hydrogelators, D-Leu-L-Phe and L-Leu-L-Phe, both qualitative and quantitative biological assays *in vitro* were performed on NIH3T3 fibroblast cell culture. For these assays, the hydrogel D-Phe-L-Leu was not taken into account due to its metastability that occurred within an hour. Both gels were tested for live/dead fluorescence staining using acridine orange (AO) and propidium iodide (PI) as fluorescent dyes (**Figure 5.11**) in a microwell slide (**Figure 5.12**). The combination of the two fluorescent dyes, acridine orange (AO) and propidium iodide (PI), allowed to evaluate simultaneously the presence of cells with intact and with compromise membrane

and their morphological features. Acridine orange (AO) and propidium iodide (PI) are responsible of the green and red fluorescence, respectively [44].

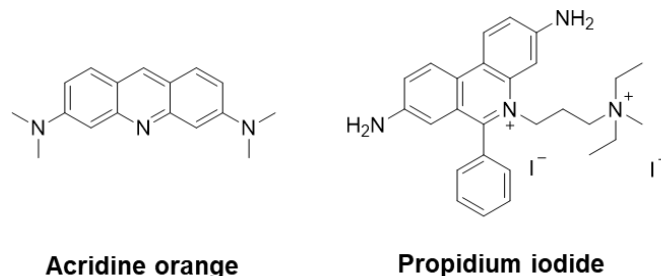


Figure 5.11. Structure of the two fluorescent colour dyes used for live/dead assay

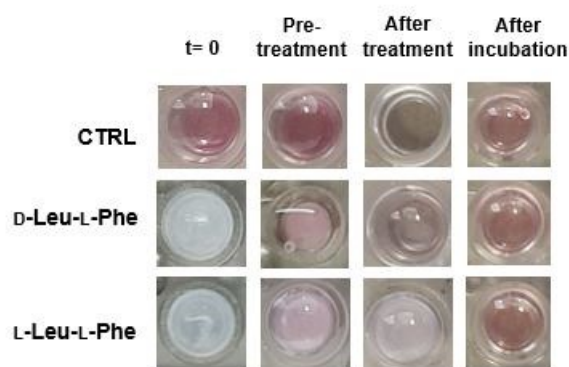


Figure 5.12. Photographs of representative μ slide wells (Ibidi, Germany) used for live/dead assay on fibroblast.

No significant differences in cell morphology were observed relative to the control for the two gels tested, and high numbers of proliferative cells were noted, without signs of cytotoxicity (**Figure 5.13**). After 24 h of incubation, both hydrogels partially dissolved and lifted off the plastic, especially the heterochiral peptide D-Leu-L-Phe. This data may suggest some potential limitation in terms of gel durability under cell culture conditions (**Figure 5.12**).

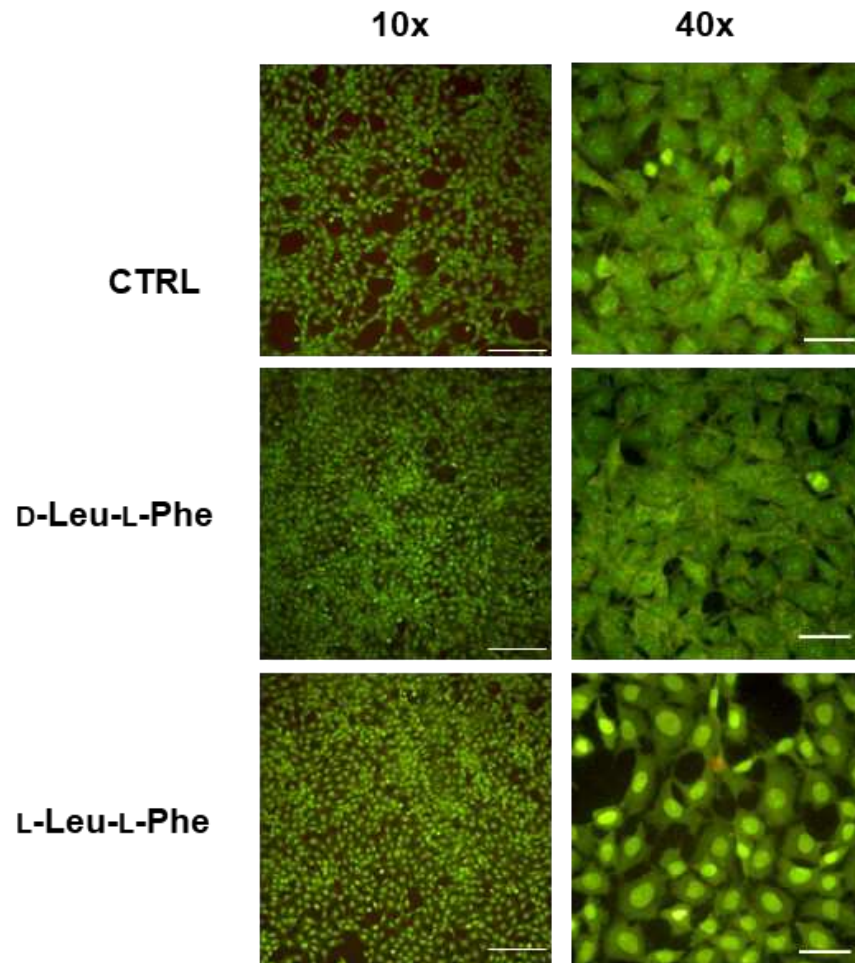


Figure 5.13. Live(green)/dead(red) fluorescence microscopy on mammalian cells (fibroblast). Cells are simply grown on tissue culture plastic surface as a control. Scale bar 200 μm (objective 10x) and 50 μm (objective 40x).

The cytotoxicity of the two dipeptides was also tested in solution by means of the quantitative MTT assay (**Figure 5.14**) 1 mM was considered the highest concentration to have the peptide still in solution. Even at the at the highest concentration tested a good cell viability was observed for both dipeptides. This finding is highly encouraging in terms of the biocompatibility of this type of scaffold, although for applications it may require enhanced durability.

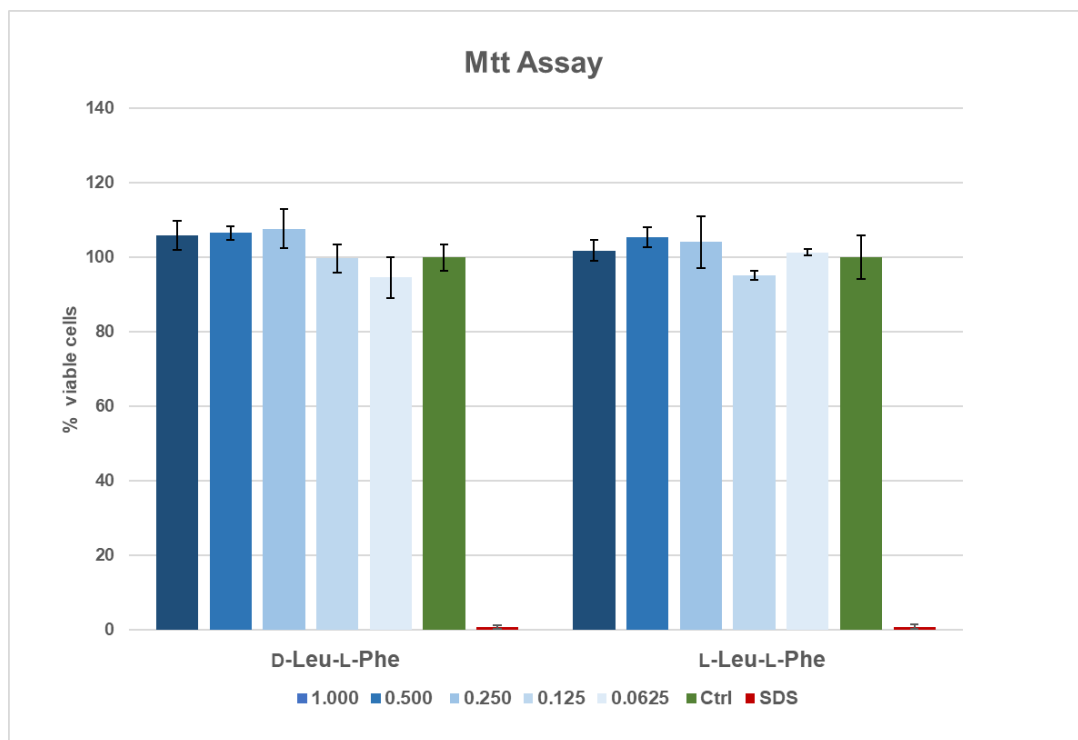


Figure 5.14. Quantitative MTT assay on fibroblast cells (NIH/3T3 cell line) incubated with D-Leu-L-Phe and L-Leu-L-Phe in solution, in presence of different concentrations of each compound.

5.7. Conclusions

In this work, the four dipeptides L-Leu-L-Phe, D-Leu-L-Phe, L-Phe-L-Leu, and D-Phe-L-Leu were investigated for self-assembly into hydrogels in phosphate buffer. They represented all possible combinations of Leu and Phe in unprotected dipeptides, since their mirror-images D-Leu-D-Phe, L-Leu-D-Phe, D-Phe-D-Leu, and L-Phe-D-Leu display analogous supramolecular behaviour in an achiral environment. Except for L-Phe-L-Leu, all the other compounds gelled, albeit D-Phe-L-Leu metastable hydrogel converted into crystals within an hour. The hydrogels arose from a network of fibrils, often bundling into rigid fibers of heterogeneous size, as shown by TEM. Overall, the presence of Phe at the C-terminus was associated with better gelling ability, and heterochirality increased dipeptide hydrophobicity, and promoted hydrogelation.

CD analysis suggested a different distribution of conformations in solution for the non-gelling L-Phe-L-Leu, relative to the other dipeptides, whose spectra were similar to D-Phe-L-Phe-L-Leu [41] and L-Phe-D-Leu-L-Phe [19]. Spectroscopic and single-crystal X-ray diffraction analyses suggested a very similar, and extended, hydrogen bonding network between N- and C-termini, together with Phe zippers, as distinctive features of stable gelators, in agreement with the literature [29].

Overall, preliminary biological assays *in vitro* revealed a good biocompatibility of D-Leu-L-Phe and L-Leu-L-Phe when tested on murine fibroblasts, which is encouraging for future biomedical applications. We can conclude that there was no single parameter that was crucial for the determination of a dipeptide gelling ability, which appeared to be the result of a fine equilibrium between different properties.

In any case, while gelling or non-gelling compounds clearly displayed a rather diverse set of features in terms of ability to form nanotubes, only stable gelators featured extended networks of hydrogen bonds and Phe zippers [20][45] It is possible that this latter feature, which is well-established for amyloids [46,47] promotes stability of this kind of hydrogels that are driven by the hydrophobic collapse in water. Further studies on other sequences will be needed to verify this hypothesis and clearly identify key features for the future design of supramolecular systems based on unprotected dipeptides for potential use in biomedicine.

***Note:** The biological assays and the thermoreversibility test reported in this **Chapter 5** are not included in the *Manuscript 4*.

References

- [1] O. Bellotto, S. Kralj, R. De Zorzi, S. Geremia, S. Marchesan, *Soft Matter* **2020**, *16*, 10151–10157.
- [2] M. Gallego, L. Mora, F. Toldrá, *Food Prod. Process. Nutr.* **2019**, *1*, 2.
- [3] S. Chakrabarti, S. Guha, K. Majumder, *Nutrients* **2018**, *10*, 1738.
- [4] J. L. Zambonino Infante, C. L. Cahu, A. Peres, *J. Nutr.* **1997**, *127*, 608–614.
- [5] T. Verri, A. Barca, P. Pisani, B. Piccinni, C. Storelli, A. Romano, *J. Comp. Physiol. B* **2017**, *187*, 395–462.
- [6] J. M. Rouanet, J. L. Z. Infante, B. Caporiccio, C. Pejoan, *Ann. Nutr. Metab.* **1990**, *34*, 175–182.
- [7] T. Mizushige, T. Uchida, K. Ohinata, *Sci. Rep.* **2020**, *10*, 2257.
- [8] T. Mizushige, N. Kanegawa, A. Yamada, A. Ota, R. Kanamoto, K. Ohinata, *Neurosci. Lett.* **2013**, *543*, 126–129.
- [9] S. Ono, M. Hosokawa, K. Miyashita, K. Takahashi, *Int. J. food Sci. Technol.* **2006**, *41*, 383–386.

- [10] A. Dalpiaz, A. Scatturin, G. Vertuani, R. Pecoraro, P. A. Borea, K. Varani, S. Traniello, S. Spisani, *Eur. J. Pharmacol.* **2001**, *411*, 327–333.
- [11] A. Dalpiaz, M. E. Ferretti, R. Pecoraro, E. Fabbri, S. Traniello, A. Scatturin, S. Spisani, *Biochim. Biophys. Acta* **1999**, *1432*, 27–39.
- [12] J. D. 3rd Higgins, G. J. Bridger, C. K. Derian, M. J. Beblavy, P. E. Hernandez, F. E. Gaul, M. J. Abrams, M. C. Pike, H. F. Solomon, *J. Med. Chem.* **1996**, *39*, 1013–1015.
- [13] M. P. Conte, N. Singh, I. R. Sasselli, B. Escuder, R. V Ulijn, *Chem. Commun.* **2016**, *52*, 13889–13892.
- [14] M. Kurbasic, S. Semeraro, A. M. Garcia, S. Kralj, E. Parisi, C. Deganutti, R. De Zorzi, S. Marchesan, *Synthesis (Stuttg.)* **2019**, *51*, 2829–2838.
- [15] C. Balachandra, T. Govindaraju, *J. Org. Chem.* **2020**, *85*, 1525–1536.
- [16] J. Karcher, Z. L. Pianowski, *Chem. – A Eur. J.* **2018**, *24*, 11605–11610.
- [17] A. J. Kleinsmann, B. J. Nachtsheim, *Org. Biomol. Chem.* **2020**, *18*, 102–107.
- [18] A. J. Kleinsmann, B. J. Nachtsheim, *Chem. Commun.* **2013**, *49*, 7818–7820.
- [19] A. M. Garcia, D. Iglesias, E. Parisi, K. E. Styan, L. J. Waddington, C. Deganutti, R. De Zorzi, M. Grassi, M. Melchionna, A. V. Vargiu, S. Marchesan, *Chem* **2018**, *4*, 1862–1876.
- [20] S. Marchesan, L. Waddington, C. D. Easton, D. A. Winkler, L. Goodall, J. Forsythe, P. G. Hartley, *Nanoscale* **2012**, *4*, 6752–6760.
- [21] D. Iglesias, M. Melle-Franco, M. Kurbasic, M. Melchionna, M. Abrami, M. Grassi, M. Prato, S. Marchesan, *ACS Nano* **2018**, *12*, 5530–5538.
- [22] A. V Vargiu, D. Iglesias, K. E. Styan, L. J. Waddington, C. D. Easton, S. Marchesan, *Chem. Commun.* **2016**, *52*, 5912–5915.
- [23] H. L. Bolt, C. E. J. Williams, R. V Brooks, R. N. Zuckermann, S. L. Cobb, E. H. C. Bromley, *Pept. Sci.* **2017**, *108*, e23014.
- [24] J. Wang, K. Liu, R. Xing, X. Yan, *Chem. Soc. Rev.* **2016**, *45*, 5589–5604.
- [25] A. M. Garcia, R. Lavendomme, S. Kralj, M. Kurbasic, O. Bellotto, M. C. Cringoli, S. Semeraro, A. Bandiera, R. De Zorzi, S. Marchesan, *Chem. - A Eur. J.* **2020**, *26*, 1880–1886.
- [26] C. H. Görbitz, *Chem. - A Eur. J.* **2001**, *7*, 5153–5159.

- [27] C. H. Görbitz, *Acta Crystallogr. Sect. B* **2018**, *74*, 311–318.
- [28] C. H. Görbitz, *Chem. – A Eur. J.* **2007**, *13*, 1022–1031.
- [29] N. S. De Groot, T. Parella, F. X. Aviles, J. Vendrell, S. Ventura, *Biophys. J.* **2007**, *92*, 1732–1741.
- [30] C. Görbitz, *Acta Crystallogr. C.* **2004**, *60*, o371-373.
- [31] C. H. Görbitz, *Acta Crystallogr. Sect. B* **2002**, *58*, 512–518.
- [32] C. H. Görbitz, *Acta Crystallogr. Sect. C* **2000**, *56*, 1496–1498.
- [33] M. R. Sawaya, S. Sambashivan, R. Nelson, M. I. Ivanova, S. A. Sievers, M. I. Apostol, M. J. Thompson, M. Balbirnie, J. J. W. Wiltzius, H. T. McFarlane, A. Ø. Madsen, C. Riek, D. Eisenberg, *Nature* **2007**, *447*, 453–457.
- [34] N. Amdursky, M. M. Stevens, *ChemPhysChem* **2015**, *16*, 2768–2774.
- [35] U. Orce, M. De Poli, M. De Zotti, J. Clayden, *Chem. – A Eur. J.* **2013**, *19*, 16357–16365.
- [36] S. Marchesan, K. E. Styan, C. D. Easton, L. Waddington, A. V. Vargiu, *J. Mater. Chem. B* **2015**, *3*, 8123–8132.
- [37] Y. Fu, B. Li, Z. Huang, Y. Li, Y. Yang, *Langmuir* **2013**, *29*, 6013–6017.
- [38] M. Wang, P. Zhou, J. Wang, Y. Zhao, H. Ma, J. R. Lu, H. Xu, *J. Am. Chem. Soc.* **2017**, *139*, 4185–4194.
- [39] S. Lin, Y. Li, B. Li, Y. Yang, *Langmuir* **2016**, *32*, 7420–7426.
- [40] Q. Xing, J. Zhang, Y. Xie, Y. Wang, W. Qi, H. Rao, R. Su, Z. He, *ACS Nano* **2018**, *12*, 12305–12314.
- [41] M. C. Cringoli, C. Romano, E. Parisi, L. J. Waddington, M. Melchionna, S. Semeraro, R. De Zorzi, M. Grönholm, S. Marchesan, *Chem. Commun.* **2020**, *56*, 3015–3018.
- [42] E. Goormaghtigh, J.-M. Ruysschaert, V. Raussens, *Biophys. J.* **2006**, *90*, 2946–2957.
- [43] Z. Gu, R. Zambrano, A. McDermott, *J. Am. Chem. Soc.* **1994**, *116*, 6368–6372.
- [44] K. Mascotti, J. McCullough, S. R. Burger, *Transfusion* **2000**, *40*, 693–696.
- [45] S. Mondal, L. Adler-Abramovich, A. Lampel, Y. Bram, S. Lipstman, E. Gazit, *Nat. Commun.* **2015**, *6*, 8615.

- [46] M. R. Sawaya, S. Sambashivan, R. Nelson, M. I. Ivanova, S. A. Sievers, M. I. Apostol, M. J. Thompson, M. Balbirnie, J. J. W. Wiltzius, H. T. McFarlane, A. Ø. Madsen, C. Riek, D. Eisenberg, *Nature* **2007**, *447*, 453–457.
- [47] L.K. Chang, J.-H. Zhao, H.-L. Liu, J. W. Wu, C.-K. Chuang, K.-T. Liu, J.-T. Chen, W.-B. Tsai, Y. Ho, *J. Biomol. Struct. Dyn.* **2010**, *28*, 39–50.

Chapter 6. Self-assembly of Ile-Phe and Phe-Ile dipeptides

This chapter contains the work of the *Manuscript 5** entitled “*Self-Assembly of Unprotected Dipeptides into Hydrogels: Water-Channels Make the Difference*” [1].

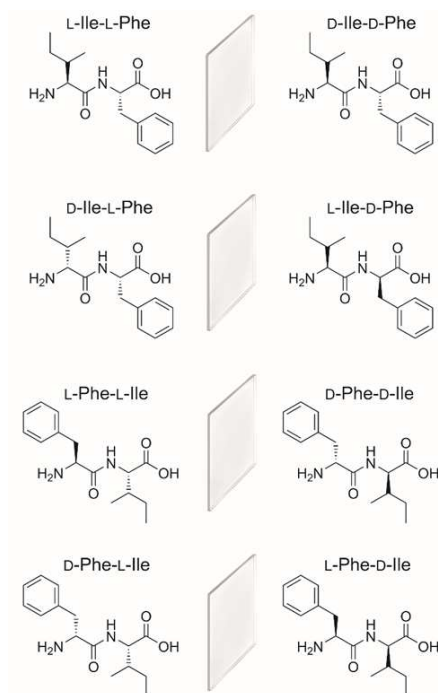
6.1. Introduction

In recent years, there has been an increasing interest in the development of supramolecular hydrogels, especially for applications in medicine, owing to their ability to mimic natural tissues [2]. Researchers have been studying a large diversity of components to tailor hydrogel properties, spanning from large biomolecules, such as proteins, [3] DNA and nucleic acids, [4] to synthetic polymers, [5] nanoparticles, [6] and carbon nanostructures [7–9]. Among the various building blocks, minimalistic peptides have gained increasing attention in light of their ease of preparation and inherent biocompatibility, as well as the low-cost of their production on a large scale [10]. Whereas the majority of them exploit polyaromatic N-capping groups to facilitate hydrophobicity-driven self-organization in water, there are still concerns over the biocompatibility of such N-caps *in vivo* [11]. To this end, the search is very active towards the discovery of N-caps whose structure can promote self-assembly and whose fate *in vivo* is benign [12–14]. An alternative could be the use of short peptides with unprotected termini, yet the rules for their design to achieve hydrogels are still eluding scientists [15,16]. In the case of dipeptides, those containing phenylalanine (Phe) are the obvious choice for self-assembly, in light of the high propensity of this aromatic amino acid towards self-organization in water [17]. Phe-Phe was recently reported to form metastable hydrogels [18,19]. Interestingly, simple structural modifications were sufficient to stabilize the soft matter, for instance through dipeptide cyclization or Phe *p*-substitution, [19] or change of stereoconfiguration into D-Phe-L-Phe [20]. Hydrophobicity is a well-known factor to drive peptide self organization in water, [16] thus the search for unprotected dipeptides that gel could reasonably start from aliphatic amino acids. In particular, a sensible choice would fall on the most hydrophobic ones with butyl groups as the side chains, *i.e.*, leucine (Leu) or isoleucine (Ile). In fact, removal of even just one methylene unit to yield the lesser hydrophobic valine (Val) could compromise self-assembly. This hypothesis was confirmed by studies on Val-Phe, [21] and Phe-Val, [19] that concluded the inability to self-assemble of these dipeptides even at concentrations as high as 100 mM. The case of Leu-Phe and Phe-Leu self-assembly in water was recently described [22]. Interestingly, both homochiral and heterochiral Leu-Phe stereoisomers (*i.e.*, LL, DL, LD, or DD) formed stable hydrogels at physiological conditions. On the contrary, only heterochiral Phe-Leu (*i.e.*, LD, or DL), but not their homochiral stereoisomers (*i.e.*, LL, or DD) formed metastable hydrogels that rearranged into crystals in less than an hour. It was noted

that stable gels arose from peptides that could establish both, extended hydrophilic interactions based on H-bonding networks and N-to-C salt bridges between peptides, and steric zippers, which are an established feature that stabilizes amyloids [23]. The possibility that the presence of Phe at the C terminus could somehow favour hydrogelation was also considered, but the small dataset provided was not sufficient to verify this hypothesis, for which further examples were needed. Surprisingly, thus far no study was reported on chirality effects on Ile-Phe or Phe-Ile, despite the fact that homochiral Ile-Phe was observed to gel, although at concentrations as high as ca. 70 mM that required a small amount of organic solvent to aid its dissolution [21]. This study thus aims at filling this gap and verifying whether the self-assembling trends observed for Leu-Phe and Phe-Leu stereoisomers apply also to their Ile-containing counterparts. In this manner, our understanding of self-assembling unprotected dipeptides could advance to assist with the future design of biomolecule-based supramolecular hydrogels from simple and low-cost building blocks.

6.2. Dipeptides synthesis and molecular characterization

If we consider all possible stereoconfigurations of Ile and Phe into a dipeptide sequence, we will obtain 8 possible compounds, *i.e.*, L-Ile-L-Phe, D-Ile-L-Phe, L-Ile-D-Phe, D-Ile-D-Phe, L-Phe-L-Ile, D-Phe-L-Ile, L-Phe-D-Ile, and D-Phe-D-Ile (**Scheme 6.1**).



Scheme 6.1. All possible stereocombinations of Ile and Phe in dipeptide sequences identify 8 compounds, which consist of 4 enantiomeric pairs, which are mirror-image of each other (represented by a mirror between the two enantiomers). Reproduced with permission from ref. [1] © 2022 John Wiley and Sons.

Enantiomers have the same physicochemical properties, thus self-assembling behaviour, in achiral environments, although they display different optical activity [24]. It is worth to note that experimental works have sometimes reported differences, although these are likely ascribed to the level of purity across samples [25]. This means that a smaller set, such as L-Ile-L-Phe, D-Ile-L-Phe, L-Phe-L-Ile, and D-Phe-L-Ile, will be representative also of the supramolecular behaviour in water of the mirror-images (*i.e.*, D-Ile-D-Phe, L-Ile-D-Phe, D-Phe-D-Ile, and L-Phe-D-Ile, respectively), thus allowing to understand the self-assembly of all possible stereoconfigurations of Ile and Phe into dipeptides. Thus, in this study the supramolecular behaviour of the former four compounds was assessed to shed light on the sequences that gel in phosphate buffered saline and provide an initial screening for future studies.

The four compounds L-Ile-L-Phe, D-Ile-L-Phe, L-Phe-L-Ile, and D-Phe-L-Ile (shown on the left column of **Scheme 6.1**), were synthesized by solid-phase using a standard Fmoc-protection strategy, with HBTU/HOAt activation, and a final cleavage from the 2-chlorotrytil resin in acidic conditions [26]. The crudes were then purified by reversed-phase HPLC and characterized by ¹H-NMR and ¹³C-NMR spectroscopy, and LC-MS (see **Materials and Methods** and **Appendix**). Interestingly, the HPLC retention times, which are an experimental measure of hydrophobicity, [27] were as follows: 10.6 min (L-Phe-L-Ile), 11.3 min (L-Ile-L-Phe), 12.9 min (D-Ile-L-Phe), and 13.0 min (D-Phe-L-Ile). This data suggested that heterochirality increased peptide hydrophobicity, in agreement with previous observations [22]. This could be the result of the spatial orientation of the side-chains, which in the heterochiral compounds could be oriented on the same side of the peptide backbone, thus exposing the hydrophobic groups, and favouring the rise of amphipathic assemblies with net segregation between hydrophobic and hydrophilic components [28].

Dipeptide sequence	Rt (min)
L-Phe-L-Ile	10.6
L-Ile-L-Phe	11.3
D-Ile-L-Phe	12.9
D-Phe-L-Ile	13.0

Table 6.1. Hplc retention times (minutes) of the four dipeptides bearing Ile and Phe studied in this Manuscript.

6.3. Self-assembly into hydrogel or crystals and optical microscopic investigation

Hydrogelation was probed according to an established procedure, whereby the hydrophobic peptides were first dissolved in phosphate buffered saline (PBS, pH 7.3) with heating, and then samples were left to cool down to room temperature [22]. Homochiral L-Ile-L-Phe and L-Phe-L-Ile yielded solutions even at concentrations as high as 70 mM, although at 50 mM or above it was possible to see the presence of rare instances of microfibrils floating in solution, suggesting a tendency to fibrillate (see **Figure 6.2**).

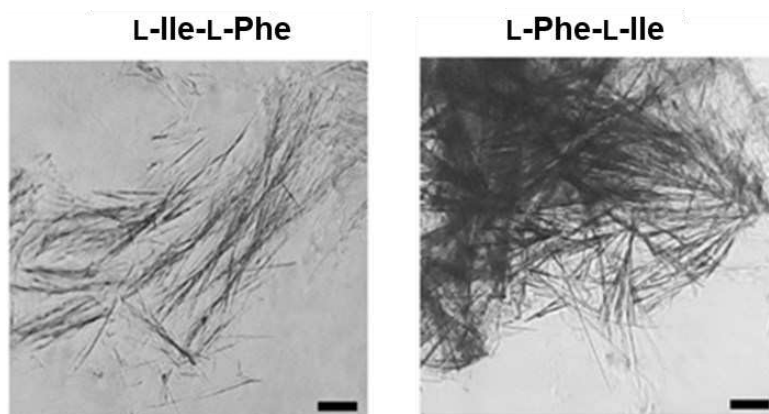


Figure 6.2. Optical microscopy images of anisotropic microstructures formed by peptides L-Ile-L-Phe (*left*), L-Phe-L-Ile (*right*) (at concentrations ≥ 50 mM). Scale bar = 50 μm . Reproduced with permission from ref. [1] © 2022 John Wiley and Sons.

However, the more hydrophobic compound of the two, *i.e.*, L-Ile-L-Phe, was previously reported to gel at concentrations of 50–70 mM, but in a different solvent system [21]. For this reason, here it was tested up to 100 mM in PBS, yet no gel was formed. Rheology confirmed the presence of a solution ($G' < G''$), with an increase of the viscous component G'' over the first 10 minutes (**Figure 6.3**), which was ascribed to the presence of fibrils.

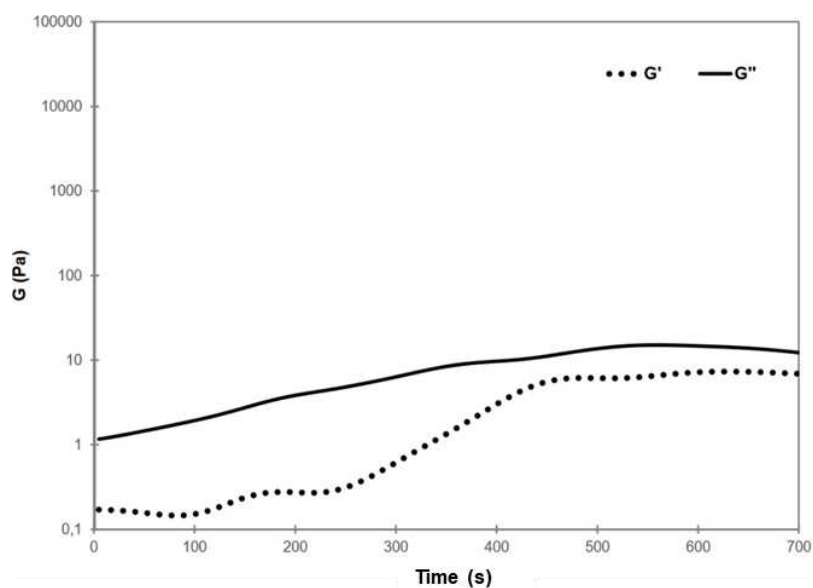


Figure 6.3. Time sweep analysis of homochiral Ile-Phe (40 mM) viscous solution ($G'' > G'$) in PBS. Reproduced with permission from ref. [1] © 2022 John Wiley and Sons.

Different was the outcome in the case of the two more hydrophobic, heterochiral analogues. Increasing the concentration of D-Ile-L-Phe to 40 mM and above, resulted in the formation of crystals (**Figure 6.4A**), which were suitable for X-ray diffraction analysis (*vide infra*), while D-Phe-L-Ile yielded microfibers already at 10 mM (**Figure 6.4B**), and an opaque hydrogel with a minimum gelling concentration (mgc) of 20 mM (**Figure 6.5**).

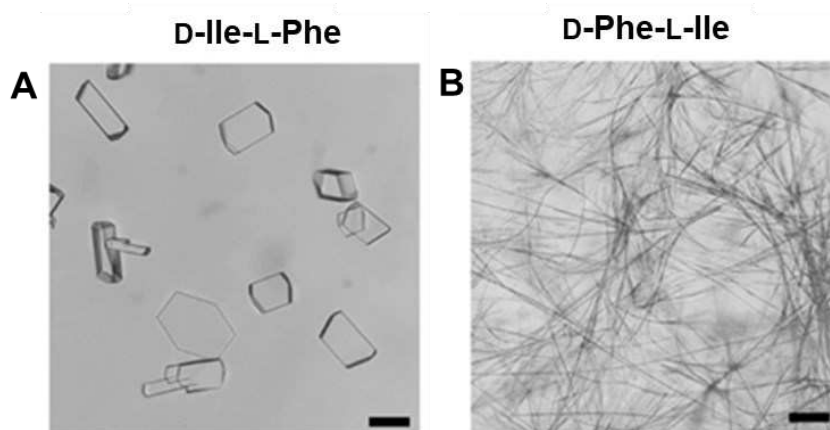


Figure 6.4. Optical microscopy images of anisotropic microstructures formed by peptides D-Ile-L-Phe, (at concentrations ≥ 50 mM), and D-Phe-L-Ile (10 mM) in PBS. Scale bar = 50 μm . Reproduced with permission from ref. [1] © 2022 John Wiley and Sons.

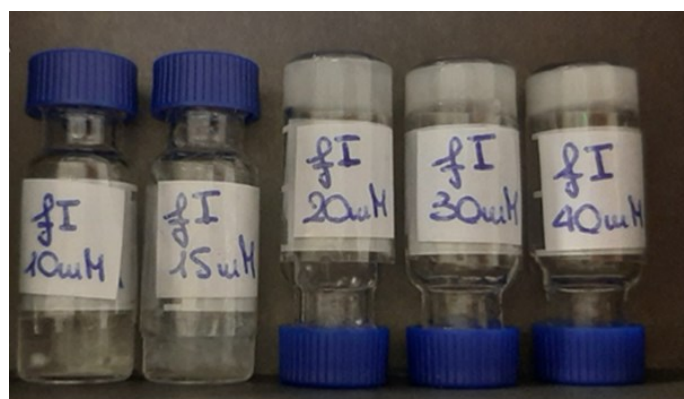


Figure 6.5. Hydrogels of D-Phe-L-Ile at 20 mM (mgc, centre) or above (30 mM or 40 mM, right). At lower concentrations (10 or 15 mM, left), heterogenous systems contained both liquid and solid phases. Reproduced with permission from ref. [1] © 2022 John Wiley and Sons.

For comparison, its structural isomer D-Phe-L-Leu under analogous experimental conditions (40 mM in PBS) was reported to yield a metastable hydrogel that converted into crystal within an hour [22], while the other gelling isomers L-Leu-L-Phe and D-Leu-L-Phe formed stable hydrogels [22]. To allow for a meaningful comparison with the literature data on Leu-Phe and Phe-Leu isomers, the concentration of 40 mM was chosen for the tests. No hydrogel was formed for any of the other three compounds (*i.e.*, L-Ile-L-Phe, D-Ile-L-Phe, and L-Phe-L-Ile), as visible in **Figure 6.6**.

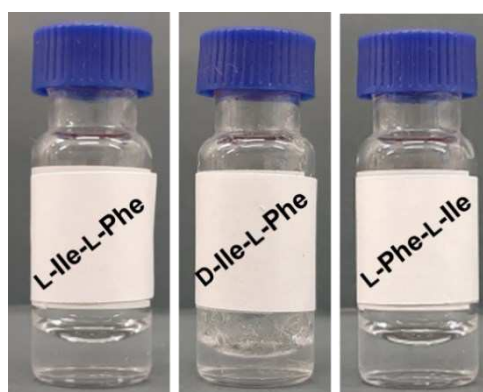


Figure 6.6 Photographs of self-assembly tests for each dipeptide at 40 mM, L-Ile-L-Phe, D-Ile-L-Phe, and L-Phe-L-Ile.

Using 10 mM PBS or deionized water adjusted to the same pH led to analogous results (**Figure 6.7**).

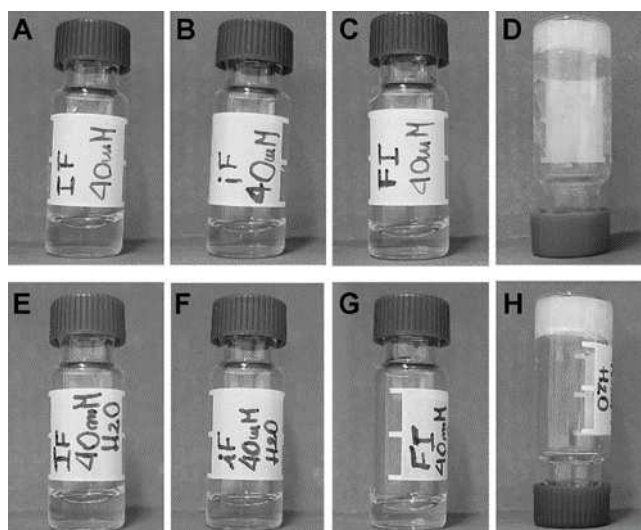


Figure 6.7. Photographs of self-assembly tests in 10 mM PBS (A-D) or deionized water adjusted to the same pH (E-H) for each dipeptide at 40 mM: (A, E) L-Ile-L-Phe, (B, F) D-Ile-L-Phe, (C, G) L-Phe-L-Ile, and (D, H) D-Phe-L-Ile. Reproduced with permission from ref. [1] © 2022 John Wiley and Sons.

In contrast, D-Phe-L-Ile gelled at all conditions within 20 seconds, also when residual trifluoroacetate was exchanged to chloride as a counterion.



Figure 6.8. Photograph of the gel of D-Phe-L-Ile (40 mM) with chloride counterion in PBS. Reproduced with permission from ref. [1] © 2022 John Wiley and Sons.

6.4. Oscillatory rheology and thermoreversibility test for the hydrogelator D-Phe-L-Ile

Oscillatory rheology was thus employed to confirm visual observations and to characterize the hydrogel formed by D-Phe-L-Ile (**Figure 6.9**).

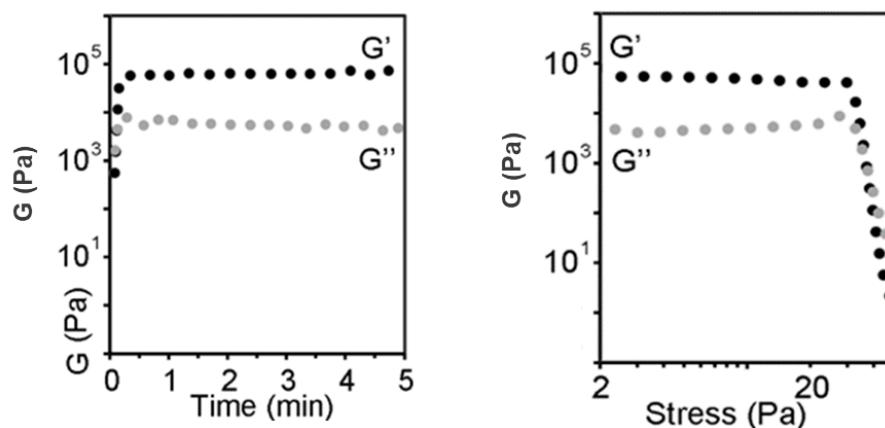


Figure 6.9. Rheology data confirmed the immediate gelation of D-Phe-L-Ile at 40 mM, reaching a plateau within one minute, and stress sweeps showed a gel-to-sol transition at ca. 46 Pa. Reproduced with permission from ref. [1] © 2022 John Wiley and Sons.

In PBS, it reached an elastic modulus of ca. 7.0×10^4 Pa at plateau within minutes (**Figure 6.9, left**) and it appeared to be a better gelator in comparison to its structural isomer D-Phe-L-Leu, which, under analogous experimental conditions (40 mM in PBS), yielded a metastable hydrogel with an elastic modulus of 1 kPa that disassembled within minute [22]. Stress sweeps revealed a gel-to-sol transition occurring at 46 Pa (**Figure 6.9, right**). Frequency sweeps confirmed the hydrogel nature, with the elastic modulus (G') higher than the viscous modulus (G''), with both being independent from the applied frequency (**Figure 6.10**).

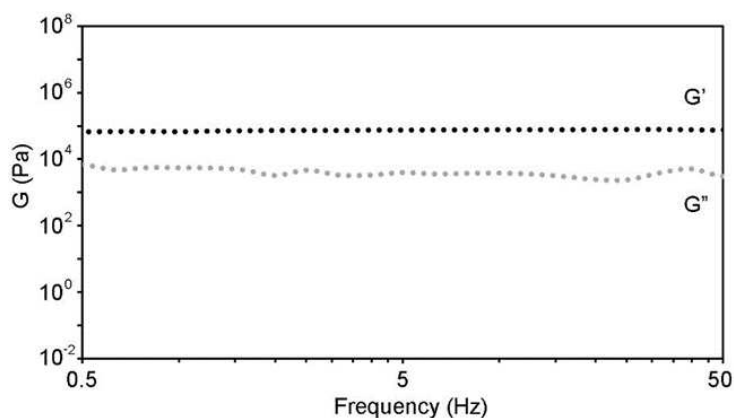


Figure 6.10. Frequency sweep for D-Phe-L-Ile at 40 mM. Reproduced with permission from ref. [1] © 2022 John Wiley and Sons.

The hydrogel thermal stability and its thermoreversibility have been investigated by heating it up in a water bath from 25 °C to 85 °C. The re-assembly has been easily achieved by cooling down the system at room temperature, within one hour. A melting temperature of 80-85 °C was observed. Unfortunately, it was not possible to determine the melting temperature (T_m) by using the CD with a temperature ramp up to 85 °C due to the scattering because of the high concentration of the sample (40 mM). Therefore, the thermoreversibility has been verified only by visual observation as reported in **table 6.2**.

Sequence	MGC	RT	80°C	85°C	RT after 1h	RT after O/N
D-Phe-L-Ile	40 mM					

Table 6.2. Photographs of thermoreversibility test for D-Phe-L-Ile hydrogel. Both its melting temperature and its reassembled state are represented.

6.5. Nanomorphologies of dipeptides' assembly

TEM micrographs were acquired to shed light on the ability of each of the four dipeptides to self-organize into nanostructures. Surprisingly, nanofibrils were observed in all cases (**Figure 6.11**), despite their diverse ability to form hydrogels. There was no significant difference in terms of average fibril diameter across samples (11.6 ± 4.9 nm, 11.9 ± 2.1 nm, 11.6 ± 2.9 nm, and 11.8 ± 2.9 nm, for L-Ile-L-Phe, D-Ile-L-Phe, L-Phe-L-Ile, and D-Phe-L-Ile, respectively, with $n=100$). Compared to gelling dipeptides L-Leu-L-Phe and D-Leu-L-Phe, [22] fibrils were significantly thinner, in agreement with previous observations that the β -branching on the side chain of Ile, near the peptide backbone, disfavours fibril bundling compared to analogues bearing the γ -branched Leu [29]. It was evident that only in the case of gelling D-Phe-L-Ile, fibrils consistently exceeded several microns in length, effectively creating an interconnected network. In all the other cases fibrils were rarely longer than 1–2 microns, thus yielding isolated clusters with limited interconnectivity (**Figure 6.11**). These observations were in agreement with the gelation ability noted only for D-Phe-L-Ile in PBS, and we inferred a similar supramolecular organization for all isomers at the nanoscale, with only minor differences that were amplified at the micro-scale.

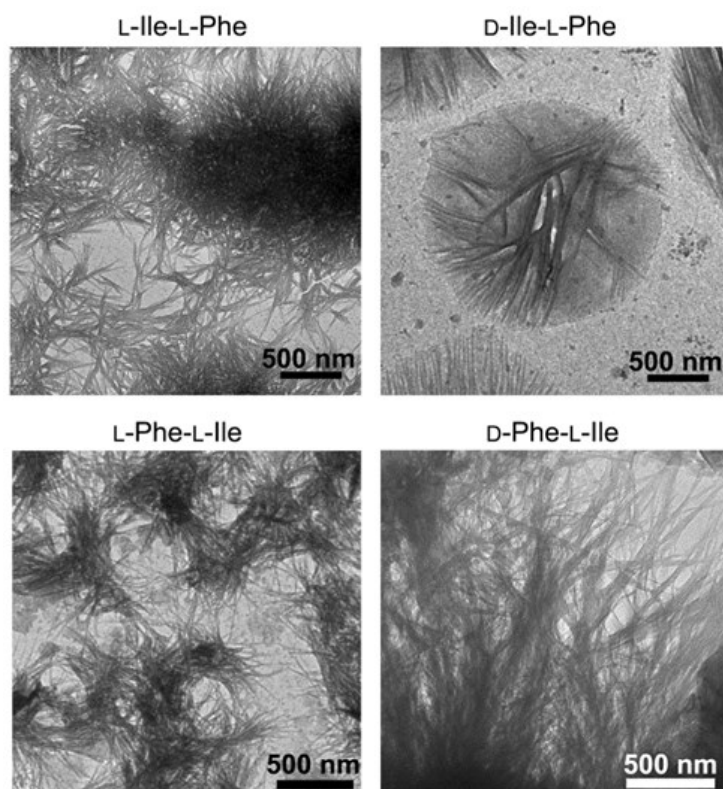


Figure 6.11. TEM micrographs of the four compounds (40 mM). Nanofibrils were present in all samples, although only in the case of gelling D-Phe-L-Ile (bottom right) they reached several microns in length. In all the other cases, clusters of shorter fibrils were mainly present, with recurrent sub-micron lengths. Reproduced with permission from ref. [1] © 2022 John Wiley and Sons.

Furthermore, in the case of D-Ile-L-Phe, HR-TEM microscopy (high resolution transmission electron microscopy) also revealed the presence of also microcrystals (**Figure 6.12**) besides the nanofibrils, in agreement with optical microscopy imaging.

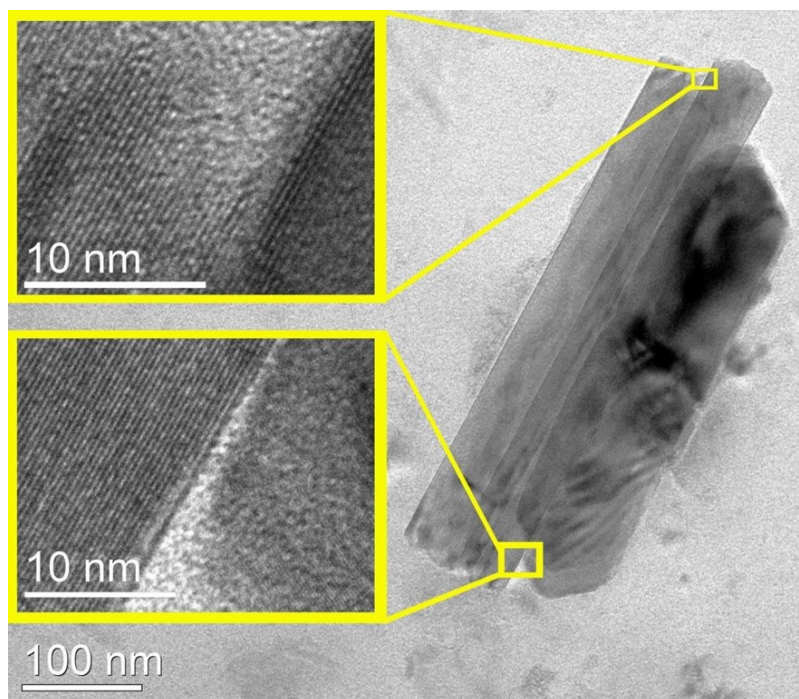


Figure 6.12. HR-TEM showing presence of microcrystals for D-Ile-L-Phe, as confirmed by the presence of diffraction lines (insets), in agreement with optical microscopy data. Reproduced with permission from ref. [1] © 2022 John Wiley and Sons.

6.6 Spectroscopic analysis of peptide conformations

Each compound was also characterized by circular dichroism (CD) and attenuated-total-reflectance infrared (ATR-IR) spectroscopies to shed light on peptide conformations leading to the observed nanostructures. CD offers useful information regarding the spatial arrangement of chiral molecules. In the case of longer peptides, it is widely applied to determine secondary conformations, such as α -helices, β -sheets, etc., which display characteristic signatures. Dipeptides, such as those studied herein, are too short as sequences to satisfy the requirements that define such conformations. However, also single amino acids display CD spectra, which are positive in the 200–250 nm region for those with L-stereo configuration [32]. Therefore, their D-enantiomers will display mirror-imaged negative spectra in the same region. Yet, the case of heterochiral dipeptides is far more complex to predict. While some studies reported that the stereo configuration of the amino acids at the peptide termini dictated the sign of the CD spectrum, [33][34][35] others showed that multiple factors come into play, such as solvent [36,37]. Interestingly, the CD spectra of the four dipeptides studied herein (**Figure 6.13**) were strikingly similar to those of their analogues with Leu in place of Ile [22].

In both cases, the only negative spectrum was the one of the dipeptides bearing D-Phe at the N-terminal. Since enantiomers are expected to display mirror-imaged CD spectra, we can conclude that in the small library of 16 dipeptides that arise from the combination of Phe with either Leu or Ile (*i.*

e., the 8 sequences shown in **Scheme 6.1** and the corresponding 8 analogues with Leu in place of Ile), it is the stereoconfiguration of Phe that dictates the sign of the CD spectrum, irrespective of its position along the sequence (*i.e.*, at the N- or C-terminus of the dipeptide). The spectra, characterized by maxima (for L-Ile-L-Phe, D-Ile-L-Phe, and L-Phe-L-Ile) or minima (for D-Phe-L-Ile) at 198 and 218 nm, were reminiscent of the signatures reported for the self-assembling L-Phe-D-Ile-L-Phe [29]. In that case, a thorough experimental and *in silico* investigation allowed to decipher it as indication of a population of conformations, of which the most visited ones featured dihedral angles typical of β -structures (sheets and turns) [29].

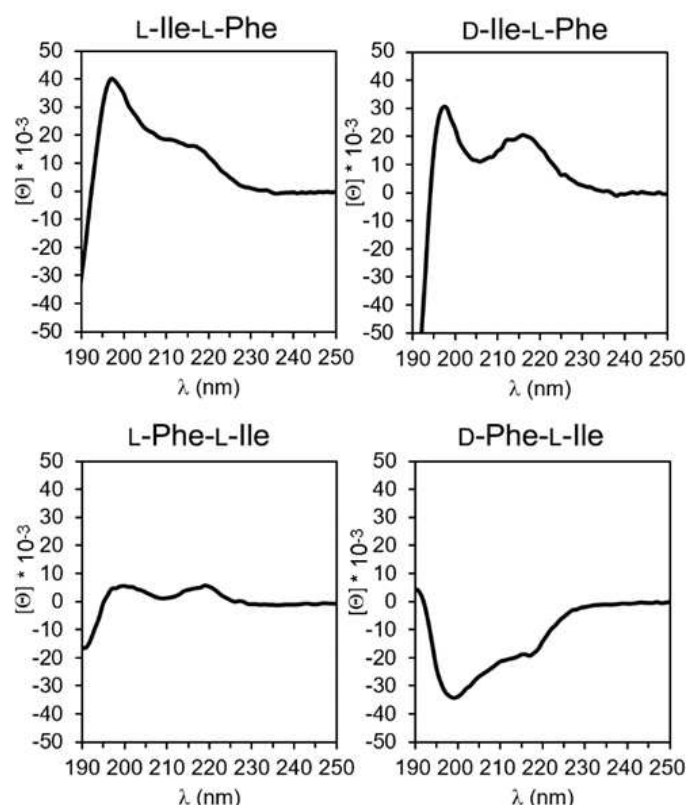


Figure 6.13. CD spectra of the four compounds. Reproduced with permission from ref. [1] © 2022 John Wiley and Sons.

Dipeptide conformation was also probed by ATR-IR. The amide region (**Figure 6.14**) is indicative of the hydrogen bonding pattern, hence, for longer peptides, of their conformation. All spectra featured a characteristic peak in the 1670–1680 cm^{-1} range, where β -turns are located for longer sequences [38]. Another signal, which was clearly visible only for Phe-Ile stereoisomers, occurred in the β -structure range (1600–1620 cm^{-1}). The amide II featured a peak at 1570 cm^{-1} for Ile-Phe stereoisomers, and another one at 1535 cm^{-1} for L-Ile-L-Phe, which was shifted to 1545–1553 cm^{-1} for the other three analogues. The signal at 1570 cm^{-1} was already reported for L-Ile-L-Phe, and it had

been attributed to the strong association between the charged peptide termini in the supramolecular state.

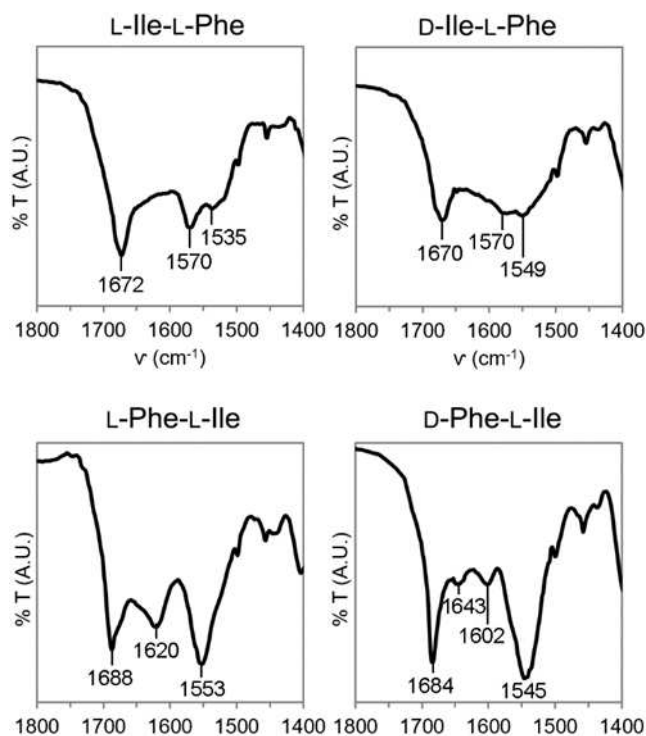


Figure 6.14. Amide I region of ATR-IR spectra of the four compounds. Reproduced with permission from ref. [1] © 2022 John Wiley and Sons.

6.6. Single-crystal X-ray diffraction analysis

The ionic interactions between charged termini were confirmed by single-crystal XRD analysis (**Figure 6.15**). The structures of the homochiral dipeptides L-Ile-L-Phe [39] and L-Phe-L-Ile [40] were already described in the literature, while those of D-Ile-L-Phe and D-Phe-L-Ile were solved in this work. We also attempted the crystallization of the homochiral compounds in different experimental conditions (*i.e.*, sample concentration, buffer solution, ionic strength, temperature) with no success. In all cases of non-gelling dipeptides, molecules self-organized into amphiphilic layers that consisted of parallel stacks with an extended H-bonding network. However, water molecules bridged peptide-peptide interactions along the stack through H-bonds. In particular, L-Phe-L-Ile displayed the most complex packing of the three isomers, with two independent dipeptide molecules in the cell unit, each with a very different conformation (*see Supplementary Information of the article, Table S2*)[40].

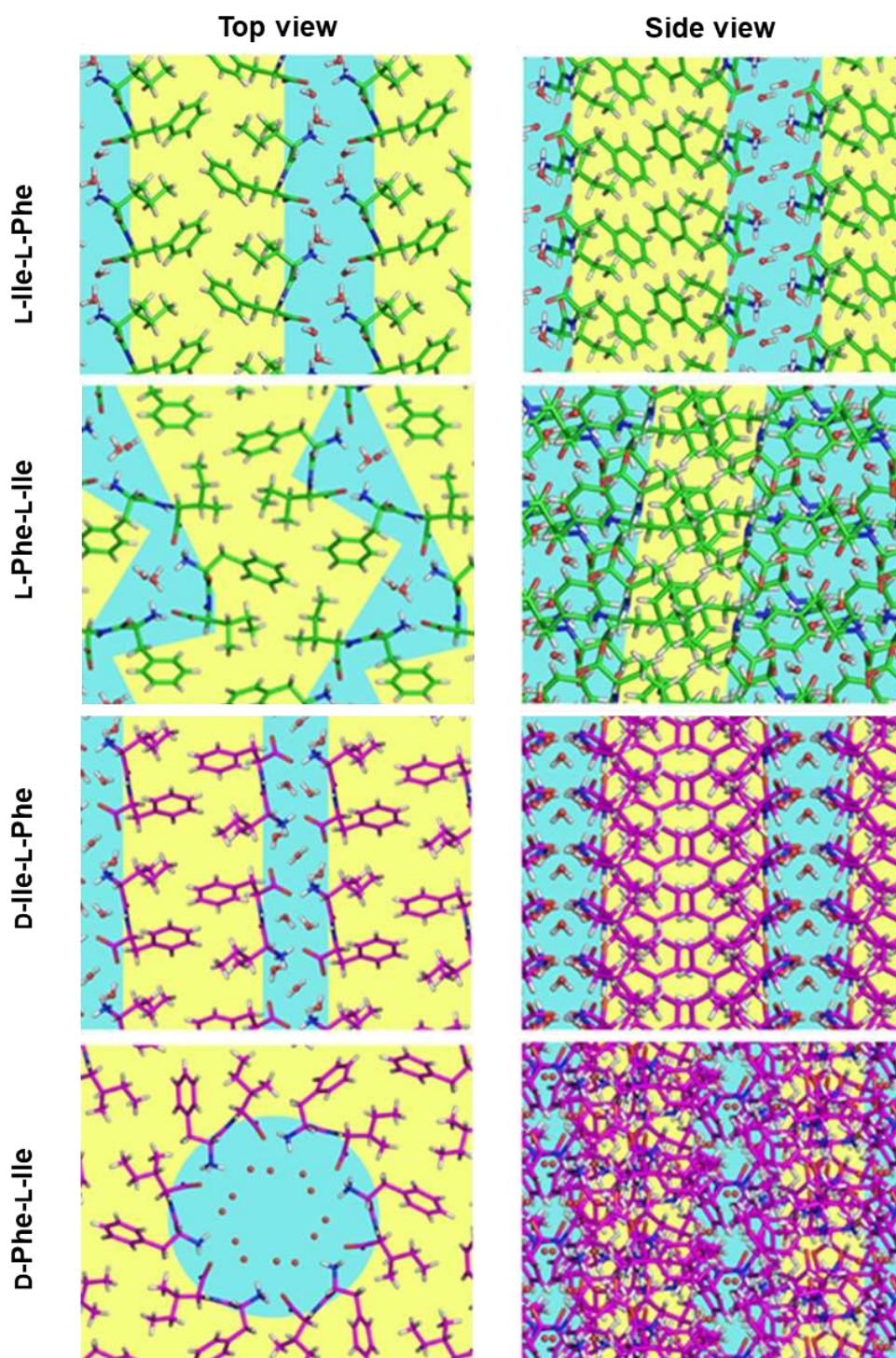


Figure 6.15. Single-crystal XRD structures of L-Ile-L-Phe,[39] L-Phe-L-Ile [40], D-Ile-L-Phe (CCDC 109139) and D-Phe-L-Ile (CCDC 109138). The first three dipeptides formed parallel stacks (top-view on the left, and side-view on the right) that defined amphipathic layers (hydrophilic regions with solvent molecules are shown in light blue, hydrophobic areas in yellow, and hydrophobic Phe rings of L-Phe-L-Ile in a hydrophilic area in light green). The only PBS gelator D-Phe-L-Ile formed instead amphipathic water channels whose cavity was defined by six zwitterionic molecules arranged head-to-tail. Reproduced with permission from ref. [1] © 2022 John Wiley and Sons.

By contrast, for L-Ile-L-Phe, [39] and D-Ile-L-Phe, just one independent dipeptide molecule was present in the cell unit. Moreover, only in the former instance there was an evident steric zipper defined by the aromatic rings, and this is a well-known stabilizing feature for amyloid structures [23] that could justify its ability to gel in different conditions [21] than those probed here. Remarkably, only the gelator D-Phe-L-Ile displayed a supramolecular arrangement analogous to Phe-Phe,[20] with six peptide zwitterions arranged head-to-tail so as to define an amphipathic water channel, with a hydrophilic interior and hydrophobic exterior, with a clear separation between hydrophilic and hydrophobic regions (**Figure 6.15**). In particular, peptides arranged in a tubular fashion along the *c* crystallographic direction, through H-bonds between amides. Interestingly, molecules forming the walls of the tube are related by the 3-fold crystallographic axis, a symmetry element belonging to the R3 space group of the crystal, but also by a 6-fold non crystallographic symmetry that relates the two independent peptide molecules present in the unit cell, and two of the independent water molecules with the other two (*see Supporting Information of the manuscript*). Tubes held together by hydrophilic interactions interact with each other through weaker intermolecular and intramolecular CH- π interactions, between the Phe and Ile side-chains (*see Supporting Information of the manuscript*).

6.7. Biocompatibility assays of D-Phe-L-Ile hydrogel

Both qualitative and quantitative preliminary assays were performed *in vitro* to assess the cytotoxicity of the only gelling peptide D-Phe-L-Ile on murine fibroblasts, chosen as model line for such studies. Live/Dead assay was performed using two fluorescent dyes, orange (AO) and propidium iodide (PI) in a μ -well slide for 24 hour (**Figure 6.16**). The simultaneous use of the two fluorescent dyes, acridine orange (AO) and propidium iodide (PI), allowed to assess the cell morphology and to detect both live and dead cells in the same experiment, using a fluorescence microscope. The green and red fluorescence are the results of the interactions between cell nucleic acids and acridine orange (AO) or propidium iodide (PI), respectively.

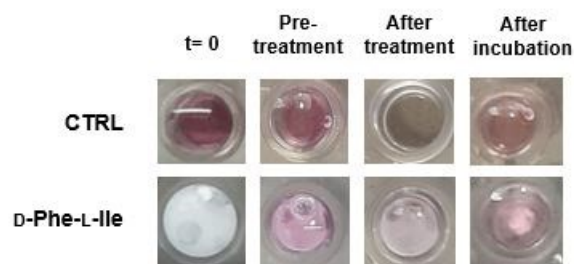


Figure 6.16. Photographs of representative μ -slide wells (Ibidi, Germany) used for live/dead assay on fibroblast at the different time-points of the assay.

A high cell viability and a comparable cell morphology were observed in comparison to the control, without significant cytotoxicity signals. Before the incubation, the gel prepared from D-Phe-L-Ile was opaque and strong with a fast kinetic of formation (see **Figure 6.9**), that required a speedy procedure of preparation. After 24 h of incubation, the hydrogel appeared partially dissolved but still present, and led to a high degree of cell spreading in the hydrogel scaffold (**Figures 6.16** and **6.17**). The apparently low cell density observed in the gel in comparison to the control may be due to the fact the the former is a 3D scaffold, while the latter is a 2D surface. Indeed, the saturated fluorescence in the bottom-left panel of **Figure 6.17** could be ascribed with high cell numbers through the thickness of the gel.

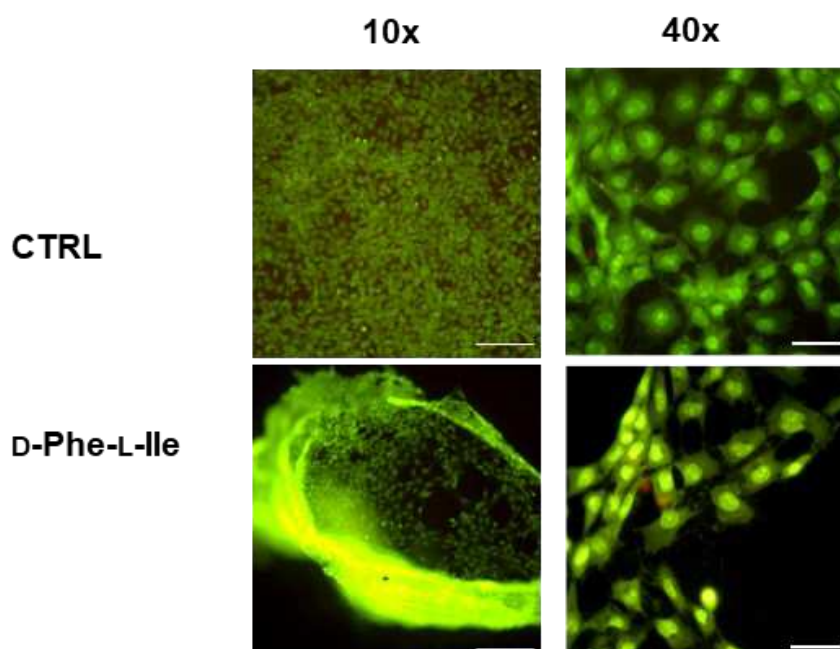


Figure 6.17. Live/Dead assay on fibroblast cells (NIH/3T3) growth on the gel D-Phe-L-Ile as scaffold. Scale bar 200 μm (objective 10x) and 50 μm (objective 40x).

The cytotoxicity of the dipeptide D-Phe-L-Ile in solution was evaluated by performing the quantitative MTT assay for 24 hours, to be coherent with the live/dead assay (**Figure 6.18**). Two independent experiments were performed, and 1 mM was assumed the highest concentration to have the peptide still in solution. At all concentrations tested, even at the at the highest one, a good cell viability was observed for the D-Phe-L-Ile, and these data agreed with live/dead fluorescence assay. Overall, biological results are very promising and highly encouraging in terms of the biocompatibility of D-Phe-L-Ile, especially because of its high viability on murine fibroblasts as hydrogel matrix and as a free molecule in solution.

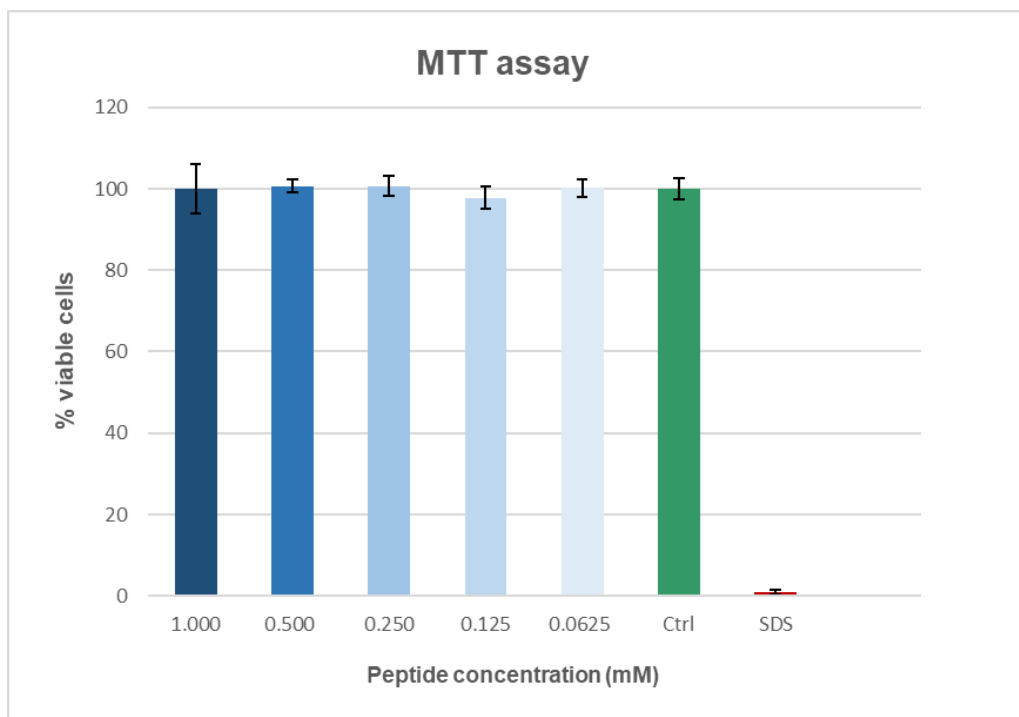


Figure 6.18. Quantitative Mtt assay results on fibroblast (NIH/3T3) incubated with the hydrogelator D-Phe-L-Ile in solution. Different concentrations were tested (from 1 to 0.0625 mM).

6.8. Conclusions

In conclusion, this work reported D-Phe-L-Ile as a new hydrogelator in PBS with mgc of 20 mM, and with the ability to self-organize into amphipathic water channels. Interestingly, the other stereo- and regio-isomers did not gel in PBS at concentrations as high as 70 mM, despite their ability to self-organize into anisotropic nanostructures as confirmed by microscopy. In particular, although all compounds could form fibrils of analogous diameter, their length varied, with only the gelling D-Phe-L-Ile being able to form several-micron long fibrils that effectively entangled in a three-dimensional network that yielded a macroscopic hydrogel. Comparison with the analogous dipeptide series containing Leu and Phe, [22] revealed that heterochirality overall increased hydrophobicity, which promoted self-assembly, although this was not sufficient as a parameter on its own for hydrogelation to occur. All the gelling dipeptides showed the presence of recurrent packing features, *i.e.*, 1) the ability to segregate hydrophilic and hydrophobic components into separate areas, with polar solvent molecules being confined in the former; 2) the establishment of an extended network of H-bonds between amides of adjacent dipeptides, as well as salt bridges between charged termini; 3) the ability to form steric zippers especially with Phe side-chains that is a well-known amyloid stabilizing feature. Overall, it appears evident that the supramolecular behaviour and gelling ability of simple biomolecules such as unprotected dipeptides is difficult to predict a priori, yet recurrent features in

terms of the supramolecular packing of gelators are being identified as research in the field advances. The emergence of simple design rules for their self-organization into soft matter will ultimately accelerate developments for finding applications in a variety of fields, spanning from nanotechnology and smart materials to innovative therapeutics. Ultimately, they may shed further light on prebiotic chemistry and the origins of life.

Furthermore, promising results for the biocompatibility versus mammalian cells for the gelling D-Phe-L-Ile have been provided by means of both preliminary qualitative and quantitative assays on murine fibroblasts although some potential limitations in terms of gel durability under cell culture conditions. Further studies need to be performed for instance, by testing the biocompatibility of the hydrogel on other mammalian cell lines, such as keratinocytes, to confirm the potential of applicability of this simple dipeptide such as scaffold for future applications in biomedicine.

***Note:** Thermoreversibility test and biological assays were not included in *Manuscript 5*.

References

- [1] O. Bellotto, S. Kralj, M. Melchionna, P. Pengo, M. Kisovec, M. Podobnik, R. De Zorzi, S. Marchesan, *ChemBioChem* **2022**, *23*, e202100518.
- [2] J. Y. C. Lim, Q. Lin, K. Xue, X. J. Loh, *Mater. Today Adv.* **2019**, *3*, 100021.
- [3] W. Ahn, J.-H. Lee, S. R. Kim, J. Lee, E. J. Lee, *J. Mater. Chem. B* **2021**, *9*, 1919–1940.
- [4] Y. Shao, H. Jia, T. Cao, D. Liu, *Acc. Chem. Res.* **2017**, *50*, 659–668.
- [5] C. Diaferia, G. Morelli, A. Accardo, *J. Mater. Chem. B* **2019**, *7*, 5142–5155.
- [6] Y. Jiang, N. Krishnan, J. Heo, R. H. Fang, L. Zhang, *J. Control. release Off. J. Control. Release Soc.* **2020**, *324*, 505–521.
- [7] J. K. Wychowaniec, M. Iliut, M. Zhou, J. Moffat, M. A. Elsayy, W. A. Pinheiro, J. A. Hoyland, A. F. Miller, A. Vijayaraghavan, A. Saiani, *Biomacromolecules* **2018**, *19*, 2731–2741.
- [8] M. Mba, A. I. Jiménez, A. Moretto, *Chemistry* **2014**, *20*, 3888–3893.
- [9] L. Milli, N. Zanna, A. Merlettini, M. Di Giosia, M. Calvaresi, M. L. Focarete, C. Tomasini, *Chemistry* **2016**, *22*, 12106–12112.
- [10] P. Makam, E. Gazit, *Chem. Soc. Rev.* **2018**, *47*, 3406–3420.
- [11] W. T. Truong, Y. Su, D. Gloria, F. Braet, P. Thordarson, *Biomater. Sci.* **2015**, *3*, 298–307.
- [12] A. D. Martin, P. Thordarson, *J. Mater. Chem. B* **2020**, *8*, 863–877.
- [13] V. R. Aldilla, R. Chen, A. D. Martin, C. E. Marjo, A. M. Rich, D. S. Black, P. Thordarson, N. Kumar, *Sci. Rep.* **2020**, *10*, 770.
- [14] A. D. Martin, J. P. Wojciechowski, A. B. Robinson, C. Heu, C. J. Garvey, J. Ratcliffe, L. J.

- Waddington, J. Gardiner, P. Thordarson, *Sci. Rep.* **2017**, *7*, 43947.
- [15] K. H. Chan, B. Xue, R. C. Robinson, C. A. E. Hauser, *Sci. Rep.* **2017**, *7*, 12897.
- [16] P. W. J. M. Frederix, G. G. Scott, Y. M. Abul-Haija, D. Kalafatovic, C. G. Pappas, N. Javid, N. T. Hunt, R. V Ulijn, T. Tuttle, *Nat. Chem.* **2015**, *7*, 30–37.
- [17] T. Das, M. Häring, D. Haldar, D. Díaz Díaz, *Biomater. Sci.* **2018**, *6*, 38–59.
- [18] M. P. Conte, N. Singh, I. R. Sasselli, B. Escuder, R. V Ulijn, *Chem. Commun.* **2016**, *52*, 13889–13892.
- [19] M. Kurbasic, S. Semeraro, A. M. Garcia, S. Kralj, E. Parisi, C. Deganutti, R. De Zorzi, S. Marchesan, *Synthesis (Stuttg.)* **2019**, *51*, 2829–2838.
- [20] S. Kralj, O. Bellotto, E. Parisi, A. M. Garcia, D. Iglesias, S. Semeraro, C. Deganutti, P. D’Andrea, A. V. Vargiu, S. Geremia, R. De Zorzi, S. Marchesan, *ACS Nano* **2020**, *14*, 16951–16961.
- [21] N. S. De Groot, T. Parella, F. X. Aviles, J. Vendrell, S. Ventura, *Biophys. J.* **2007**, *92*, 1732–1741.
- [22] O. Bellotto, S. Kralj, R. De Zorzi, S. Geremia, S. Marchesan, *Soft Matter* **2020**, *16*, 10151–10157.
- [23] M. R. Sawaya, S. Sambashivan, R. Nelson, M. I. Ivanova, S. A. Sievers, M. I. Apostol, M. J. Thompson, M. Balbirnie, J. J. W. Wiltzius, H. T. McFarlane, A. Ø. Madsen, C. Riek, D. Eisenberg, *Nature* **2007**, *447*, 453–457.
- [24] D. W. Deamer, R. Dick, W. Thiemann, M. Shinitzky, *Chirality* **2007**, *19*, 751–763.
- [25] S. Marchesan, C. D. Easton, K. E. Styan, L. J. Waddington, F. Kushkaki, L. Goodall, K. M. McLean, J. S. Forsythe, P. G. Hartley, *Nanoscale* **2014**, *6*, 5172–5180.
- [26] D. Iglesias, M. Melle-Franco, M. Kurbasic, M. Melchionna, M. Abrami, M. Grassi, M. Prato, S. Marchesan, *ACS Nano* **2018**, *12*, 5530–5538.
- [27] H. L. Bolt, C. E. J. Williams, R. V Brooks, R. N. Zuckermann, S. L. Cobb, E. H. C. Bromley, *Pept. Sci.* **2017**, *108*, e23014.
- [28] A. V Vargiu, D. Iglesias, K. E. Styan, L. J. Waddington, C. D. Easton, S. Marchesan, *Chem. Commun.* **2016**, *52*, 5912–5915.
- [29] A. M. Garcia, D. Iglesias, E. Parisi, K. E. Styan, L. J. Waddington, C. Deganutti, R. De Zorzi, M. Grassi, M. Melchionna, A. V. Vargiu, S. Marchesan, *Chem* **2018**, *4*, 1862–1876.
- [30] S. Marchesan, L. Waddington, C. D. Easton, D. A. Winkler, L. Goodall, J. Forsythe, P. G. Hartley, *Nanoscale* **2012**, *4*, 6752–6760.
- [31] M. C. Cringoli, C. Romano, E. Parisi, L. J. Waddington, M. Melchionna, S. Semeraro, R. De Zorzi, M. Grönholm, S. Marchesan, *Chem. Commun.* **2020**, *56*, 3015–3018.

- [32] N. Amdursky, M. M. Stevens, *ChemPhysChem* **2015**, *16*, 2768–2774.
- [33] U. Orcel, M. De Poli, M. De Zotti, J. Clayden, *Chem. – A Eur. J.* **2013**, *19*, 16357–16365.
- [34] M. Wang, P. Zhou, J. Wang, Y. Zhao, H. Ma, J. R. Lu, H. Xu, *J. Am. Chem. Soc.* **2017**, *139*, 4185–4194.
- [35] Y. Fu, B. Li, Z. Huang, Y. Li, Y. Yang, *Langmuir* **2013**, *29*, 6013–6017.
- [36] Y. Li, B. Li, Y. Fu, S. Lin, Y. Yang, *Langmuir* **2013**, *29*, 9721–9726.
- [37] Q. Xing, J. Zhang, Y. Xie, Y. Wang, W. Qi, H. Rao, R. Su, Z. He, *ACS Nano* **2018**, *12*, 12305–12314.
- [38] E. Goormaghtigh, J.-M. Ruyschaert, V. Raussens, *Biophys. J.* **2006**, *90*, 2946–2957.
- [39] C. Görbitz, *Acta Crystallogr. C.* **2004**, *60*, o371-373.
- [40] C. Görbitz, *Acta Crystallogr. C.* **2004**, *60*, o810-2.

Chapter 7. Self-assembly of Val-Phe and Phe-Val dipeptides

This chapter describes the work of the *Manuscript 6* entitled “*Dipeptide self-assembly into water-channels and gel biomaterial*” [1].

7.1. Introduction

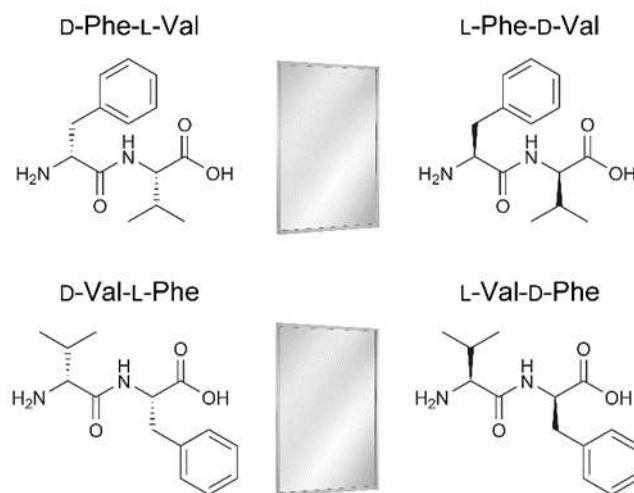
In **Chapters 5** and **6**, we described the self-assembly of dipeptides, comprising all possible stereoisomer and regioisomer combinations of Phe with either Leu or Ile. It was noted that heterochirality increased hydrophobicity and favoured assembly into crystals or hydrogels. However, the formation of water-filled nanotubes with a cavity defined by six peptide molecules connected head-to-tail, as with Phe-Phe, was confirmed only for one compound out of 8, *i.e.*, D-Phe-L-Ile [2,3]

Water-filled nanotubes are particularly interesting as they could potentially insert into membranes and alter cell permeability. Phe-Phe was indeed shown to do so selectively on bacteria, thus exerting an antimicrobial effect [4]. Stacks of cyclopeptides into nanotubes were also effectively used to the same end [5,6]. Furthermore, applications can go well beyond the treatment of infections. For instance, they have shown proton conductivity both in the wet and dry state, a property that could be useful to develop innovative, green devices for energy storage and conversion that do not persist in the environment [7]. To this end, the formation of water-channels in crystalline structures obtained from simple, linear, short peptides is very attractive, and was successfully demonstrated to display evaporation-induced actuation [8]. However, design rules to understand which short sequences can form water-channels, and which don't, are still lacking.

To shed light on this unanswered question, in this work we studied the self-assembly behaviour of heterochiral Val-Phe and Phe-Val. Valine shares the feature of a β -branched hydrophobic sidechain with Ile and Phe, and both D-Phe-L-Ile (but not D-Ile-L-Phe) [3] and D-Phe-L-Phe [9] maintained the ability to self-assemble into water-filled nanotubes. Previous studies on homochiral Val-Phe [10] and Phe-Val [11] revealed no fibrillation, and their crystal structures were formed by amphipathic layers [12,13] devoid of water-channels. However, heterochirality was shown to increase dipeptide hydrophobicity, relative to homochiral stereoisomers, and promote fibrillation in aqueous solutions [2,3], thus giving scope for the present study.

7.2. D-Phe-L-Val and D-Val-L-Phe conformation analysis in solution

The four possible heterochiral dipeptides from Val and Phe are shown in **Scheme 7.1**. Enantiomers display identical supramolecular behaviour in achiral environments; therefore D-Phe-L-Val and D-Val-L-Phe (**Scheme 7.1**, left) are representatives of the four enantiomeric pairs. They were synthesised by standard solid-phase methods, purified by HPLC, and identified by LC-MS, $^1\text{H-NMR}$ and $^{13}\text{C-NMR}$ (see **Materials and Methods** and **Appendix**).



Scheme 7.1. Chemical structures of the 4 heterochiral dipeptides from Val and Phe. Reproduced from Ref. [1] with permission from © 2022 Royal Society of Chemistry.

When analysed by reversed-phase HPLC, the two dipeptides displayed nearly identical retention times, which can be considered an experimental measure for hydrophobicity (**Figure 7.1**) [14].

In diluted solutions, at concentration of 1 mM, the circular dichroism (CD) spectra were reminiscent of their analogues with Ile instead of Val (**Figure 7.2**) [3]. In all cases, considering that enantiomers are expected to display mirror-imaged CD spectra with opposite ellipticity, we can conclude that the sign of the CD signal above 200 nm is determined by Phe chirality (*i.e.*, negative for D-Phe and positive for L-Phe) [15], regardless of its position along the sequence (*i.e.*, at the N- or C-terminus). This type of CD signature with two peaks at 198 and 218 nm can be representative of a population of conformations, whose majority have dihedral angles typical of β -structures, and which can be found also for non-assembling analogues [16,17].

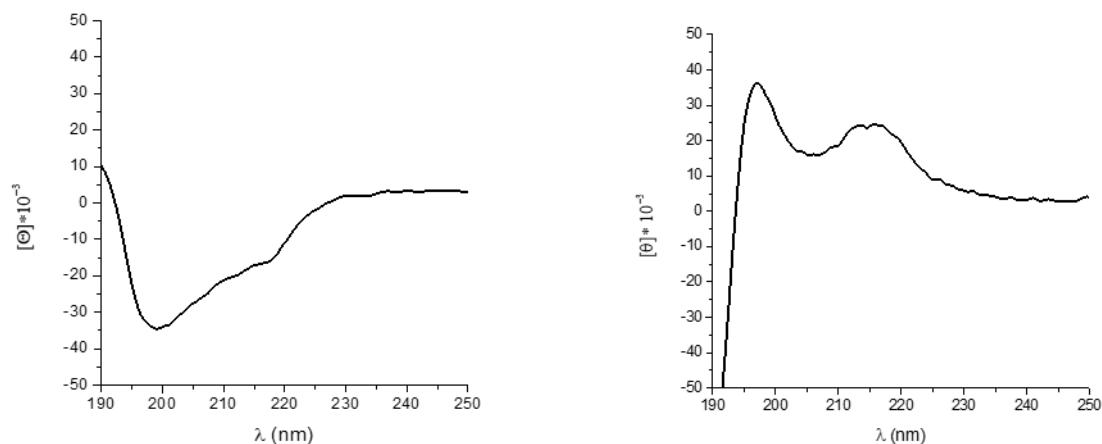


Figure 7.2. CD spectra of D-Phe-L-Val (left) and D-Val-L-Phe (right) in solution at 1 mM. Reproduced from Ref. [1] with permission from © 2022 Royal Society of Chemistry.

7.3. Self-assembly and hydrogelation of D-Phe-L-Val and D-Val-L-Phe

The ability to self-assemble and gel was probed by using a standard protocol reported in our previous works, to assess the influence of the dipeptide sequence on the supramolecular behaviour [2][3]. The dipeptides were first dissolved in PBS upon heating, and subsequent cooling down to room temperature (**Figure 7.3**) afforded an opaque gel solely for D-Phe-L-Val (minimum gelling concentration, mgc of 40 mM). Conversely, D-Val-L-Phe rapidly crystallised when tested at concentrations that were higher than its solubility (*i.e.*, 100 mM, **Figure 7.3**). Optical microscopy images revealed fibers for the former (**Figure 7.3 A**), and crystals for the latter (**Figure 7.3 B**), which were of suitable quality for single-crystal X-ray (XRD) diffraction.

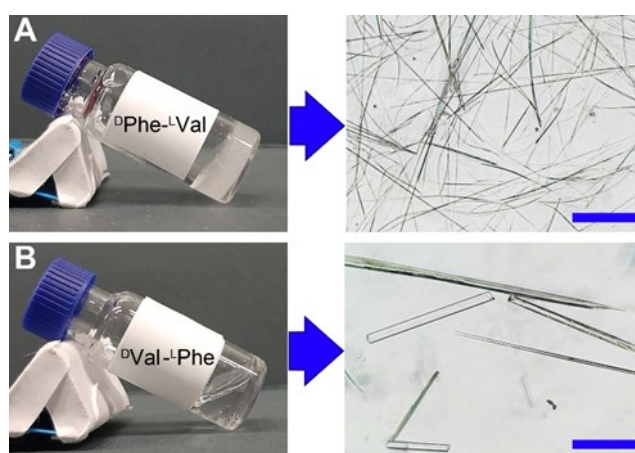


Figure 7.3. Photographs and optical microscopy images of (A) D-Phe-L-Val and (B) D-Val-L-Phe in PBS at concentrations above their solubility. Scale bar = 100 μm . Reproduced from Ref. [1] with permission from © 2022 Royal Society of Chemistry.

Transmission electron microscopy (TEM) confirmed the presence of fibers for D-Phe-L-Val with a median diameter of ~ 1 micron ($n = 50$; **Figure 7.4**).

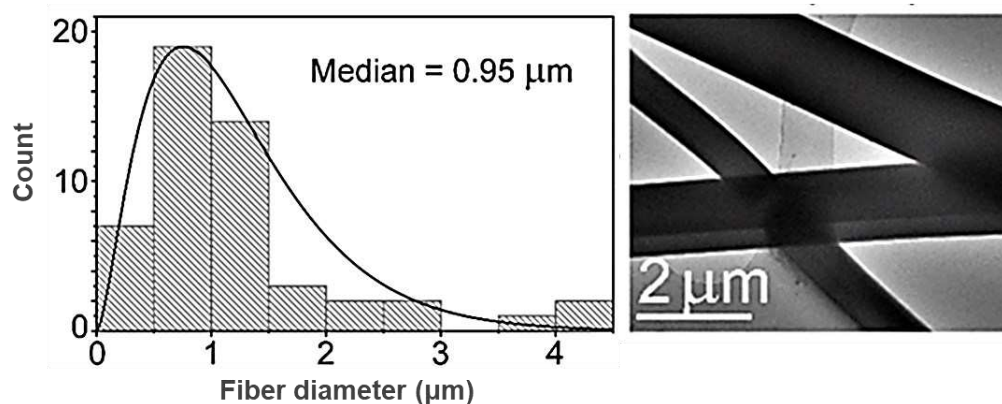


Figure 7.4. Transmission electron micrographs (TEM) for the only hydrogelator D-Phe-L-Val (right). Microfibers observed with a median diameter of ~ 1 micron (left). Reproduced from Ref. [1] with permission from © 2022 Royal Society of Chemistry.

By contrast, D-Val-L-Phe formed amorphous aggregates at the same concentration (**Figure 7.5**).

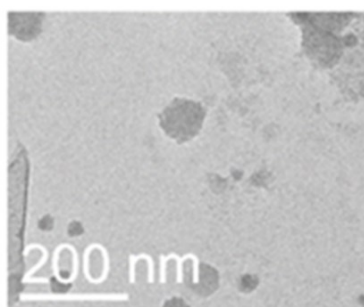


Figure 7.5. Transmission electron micrographs (TEM) for D-Val-L-Phe. Reproduced from Ref. [1] with permission from © 2022 Royal Society of Chemistry.

7.4. D-Phe-L-Val and D-Val-L-Phe conformational analysis in the assembled state

Interestingly, both compounds tested negative for thioflavin-T (ThT) fluorescence (**Figure 7.6**), which is a standard assay used to probe for the presence of amyloids and quantify the critical aggregation concentration [18]. The dye features a benzothiazole moiety linked to a dimethylanilino ring via a C-C bond, whose rotation is impeded when the dye binds onto hydrophobic grooves of amyloid fibrils, leading to fluorescence [19]. Considering that D-Phe-L-Val does fibrillate, as confirmed by transmission electron microscopy analysis as reported in **Figure 7.5**, we can conclude that the topography of its fibers is not suitable for effective binding of ThT. The dye was shown to

bind to β -sheets composed of at least four consecutive β -strands [20], therefore we used Fourier-transformed infrared spectroscopy to analyse the peptide conformation.

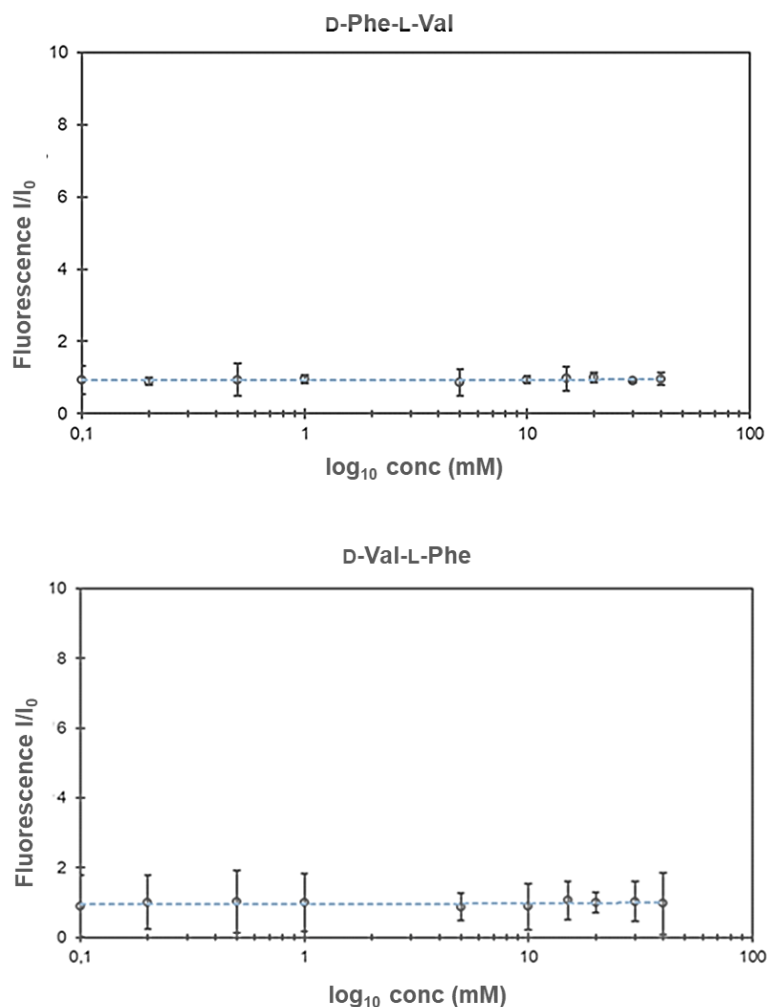


Figure 7.6. Thioflavin T fluorescence assay for D-Phe-L-Val (up) and D-Val-L-Phe (bottom) respectively, reveals lack of fluorescence with a signal intensity (I) that is not significant different relative to the control without peptide (I_0) across all concentrations tested, both in solution and gel phase for D-Phe-L-Val (mgc = 40 mM). Reproduced from Ref. [1] with permission from © 2022 Royal Society of Chemistry.

The amide I and II regions of FT-IR spectra (**Figure 7.7**), revealed sharper peaks for D-Phe-L-Val, relative to D-Val-L-Phe, and this finding can be an indication of the higher supramolecular order of the former relative to the latter. Both compounds displayed peaks in the region where β -turns are found for longer sequences (*i.e.*, 1682 and 1674 cm^{-1} , respectively), as previously found for Ile analogs [3]. However, only gelling D-Phe-L-Val had a signal at 1640 cm^{-1} that is in the range between β -structures and disordered conformations.

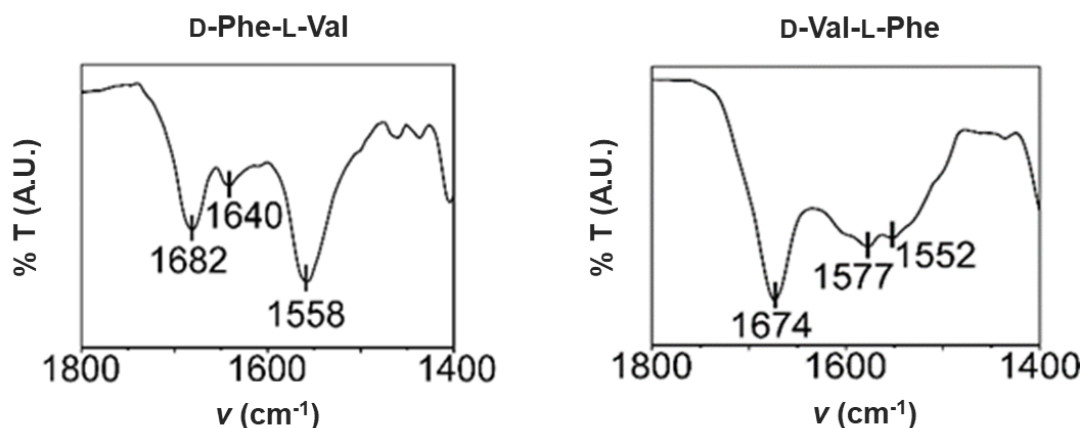


Figure 7.7. Amide I-II region of the FT-IR spectra of the two dipeptides at 40 mM. Reproduced from Ref. [1] with permission from © 2022 Royal Society of Chemistry.

7.5. Raman microspectroscopy of D-Phe-L-Val and D-Val-L-Phe assemblies

Raman microspectroscopy is another useful technique to investigate these systems (**Figure 7.8 A-D**). In all cases, spectra were dominated by the aromatic signal at 1005 cm^{-1} that can be used for mapping of the microstructures (**Figure 7.8 A-B**). D-Phe-L-Val self-assembly was accompanied by the rising of signals at 1266 cm^{-1} in the amide III region, and 1694 cm^{-1} in the amide I range (**Figure 7.8 C** blue asterisks), as a result of the supramolecular stacking through establishment of H-bonding networks involving the amide bonds. Another signal of interest is at 1294 cm^{-1} that likely corresponds to C-H bending modes [21]. The same set of signals arose with crystallization of D-Val-L-Phe, although in this case they were all downshifted to 1257 cm^{-1} , 1277 cm^{-1} and 1672 cm^{-1} (**Figure 7.8 D**). Upshifts can result from extended H-bonding networks [9,22], suggesting a more pronounced effect for the gelator D-Phe-L-Val relative to D-Val-L-Phe. Single-crystal XRD structures of hydrophobic dipeptides had shown that in the case of non-gelling isomers water molecules were mediating peptide-peptide H-bonds through the amides, while in the case of gelators, peptide molecules were interacting directly in extended stacks [2,3]. To verify whether this is a general rule that applies also to D-Phe-L-Val and D-Val-L-Phe, single-crystal XRD analyses were performed.

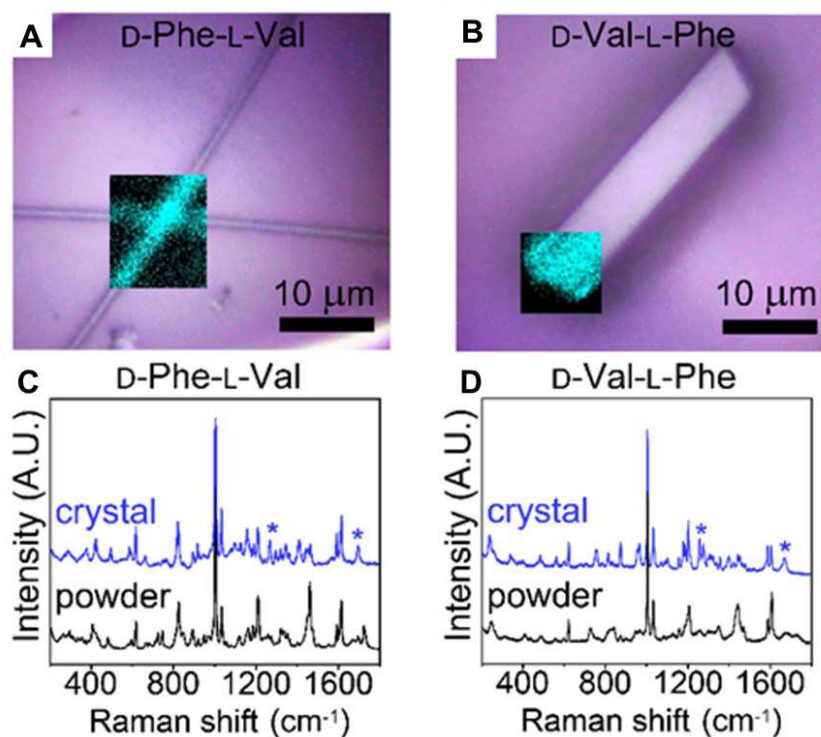


Figure 7.8. A-B) Raman mapping of the aromatic signal at 1005 cm^{-1} (cyan) overlaid on the optical microscopy images of fibers (A) and crystals (B). C-D) Raman spectra. Blue asterisks denote signal rising with assembly in the amide I-III region. Reproduced from Ref. [1] with permission from © 2022 Royal Society of Chemistry.

7.6. Single-crystal X-ray diffraction analysis of D-Phe-L-Val and D-Val-L-Phe

Single-crystal XRD structures of both compounds were solved using synchrotron radiation. D-Phe-L-Val microfibers evolved into crystals over the course of several days (**Figures 7.9 and 7.10 A-D**). The dipeptide crystallises in a tetragonal unit cell system (space group $I4$). Four hydrophobic dipeptides arrange head-to-tail inducing the formation of a hydrophilic amide-rich channel filled with water molecules and a hydrophobic region defined by the aminoacidic sidechains establishing weak hydrophobic interactions. The channels are parallel to the shortest c axis and are filled with water molecules, which do not show full occupancy. According to Görbitz's classification [23], D-Phe-L-Val can be considered as a member of the Phe-Phe class of dipeptides forming porous structures. The members of this class show a specific H-bond pattern, where two amino H atoms interact with two carboxylic oxygen atoms of two different dipeptides, while the third interacts with a water molecule inside the channel (**Figure 7.11**). Notably, L-Phe-L-Val [12] crystallises as an anhydrous crystal form, a not-so common feature for dipeptides.

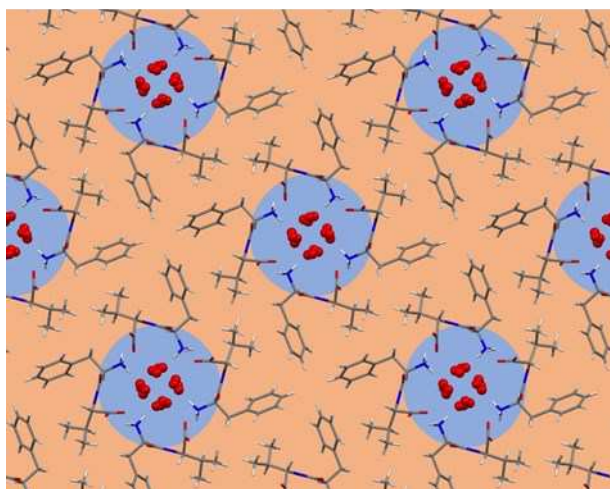


Figure 7.9. The figure shows the water channels in the crystal structure of D-Phe-L-Val (shown in blue) surrounded by four dipeptides arranged head-to-tail. Atom types: C grey, H white, O red, N blue. Water molecules are depicted in ball-and-stick style. Reproduced from Ref. [1] with permission from © 2022 Royal Society of Chemistry.

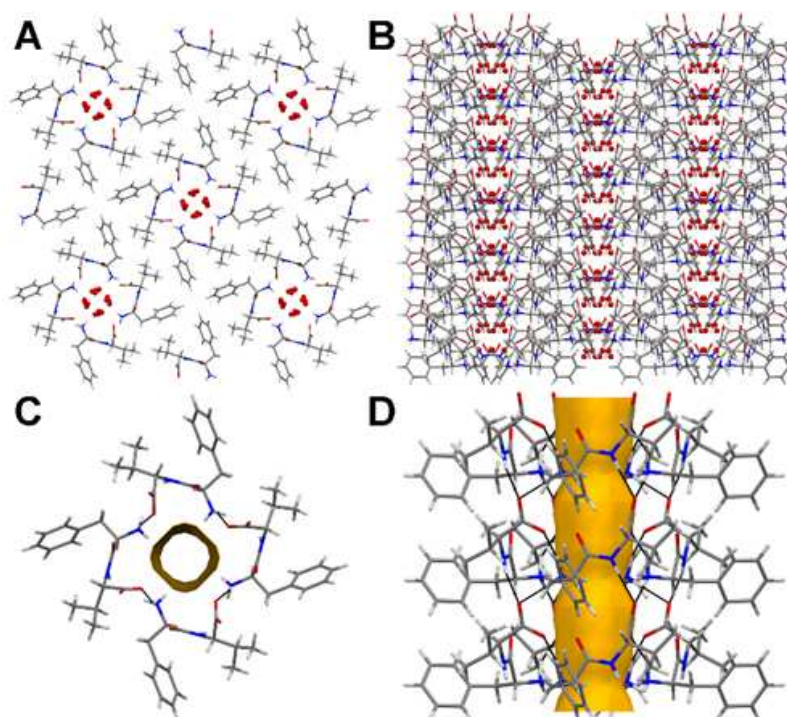


Figure 7.10. Single-crystal XRD data for D-Phe-L-Val (CCDC 2160978). A-B) Crystal packing along the c and a axis, respectively. C-D) Detailed view of the water-channel (gold). Reproduced from Ref. [1] with permission from © 2022 Royal Society of Chemistry.

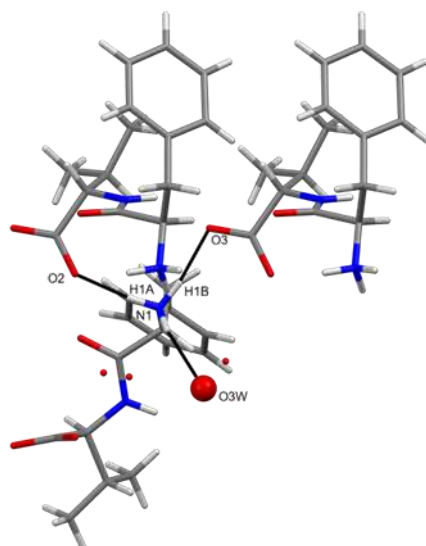


Figure 7.11. Typical hydrogen bond pattern of Phe-Phe dipeptide group. Only the interacting water molecule O3W is reported in ball-and-stick style. Reproduced from Ref. [1] with permission from © 2022 Royal Society of Chemistry.

Conversely, D-Val-L-Phe crystallises as an amphipathic layered structure in a monoclinic unit cell system (space group $C2$). To properly describe the self-organisation of D-Val-L-Phe we refer to hydrophilic and hydrophobic regions (**Figures 7.12 and 7.13 A-C**). The former is characterised by a H-bond network involving the atoms of the dipeptide backbone and water molecules, while the latter is defined by the hydrophobic side chains. This arrangement is very similar to the solid-state assembly of D-Ile-L-Phe dipeptides [3]. Moreover, comparing the crystal packing of D-Val-L-Phe with the L-homochiral counterpart, the similarities with the solid-state assembly of the dihydrate crystal form are obvious. As for the dihydrate crystal form of L-Val-L-Phe [12], the NH_3^+ and COO^- hydrogen-bond pattern is missing, all amino H atoms interact with guest water molecules, and the dipeptides organise themselves in a layered structure. Water molecules, aligned along the shortest b axis, play a crucial role in the solid-state assembly of this dipeptide. To help the reader and simplify the visualisation of the interactions established by water molecules, we decided to depict the guest interactions with different colours (**Figures 7.13**). As can be seen in **Figures 7.13 A-B**, O2W (orange) favours the dipeptides' alignment along the direction of the screw axis (interactions depicted in orange), while O1W (magenta) and O3W (green) are directly involved in the solid-state assembly along the a axis. In particular, water molecule O1W bridges together four dipeptides acting as an acceptor and donor of H-bonds. The presence of water molecules mediating peptide-peptide interactions is thus confirmed as a distinctive feature of non-gelling dipeptides, in agreement with Leu/Ile analogs [2,3]. The main host-host interaction favours the dipeptides' assembly along the b axis. Another weak hydrogen bond can be highlighted between the dipeptides aligned along the screw

axis, though its role is secondary considering the importance of the interaction with the water molecule O2W.

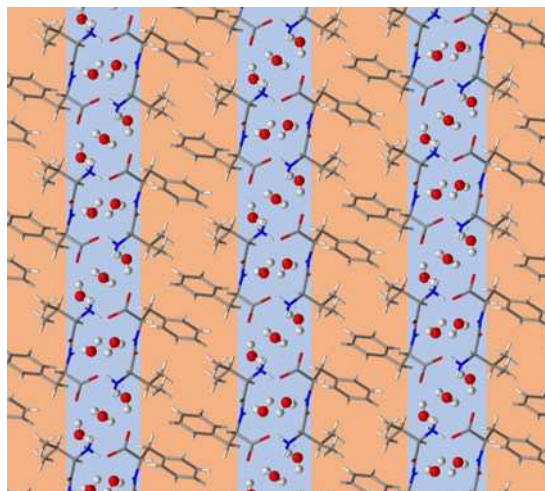


Figure 7.12. Amphipathic layers in crystal structure of D-Val-L-Phe (hydrophilic regions with solvent molecules are shown in light blue and hydrophobic areas in pink). Atom types: C grey, H white, O red, N blue. Water molecules are depicted in ball-and-stick style. Reproduced from Ref. [1] with permission from © 2022 Royal Society of Chemistry.

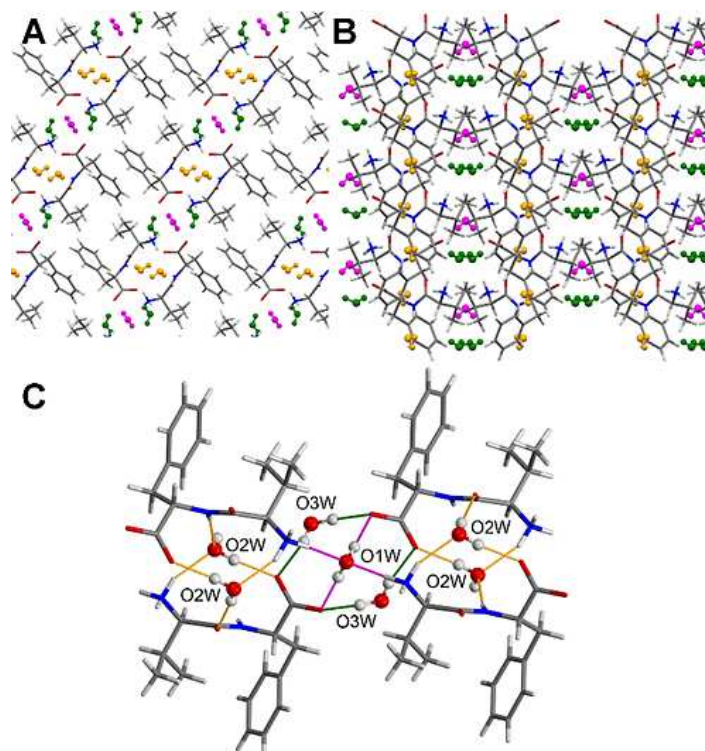


Figure 7.13. Single-crystal XRD data for D-Val-L-Phe (CCDC 2160976). A-B) Crystal packing along the *b* and *c* axes, respectively. (O1W in magenta, O2W in orange, O3W in green). C) Host-guest hydrogen bonds in crystal structure of D-Val-L-Phe (as viewed along the *b* axis). Reproduced from Ref. [1] with permission from © 2022 Royal Society of Chemistry.

7.7. Oscillatory rheology and thermoreversibility of D-Phe-L-Val and D-Val-L-Phe assembly

Oscillatory rheology confirmed the gel nature solely for samples of D-Phe-L-Val (**Figures 7.14-7.16**). Time sweeps confirmed the gelation reached a plateau within 500 seconds, with an elastic modulus G' of $1.23 \pm 0.12 \times 10^5$ Pa, at the mgc of 40 mM (**Figure 7.14**). Stress sweeps revealed a gel-to-sol transition at 34 ± 8 Pa (**Figures 7.16**).

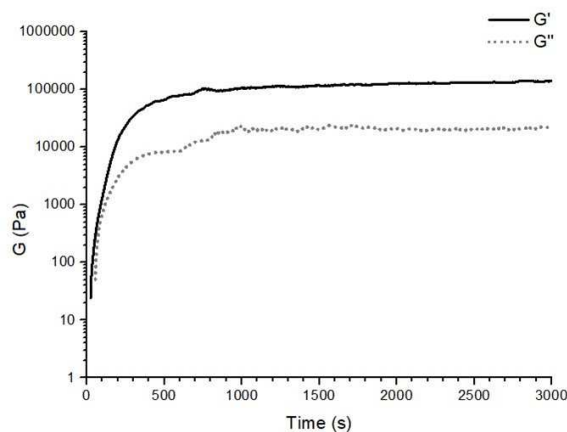


Figure 7.14. Time sweep of the hydrogelator D-Phe-L-Val at 40 mM Reproduced from Ref. [1] with permission from © 2022 Royal Society of Chemistry.

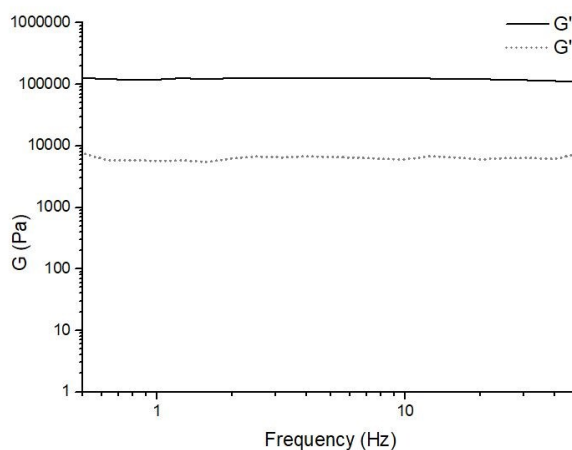


Figure 7.15. Frequency sweep of the hydrogelator D-Phe-L-Val at 40 mM (from 0.5 to 50 Hz). Reproduced from Ref. [1] with permission from © 2022 Royal Society of Chemistry.

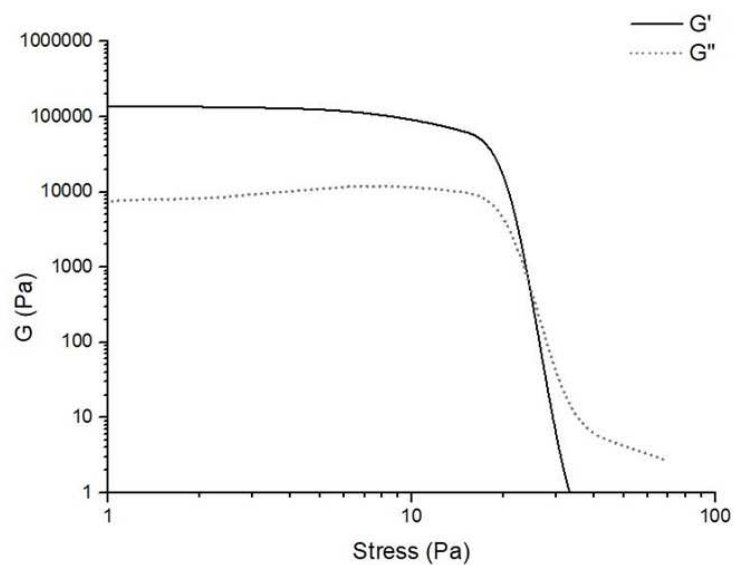


Figure 7.16. Stress sweep of the hydrogelator D-Phe-L-Val at 40 mM Reproduced from Ref. [1] with permission from © 2022 Royal Society of Chemistry.

Furthermore, the inability of D-Val-L-Phe to self-assemble into a hydrogel was also confirmed by time sweep analysis ($G' < G''$) performed on freshly prepared samples.

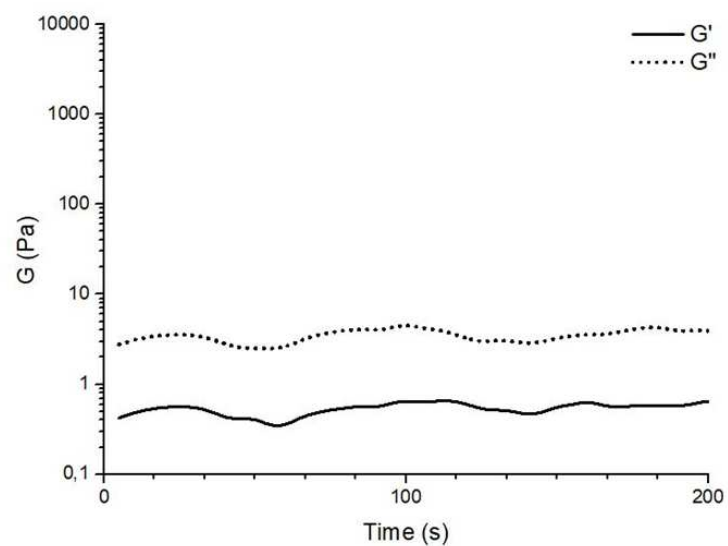


Figure 7.17. Time sweep of the D-Val-L-Phe at 40 mM. Reproduced from Ref. [1] with permission from © 2022 Royal Society of Chemistry.

The hydrogel D-Phe-L-Val was thermoreversible (**Figure 7.18**). The thermoreversibility propensity of the D-Phe-L-Val hydrogel at 40 mM was probed by the “water-bath test”. After 1 h of self-assembly, the hydrogel was kept in a water-bath and the water temperature was increased from 25 °C to 85 °C with a ramp of ~5 °C/min. Unfortunately, it was not possible to determine the melting temperature (T_m) by using also the CD with a temperature ramp up to 85 °C due to the scattering related to the high concentration of the sample (40 mM).



Figure 7.18. Thermoreversibility test for D-Phe-L-Val hydrogel with a melting temperature between 55-60 °C. Reproduced from Ref. [1] with permission from © 2022 Royal Society of Chemistry.

7.8. Biocompatibility assessment of D-Phe-L-Val

The hydrogel was thus tested *in vitro* for biocompatibility on fibroblast cell culture *in vitro* (**Figure 7.19**). First, a quantitative MTT assay was performed to assess the cytotoxicity of the D-Phe-L-Val in solution at different concentrations. 1 mM was considered the highest concentration to have the peptide still in solution, not in an assembled state. Overall, no cytotoxicity was observed at concentrations as high as 1 mM (**Figure 7.19**).

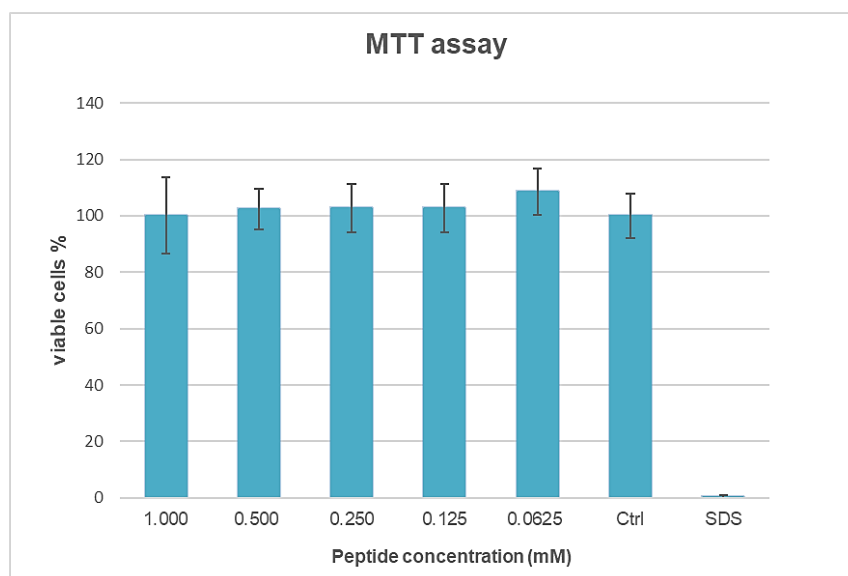


Figure 7.19. MTT assay on NIH/3T3 (fibroblast) cell line. The peptide was tested in solution at concentrations as high as 1 mM. Reproduced from Ref. [1] with permission from © 2022 Royal Society of Chemistry.

The opaque gel was also tested for live/dead fluorescence staining using a microwell assay (**Figures 7.20-7.21**). The combination of the two fluorescent dyes, acridine orange (AO) and propidium iodide (PI), allowed to evaluate simultaneously the presence of cells with intact and with compromised membrane, respectively, and their morphological features. Acridine orange (AO) and propidium iodide (PI) are responsible of the green and red fluorescence, respectively [45].

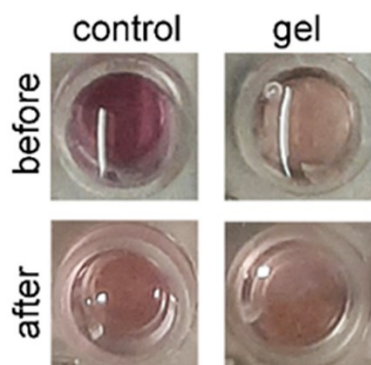


Figure 7.20. Photographs of representative wells with the hydrogel and media before and after cell culture. Reproduced from Ref. [1] with permission from © 2022 Royal Society of Chemistry.

High numbers of proliferative cells were found, with no significant differences in morphology relative to the control. The hydrogel after 24 h partially dissolved and lifted off the plastic, suggesting limited durability under cell culture conditions.

Interestingly, cells were found in high numbers inside the gel, also as it lifted off (**Figure 7.21**), as they grew preferentially inside its matrix as opposed to the plastic bottom. This finding is highly encouraging in terms of the biocompatibility of this type of scaffold, although for applications it may require enhanced durability.

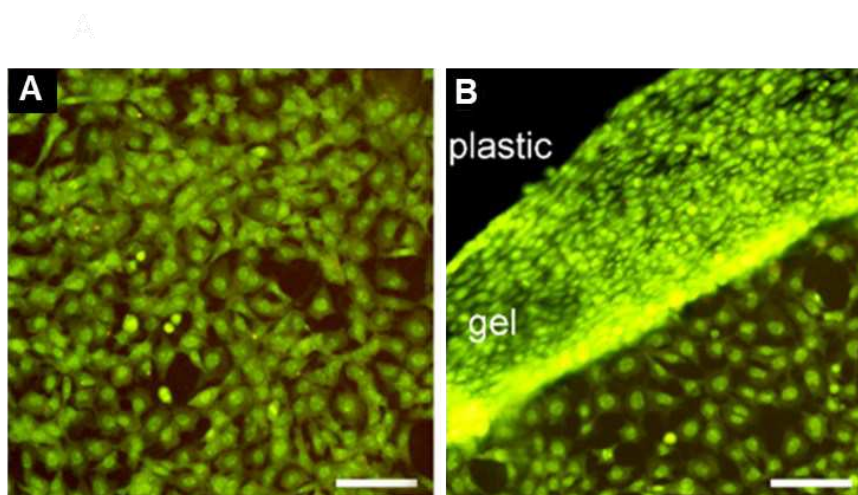


Figure 7.21. Fibroblast live/dead cell assay. A) control sample. B) hydrogel sample. Scale bar = 100 μm . Reproduced from Ref. [1] with permission from © 2022 Royal Society of Chemistry.

7.9. Conclusions

This work reveals for the first time that a Phe-Val dipeptide can self-assemble into water-channels and yield a microfibrillar gel with excellent biocompatibility *in vitro*. Until now, unprotected dipeptides' high hydrophilicity was considered a main limitation that hindered assembly of homochiral Val-Phe and Phe-Val, since hydrogelation required more hydrophobic sequences containing at least another carbon atom in the sidechain (*i.e.*, as in Leu/Ile). Interestingly, the hydrogel tested negative for the Thioflavin T amyloid stain, despite spectroscopic similarities with other heterochiral hydrophobic tripeptides with amyloid character.

Comparison with non-assembling isomer Val-Phe suggests hydrophobicity *per se* is not the only parameter to enable gelation, since the two isomers display almost identical HPLC retention times. Single-crystal XRD analyses confirmed that only D-Phe-L-Val self-assembled into water-channels whose inner cavity is defined by four peptide molecules connected head-to-tail. The ability to form water-channels is shared with D-Phe-L-Ile and D-Phe-L-Phe gelators, but not with non-gelling D-Ile-L-Phe, suggesting that the presence of Phe at the N-terminus of these heterochiral dipeptides as a favourable factor. However, D-Phe-L-Val is the first heterochiral dipeptide whose water-channels' inner cavity is defined by 4 peptide molecules, as opposed to the typical 6 in the other cases [3,9] thus demonstrating that it is possible to attain cavities of different size depending on the peptide sequence (*i.e.*, 0.95 nm for D-Phe-L-Ile, and 0.51 nm for D-Phe-L-Val). This finding is of potential interest to develop supramolecular channels that mediate selective transport of guests through membranes; this is becoming a hot topic for innovative therapies to target diseases as diverse as channelopathies and chronic pain [24]. Besides ion-channels, also water-transport is attracting interest as demonstrated by

aquaporin mimicry research for desalination and purification [25]. Further, the presence of water molecules mediating peptide-peptide interactions appears as a distinctive feature of non-gelling dipeptides, as previously found for tripeptides [17]. Conversely, gelling dipeptides display a continuous network of H-bonds between adjacent amide groups of stacked gelators. Overall, this study confirmed that heterochirality is an effective strategy to attain fibrillation and gelation from otherwise non-gelling dipeptides (*i.e.*, homochiral Phe-Val) into biomaterials with promising biocompatibility profile *in vitro*. As we advance our understanding of the design of these simple biomolecules to form water-channels and hierarchical assemblies into macroscopic and biocompatible soft materials, we anticipate future translation through the incorporation of bioactive sequences to guide cell fate.

References

- [1] O. Bellotto, G. Pierri, P. Rozhin, M. Polentarutti, S. Kralj, P. D'Andrea, C. Tedesco, S. Marchesan, *Org. Biomol. Chem.* **2022**, *20*, 6211-6218.
- [2] O. Bellotto, S. Kralj, R. De Zorzi, S. Geremia, S. Marchesan, *Soft Matter* **2020**, *16*, 10151–10157.
- [3] O. Bellotto, S. Kralj, M. Melchionna, P. Pengo, M. Kisovec, M. Podobnik, R. De Zorzi, S. Marchesan, *ChemBioChem* **2022**, *23*, e202100518.
- [4] L. Schnaider, S. Brahmachari, N. W. Schmidt, B. Mensa, S. Shaham-Niv, D. Bychenko, L. Adler-Abramovich, L. J. W. Shimon, S. Kolusheva, W. F. DeGrado, E. Gazit, *Nat. Commun.* **2017**, *8*, 1365.
- [5] B. Claro, E. González-Freire, M. Calvelo, L. J. Bessa, E. Goormaghtigh, M. Amorín, J. R. Granja, R. Garcia-Fandiño, M. Bastos, *Colloids Surfaces B Biointerfaces* **2020**, *196*, 111349.
- [6] S. Fernandez-Lopez, H. S. Kim, E. C. Choi, M. Delgado, J. R. Granja, A. Khasanov, K. Kraehenbuehl, G. Long, D. A. Weinberger, K. M. Wilcoxon, M. R. Ghadiri, *Nature* **2001**, *412*, 452–455.
- [7] J. Lerner Yardeni, M. Amit, G. Ashkenasy, N. Ashkenasy, *Nanoscale* **2016**, *8*, 2358–2366.
- [8] R. Piotrowska, T. Hesketh, H. Wang, A. R. G. Martin, D. Bowering, C. Zhang, C. T. Hu, S. A. McPhee, T. Wang, Y. Park, P. Singla, T. McGlone, A. Florence, T. Tuttle, R. V. Ulijn, X. Chen, *Nat. Mater.* **2021**, *20*, 403–409.

- [9] S. Kralj, O. Bellotto, E. Parisi, A. M. Garcia, D. Iglesias, S. Semeraro, C. Deganutti, P. D'Andrea, A. V. Vargiu, S. Geremia, R. De Zorzi, S. Marchesan, *ACS Nano* **2020**, *14*, 16951–16961.
- [10] N. S. De Groot, T. Parella, F. X. Aviles, J. Vendrell, S. Ventura, *Biophys. J.* **2007**, *92*, 1732–1741.
- [11] M. Kurbasic, S. Semeraro, A. M. Garcia, S. Kralj, E. Parisi, C. Deganutti, R. De Zorzi, S. Marchesan, *Synthesis (Stuttg.)* **2019**, *51*, 2829–2838.
- [12] C. H. Görbitz, *Acta Crystallogr. Sect. B* **2002**, *58*, 512–518.
- [13] C. H. Görbitz, *Acta Crystallogr. Sect. C* **2000**, *56*, 1496–1498.
- [14] H. L. Bolt, C. E. J. Williams, R. V Brooks, R. N. Zuckermann, S. L. Cobb, E. H. C. Bromley, *Pept. Sci.* **2017**, *108*, e23014.
- [15] N. Amdursky, M. M. Stevens, *ChemPhysChem* **2015**, *16*, 2768–2774.
- [16] A. M. Garcia, D. Iglesias, E. Parisi, K. E. Styan, L. J. Waddington, C. Deganutti, R. De Zorzi, M. Grassi, M. Melchionna, A. V. Vargiu, S. Marchesan, *Chem* **2018**, *4*, 1862–1876.
- [17] A. M. Garcia, M. Melchionna, O. Bellotto, S. Kralj, S. Semeraro, E. Parisi, D. Iglesias, P. D'Andrea, R. De Zorzi, A. V Vargiu, S. Marchesan, *ACS Nano* **2021**, *15*, 3015–3025.
- [18] V. Castelletto, P. Ryumin, R. Cramer, I. W. Hamley, M. Taylor, D. Allsop, M. Reza, J. Ruokolainen, T. Arnold, D. Hermida-Merino, C. I. Garcia, M. C. Leal, E. Castaño, *Sci. Rep.* **2017**, *7*, 43637.
- [19] N. Amdursky, Y. Erez, D. Huppert, *Acc. Chem. Res.* **2012**, *45*, 1548–1557.
- [20] M. Biancalana, K. Makabe, A. Koide, S. Koide, *J. Mol. Biol.* **2009**, *385*, 1052–1063.
- [21] D. Iglesias, M. Melle-Franco, M. Kurbasic, M. Melchionna, M. Abrami, M. Grassi, M. Prato, S. Marchesan, *ACS Nano* **2018**, *12*, 5530–5538.
- [22] B. Lekprasert, V. Korolkov, A. Falamas, V. Chis, C. J. Roberts, S. J. B. Tandler, I. Notingher, *Biomacromolecules* **2012**, *13*, 2181–2187.
- [23] C. H. Görbitz, *Chem. – A Eur. J.* **2007**, *13*, 1022–1031.
- [24] G. Picci, S. Marchesan, C. Caltagirone, *Biomedicines* **2022**, *10*, 885.
- [25] L.-B. Huang, M. Di Vincenzo, Y. Li, M. Barboiu, *Chem. – A Eur. J.* **2021**, *27*, 2224–2239.

Chapter 8. Conclusions

In this thesis, the self-assembly of a Phe derivative, and of all non-enantiomeric regioisomers and stereoisomers of dipeptides with Phe and Leu, Ile, or Val, has been described. *N*-(4-nitrobenzoyl)-Phe proved to be an interesting minimalistic hydrogelator that forms parallel stacks and yields hydrogels with promising biocompatibility *in vitro* and mild antibacterial activity against *E.coli*. The antibacterial activity was observed to be present also in solution, thus not being ascribed to the supramolecular structure, but possibly being due to the amphipathic character of the compound, which may interfere with membrane organization as observed for similar analogs. Further biochemical tests should however verify this hypothesis, for instance by looking at membrane disruption events through standard fluorescence assays.

Interestingly, heterochiral Phe-Phe demonstrated to be able to form water-channels analogously to its homochiral stereoisomer, maintaining the backbone conformation, albeit with a different spatial organization of the side chains. As a result, the aromatic rings of the heterochiral Phe-Phe can engage in intramolecular interactions at the expense of intermolecular ones, thus hindering hierarchical assembly into toxic microtubes, and stabilizing instead 4-nm wide nanotubes defined by two layers of peptides and with promising biocompatibility *in vitro*. This supramolecular arrangement also in the gel phase has been confirmed by a plethora of techniques, including single-crystal and powder XRD analysis of the crystals and gels, respectively, as well as electron microscopy (*i.e.*, TEM) and Raman microspectroscopy.

Mono-halogenation of Phe-Phe at the N-terminus has a modest effect on the supramolecular packing relative to that at the C-terminus. In particular, N-terminal fluorination at any position on the aromatic ring of Phe maintained the ability of heterochiral Phe-Phe to self-assemble into nanotubes, albeit with differing degrees of bundling. By contrast, iodination hindered water-channel formation, although it maintained the gelation ability. Conversely, monohalogenation of the C-terminus maintained the ability to gel solely for the compounds fluorinated in the *ortho* or *para* positions of Phe, while the *meta* fluorinated and *para* iodinated analogs self-assembled into crystals, as opposed to gels. The data acquired indicated that the differing supramolecular behavior of this series is not simply ascribed to differing magnitude and/or orientation of the molecular dipole moment, but more likely it is ascribed to more complex electronic effects. It is plausible that the two gelators fluorinated at the C-terminus maintained the ability to form water channels displayed by the N-terminal fluorinated analogs, although this hypothesis unfortunately could not be unambiguously proven by the data acquired, especially due to the lack of single-crystal XRD data, despite the great efforts spent at crystallising

this compounds that constantly gelled instead. In any case, all halogenated compounds demonstrated poorer biocompatibility *in vitro* relative to the non-halogenated parent D-Phe-L-Phe.

Substitution of Phe with an aliphatic amino acid, such as Leu, Ile, or Val, maintained the ability to form water-channels and hydrogels, albeit not in all cases. In particular, heterochirality increased the molecular hydrophobicity as experimentally measured by HPLC retention times. This trend was key to enable hydrogelation and water-channel formation for heterochiral Phe-Val, in contrast with all the other analogs of this series. Homochiral Phe-Val and Val-Phe were too hydrophilic to fibrillate.

In the case of dipeptides with Leu, all gelled except for heterochiral Leu-Phe. Homochiral Phe-Leu and Leu-Phe formed water channels whose diameter were defined by four dipeptide molecules, analogously to D-Phe-L-Val. Hydrogelation withing this series was ascribed to the ability of the dipeptides to adopt an amphipathic conformation with net segregation between hydrophilic and hydrophobic components, and to establish 1) steric zippers between the hydrophobic amino acid sidechains, to exclude water from such dry surfaces that stabilized the supramolecular architecture, and 2) an extended H-bond network established directly between peptide molecules without the intermediation of water.

These latter two features were confirmed in the case of the dipeptide series with Phe and Ile. However, in this series, only one compound gelled, and did so by forming water channels whose diameter was deinfed by 6 peptide molecules, analogously to Phe-Phe. Clearly, the branching of the sidechain closer to the backbone (*i.e.*, in the β -carbon, as opposed to the γ -carbon as in Leu) was a discriminant factor that impeded self-assembly in most cases. Furthermore, the hydrogel formed by D-Phe-L-Ile demonstrated a good biocompatibility *in vitro*, although also limited durability in cell culture conditions, analogously to the other dipeptide gels.

Finally, all heterochiral dipeptides with Phe at the N-terminus formed metastable hydrogels that over time underwent a phase transition into crystals. The plethora of data acquired unfortunately did not allow to clearly pinpoint the reasons behind this observation, although it is worth noting that self-assembly is a cooperative process whereby minimal structural differences in the molecular building blocks are amplified in a way that is difficult to predict. For the future, it will be interesting to analyse the self-assembling behavior of analogs with linear sidechains, as the non-natural norvaline and norleucine, to better discriminate supramolecular effects arising from the different atom connections between the amino acid regioisomers with butyl or propyl sidechains.

Interestingly, the ability of dipeptides to form water channels with differing diameters defined by either 4 or 6 peptide molecules (*i.e.*, ca. 0.4 or 1.0 nm) is an interesting feature that in the future could be further exploited to functionalize the building blocks towards the design of stabilized channels for membrane insertion and able to translocate not just water, but ideally also ions, depending on the

functionalization. Potential applications are varied, and could be envisaged to span from innovative therapeutic means to address pathologies with altered membrane transport, to antimicrobial agents, and membranes for water purification. Dynamic covalent chemistry could offer a valuable strategy for the stabilization of the channels, and selectivity not only of the guest to transport, but also of the cells where they insert will represent key challenges to overcome, to provide innovative solutions in this exciting field.

Chapter 9. Materials & Methods

“This Chapter describes solely the methods for the experiments that I carried out myself. The other methods, carried out by the co-authors on our joint publications, can be found in the corresponding scientific articles or supplementary information.”

Manuscript 1. “Self-assembly of an amino acid derivative into an antimicrobial hydrogel biomaterial” described in Chapter 3.

1.1. Peptide self-assembly

The hydrogel was prepared in phosphate buffer saline (PBS) by dissolving a tablet (#P4417 from Sigma-Aldrich) according to the manufacturers' instructions. The sample with the hydrogelator at a final concentration of 20 mM was heated until complete dissolution and the gel was formed upon cooling down to room temperature with a final pH of 6.0 ± 0.2 . The PBS solution was filtered ($0.2 \mu\text{m}$) prior to use. For cell culture assays, the PBS solution was first brought to a pH of 11.8 by addition of NaOH; subsequent dissolution of the gelator lowered the pH to 7.3 ± 0.2 .

1.2. Cytotoxicity assay

To test the potential bio-applications of the hydrogel, a qualitative assay (*live/dead*) was performed on relevant cell types, *i.e.*, fibroblast and keratinocytes. This assay allows to test the toxicity of the material once in contact with living cells.

Dulbecco's Modified Eagle's Medium (DMEM), fetal bovine serum (FBS), the antimycotics and antibiotics (*i.e.*, Streptomycin and Streptavidin) were purchased from GIBCO. Trypan blue dye was purchased from Merck. Cell lines were kindly provided by the Life Sciences Dept. of the University of Trieste (Italy), in collaboration with the prof. Antonella Bandiera and researcher Sabrina Semeraro.

1.2.1. Trypan blue test for cell viability and cell count

All the solutions used were purchased sterile or they were sterilized with $0.2 \mu\text{m}$ filter prior to use. Before performing each experiment, the cells were counted to seed the fixed number of cells at the same density in each well. The cells were provided with standard DMEM (Dulbecco's Modified Eagle's Medium) supplemented with 10% fetal bovine serum (FBS) and 2% antimycotic and antibiotic and cultured into a 25 cm^2 or 75 cm^2 culture flask (T-25 or T-75 flask) in suitable incubator (37°C , 5% CO_2 , 95% air) until 80% confluence. At the confluent state, the culture medium was removed from the culture flask and the latter was briefly rinse with PBS (Phosphate buffer saline) for cell culture to remove all traces of medium. After removing the medium, cells were harvested from

the culture flasks by incubation with 0.5 mL or 1 mL of 0.05% Trypsin-EDTA (from GIBCO) for 3 min at 37 °C. To inactivate the trypsin, the cells were then re-suspended with complete growth medium and centrifugated at 9x10000 rpm for 4 min. After removing the supernatant, the cell pellet was resuspended in 1 mL of fresh medium and then moved into an Eppendorf tube before the cell counting through trypan blue exclusion test of cell viability. 10 µL of this cell suspension were diluted with 90 µL and 10 µL of the trypan blue dye, by performing a dilution 1 to 2 and 1 to 10, respectively. Finally, 10 µL of each cell-dye solution, were moved inside the Bürker cell counting chamber (**Figure 1.1.**), one at the top and the other at the bottom of the chamber, and the cells were counted by an inverted optical microscope (*Leitz Labovert instrument*) with 6x objective. The use of trypan blue dye allows to count the cell number and to assess cell viability as well. Indeed, the trypan blue exclusion test is based upon the principle that living cells with intact membrane do not take up impermeable dyes while dead cells cannot exclude the dye and will appear blue.

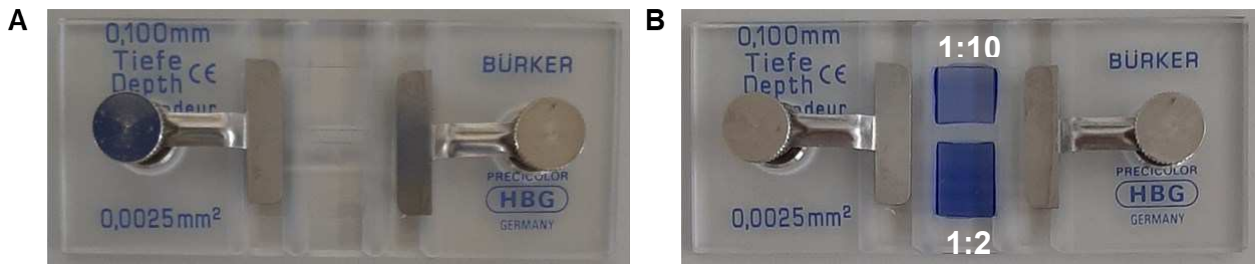


Figure 1.1. Bürker cell counting chamber used for these experiments before the count (A) and after the addition of the cells-dye solutions to be analyzed (B).

The Bürker cell counting chamber, reported in **Figure 1.2.**, consists of 9 large squares (3x3) (1 mm² each) and each of them is divided into 16 small squares through double lines. Such double lines form small 0.0025 mm² squares, and the depth of the cell chamber is 0.1 mm. The cell count is usually performed by the following procedure. Briefly, after adding 10 µL of each cell-dye solution prepared (1:2 and 1:10) at the top and at the bottom of the chamber respectively, the cells were count in each of the large squares (identified by the triple line). At the end of the count, the average of the readings was done, and the total cell concentration was calculated as follows: [1]

$$\frac{[Cell]}{mL} = \frac{[\Sigma \text{ cell counted in } x \text{ large squares}]}{x \text{ large squares}} \times (\text{dilution factor}) \times (V) \times 10^4$$

x = number of large squares considered; V = cell suspension volume in fresh medium; 10^4 = factor of conversion from µL to mL

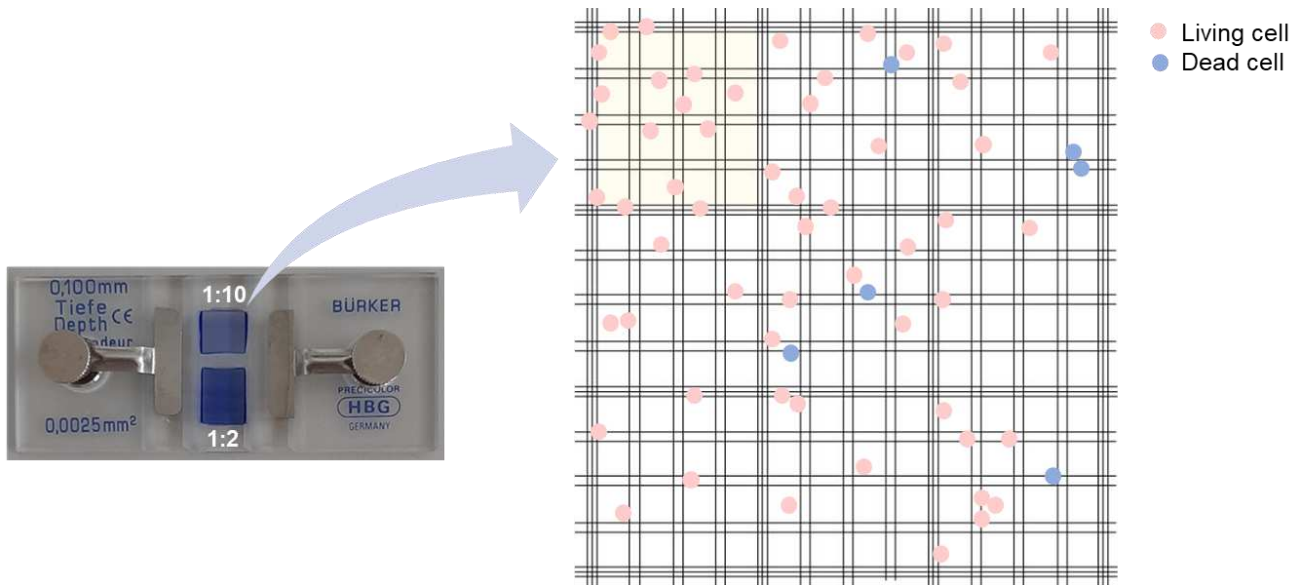


Figure 1.2. Photograph of the Bürker cell counting chamber after the addition of the trypan blue dye (*left*) and its magnification for the dilution 1:10 (*right*). In yellow, one of the 9 large squares.

1.2.2. Live/Dead assay

For all the experiments described in the *Manuscript 1 (Chapter 3)*, the hydrogel was prepared in phosphate buffer saline (PBS, 0.1M) by heating the sample until complete dissolution at a final concentration of 20 mM. After this, the gel was formed upon cooling the solution down to room temperature with a final pH of 6.0 ± 0.2 . For cell culture assays, the experimental procedure of the hydrogel preparation was slightly modified to achieve sterility and promote cell growth. First, the PBS buffer used for biological assays was filtered ($0.2 \mu\text{m}$) prior to use and then the PBS solution was brought to a pH of 11.8 by addition of NaOH (1M); subsequent dissolution of the gelator lowered the pH to 7.3 ± 0.2 . The hydrogel was prepared by following the above procedure directly inside a triplicate well of a “ μ -Slide angiogenesis” slide uncoated (Ibidi, Germany) under a laminar-flow cabinet and left at room temperature overnight to achieve a complete self-assembly. Before the cell addition (10 000 cells/ μ -well), the hydrogel was pre-treated with culture medium for 1 h, for removing salts and preparing a biomaterial more suitable for cell growth. Considering the inner capacity of μ -each microwell, 20 μL of hydrogel/ μ -well and 30 μL of cells suspension/ μ -well were considered the optimal volumes to use, both to have enough material to test and to allow the cells to growth properly. After 24 h, gels were pre-treated with 30 μL of media (DMEM + 10 % fetal serum albumin, and 2 % antimycotic and antibiotic from GIBCO) for 1 h. Next, the medium was removed and HaCaT (keratinocytes) or NIH3T3 (fibroblast) cells were added to the gels (10,000 cells per well, 30 μL media), and cultured at 37°C , 5% CO_2 for 24 h, by handling the slides according to the manufacturers’ instructions. Cell viability was investigated using acridine orange (5 μL /well of a 20 μM solution in

50 mM PBS) and propidium iodide (5 μ l/well of a 30 μ M solution in 50 mM PBS). Cells were imaged on an inverted microscope (Nikon Eclipse TiU) with green and red filters and a 40x objective (N.A. 0.6).

Manuscript 2. “Heterochirality and Halogenation Control Phe-Phe Hierarchical Assembly” described in Chapter 4.

2.1. D-Phe-L-Phe synthesis

Peptide was synthesized on solid-phase by using standard protocol for Fmoc-protected amino acids (Sigma-Aldrich, Italy). All solvents were purchased of peptide-synthesis grade from Merck (Italy). O-Benzotriazole-N, N,N,N'-tetramethyl-uronium-hexafluoro phosphate (HBTU) as coupling agent, 2-chlorotriyl chloride resin and D-phenylalanine were obtained from GL Biochem (Shanghai, China). 1-Hydroxy-7-azabenzotriazole (HOAt) was purchased from ChemPep (Wellington, FL. U.S.A.). All the other chemicals were obtained from Merck (Italy). Milli-Q water (MQ water) was collected from a Millipore RiOs/Origin apparatus with a resistivity greater than 18 M Ω cm.

2.1.1. Loading of the first amino acid on the resin

1 g of resin 2-Chlorotriyl chloride resin (loading: 1.6 mmol Cl-/g resin, mesh size:100-200 mesh) was put into a plastic reaction vessel where it was swelled using dichloromethane (DCM) for 15 minutes. After the swelling, the resin was activated by the addition of 100 μ L of thionyl chloride (SOCl₂) in DCM and left to react with a gentle stirring for 1 hour. After that time, the solution was removed from the plastic vessel and the resin has been accurately washed with DCM and N, N-Dimethylformamide (DMF) at least three times. Fmoc-amino acid (1.6 mmol) of the C-terminus was dissolved in a mixture of DCM/DMF (50:50) and 0.9 mL of N, N-Diisopropylethylamine (DIPEA). All the peptide solution was added to the activated resin and left under stirring for 1.5 h at room temperature. After this time, the solution was removed, and 0.5 mL of methanol was added to cap eventually unreacted resin to avoid the formation of side products. The capping required 10 minutes and a mild stirring. Then, the resin was filtered and washed with DMF and DCM at least three times.

Before performing the Fmoc deprotection, the amount of the first amino acid loaded on the resin was calculated by using the following protocol. Three samples of the loaded resin (5-10 mg/each) were transferred and weighted in Eppendorf tubes. After drying the resin overnight, 1mL of a fresh Fmoc-deprotection solution (Piperidine 20% in DMF) was added to each sample to remove the Fmoc group from the loaded amino acid. After for 20 minutes of shaking at room temperature, each sample was centrifuged for 5 minutes at 12.000 rpm and 100 μ L of supernatant were taken from each Eppendorf

tube and transfer into glass vials containing 10 mL of DMF (dilution 1:100). The absorbance of each solution was measured three times and at the same wavelength ($\lambda = 301$ nm), corresponding to the maximum absorption wavelength of the chromophore dibenzofulvene-piperidine adduct in solution. Absorbance measurements were performed by means of a UV spectrophotometer, with a 1 cm cuvette and considering DMF solvent for the baseline.

Substitution of Fmoc-amino acid loaded on the resin was calculated for each sample according to the formula below: ^[2]

$$\text{Substitution (mmol/g)} = (101 * \text{Abs } 301\text{nm}) / (7.8 * m \text{ resin})$$

* Derived from:

$$\text{SFmoc (mmol/g)} = (\text{Abs } 301\text{nm} * 10^6 \text{mmol} * \text{mol}^{-1} * \text{mg} * \text{g}^{-1} * V * D) / \epsilon m_{\text{Resin}} * l$$

Where,

SFmoc = Fmoc substitution (mmol/g)

ϵ = Molar absorption coefficient of dibenzofulvene–piperidine adduct at 301 nm = 7800 L mol⁻¹ cm⁻¹

Abs = Absorption of the sample solution at 301 nm

m_{Resin} = Sample weight of the resin (in mg)

$10^6 \text{ mmol mol}^{-1} \text{ mg g}^{-1}$ = Factor for conversion of mol to mmol and mg-1 to g-1

V = Sample volume (in L)

l = Optical path length of the cell in cm (1 cm)

D = Dilution factor

2.1.2. N-terminal Fmoc group deprotection

After completing the loading, the N-capping group (Fmoc) was removed from the first amino acid by treating the resin with 20 % (v/v) piperidine in DMF for 7 minutes under mildly stirring and this step was repeated twice. After that, the resin was washed with DMF and DCM for at least three times. The same procedure has been repeated after the coupling of each amino acid during the peptide synthesis.

2.1.3. Colorimetric tests

To monitor both Fmoc removal from loaded amino acid and coupling reactions of the following ones, two colorimetric tests were performed: bromophenol blue and acetaldehyde/chloranil test.

2.1.3.1. Bromophenol blue test

This colorimetric test is an immediate test to detect all types of amines and for such reason it has to be performed very carefully. After each washing of the resin, traces of basis (*i.e.*, DIPEA or collidine) or acid has to be removed very well because they can provide false negative results. [3]

- *Test solution*: 0.05% bromophenol blue in DMF (stored at 4°C for one month maximum)

A few beads of the resin were placed in a small test tube and a few drops (2-5 drops) of the test solution were added. After a short mixing, the mixture was left at room temperature for few seconds and the color of the resin beads was immediately inspected with visual test or under an optical microscope.

Results:

- Positive (free amine): Dark blue beads
- Negative: Colourless beads

2.1.3.2. Acetaldehyde/chloranil test

This is a highly sensitive colorimetric test, and it has been developed for reliable detection of secondary amino groups, but it is also used to detect the presence of primary amines. [4]

- *Solution 1*: 2% acetaldehyde in DMF (stored at 4°C for one month maximum)
- *Solution 2*: 2% chloranil in DMF (stored at 4°C for one month maximum)

A few beads of the resin were placed in a small test tube and a few drops (2-5 drops) of each test solution were added sequentially. The test tube was mildly shaken and after 5 minutes, the beads were inspected with visual test or under an optical microscope.

Results:

- Positive (free amine): Dark blue to green beads
- Negative: Colourless to yellowish

2.1.4. Coupling of the second amino acid

After the loading of the first amino acid and the deprotection step of the Fmoc-protecting group, the coupling of the following amino acid was performed.

3 equivalents of the second Fmoc-amino acid were dissolved in DMF in presence of 2 equivalents of both HOAT and HBTU. After the complete dissolution of the reagents, 2 mL of a 1M DIPEA in DMF for every equivalent of loaded amino acid on resin were added to the mixture. After few minutes of pre-activation, the solution was added to the resin into the plastic reaction vessel and the reaction was left under mild stirring at room temperature for 1.5 hours. After that time, the resin was filtered and

accurately washed with DMF and DCM, for at three times. The Fmoc-group was rapidly removed from the resin by treating it with 20% piperidine (v/v) in DMF for 7 minutes. The deprotection step was repeated twice. After that, the resin was filtered again and finally washed again with DMF and DCM, for at least three times. For a further elongation of the peptide chain, the same protocol for amino acid coupling, colorimetric test and Fmoc-deprotection should be repeated.

2.1.5. Cleavage of the dipeptide from the resin

The purpose of this step is to cleave the peptide from the resin as well as remove side chain protecting groups eventually remained (*i.e.*, trityl from cysteine thiol group in cysteine containing peptides).

Considering the use of the 2-chlorotryityl chloride resin, 20 mL of the cleavage cocktail solution was prepared using 49.5% TFA, 49.5% DCM, with 0.5 % TIPS (Triisopropylsilane) and 0.5% of milli-Q water as scavengers. Indeed, during the reaction highly reactive carbocations might be generated and they have to be trapped as to avoid undesired reactions. The fresh prepared cleavage solution was added to the resin and left under gentle stirring at room temperature for 2 hours. After the reaction time, the solution containing the crude peptide was filtered from the resin in a glass tube and the resin was washed twice with further fresh cleavage cocktail. The peptide cleaved from the resin was collected in a glass tube and left to evaporate overnight under air. After the complete evaporation of the TFA in solution, the obtained oil was dissolved in the HPLC mixture (70/30, H₂O/MeCN) containing 0.05% TFA and filtered with filter 0.45 µm PTFE filter before the purification through RP-HPLC.

2.2. Peptide purification and characterization

The crude peptide was purified by reverse-phase HPLC using a semipreparative C18-column (Kinetex, 5 µm, 100 Å, 250 × 10 mm, Phenomenex) on an Agilent 1260 Infinity apparatus with a photodiode array detector (G1315C), and autosampler (G1329B). Acetonitrile (MeCN)/water with 0.1% TFA was used as an eluent mixture with the following program: t = 0–2 min. 30% MeCN; t = 12 min. 55% MeCN; t = 15 min. 95% MeCN. The product fractions were lyophilized and analyzed for identity and purity by LC-MS using an Agilent 6120 single quadrupole system. ¹H-NMR and ¹³C-NMR spectra were registered on a Varian Innova Instrument with chemical shift reported as ppm (in DMSO with tetramethylsilane as internal standard).

2.3. Peptide self-assembly

Dipeptides were dissolved at various concentrations (2× the final concentration indicated in the manuscript for the various tests) in alkaline sodium phosphate buffer (0.1 M, pH 11.8) with the aid of sonication in a Branson ultrasound bath 40 kHz at room temperature. Hydrogelation was then triggered by lowering the pH of the solution to physiological neutral (7.3 ± 0.1) with the addition of an equal volume of a mildly acidic sodium phosphate buffer (0.1 M, pH 5.8). All buffer solutions were filtered (0.2 μm) prior to use.

2.4. Cytotoxicity assay

Different biological assays both qualitative and quantitative (live/dead and MTT) were performed to test the hydrogels' cytotoxicity and to discover the most promising peptide-based biomaterials.

2.4.1. Trypan blue test for cell viability and cell count

The test was performed by following the same protocol previously reported at the point 1.2.1.

2.4.2. Live/Dead assay

All solutions were sterilized with 0.2 μm filter prior to use and gels were prepared by following the procedure indicated above. Each gel (20 μL /well) was carefully formed in the microwells of a μ -Slide for Angiogenesis uncoated slide (Ibidi, Germany) according to the manufacturer's instructions and left at room temperature for 24 h. Thirty microliters of culture media (DMEM + 10% fetal serum albumin, and 2% antimycotic and antibiotic from GIBCO) was added on the top of each gel for 1 h. The solution was then carefully removed and NIH3T3 fibroblasts were added to the gels (10 000 cells per well, 30 μL of media), and cultured at 37 °C, 5% CO₂ for 24 h, by handling the slides according to the manufacturers' instructions. Cell viability was analyzed by using acridine orange (5 μL /well of a 20 μM solution in 50 mM PBS) and propidium iodide (4 μL /well of a 30 μM solution in 50 mM PBS) as dyes. After 15 min of incubation at 37 °C, cells were imaged with a Leica microscope (DFC450C; software LASV4.13) with bright-field and fluorescence green filter (ex. 450–490 nm, em. > 520 nm) with 10× and 40× objectives. Each condition was repeated at least in triplicate, and the experiment was repeated twice.

2.4.3. MTT Assay

HaCaT cells (keratinocytes) were seeded (10 000 cells per well) on 96-well microplates (tissue-culture grade, clear, flat bottom) in 100 μL of medium (DMEM+ 10% FCS, and 2% antimycotic and antibiotic) and incubated overnight at 37 °C and 5% CO₂. The medium was removed and exchanged with 100 μL of medium with 2% DMSO and serial dilutions of each peptide concentration. One

percent SDS served as positive control (death). Cells were cultured for 24 h, then 10 μL of the MTT labeling reagent (Sigma, 0.5 mg mL^{-1}) was added, and the microplate was incubated for 4 h in a humidified atmosphere (37 $^{\circ}\text{C}$, 5% CO_2). Next, 100 μL of the solubilization solution for formazan crystals (4 mM HCl + 0.1% IGEPAL in isopropanol) was added to each well, and the microplate was kept at RT under shaking (Rocker-Shaker MR-12 Biosan, Vetrotecnica) for 30 min. After visual inspection for complete solubilization of the purple formazan crystals, the absorbance was read at 570 nm with a reference wavelength of 690 nm (light scattering) using a microplate (ELISA) reader (Synergy H1 Hybrid reader BioTeK). Three independent experiments were run in duplicate ($n = 6$).

Manuscript 3. “Single-atom substitution enables supramolecular diversity from dipeptide building blocks” described in Chapter 4.

3.1. Peptide self-assembly into hydrogels or crystals

Each peptide was dissolved in sodium phosphate buffer (0.1 M, pH 11.8). An equal volume of acidic sodium phosphate buffer (0.1 M, pH 5.8) was added to reach the final concentration.

3.2. Oscillatory rheology

Hydrogels were prepared in situ using a Kinexus Plus rheometer (Malvern) with a stainless-steel parallel plate geometry. Each experiment was performed with a 1 mm gap at 25 $^{\circ}\text{C}$ (Peltier). Time sweeps were measured at 1 Pa and 1 Hz, frequency sweeps were measured at 1 Pa and stress sweeps were measured at 1 Hz. Each sample was analysed at least three times.

3.3. Transmission Electron Microscopy (TEM)

Samples were prepared as described above at their mgc for 2-F and 4-F and at 10 mM (3-F) or 4 mM (4-I). They were transferred onto TEM carbon grids previously exposed to a UV-Ozone Procleaner Plus for 5 min. A drop of aqueous tungstate phosphate solution (pH 7.2) was added as the contrast agent and all the samples were dried in vacuo. TEM images were acquired using a Jeol JEM 2100 microscope (Japan) at 100 kV and analysed using the FIJI free software.

3.4. Circular dichroism (CD) spectroscopy

Peptides were dissolved at the desired concentration (1 mM for 2-F, 3-F and 4-F; 0.1 mM for 4-I) using the method described above. Samples were placed in a 0.1 mm quartz cuvette on a Jasco J-815 spectropolarimeter at 25 $^{\circ}\text{C}$ (Peltier), with a 1 nm resolution. 5–10 spectra were averaged to reduce noise. CD spectra were also acquired at higher concentrations to monitor evolution upon assembly. Precisely, for 2-F at 5 mM and 4-F at 14 mM.

3.5. Attenuated Total Reflectance (ATR) Infrared Spectroscopy

Samples were prepared at their mgc for the two gelators (7 mM for 4-F and 15 mM for 2-F) or above their solubility limit for 3-F (10 mM) and 4-I (4 mM) and left to dry under vacuum overnight using a 1 cm² piece of silicon wafer for ATR or on a glass slide for Raman. ATR-IR spectra were acquired using an IRAffinity-1S spectrophotometer (Shimadzu) at 4 cm⁻¹ resolution and 240 scans.

3.6. Single-crystal XRD data

Single crystals of **3-F** (CCDC 2130532) and **4-I** (CCDC 2130533) were obtained upon assembly as described above (see point 3.1.). The two dipeptides, D-Phe-L-(3-F)-Phe and D-Phe-L-(4-I)-Phe, after the sample preparation were not able to form a gel and consistently crystallized.

Deposition numbers **2130532** and **2130533** refer to the crystallographic data deposited at the Cambridge Crystallographic Data Centre (CCDC).

Manuscript 4. “Supramolecular hydrogels from unprotected dipeptides: a comparative study on stereoisomers and structural isomers” described in Chapter 5.

4.1. Peptide synthesis

Each dipeptide was synthesised by standard solid-phase methods (SPPS). 2-chlorotrityl resin, O-Benzotriazole-N,N,N,N'-tetramethyluronium-hexafluoro-phosphate (HBTU), and Fmoc protected amino acids were purchased from GL Biochem (Shanghai) Ltd. All solvents were purchased from Merck, at analytical grade. Piperidine, trifluoroacetic acid (TFA), N,N-diisopropyl ethylamine (DIPEA), triisopropyl silane (TIPS) were from Acros. Sodium dihydrogen phosphate and disodium hydrogen phosphate were from BDH AnalaR. High purity Milli-Q-water with a resistivity greater than 18 M Ω cm was obtained from an in-line Millipore RiOs/Origin system.

The synthesis was performed by following the same procedures previously reported from the point 2.1.1. to 2.1.5.

4.2. Peptide purification

Each peptide was purified by reverse-phase HPLC. The method used consisted of a mixture of MeCN/water with 0.05% trifluoroacetic acid, 3 ml/min, solvent gradient: 0–3 min 25% MeCN, 16 min 95% MeCN using a C-18 column (Kinetex, 5 μm, 100 Å, 250×10 mm, Phenomenex).

4.3. Peptide characterization

¹H-NMR and ¹³C-NMR spectra were recorded at 400 MHz and 100 MHz, respectively, on a Varian Innova Instrument with chemical shift reported as ppm (in DMSO with tetramethylsilane as internal standard). ESI-MS spectra were recorded on an Agilent 6120 single quadrupole LC-MS system, by using water/MeCN gradient system from 5% to 95% MeCN with 0.1% formic acid over 17 min, flow of 0.3 ml/min and an analytical C-18 column (Luna, 5 μm, 100 Å, 150 x 2 mm, Phenomenex).

4.4. Peptide self-assembly

Each dipeptide was dissolved in phosphate-buffered saline solution at the desired concentration (40 mM, unless otherwise indicated) with the aid of an ultrasound bath (Branson 500) for a few seconds, followed by vial immersion in an oil bath at 100 °C until a clear solution was obtained. Upon cooling to room temperature, hydrogels formed, except for L-Phe-L-Leu, which precipitated into amorphous aggregates.

4.5. Oscillatory rheology

Dynamic time sweep rheological analysis was conducted on a Malvern Kinexus Ultra Plus Rheometer (Alfatest, Milan, Italy) with a 20 mm stainless steel parallel plate geometry. The temperature was maintained at 25 °C using a Peltier temperature controller. Samples were prepared and immediately analysed with a gap of 1 mm. Time sweeps were recorded using a frequency of 1 Hz and a controlled stress of 1.00 Pa or 0.50 Pa for the metastable hydrogel. Frequency sweeps were recorded using a controlled stress of 1.00 Pa, except for the metastable gel for which a value of 0.50 Pa was set, and then stress sweeps were recorded using a frequency of 1 Hz for all compounds.

4.6. Transmission Electron Microscopy (TEM)

The peptide self-organization was visualized with a transmission electron microscope (TEM). The peptide self-organization was visualized with a transmission electron microscope (TEM). Briefly, 5 μL of the peptide samples were poured on a copper-lacey carbon-coated 300-mesh grids, while a TEM grid was exposed for 6 min. under ultraviolet (UV) ozone cleaner just before material deposition. After 1 min of adsorption, the excess material was drawn off, and 5 μL of a 2% aqueous potassium phosphotungstate at pH 7.2 was poured on the grids. Grids were air-dried until needed and TEM images were acquired using Jeol JEM 2100 instrument at 100 kV.

4.7. Circular dichroism (CD) spectroscopy

A 0.1 mm quartz cell was used on a Jasco J815 Spectropolarimeter, with 1 s integrations, 1 accumulation and a step size of 1 nm with a bandwidth of 1 nm at 20 °C. Samples were prepared at a peptide concentration of 1 mM in milliQ water to analyse the non-assembled state, or at 40 mM in

PBS to analyse the assembled form. Each spectrum is the result of an average of at least 5 measurements.

4.8. Attenuated Total Reflectance (ATR) Infrared Spectroscopy

The Infrared (IR) spectra were recorded with a Jasco 4700 FT-IR, equipped with an ATR Pro One. A drop of a freshly prepared hydrogel was placed on a silicon wafer, and then dried under vacuum overnight. Spectra were acquired with 132 accumulations and 2 cm⁻¹ resolution.

4.9. Single-crystal XRD data

Single crystals of D-Phe-L-Leu (CCDC 2012848) were obtained after approximately 1 hour of hydrogel preparation as described above (see section 4.4.). Indeed, D-Phe-L-Leu formed a metastable hydrogel that converted into crystals within about 1 hour.

Deposition number 2012848 refers to the crystallographic data deposited at the Cambridge Crystallographic Data Centre (CCDC).

4.10. Cytotoxicity assays

To evaluate the biocompatibility of the hydrogelators D-Leu-L-Phe and L-Leu-L-Phe, two different biological assays both qualitative (*live/dead*) and quantitative (*Mtt*) were performed on NIH3T3 (fibroblasts) cell line.

4.10.1. Trypan blue test for cell viability and cell count

The test was performed by following the same protocol previously reported at the point 1.2.1

4.10.2. Live/Dead assay

All the solutions were filtered with a 0.2 µm sterile filter prior to use. The hydrogels D-Leu-L-Phe and L-Leu-L-Phe (20 µl/well) were prepared at 70 mM in 0.01M PBS, pH-adjusted with NaOH, directly in triplicate wells of a “µ-Slide angiogenesis” treated slide (Ibidi, Germany). After 24 h, 30 µl of media (DMEM + 10 % fetal serum albumin, and 2 % antimycotic and antibiotic from GIBCO) were added to pre-treat the gel for 1.5 h. Next, the medium was removed and NIH3T3 (fibroblast) cells were added to the gel (10k cells/well, 30 µl media), and cultured at 37 °C, 5% CO₂ for 24 h, by handling the slides according to the manufacturers’ instructions. Cell viability was investigated using acridine orange (5 µl/well of a 20 µM solution in 50 mM PBS) and propidium iodide (4 µl/well of a 30 µM solution in 50 mM PBS). After 15 minutes, cells were imaged with a Leica microscope (DFC450C; software LASV4.13) with bright-field and fluorescence green filter (ex. 450–490 nm,

em. > 520 nm) with 10× and 40× objectives. Each condition was repeated at least in triplicate, and two experiments were performed independently.

4.10.3. MTT assay

NIH3T3 (fibroblast) cells were seeded (10 000 cells/well) in media (DMEM+ 10% FCS, and 2% antimycotic and antibiotic) using 100 µL/well on 96-well microplates (tissue-culture grade, clear, flat bottom, VWR) and incubated overnight at 37 °C and 5% CO₂. The medium was removed and replaced by 100 µL of fresh medium containing the peptide at the desired concentration (serial dilutions of 1 mM). 1% SDS served as positive control (death). Cells were cultured for 24 h. After this time, 10 µL of the MTT labeling reagent (Sigma, 0.5 mg mL⁻¹) were added, and the microplate was incubated for 4 h in a humidified atmosphere (37 °C, 5% CO₂). Next, 100 µL of the solubilisation solution for formazan crystals (4 mM HCl + 0.1% IGEPAL in isopropanol) was added to each well, and the microplate was kept at RT under shaking (Rocker-Shaker MR-12 Biosan, Vetrotecnica) for 30 min. The absorbance was read at 570 nm with a reference wavelength of 690 nm (light scattering) using Infinite M1000-Pro microplate reader (TECAN). Two independent experiments were run in triplicate (n = 6).

Manuscript 5. “Self-Assembly of Unprotected Dipeptides into Hydrogels: Water-Channels Make the Difference” described in **Chapter 6**.

5.1. Peptide synthesis

Peptide was synthesized on solid-phase by using standard protocol for Fmoc-protected amino acids (Sigma-Aldrich, Italy). Fmoc protected amino acids, 2-chlorotrityl resin, O-benzotriazoleN,N,N,N-tetramethyl-uronium-hexafluoro-phosphate (HBTU), and 1- hydroxy-7-azabenzotriazole (HOAt) were purchased from GL Biochem (Shanghai) Ltd. All solvents and the other chemicals were purchased from Merck, at analytical grade. High purity Milli-Q-water with a resistivity greater than 18 MΩcm was obtained from an inline Millipore RiOs/Origin system.

The synthesis was performed by following the same procedures previously reported from the point 2.1.1. to 2.1.5.

5.2. Peptide purification

Each dipeptide was synthesised by standard solid-phase methods and purified by reversed-phase HPLC. The method used consisted of a mixture of MeCN/water with 0.05% trifluoroacetic acid, 3

ml/min, solvent gradient: 0–3 min 25% MeCN, 16 min 95% MeCN using a C-18 column (Kinetex, 5 μm , 100 \AA , 250 \times 10 mm, Phenomenex).

5.3. Peptide characterization

^1H -NMR and ^{13}C -NMR spectra were recorded at a frequency of 400 MHz and 100 MHz, respectively, on a Varian Innova Instrument with chemical shift reported as ppm (with tetramethylsilane as internal standard). ESI-MS spectra were recorded on an Agilent 6120 single quadrupole LC-MS system, by using water/MeCN gradient system from 5% to 95% MeCN with 0.1% formic acid over 17 min, flow of 0.3 ml/min and an analytic C-18 column (Luna, 5 μm , 100 \AA , 150 x 2 mm, Phenomenex).

5.4. Self-assembly

Each compound was dissolved in phosphate-buffered saline solution (0.1M) at the desired concentration with the aid of an ultrasound bath (Branson 500) for a few seconds, followed by vial immersion in an oil bath at 100 $^{\circ}\text{C}$ until a clear solution was obtained (25–30 min.). Samples were then left to cool down to room temperature (1 min).

5.5. ^{19}F -NMR, TFA removal and self-assembly with chloride counterion

2.1 mg of peptide D-Phe-L-Ile was dissolved in DMSO- d_6 (0.75 mL). 8 μl of internal standard α,α,α -trifluorotoluene (Sigma-Aldrich T63703-500G, Lot# S45042V CAS:98-08-8) were added to the peptide solution to have a 1:8 of peptide to internal standard.

Then, 4.0 mg of peptide were dissolved in milliQ water (1.0 mg/mL) and 104 μL of a 100 mM solution of HCl were added to remove the trifluoroacetate (TFA) peptide counterion and exchange it with chloride. The solution was mixed by vortexing and sonication and left at room temperature for two minutes. The solution was lyophilized overnight, and the peptide powder was analyzed again by 400 MHz (DMSO- d_6 , TMS) as above.

5.6. Oscillatory rheology

Dynamic time sweep rheological analyses were carried out on a Malvern Kinexus Ultra Plus Rheometer (Alfatest, Milan, Italy) with a 20 mm stainless steel parallel plate geometry. The temperature was maintained at 25 $^{\circ}\text{C}$ using a Peltier temperature controller. Samples were prepared in situ and immediately analysed with a gap of 1 mm. Time sweeps were recorded at 1 Hz and 1 Pa. Frequency sweeps were recorded at 1 Pa, and then stress sweeps were recorded using a frequency of 1 Hz.

5.7. Transmission electron microscopy (TEM) and optical microscopy

Dipeptide nanostructures were visualized with a Jeol JEM 2100 instrument at 100 kV. Briefly, 5 μ L of dipeptide samples were transferred with a micropipette onto a carbon-coated 300-mesh grid, which was previously exposed for 6 min. under ultraviolet (UV) ozone cleaner just before material deposition. After 1 min of adsorption, the excess material was drawn off, and 5 μ L of a 2% aqueous potassium phosphotungstate at pH 7.2 was poured on the grids. Samples were then dried in a desiccator in vacuo prior to imaging.

Optical microscope images were acquired on a *Leitz Labovert instrument* with a 20 \times magnification objective on a drop of fresh samples deposited on a clean glass slide.

5.8. Circular Dichroism (CD) spectroscopy

A 0.1 mm quartz cell was used on a Jasco J815 Spectropolarimeter, with 1 s integrations, 1 accumulation and a step size of 1 nm with a bandwidth of 1 nm at 25°C. Samples were prepared at a peptide concentration of 1 mM in milliQ water and the pH was adjusted to neutral with NaOH (1M). Each spectrum is the result of the average of at least 5 measurements.

5.9. Attenuated total reflectance (ATR) infrared spectroscopy

The Infrared (IR) spectra were recorded with an Affinity-1S Shimadzu FT-IR, equipped with a QATR accessory, diamond crystal. A drop of the hydrogel was placed on a silicon wafer, and then dried under vacuum overnight. Spectra were acquired with 240 accumulations and 4 cm⁻¹ resolution. Each spectrum is the result of the average of at least 3 measurements.

5.10. Single-crystal X-ray diffraction (XRD)

Single crystals of D-Ile-L-Phe (**CCDC 109139**) were obtained in PBS at 40 mM, after approximately 1 hour of sample preparation as described above (see section 5.4). Single crystals of D-Phe-L-Ile (**CCDC 109138**) were obtained under the same conditions after a month from the corresponding hydrogel.

Deposition Numbers **109139** and **109138** refer to the crystallographic data deposited at the Cambridge Crystallographic Data Centre (CCDC).

5.11. Cytotoxicity assays

To evaluate the biocompatibility of the hydrogelator D-Phe-L-Ile, two different biological assays both qualitative (*live/dead*) and quantitative (*Mtt*) were performed on NIH3T3 (fibroblasts) cell line.

5.11.1. Trypan blue test for cell viability and cell count

The test was performed by following the same protocol previously reported at the point 1.2.1

5.11.2. Live/Dead assay

All the solutions were filtered with a 0.2 μm sterile filter prior to use. The gelator D-Phe-L-Ile (20 μl /well) was prepared at 70 mM in 0.01M PBS, pH-adjusted with NaOH, directly in triplicate wells of a “ μ -Slide angiogenesis” treated slide (Ibidi, Germany). After 24 h, 30 μl of media (DMEM + 10 % fetal serum albumin, and 2 % antimycotic and antibiotic from GIBCO) were added to pre-treat the gel for 1.5 h. Next, the medium was removed and NIH3T3 (fibroblast) cells were added to the gel (10k cells/well, 30 μl media), and cultured at 37 °C, 5% CO₂ for 24 h, by handling the slides according to the manufacturers’ instructions. Cell viability was investigated using acridine orange (5 μl /well of a 20 μM solution in 50 mM PBS) and propidium iodide (4 μl /well of a 30 μM solution in 50 mM PBS). After 15 minutes, cells were imaged with a Leica microscope (DFC450C; software LASV4.13) with bright-field and fluorescence green filter (ex. 450–490 nm, em. > 520 nm) with 10 \times and 40 \times objectives. Each condition was repeated at least in triplicate, and two experiments were performed independently.

5.11.3. MTT assay

NIH3T3 (fibroblast) cells were seeded (10k cells/well) in media (DMEM+ 10% FCS, and 2% antimycotic and antibiotic) using 100 μL /well on 96-well microplates (tissue-culture grade, clear, flat bottom, VWR) and incubated overnight at 37 °C and 5% CO₂. The medium was removed and replaced by 100 μL of fresh medium containing the peptide at the desired concentration (serial dilutions of 1 mM). 1% SDS served as positive control (death). Cells were cultured for 24 h. After this time, 10 μL of the MTT labeling reagent (Sigma, 0.5 mg mL⁻¹) were added, and the microplate was incubated for 4 h in a humidified atmosphere (37 °C, 5% CO₂). Next, 100 μL of the solubilisation solution for formazan crystals (4 mM HCl + 0.1% IGEPAL in isopropanol) was added to each well, and the microplate was kept at RT under shaking (Rocker-Shaker MR-12 Biosan, Vetrotecnica) for 30 min. The absorbance was read at 570 nm with a reference wavelength of 690 nm (light scattering) using Infinite M1000-Pro microplate reader (TECAN). Two independent experiments were run in triplicate (n = 6).

Manuscript 6. “Dipeptide self-assembly into water-channels and gel biomaterial” described in Chapter 7.

6.1. Peptide synthesis

Each dipeptide was synthesised by standard solid-phase methods. Fmoc-amino acids, 2-chlorotrityl resin, and coupling agents were obtained from GL Biochem (Shanghai) Ltd. All other chemicals and solvents were acquired at analytical grade from Merck. An in-line Millipore RiOs/Origin system provided high-purity Milli-Q-water with resistivity >18 M Ω cm.

The synthesis was performed by following the same procedures previously reported from the point 2.1.1. to 2.1.5.

6.2. Peptide purification

Each dipeptide was purified using a reverse-phase HPLC (1260 Agilent Infinity System) using a semipreparative C-18 column (Kinetex, 5 μ m, 100 \AA , 250 \times 10 mm, Phenomenex) and a photodiode array detector (G1315C).

The gradient used consisted in a mixture of MeCN/H₂O with 0.05% TFA (3 ml/min) as eluent with the following programs:

- For **D-Phe-L-Val**: t = 0-3 min. 15% MeCN, t = 3 min. 15 % MeCN, t = 16 min. 45% MeCN, t = 18 min. 95 % MeCN.
- For **D-Val-L-Phe**: t = 0 min. 15% MeCN, t = 3 min. 15 % MeCN, t = 16 min. 55% MeCN t = 18 min. 95 % MeCN.

The products were then lyophilised to yield the corresponding peptide as a white powder.

6.3. Peptide characterization

¹H-NMR and ¹³C-NMR spectra were recorded at a frequency of 400 MHz and 100 MHz, respectively, on a Varian Innova Instrument with chemical shift reported as ppm (with tetramethylsilane as internal standard). ESI-MS spectra were recorded on an Agilent 6120 single quadrupole LC-MS system, by using water/MeCN gradient system from 5% to 95% MeCN with 0.1% formic acid over 17 min, flow of 0.3 ml/min and an analytic C-18 column (Luna, 5 μ m, 100 \AA , 150 x 2 mm, Phenomenex).

6.4. Self-assembly into hydrogels or crystals

Each peptide (40 mM) was dissolved in phosphate buffered saline (PBS, 0.1M) through heating in an oil-bath at 95 °C for ~ 15 min. and left to cool down to room temperature.

6.5. Oscillatory rheology

Hydrogels were freshly prepared directly on a 20-mm stainless steel parallel plate of a Kinexus Plus (Malvern). Data were recorded with 1 mm gap at 25 °C (Peltier). Time sweeps were acquired with 1 Pa and 1 Hz, frequency sweeps at 1 Pa and stress sweeps at 1 Hz. Every sample was analysed at least three times.

6.6. Transmission electron microscopy (TEM) and optical microscopy

Samples were prepared as described above at 40 mM, transferred onto TEM carbon grids previously exposed to UV-Ozone Pro cleaner Plus for 6 min, and dried *in vacuo*. TEM images were acquired on Jeol JEM 2100 (Japan) at 100 kV and analysed with FIJI free software.

Optical microscope images were acquired on a drop of fresh samples deposited on clean glass slides, using a Leitz Labovert instrument with a 20× magnification objective.

6.7. Circular dichroism (CD) spectroscopy

A 0.1 mm quartz cell was used on a Jasco J-815 Spectropolarimeter, with 1 s integrations, 25 accumulations and a step size of 0.5 nm with a bandwidth of 1 nm at 25 °C. Samples were prepared at 1 mM in milliQ water by adjusting the pH until 7 with NaOH (1M). Each spectrum is the result of the average of at least 3 measurements.

6.8. Attenuated Total Reflectance (ATR) Infrared Spectroscopy

Both peptide samples were prepared in PBS as described above at 40 mM on a 1-cm² piece of silicon wafer and dried *in vacuo* overnight. ATR-IR spectra were acquired at 4 cm⁻¹ resolution, 240 scans, with an ATR-IRAffinity-1S (Shimadzu). Every sample was analysed at least 3 times.

6.9. Thioflavin T fluorescence assay

Samples were prepared in PBS at different final concentrations (from 0.1, 0.2, 0.5, 1, 5, 10, 15, 20, 30 to 40 mM) inside a Greiner 96 U Bottom Black Polystyrene plate (VWR) (120 µl/well). After 1 hour of assembly, 30 µl of a fresh Thioflavin-T solution was added in each well (22 µM in 20 mM glycine-NaOH pH ~7.4) and kept in the dark for 15 minutes. Fluorescence was measured (ex. 446 nm, em. 490 nm, 20-nm bandwidth) on an Infinite M1000 pro microplate reader (TECAN) and the experiments were run independently twice in triplicate ($n = 6$).

6.10. Single-crystal X-ray diffraction (XRD)

Single crystals of D-Phe-L-Val (CCDC 2160978) and D-Val-L-Phe (CCDC 2160976) were obtained in PBS at 40 mM after 1 month, and at 100 mM after a few minutes, respectively.

Deposition Numbers 2160978 and 2160976 refer to the crystallographic data deposited at the Cambridge Crystallographic Data Centre (CCDC).

6.11. Cytotoxicity assays

To evaluate the biocompatibility of the hydrogelator D-Phe-L-Val, two different biological assays both qualitative (*live/dead*) and quantitative (*Mtt*) were performed on NIH3T3 (fibroblasts) cell line.

6.11.1. Trypan blue test for cell viability and cell count

The test was performed by following the same protocol previously reported at the point 1.2.1

6.11.2. Live/Dead assay

All the solutions were filtered with a 0.2 μm sterile filter prior to use. The gelator D-Phe-L-Val (20 μl /well) was prepared at 70 mM in 0.01M PBS, pH-adjusted with NaOH, directly in triplicate wells of a “ μ -Slide angiogenesis” treated slide (Ibidi, Germany). After 24 h, 30 μl of media (DMEM + 10 % fetal serum albumin, and 2 % antimycotic and antibiotic from GIBCO) were added to pre-treat the gel for 1.5 h. Next, the medium was removed and NIH3T3 (fibroblast) cells were added to the gel (10k cells/well, 30 μl media), and cultured at 37 °C, 5% CO₂ for 24 h, by handling the slides according to the manufacturers’ instructions. Cell viability was investigated using acridine orange (5 μl /well of a 20 μM solution in 50 mM PBS) and propidium iodide (4 μl /well of a 30 μM solution in 50 mM PBS). After 15 minutes, cells were imaged with a Leica microscope (DFC450C; software LASV4.13) with bright-field and fluorescence green filter (ex. 450–490 nm, em. > 520 nm) with 10 \times and 40 \times objectives. Each condition was repeated at least in triplicate, and two experiments were performed independently.

6.11.3. MTT assay

NIH3T3 (fibroblast) cells were seeded (10k cells/well) in media (DMEM+ 10% FCS, and 2% antimycotic and antibiotic) using 100 μL /well on 96-well microplates (tissue-culture grade, clear, flat bottom, VWR) and incubated overnight at 37 °C and 5% CO₂. The medium was removed and replaced by 100 μL of fresh medium containing the peptide at the desired concentration (serial dilutions of 1 mM). 1% SDS served as positive control (death). Cells were cultured for 24 h. After this time, 10 μL of the MTT labeling reagent (Sigma, 0.5 mg mL⁻¹) were added, and the microplate

was incubated for 4 h in a humidified atmosphere (37 °C, 5% CO₂). Next, 100 µL of the solubilisation solution for formazan crystals (4 mM HCl + 0.1% IGEPAL in isopropanol) was added to each well, and the microplate was kept at RT under shaking (Rocker-Shaker MR-12 Biosan, Vetrotecnica) for 30 min. The absorbance was read at 570 nm with a reference wavelength of 690 nm (light scattering) using Infinite M1000-Pro microplate reader (TECAN). Two independent experiments were run in triplicate (n = 6).

References

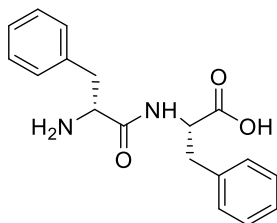
- [1] M. Gunetti, S. Castiglia, D. Rustichelli, K. Mareschi, F. Sanavio, M. Muraro, E. Signorino, L. Castello, I. Ferrero, F. Fagioli, *J. Transl. Med.* **2012**, *10*, 1–12.
- [2] S. Eissler, M. Kley, D. Bächle, G. Loidl, T. Meier, D. Samson, *J. Pept. Sci.* **2017**, *23*, 757–762.
- [3] V. Krchnák, J. Vágner, M. Lebl, *Int. J. Pept. Protein Res.* **1988**, *32*, 415–416.
- [4] T. Vojkovsky, *Pept. Res.* **1995**, *8*, 236–237.

Chapter 10. Appendix

"This Chapter describes solely the spectroscopic data for the experiments that I carried out myself. The other data can be found in the corresponding scientific articles or supplementary information."

10.1. Manuscript 2. "Heterochirality and Halogenation Control Phe-Phe Hierarchical Assembly" described in **Chapter 4**.

D-Phe-L-Phe spectroscopic data



Chemical Formula: $C_{18}H_{20}N_2O_3$

Exact Mass: 312,15

Molecular Weight: 312,37

1H -NMR (400 MHz, DMSO- d_6 , TMS)

1H -NMR (400 MHz, DMSO- d_6) δ (ppm): 8.85 (d, $J = 8.0$ Hz, 1 H, NH), 8.01 (s (br), 2H, NH₂), 7.33-7.04 (m, 10 H, ArH), 4.57 (ddd, $J = 8.8, 8.0, 4.8$ Hz, 1 H, α CH), 4.02 (dd, $J = 8.0, 4.8$ Hz, 1 H, α CH), 3.11 (dd, $J = 14.0, 4.8$ Hz, 1 H, β CH), 2.89 (dd, $J = 14.0, 4.8$ Hz, 1 H, β CH), 2.86 (dd, $J = 14.0, 8.8$ Hz, 1 H, β CH), 2.66 (dd, $J = 14.0, 8.0$ Hz, 1 H, β CH₂).

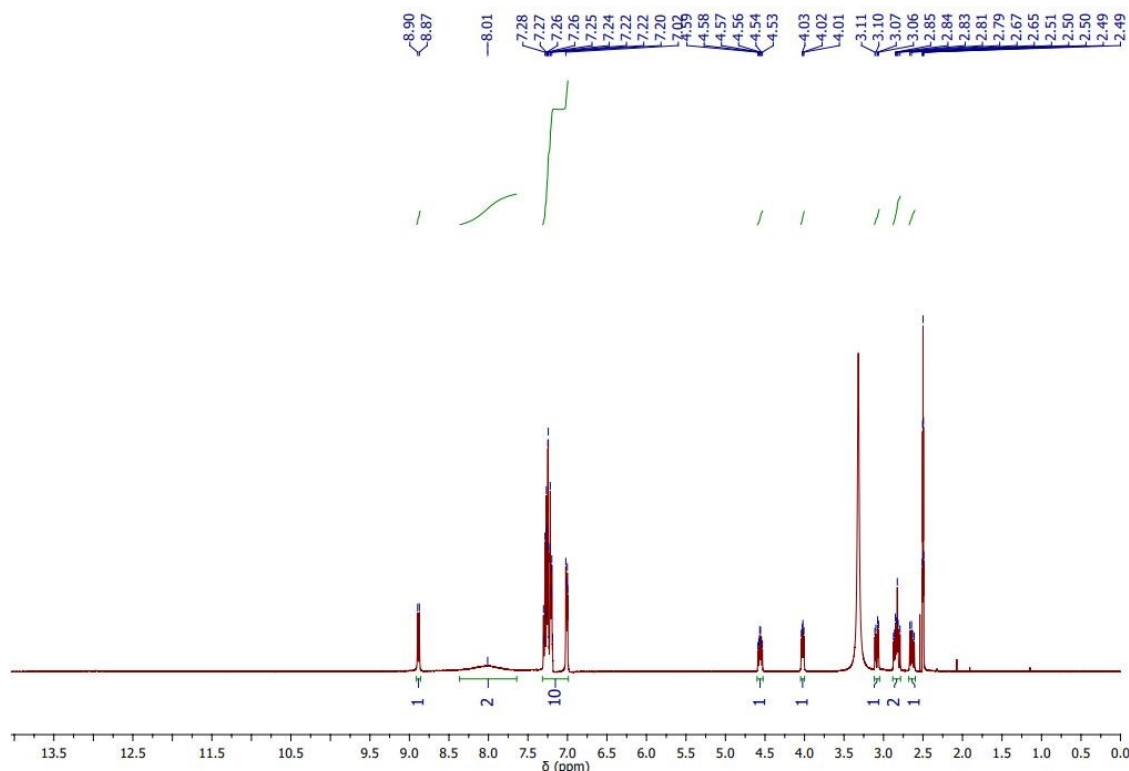


Figure 10.1. 1H -NMR spectrum of D-Phe-L-Phe.

^{13}C -NMR (100 MHz, DMSO-*d*₆, TMS)

^{13}C -NMR (100 MHz, DMSO-*d*₆, TMS) δ (ppm): 172.2, 168.3 (2x CO); 137.2, 134.8, 129.6, 129.2, 128.5, 128.3, 127.2, 126.6, 118.8 (Ar); 53.8, 53.2 (2x αC); 37.0, 36.7 (2x βC).

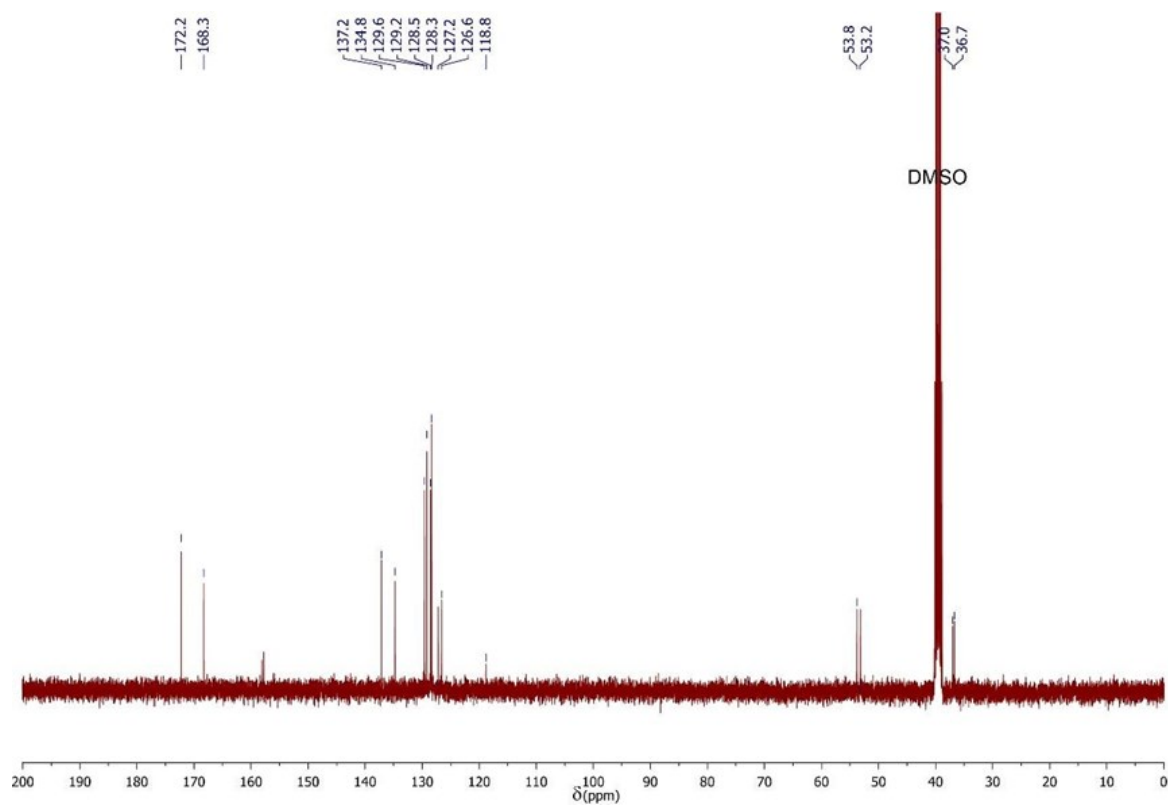


Figure 10.2. ^{13}C -NMR spectrum of D-Phe-L-Phe.

MS (ESI): m/z 313.1 ($M+H$)⁺, 311.0 ($M-H$)⁻, 624.2 ($2M-H$)⁻

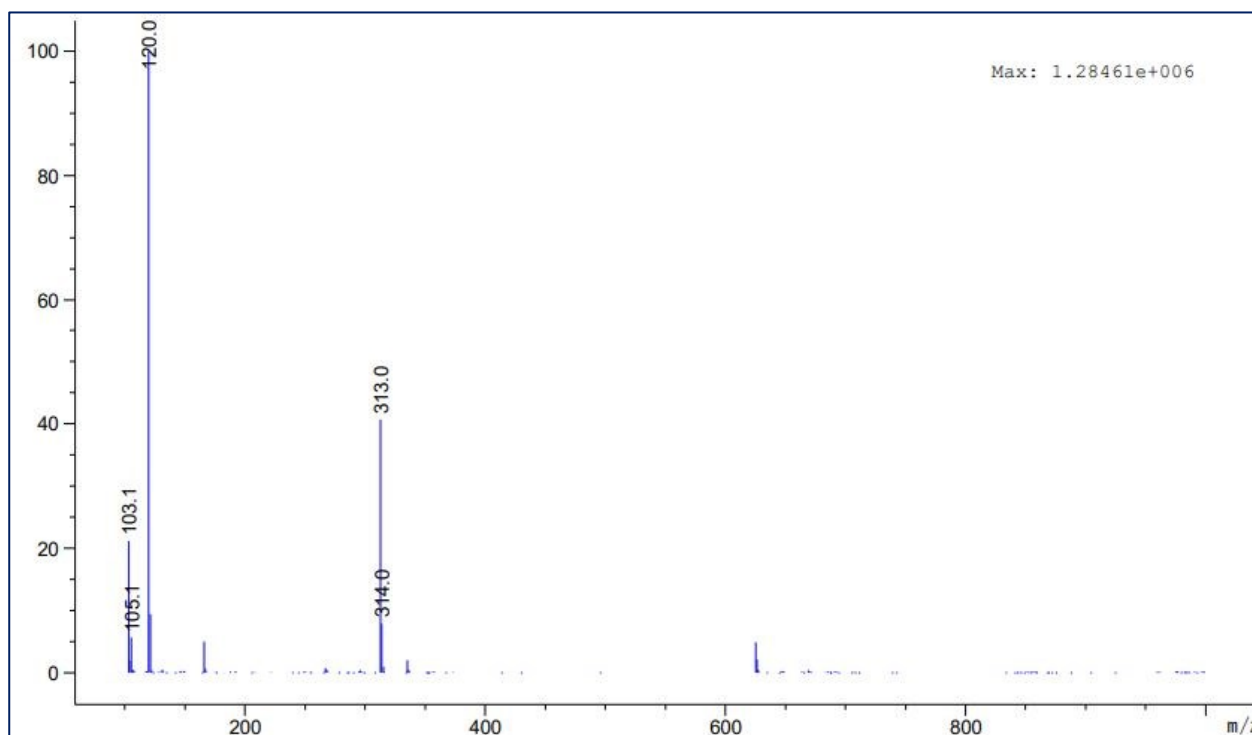


Figure 10.3.ESI-MS spectrum of D-Phe-L-Phe. (positive ion mode).

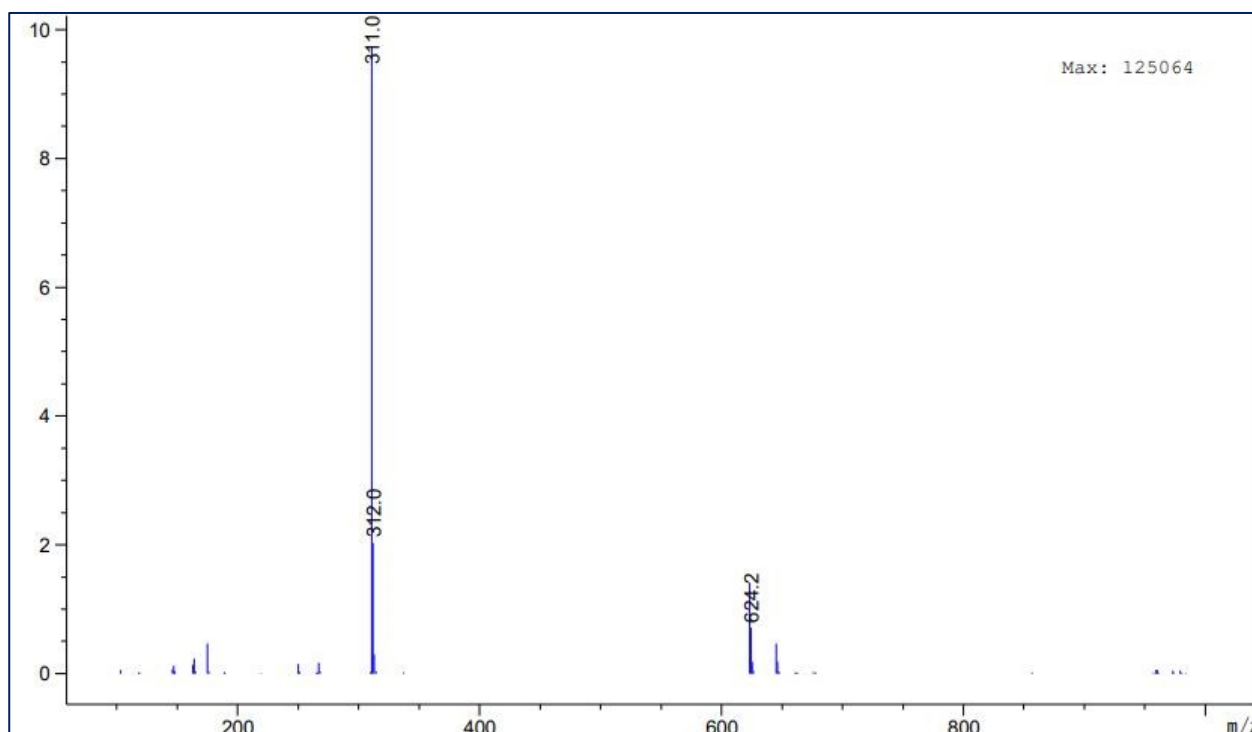
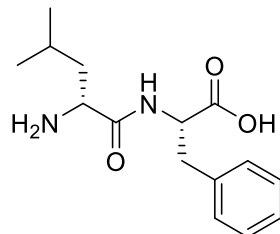


Figure 10.4.ESI-MS spectrum of D-Phe-L-Phe. (negative ion mode).

10.2. Manuscript 4. “Supramolecular hydrogels from unprotected dipeptides: a comparative study on stereoisomers and structural isomers” described in **Chapter 5**.

D-Leu-L-Phe spectroscopic data



Chemical Formula: $C_{15}H_{22}N_2O_3$

Exact Mass: 278,16

Molecular Weight: 278,35

1H -NMR (400 MHz, DMSO- d_6 , TMS)

1H NMR (400 MHz, DMSO- d_6 , TMS), δ (ppm): 8.83 (d, $J = 8.5$ Hz, 1H, NH), 8.10 (s, 2H, NH₂), 7.29 – 7.18 (m, 5H, Ar), 4.58 (m, 1H, α CH), 3.69 (m, 1H, α CH), 3.17 (dd, $J = 13.8, 4.4$ Hz, 1H, β CH₂), 2.82 (dd, $J = 13.8, 10.6$ Hz, 1H, β CH₂), 1.26 (m, 1H, γ CH), 1.23 – 1.17 (m, 2H, β CH₂), 0.74 (d, $J = 4.7$ Hz, 3H, CH₃), 0.73 (d, $J = 4.7$ Hz, 3H, CH₃).

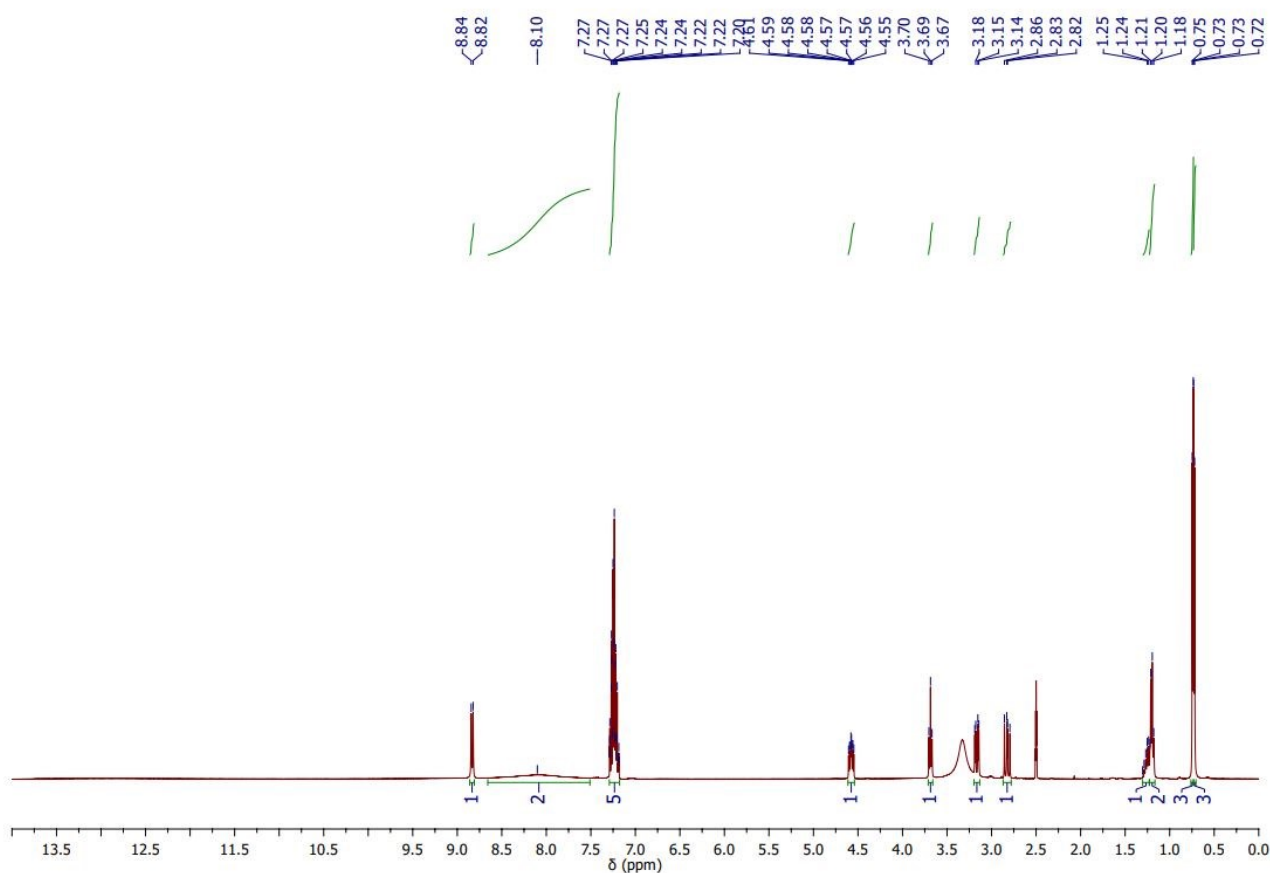


Figure 10.5. 1H -NMR spectrum of D-Leu-L-Phe.

^{13}C -NMR (100 MHz, DMSO-*d*₆, TMS)

^{13}C NMR (100 MHz, DMSO-*d*₆, TMS), δ (ppm): 172.5, 168.9 (2 x CO); 137.2, 129.2, 128.2, 126.5 (Ar); 53.4, 50.7 (2 x αC); 40.3, 37.0 (2 x βC); 23.2 (1 γC); 22.5, 21.8 (2 x δC).

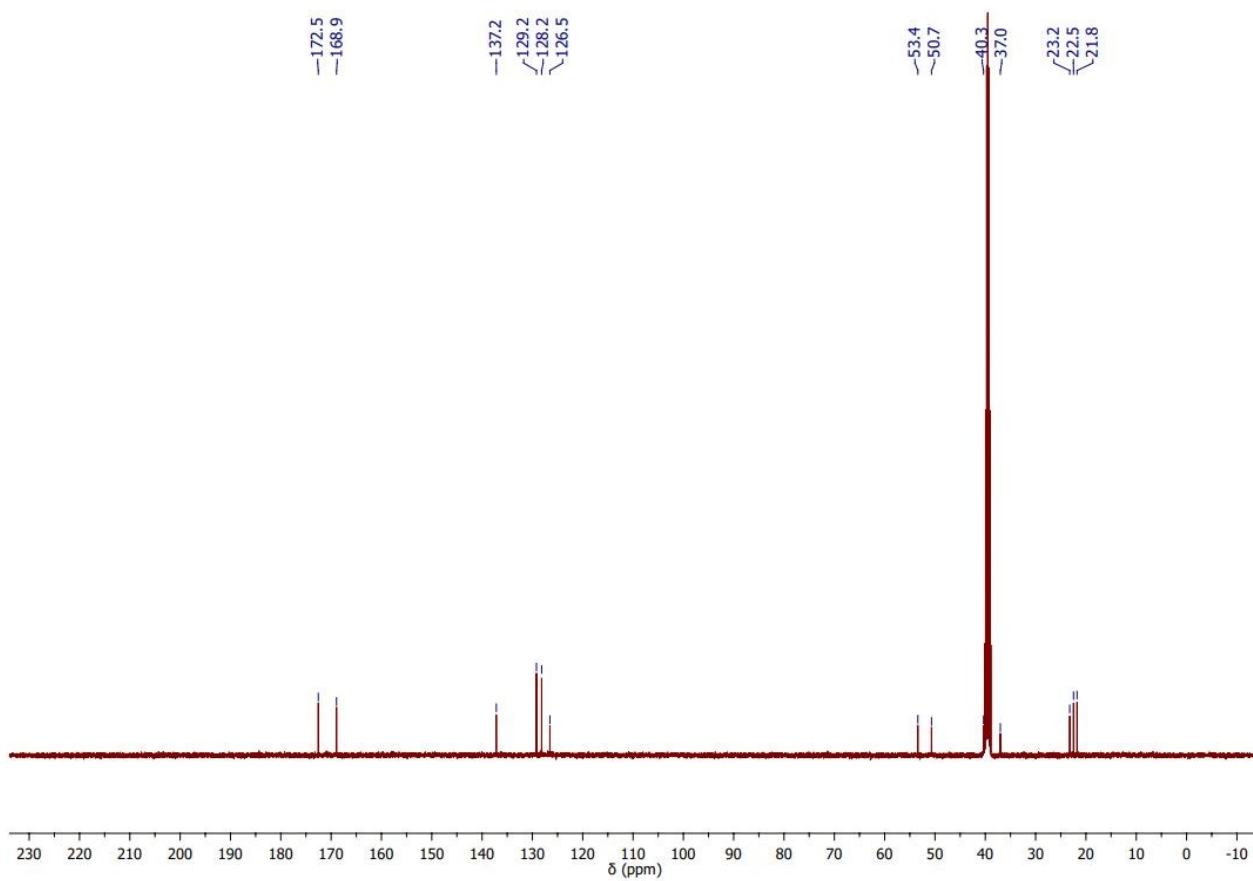


Figure 10.6. ^{13}C -NMR spectrum of D-Leu-L-Phe.

MS (ESI): m/z 279.1 ($M+H$)⁺, 301.1 ($M+Na$)⁺, 557.3 ($2M+H$)⁺; 277.1 ($M-H$)⁻, 555.3 ($2M-H$)⁻.

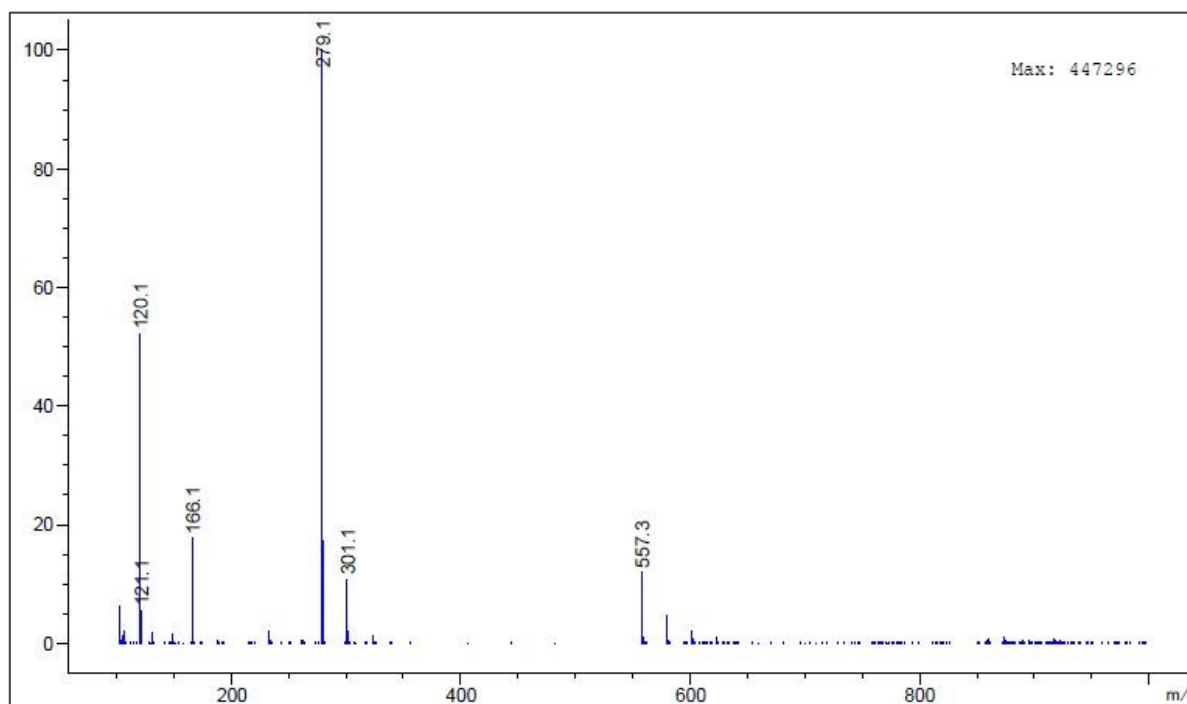


Figure 10.7. ESI-MS spectrum of D-Leu-L-Phe. (positive ion mode).

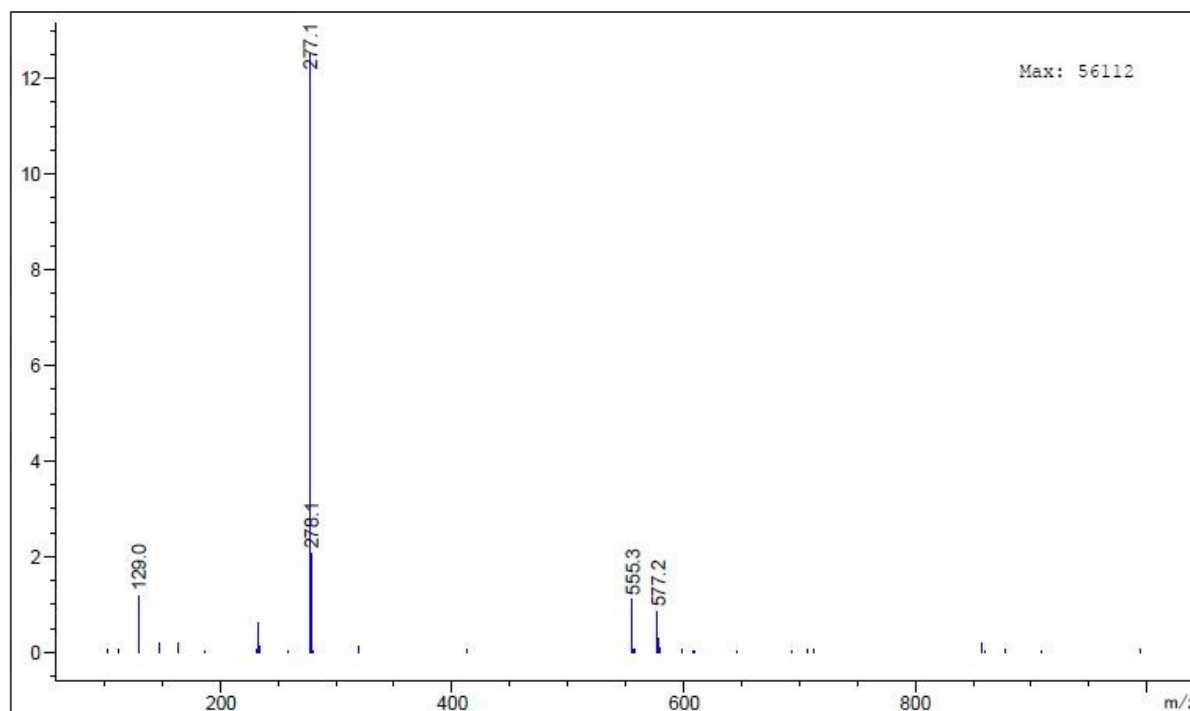
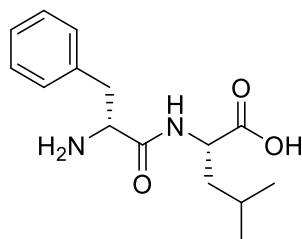


Figure 10.8. ESI-MS spectrum of D-Leu-L-Phe. (negative ion mode).

D-Phe-L-Leu spectroscopic data

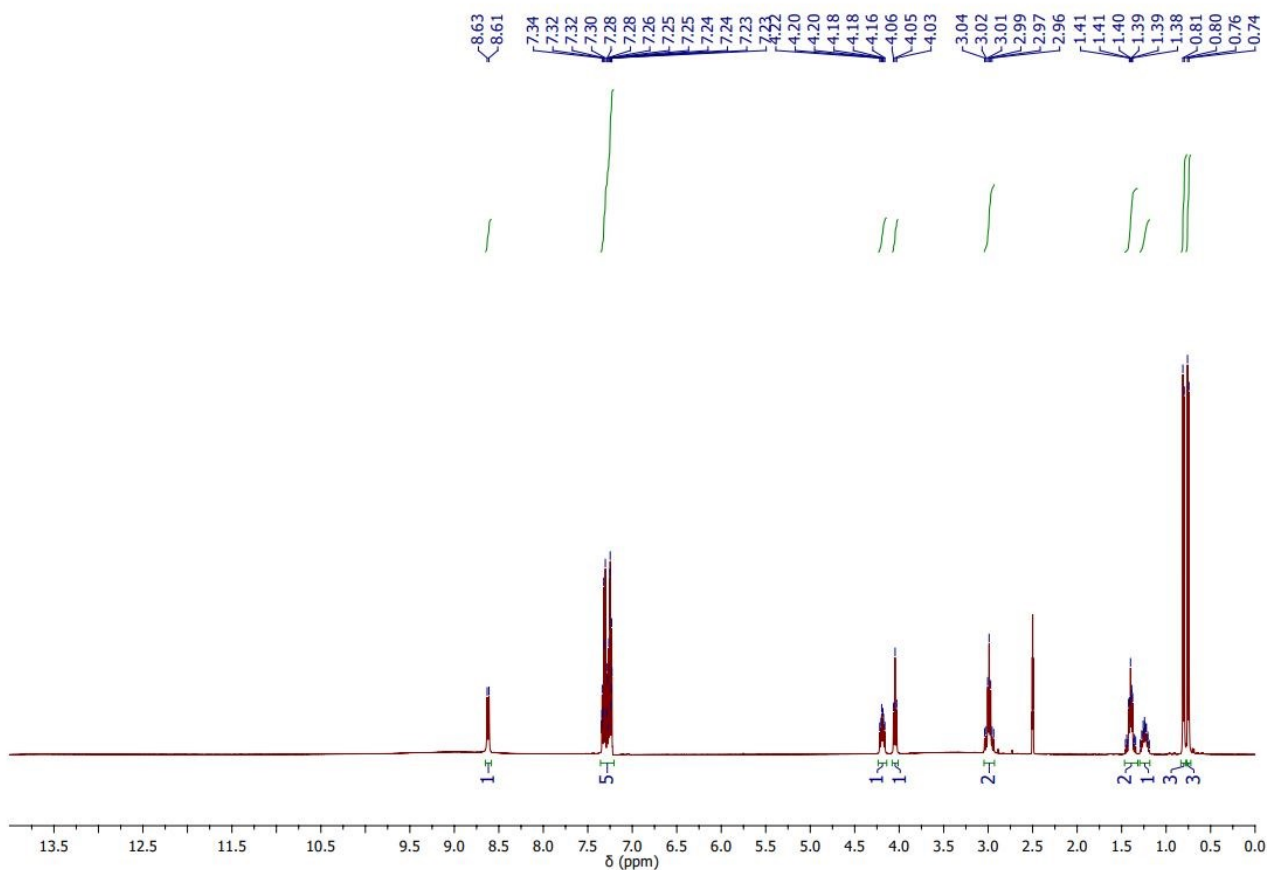
Chemical Formula: C₁₅H₂₂N₂O₃

Exact Mass: 278,16

Molecular Weight: 278,35

¹H-NMR (400 MHz, DMSO-*d*₆, TMS)

¹H NMR (400 MHz, DMSO-*d*₆, TMS), δ (ppm): 8.62 (d, *J* = 8.1 Hz, 1H, NH), 7.36 – 7.21 (m, 5H, Ar), 4.19 (m, 1H, αCH), 4.05 (dd, *J* = 7.2 Hz, 7.2 Hz, 1H, αCH), 3.05 – 2.93 (m, 2H, βCH₂), 1.47 – 1.32 (m, 2H, βCH₂), 1.30 – 1.18 (m, 1H, γCH), 0.80 (d, *J* = 6.6 Hz, 3H, CH₃), 0.75 (d, *J* = 6.5 Hz, 3H, CH₃).

Figure 10.9. ¹H-NMR spectrum of D-Phe-L-Leu

^{13}C -NMR (100 MHz, DMSO- d_6 , TMS)

^{13}C NMR (100 MHz, DMSO- d_6 , TMS), δ (ppm): 173.5, 168.2 (2 x CO); 135.0, 129.4, 128.4, 127.1 (Ar); 53.4, 50.3 (2 x αC); 40.3, 37.5 (2 x βC); 23.9 (1 γC); 22.8, 21.2 (2 x δC).

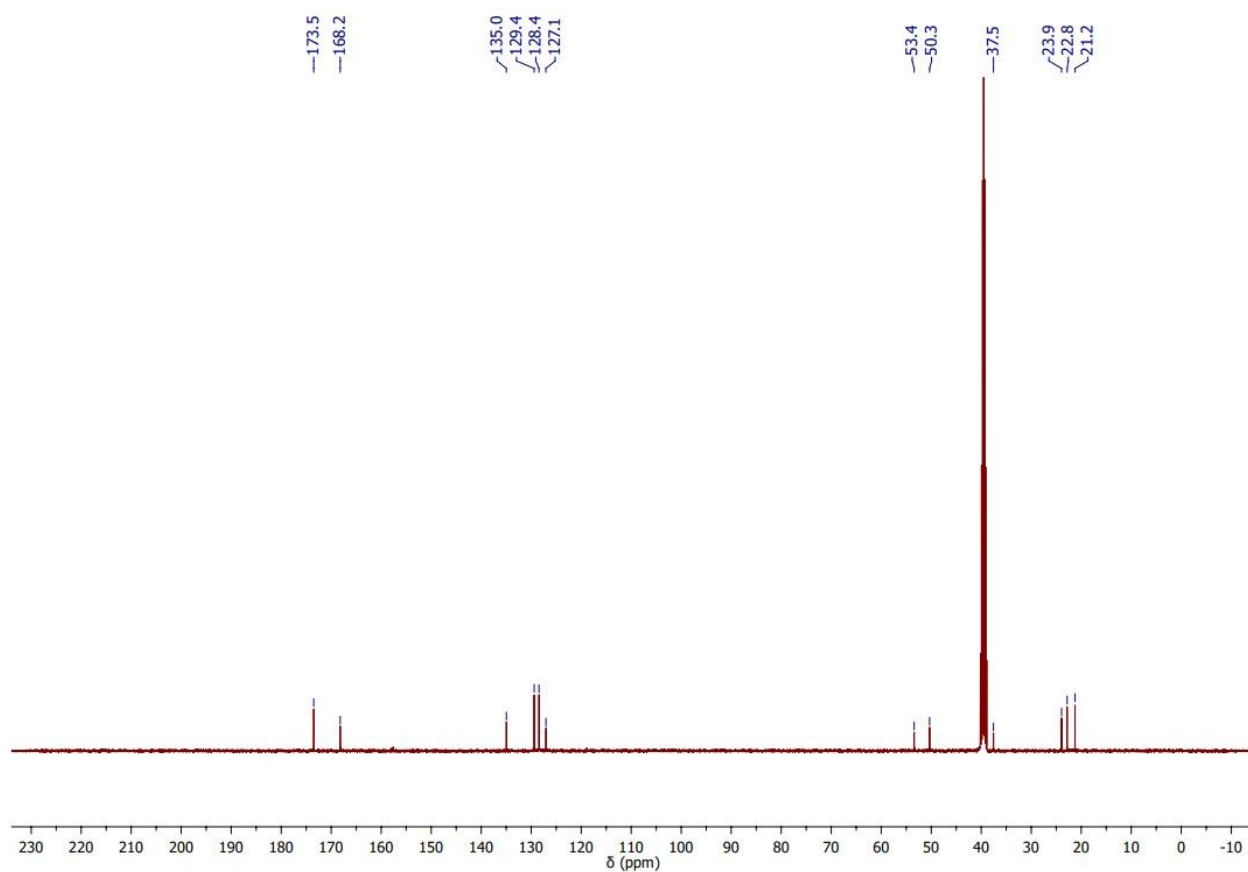


Figure 10.10. ^{13}C -NMR spectrum of D-Phe-L-Leu

MS (ESI): m/z 279.1 ($M+H$)⁺, 557.3 ($2M+H$)⁺; 277.1 ($M-H$)⁻, 555.3 ($2M-H$)⁻

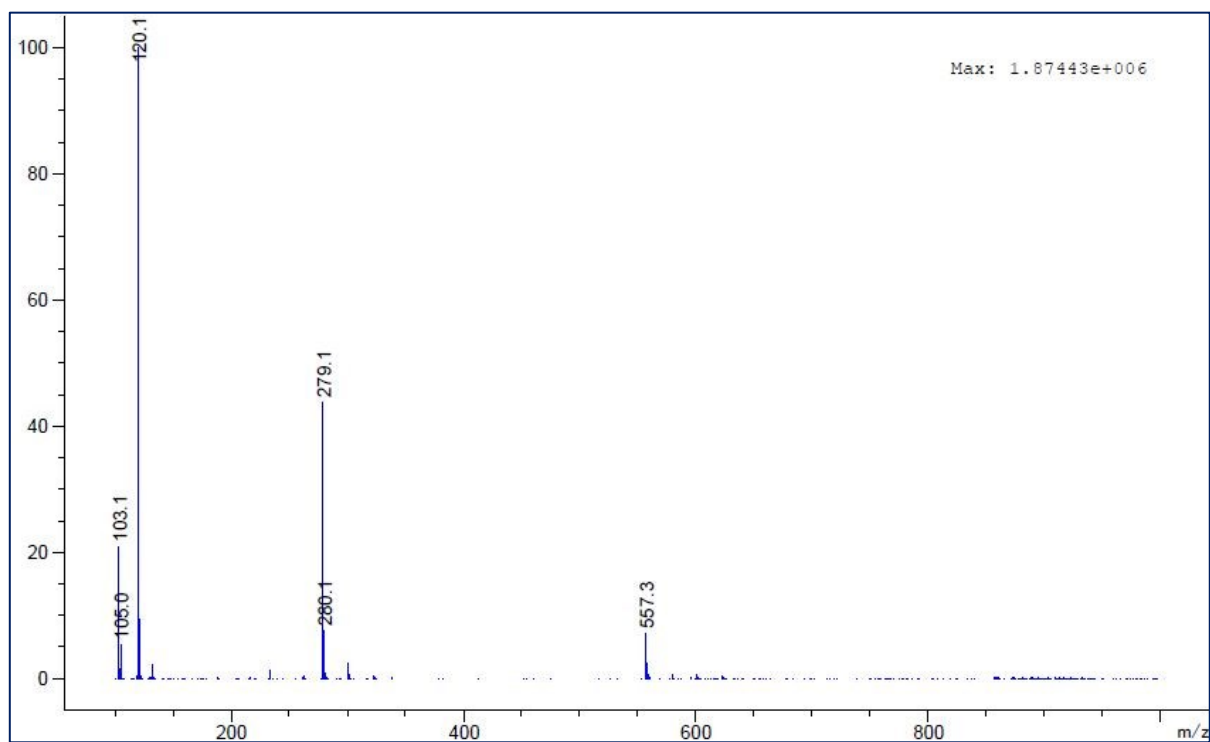


Figure 10.11. ESI-MS spectrum of D-Phe-L-Leu (positive ion mode).

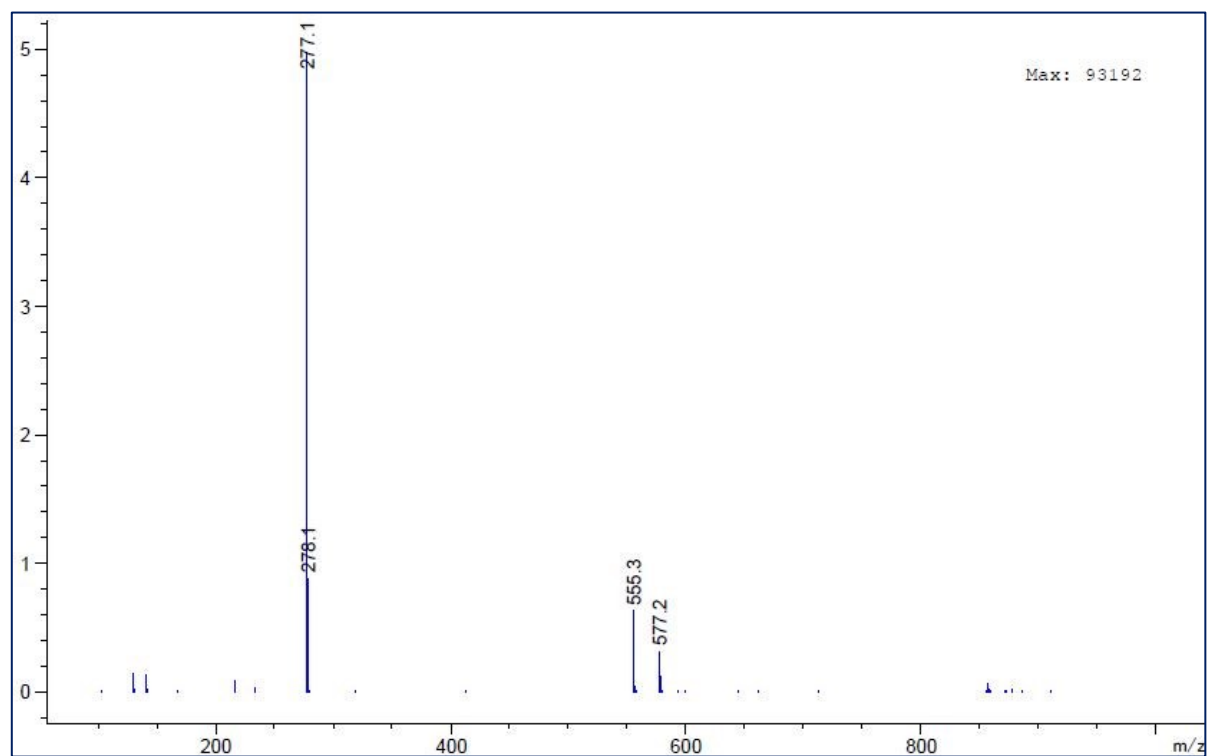
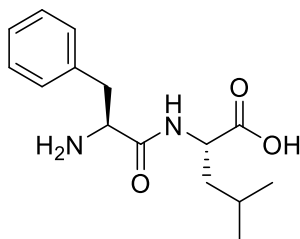


Figure 10.12. ESI-MS spectrum of D-Phe-L-Leu (negative ion mode).

L-Phe-L-Leu spectroscopic data

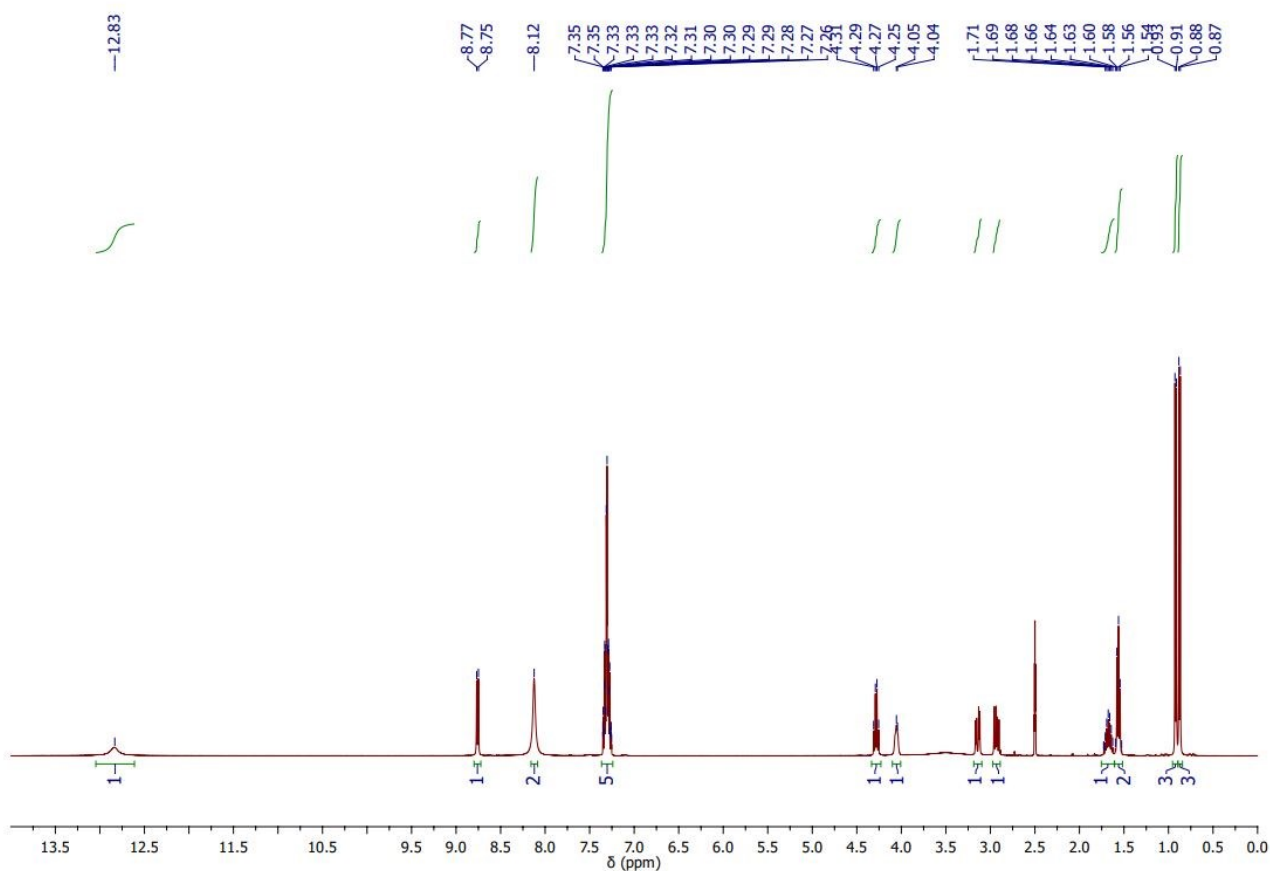
Chemical Formula: C₁₅H₂₂N₂O₃

Exact Mass: 278,16

Molecular Weight: 278,35

¹H-NMR (400 MHz, DMSO-*d*₆, TMS)

¹H NMR (400 MHz, DMSO-*d*₆, TMS), δ (ppm): 12.83 (s, 1H, COOH), 8.76 (d, *J* = 7.9 Hz, 1H, NH), 8.12 (s, 2H, NH₂), 7.37 – 7.24 (m, 5H, Ar), 4.28 (m, 1H, αCH), 4.05 (m, 1H, αCH), 3.14 (dd, *J* = 14.2, 5.0 Hz, 1H, βCH₂), 2.98 – 2.88 (m, 1H, βCH₂), 1.75 – 1.61 (m, 1H, γCH), 1.60 – 1.49 (m, 2H, βCH₂), 0.92 (d, *J* = 6.6 Hz, 3H, CH₃), 0.88 (d, *J* = 6.5 Hz, 3H, CH₃).

Figure 10.13. ¹H-NMR spectrum of L-Phe-L-Leu

^{13}C -NMR (100 MHz, DMSO- d_6 , TMS)

^{13}C NMR (100 MHz, DMSO- d_6 , TMS), δ (ppm): 173.4, 168.1 (2 x CO); 134.7, 129.6, 128.5, 127.2 (Ar); 53.2, 50.5 (2 x αC); 40.0, 36.9 (2 x βC); 24.2 (1 γC); 22.8, 21.3 (2 x δC).

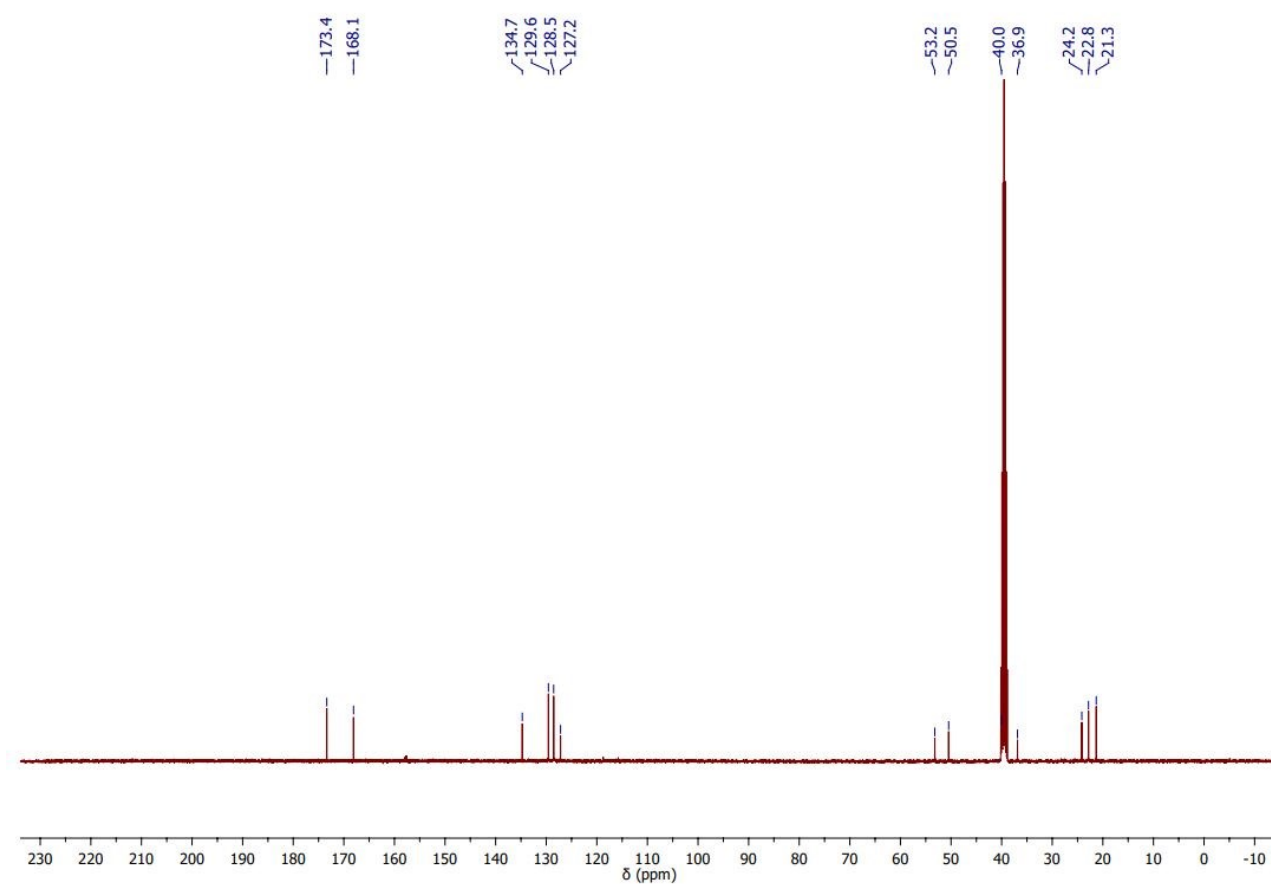


Figure 10.14. ^{13}C -NMR spectrum of L-Phe-L-Leu

MS (ESI): m/z 279.1 ($M+H$)⁺, 301.1 ($M+Na$)⁺, 579.3 ($2M+Na$)⁺; 277.1 ($M-H$)⁻, 555.3 ($2M-H$)⁻.

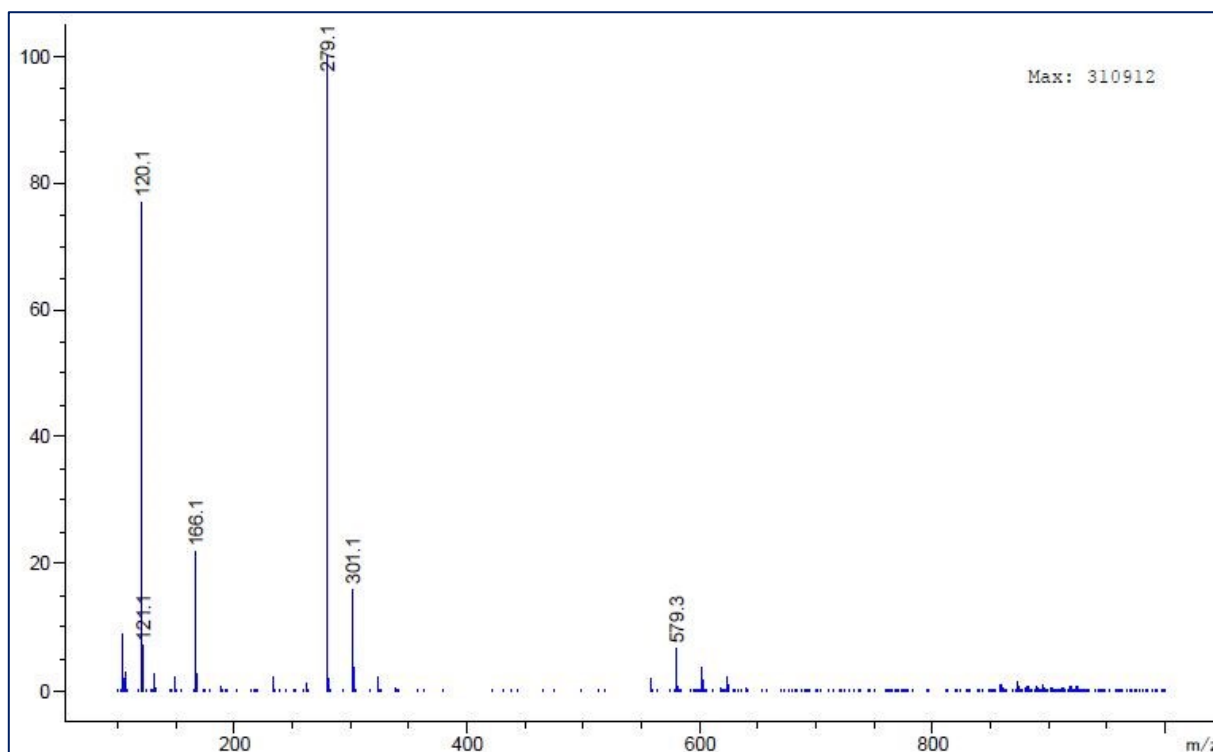


Figure 10.15. ESI-MS spectrum of L-Phe-L-Leu (positive ion mode).

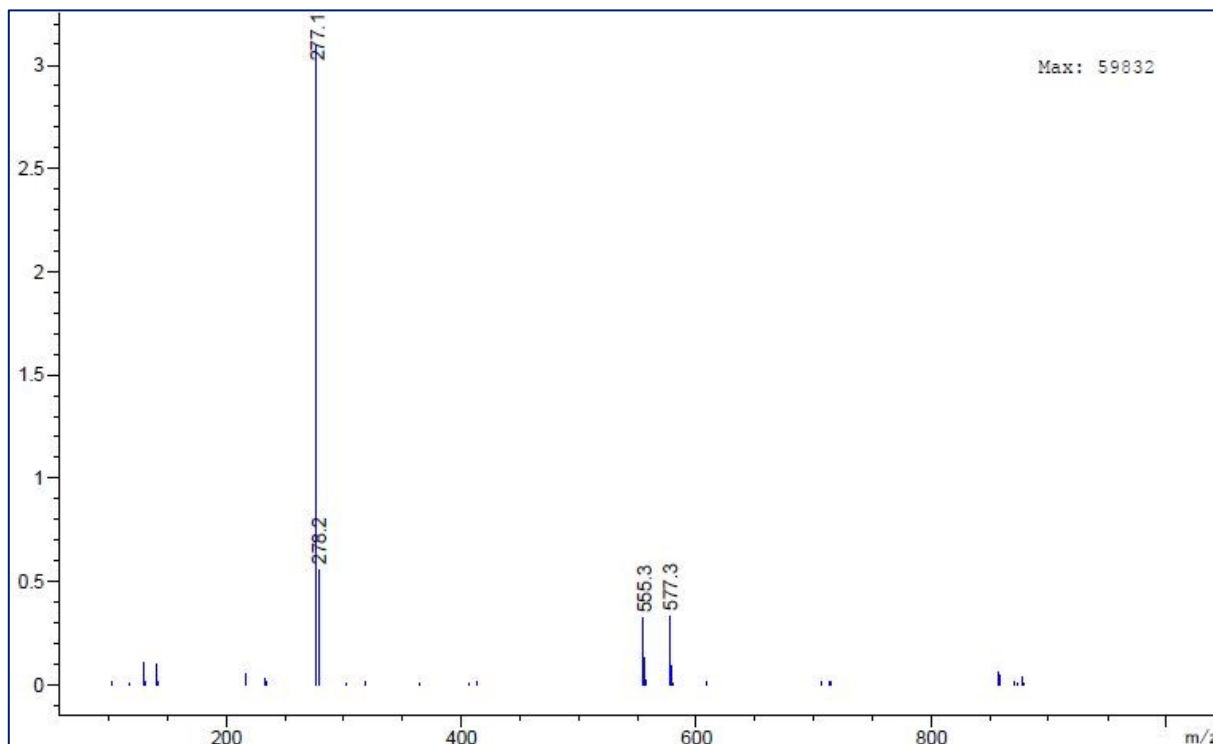
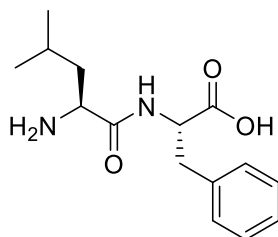


Figure 10.16. ESI-MS spectrum of L-Phe-L-Leu (negative ion mode).

L-Leu-L-Phe spectroscopic data

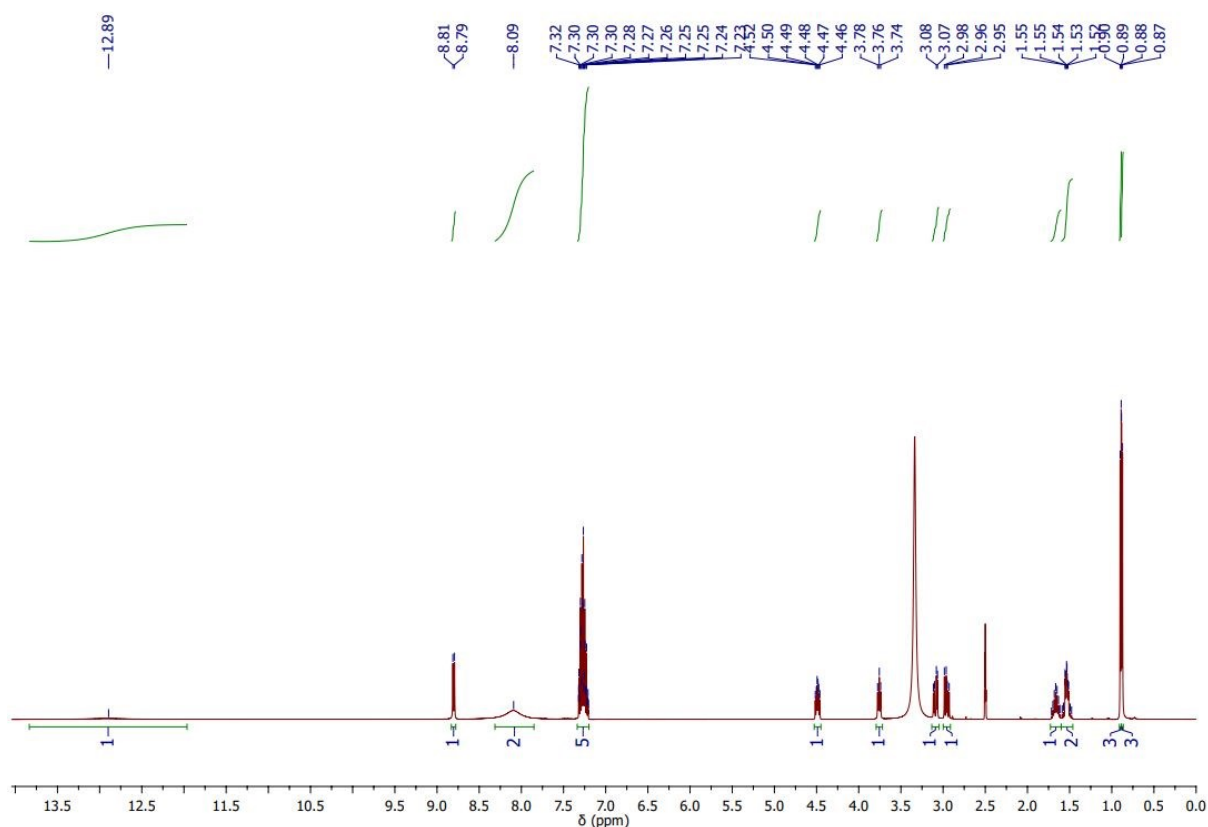
Chemical Formula: C₁₅H₂₂N₂O₃

Exact Mass: 278,16

Molecular Weight: 278,35

¹H-NMR (400 MHz, DMSO-*d*₆, TMS)

¹H NMR (400 MHz, DMSO-*d*₆, TMS), δ (ppm): 12.89 (s, 1H, COOH), 8.80 (d, *J* = 7.7 Hz, 1H, NH), 8.09 (s, 2H, NH₂), 7.34 – 7.20 (m, 5H, Ar), 4.49 (m, 1H, αCH), 3.76 (m 1H, αCH), 3.09 (dd, *J* = 14.1, 5.3 Hz, 1H, βCH₂), 2.96 (dd, *J* = 14.1, 8.8 Hz, 1H, βCH₂), 1.67 (m, 1H, γCH), 1.60 – 1.46 (m, 2H, βCH₂), 0.89 (d, *J* = 4.9 Hz, 3H, CH₃), 0.88 (d, *J* = 4.9 Hz, 3H, CH₃).

Figure 10.17. ¹H-NMR spectrum of L-Leu-L-Phe

^{13}C -NMR (100 MHz, DMSO- d_6 , TMS)

^{13}C NMR (100 MHz, DMSO- d_6 , TMS), δ (ppm): 172.3, 169.2 (2 x CO); 137.3, 129.1, 128.3, 126.6 (Ar); 53.8, 50.6 (2 x αC); 40.3, 36.4 (2 x βC); 23.3 (1 γC); 22.9, 21.6 (2 x δC).

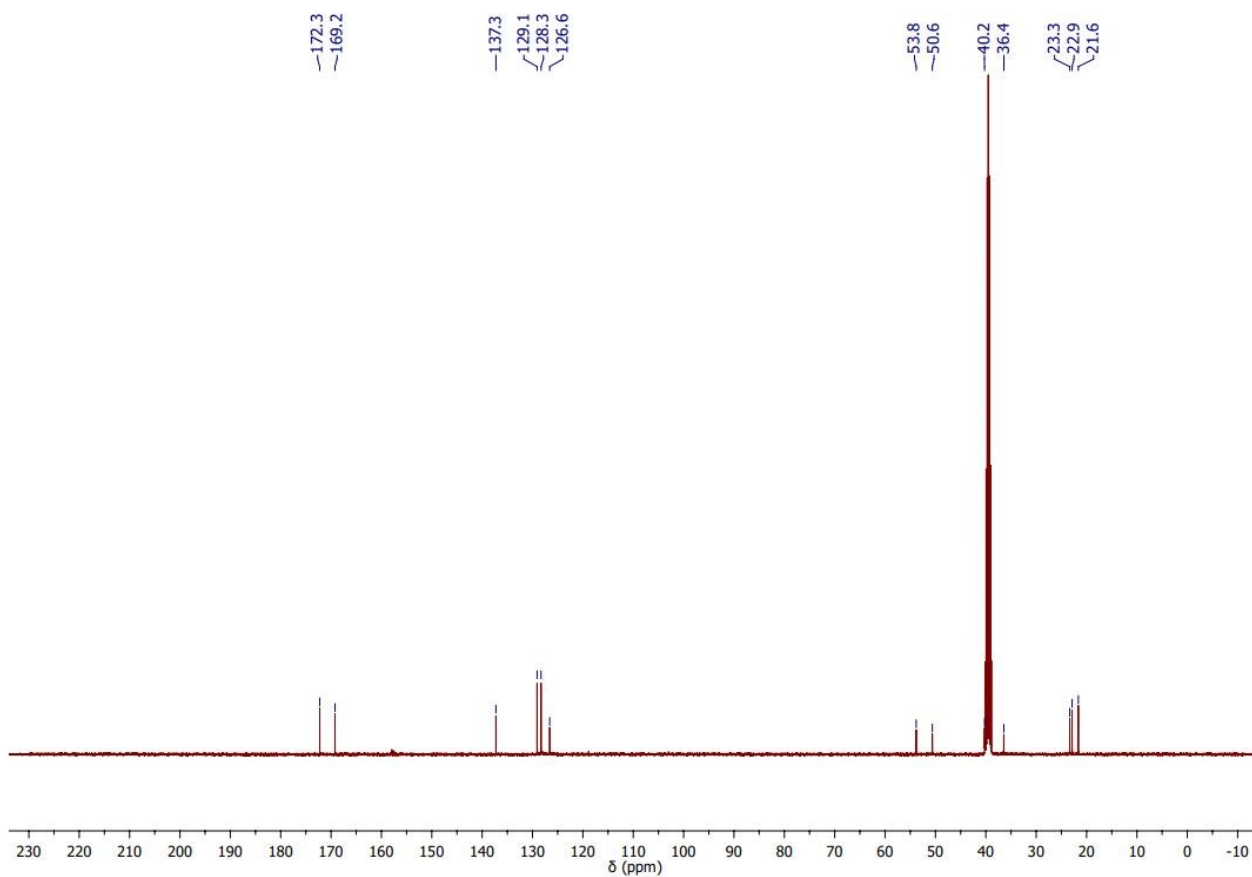


Figure 10.18. ^{13}C -NMR spectrum of L-Leu-L-Phe

MS (ESI): m/z 279.1 ($M+H$)⁺, 301.1 ($M+Na$)⁺, 579.3 ($2M+Na$)⁺; 277.1 ($M-H$)⁻, 555.3 ($2M-H$)⁻.

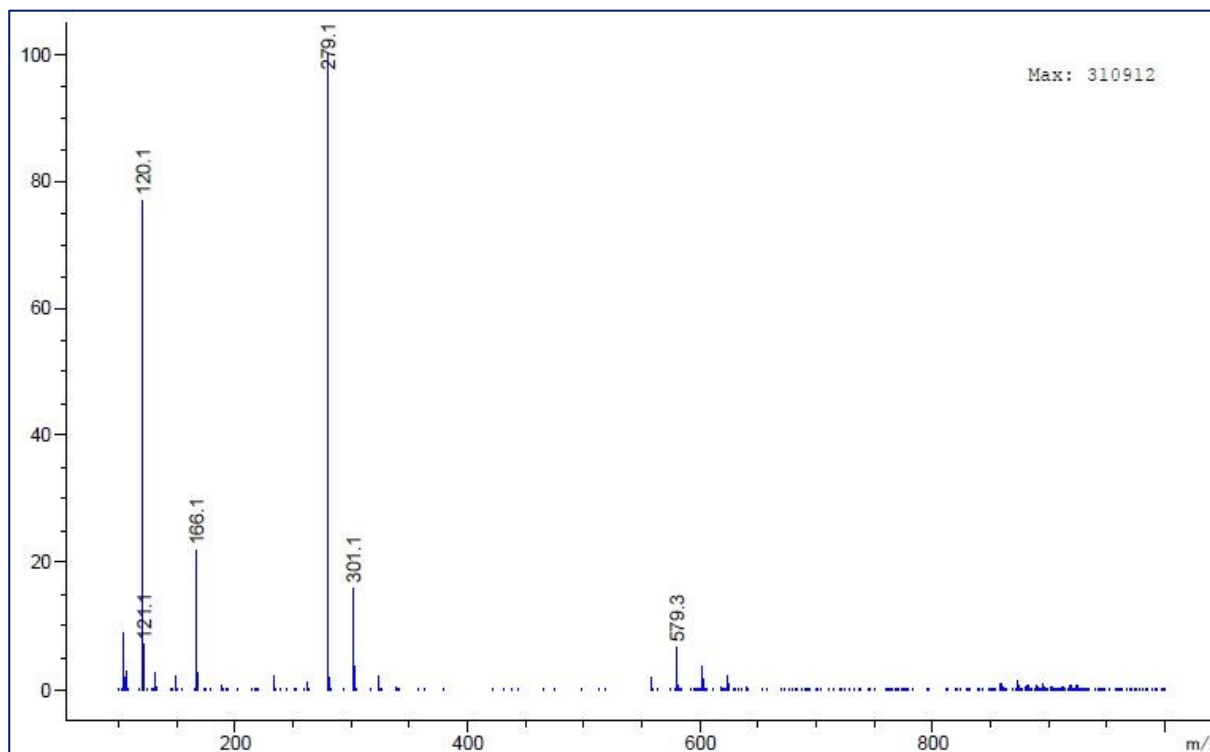


Figure 10.19. ESI-MS spectrum of L-Leu-L-Phe (positive ion mode).

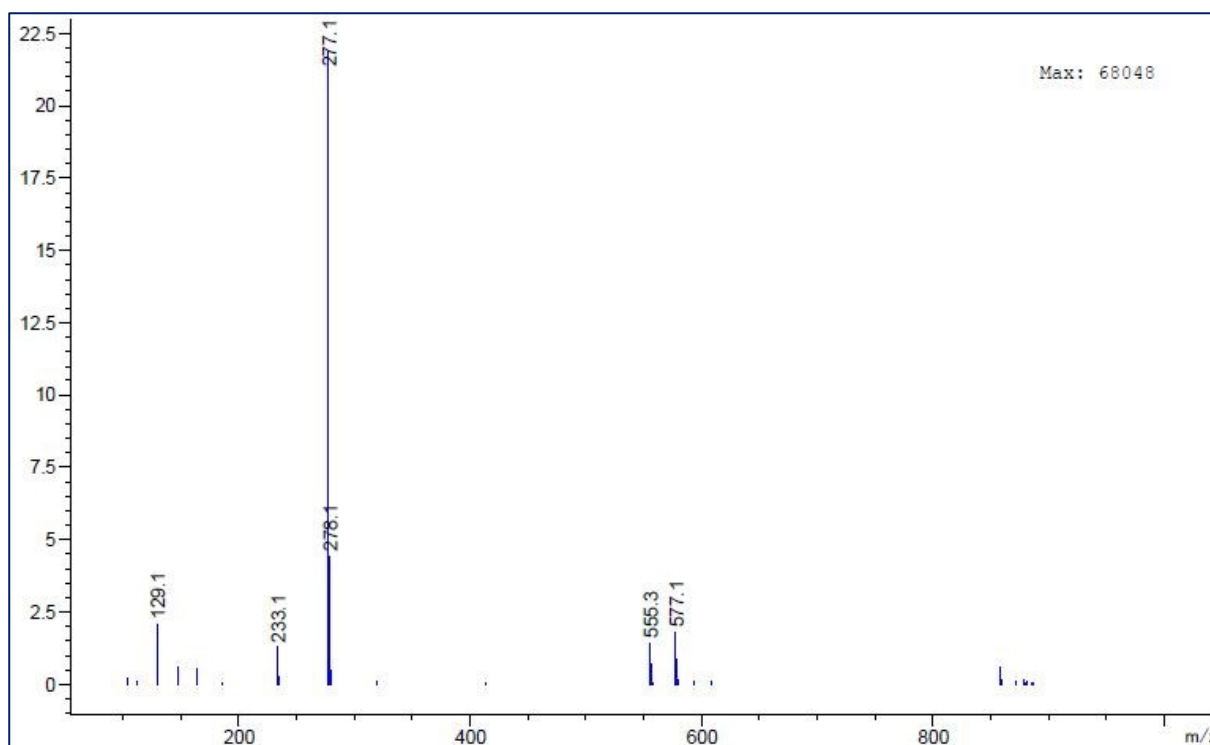


Figure 10.20. ESI-MS spectrum of L-Leu-L-Phe (negative ion mode)

^{13}C -NMR (100 MHz, DMSO- d_6 , TMS)

^{13}C NMR (100 MHz, DMSO- d_6 , TMS), δ (ppm): 172.6, 167.8 (2 x CO); 137.3, 129.0, 128.2, 126.5, (Ar); 56.7, 53.6 (2 x αC); 36.9, 36.1 (2 x βC); 23.2 (1 γC); 14.3 (1 γC); 11.3 (1 δC).

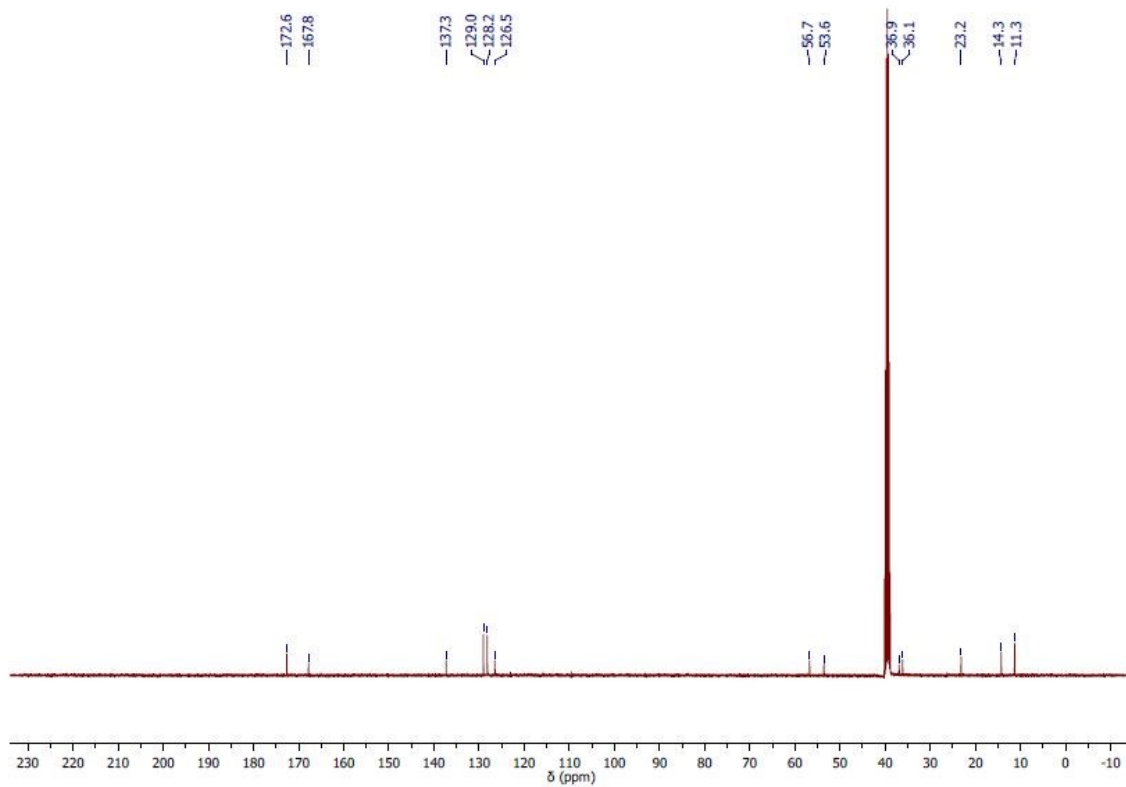


Figure 10.22. ^{13}C -NMR spectrum of D-Ile-L-Phe

MS (ESI): m/z 279.1 ($M+H$)⁺, 301.0 ($M+Na$)⁺, 558.2 ($2M+H$)⁺; 277.1 ($M-H$)⁻, 555.2 ($2M-H$)⁻.

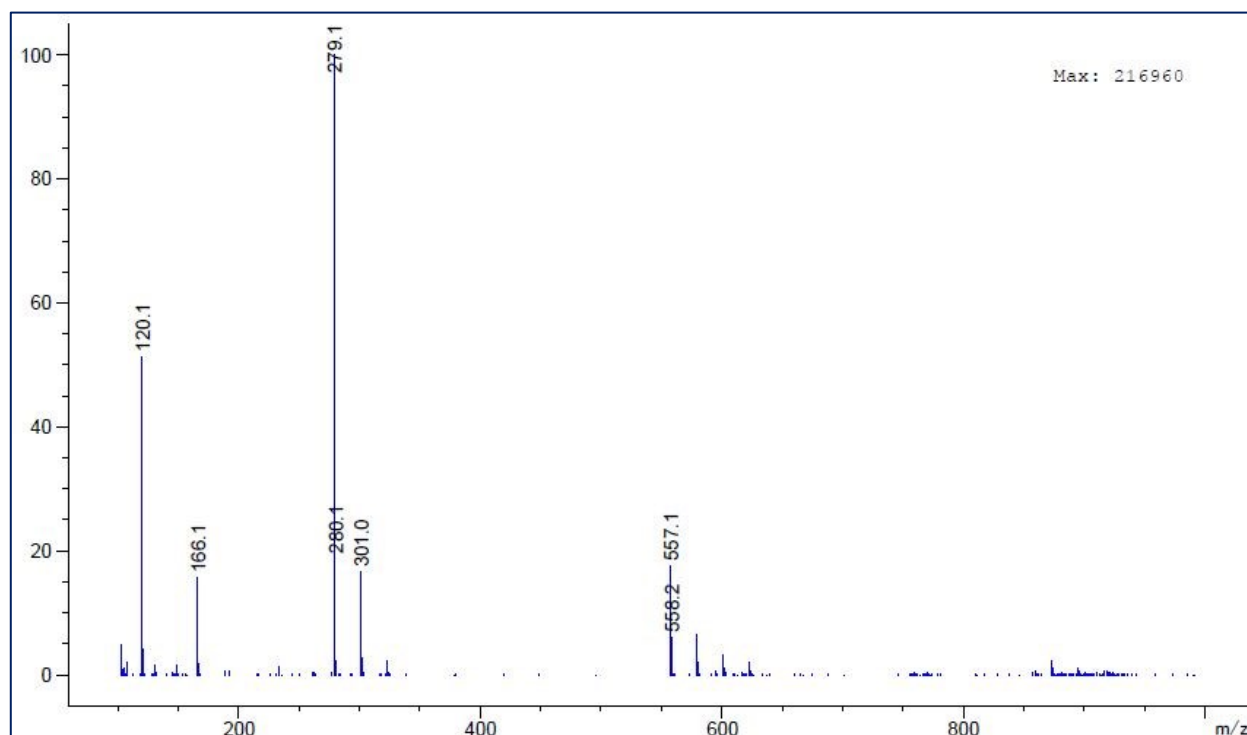


Figure 10.23. ESI-MS spectrum of D-Ile-L-Phe (positive ion mode)

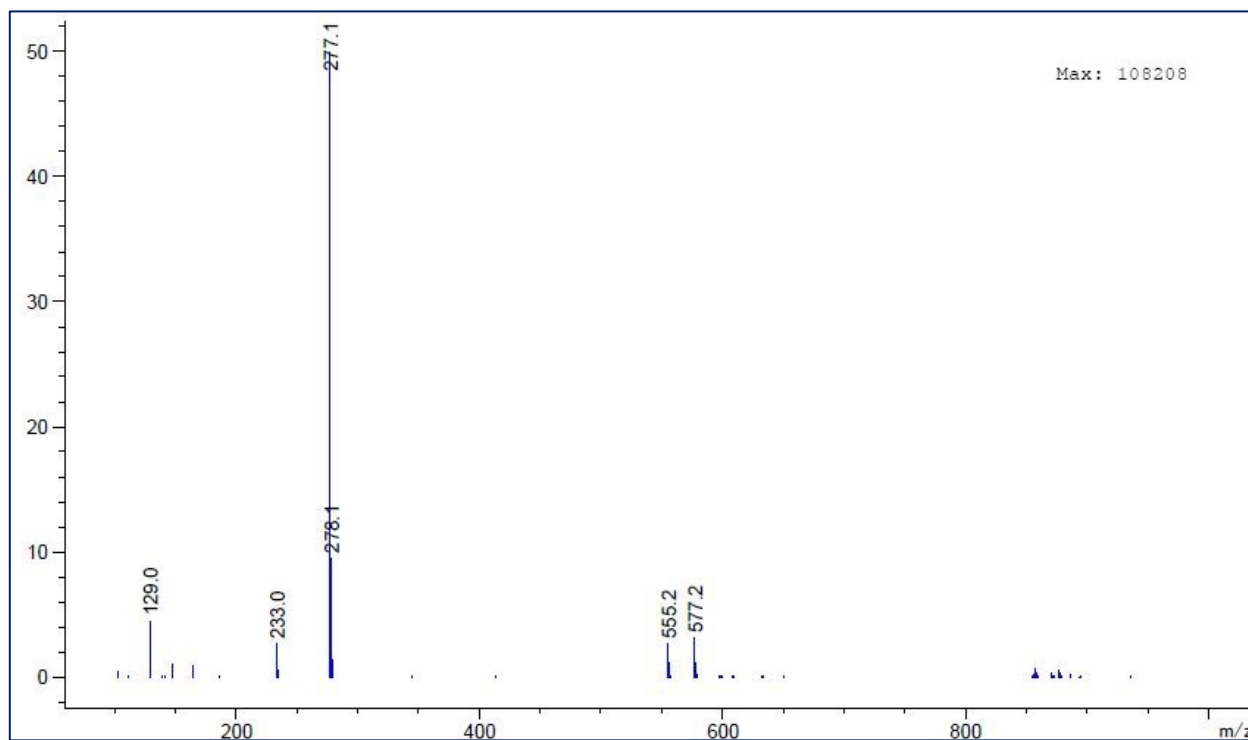
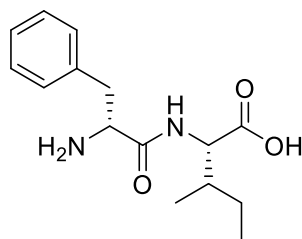


Figure 10.24. ESI-MS spectrum of D-Ile-L-Phe (negative ion mode)

D-Phe-L-Ile spectroscopic data

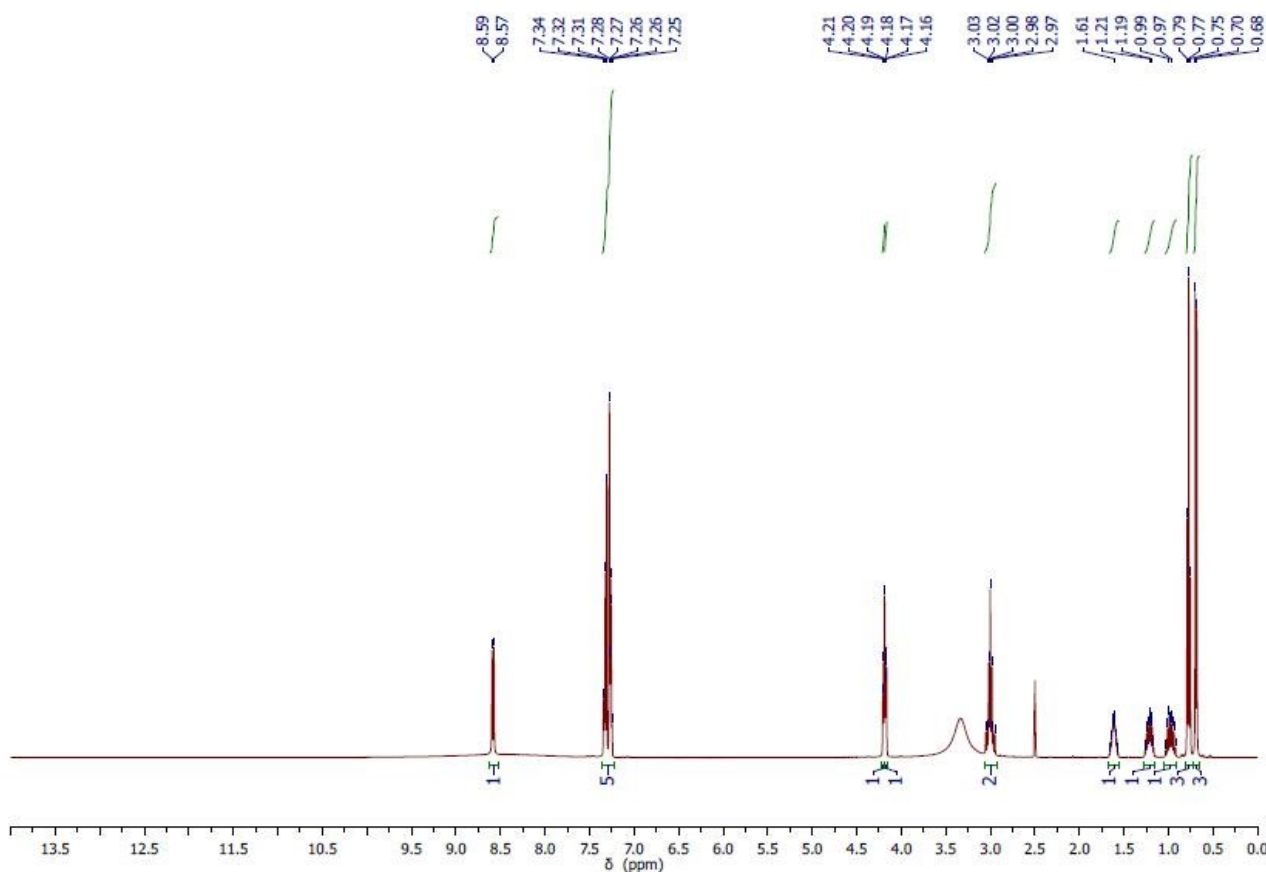
Chemical Formula: C₁₅H₂₂N₂O₃

Exact Mass: 278,16

Molecular Weight: 278,35

¹H NMR (400 MHz, DMSO-*d*₆, TMS)

¹H NMR (400 MHz, DMSO-*d*₆, TMS), δ (ppm): 8.58 (d, *J* = 8.4 Hz, 1H, NH), 7.36 – 7.22 (m, 5H, Ar), 4.18 (m, 2H, αCH Ile, αCH Phe), 3.03 (dd, *J* = 7.2, 13.6 Hz, 1H, βCH₂), 2.97 (dd, *J* = 7.6, 13.6 Hz, 1H, βCH₂), 1.61 (m, 1H, βCH), 1.22 (m, 1H, γCH₂), 0.97 (m, 1H, γCH₂), 0.77 (dd, *J* = 7.2, 7.2 Hz, 3H, CH₃), 0.69 (d, *J* = 6.8 Hz, 3H, CH₃).

Figure 10.25. ¹H-NMR spectrum of D-Phe-L-Ile

^{13}C -NMR (100 MHz, DMSO- d_6 , TMS)

^{13}C NMR (100 MHz, DMSO- d_6 , TMS), δ (ppm): 172.3, 168.0 (2 x CO); 134.8, 129.5, 128.5, 127.1 (Ar); 56.3, 53.1 (2 x αC); 37.5, 36.7 (2 x βC); 24.4, 15.3 (2 γC); 11.2 (1 δC).

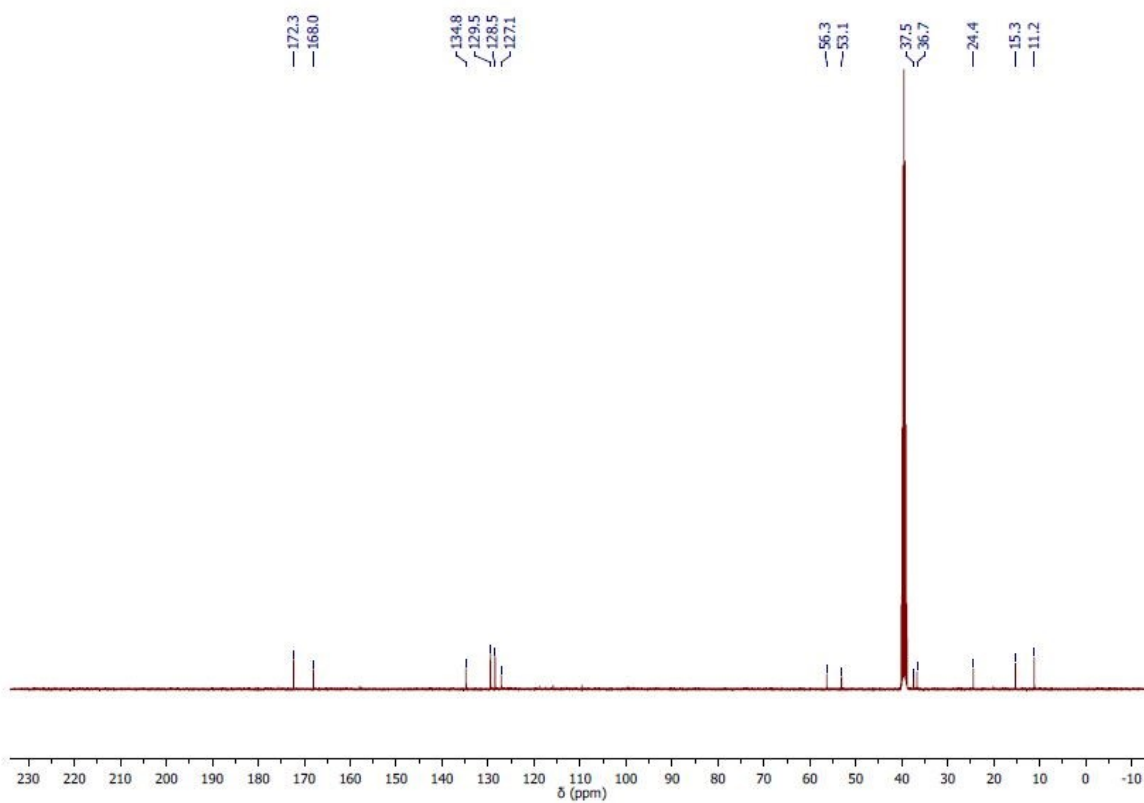


Figure 10.26. ^{13}C -NMR spectrum of D-Phe-L-Ile

MS (ESI): m/z 279.1 ($M+H$)⁺, 277.1 ($M-H$)⁻, 557.2 ($2M+H$)⁺; 277.1 ($M-H$)⁻, 555.2 ($2M-H$)⁻.

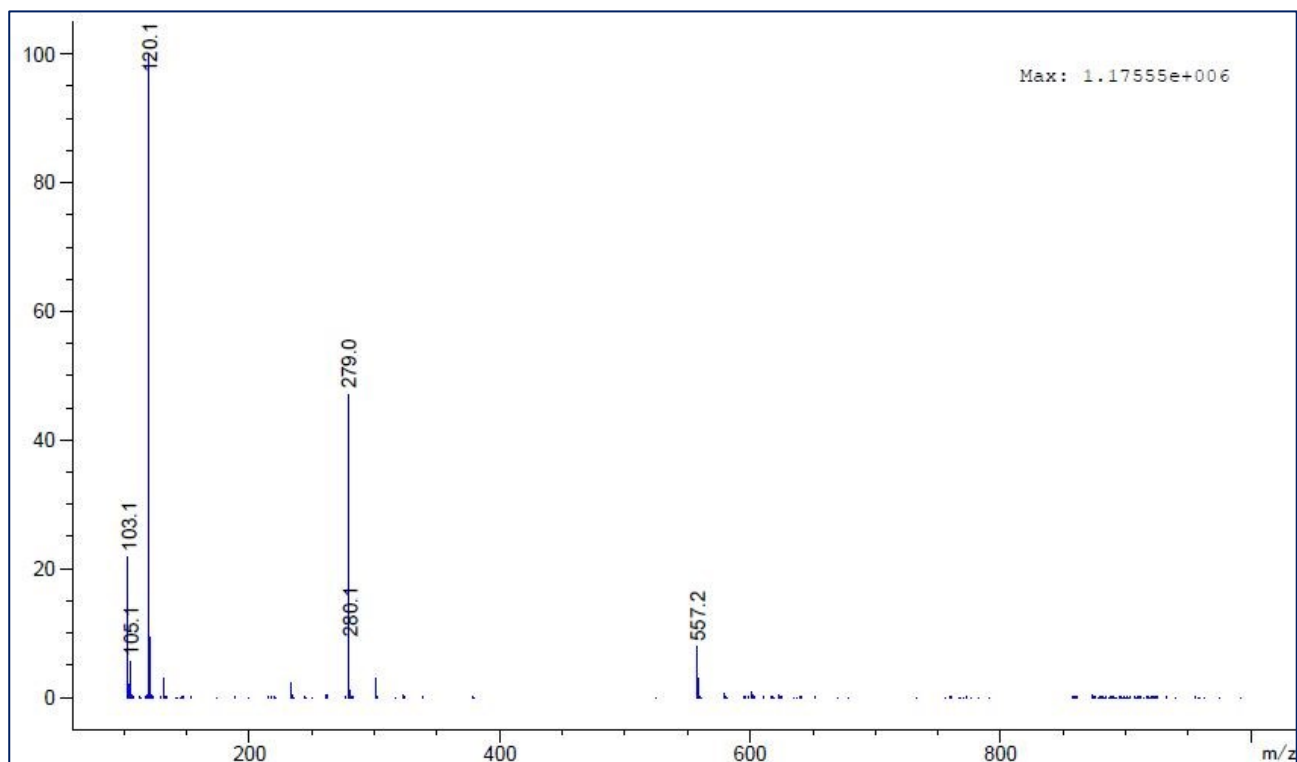


Figure 10.27. ESI-MS spectrum of D-Phe-L-Ile (positive ion mode)

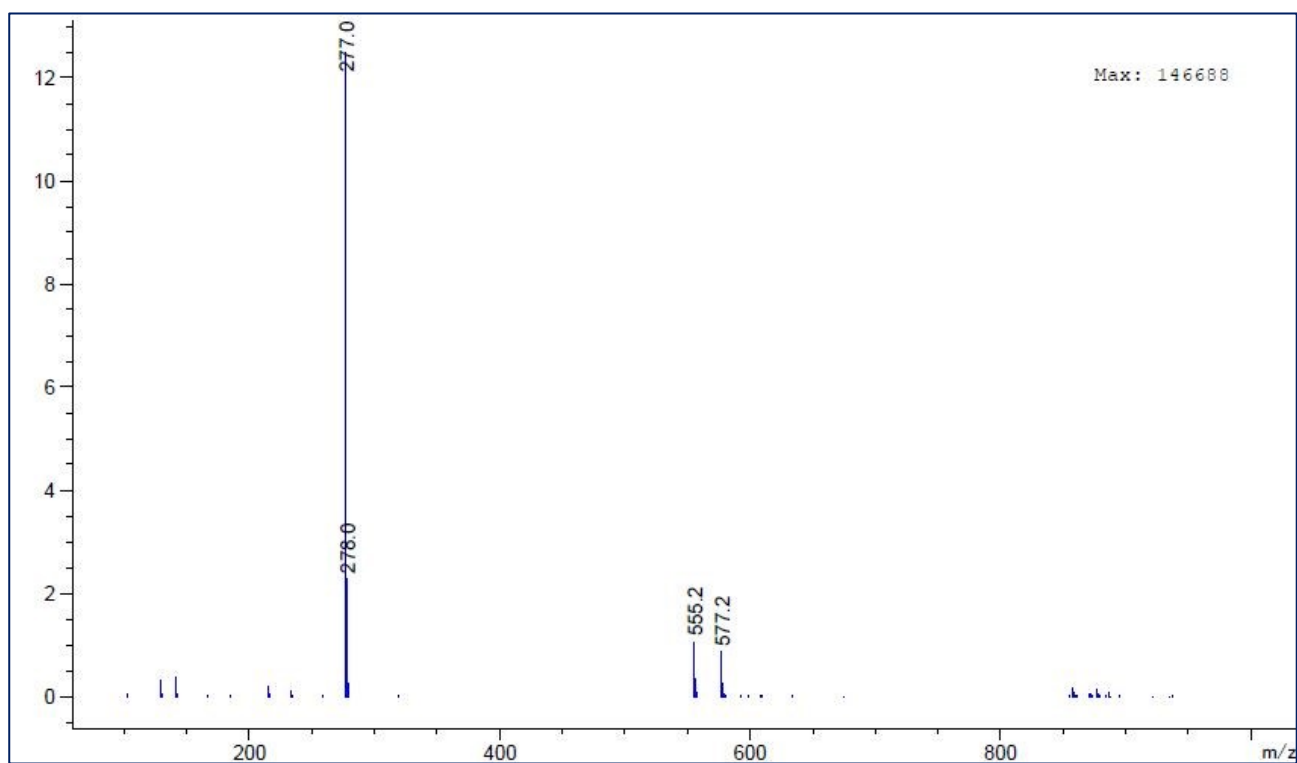


Figure 10.28. ESI-MS spectrum of D-Phe-L-Ile (negative ion mode)

^{13}C -NMR (100 MHz, DMSO- d_6 , TMS)

^{13}C NMR (100 MHz, DMSO- d_6 , TMS), δ (ppm): 172.2, 168.1 (2 x CO); 134.7, 129.5, 128.5, 127.2 (Ar); 56.5, 53.1 (2 x αC); 37.0, 36.6 (2 x βC); 24.7, 15.5 (2 x γC); 11.4 (1 δC).

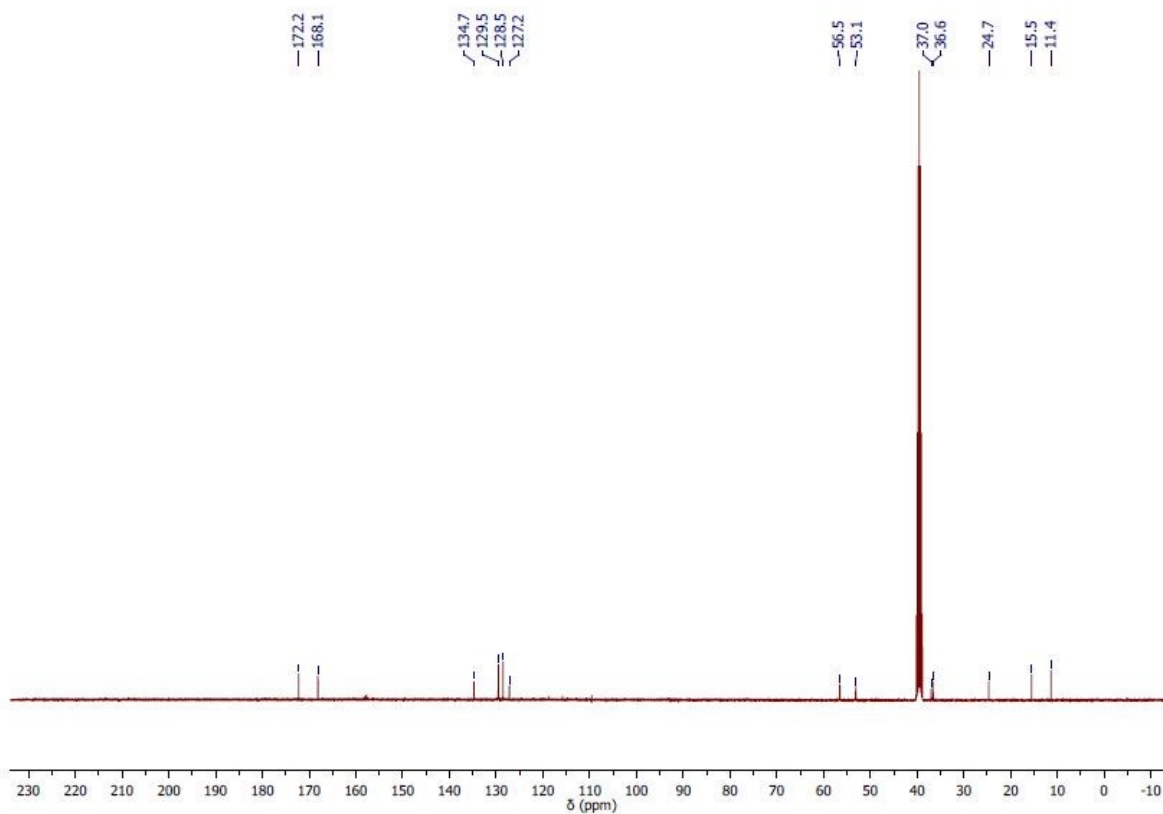


Figure 10.30. ^{13}C -NMR spectrum of L-Phe-L-Ile

MS (ESI): m/z 279.1 ($M+H$)⁺; 277.1 ($M-H$)⁻; 555.2 ($2M-H$)⁻

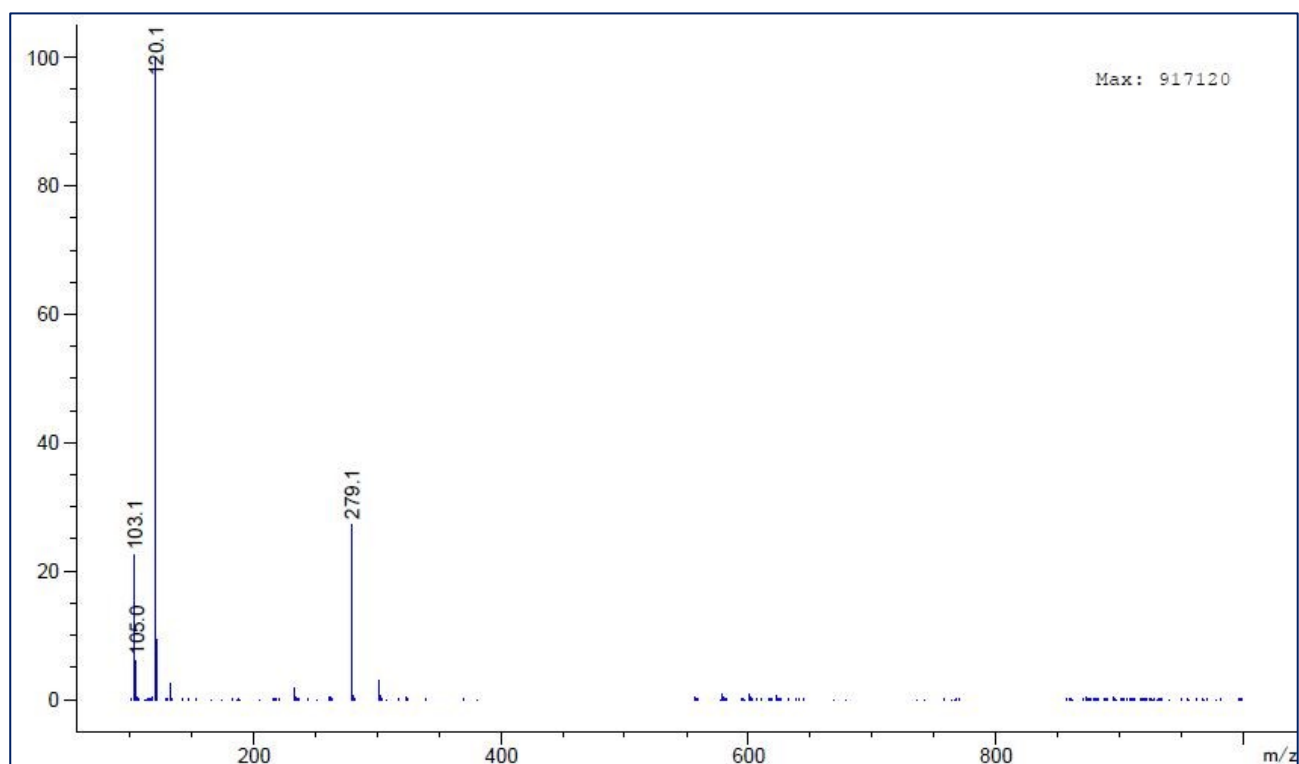


Figure 10.31. ESI-MS spectrum of L-Phe-L-Ile (positive ion mode)

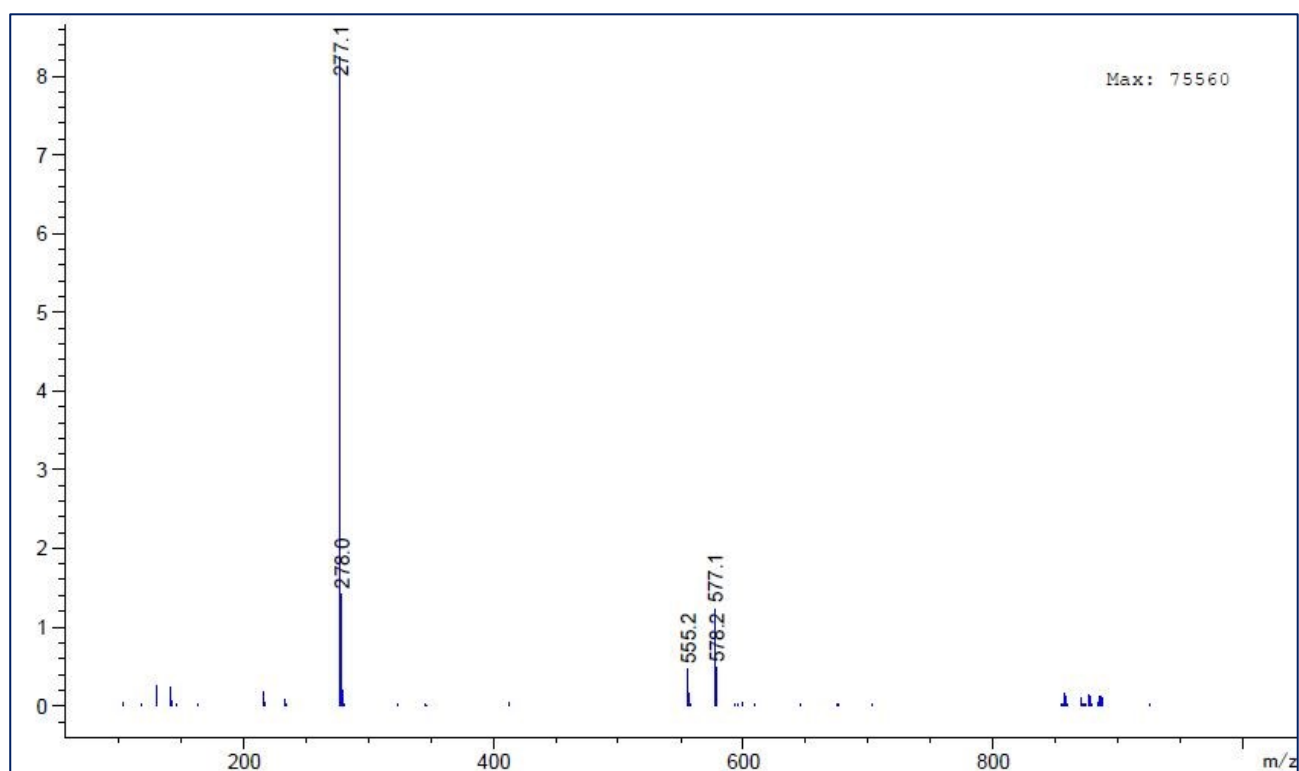
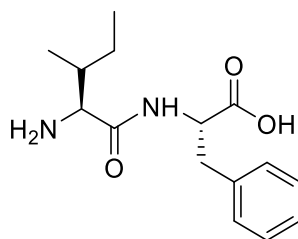


Figure 10.32. ESI-MS spectrum of L-Phe-L-Ile (negative ion mode)

L-Ile-L-Phe spectroscopic data

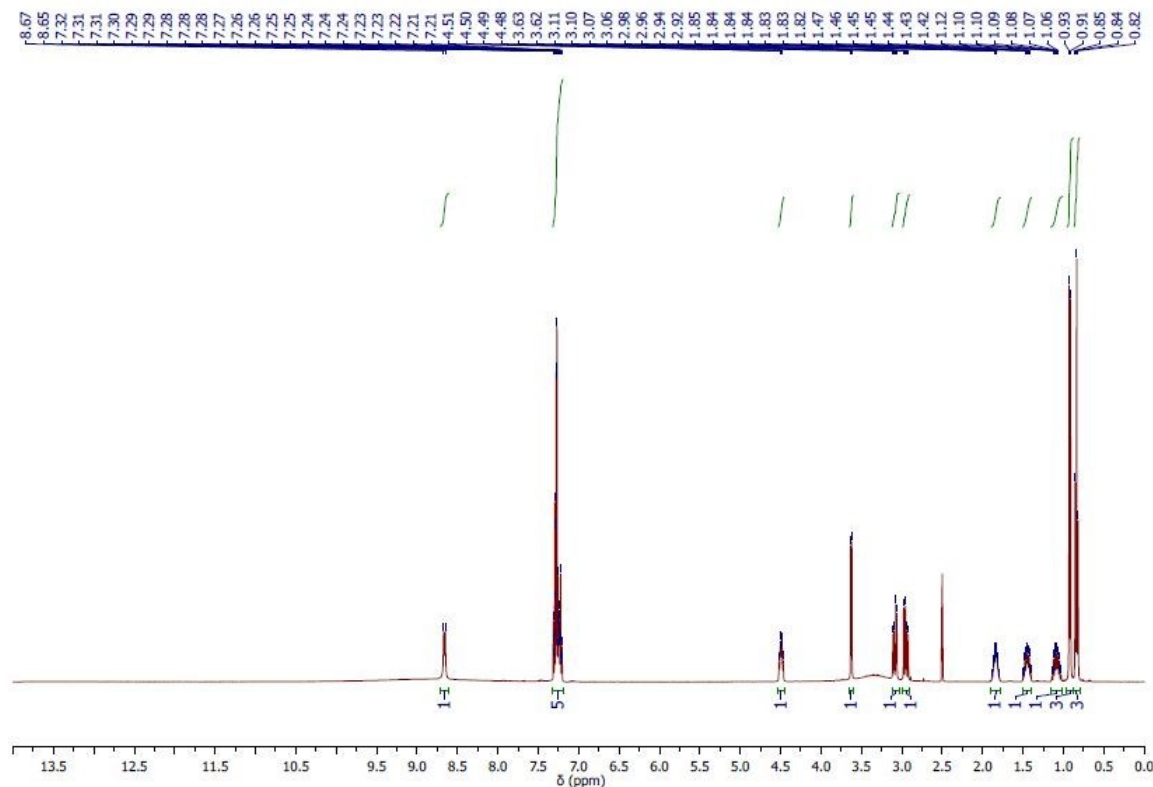
Chemical Formula: C₁₅H₂₂N₂O₃

Exact Mass: 278,16

Molecular Weight: 278,35

¹H NMR (400 MHz, DMSO-*d*₆, TMS)

¹H NMR (400 MHz, DMSO-*d*₆, TMS), δ (ppm): 8.66 (d, *J* = 8.0 Hz, 1H, NH), 7.32 – 7.19 (m, 5H, Ar), 4.49 (ddd, *J* = 8.0, 8.0, 5.2 Hz, 1H, αCH Phe), 3.63 (d, *J* = 5.1 Hz, 1H, αCH Ile), 3.09 (dd, *J* = 14.4, 5.2 Hz, 1H, βCH₂), 2.95 (dd, *J* = 14.1, 8.7 Hz, 1H, βCH₂), 1.90 – 1.77 (m, 1H, βCH), 1.45 (dddd, *J* = 14.8, 7.4, 7.4, 3.6 Hz, 1H, γCH₂), 1.08 (m, 1H, γCH₂), 0.92 (d, *J* = 6.8 Hz, 3H, CH₃), 0.84 (dd, *J* = 7.4, 7.4 Hz, 3H, CH₃).

Figure 10.33. ¹H-NMR spectrum of L-Ile-L-Phe

^{13}C -NMR (100 MHz, DMSO- d_6 , TMS)

^{13}C NMR (100 MHz, DMSO- d_6 , TMS), δ (ppm): 172.3, 168.2 (2 x CO); 137.2, 129.1, 128.3, 126.6 (Ar); 56.5, 53.8 (2 x αC); 36.5, 36.4 (2 x βC); 23.4, 14.6 (2 x γC); 11.2 (1 δC).

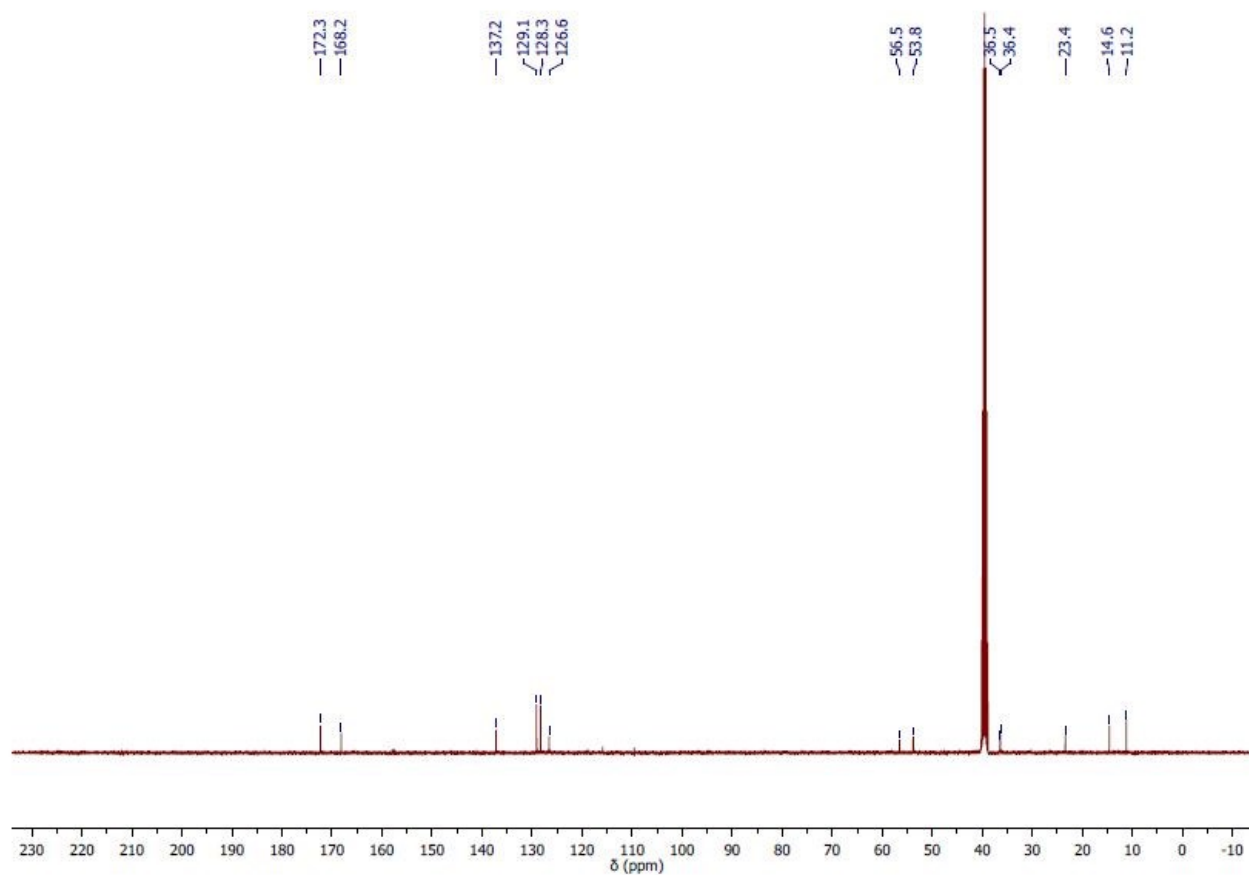


Figure 10.34. ^{13}C -NMR spectrum of L-Ile-L-Phe

MS (ESI): m/z 279.1 ($M+H$)⁺, 301.1 ($M+Na$)⁺, 579.2 ($2M+Na$)⁺; 277.1 ($M-H$)⁻, 555.2 ($2M-H$)⁻.

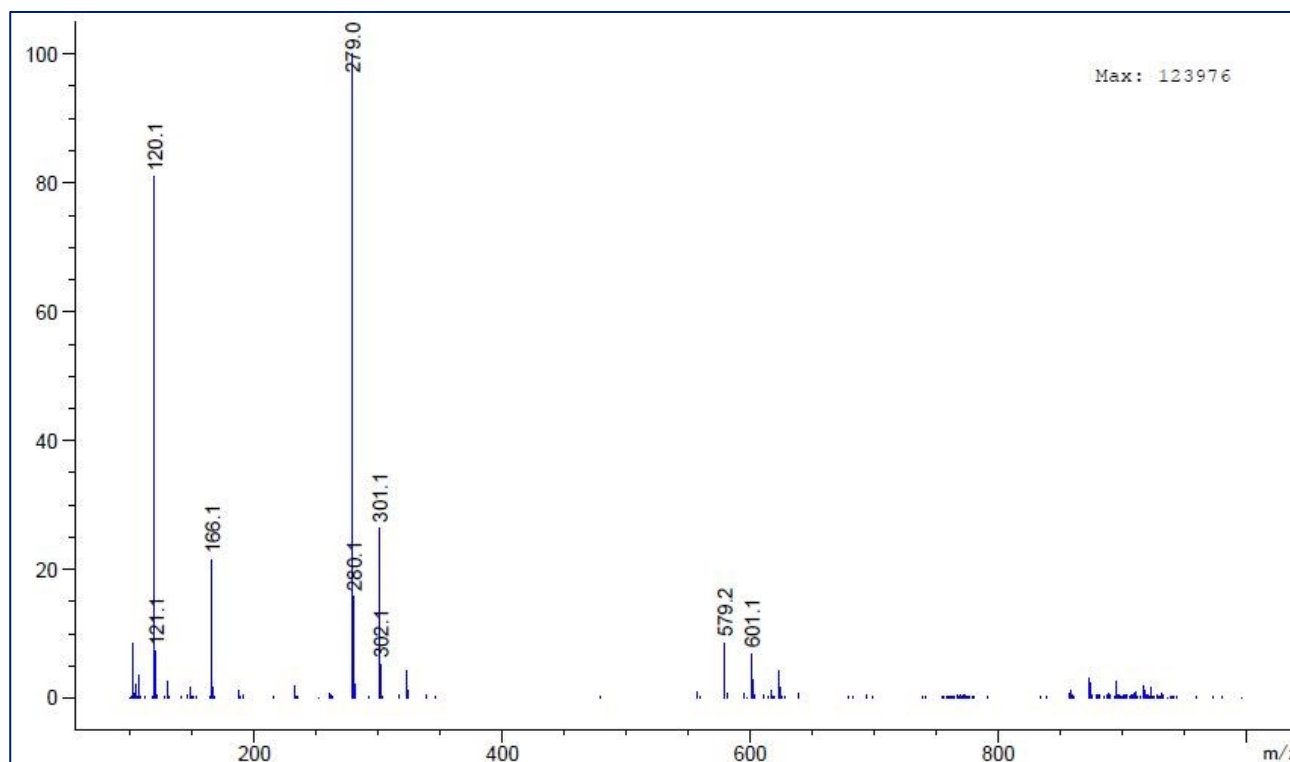


Figure 10.35. ESI-MS spectrum of L-Ile-L-Phe (positive ion mode)

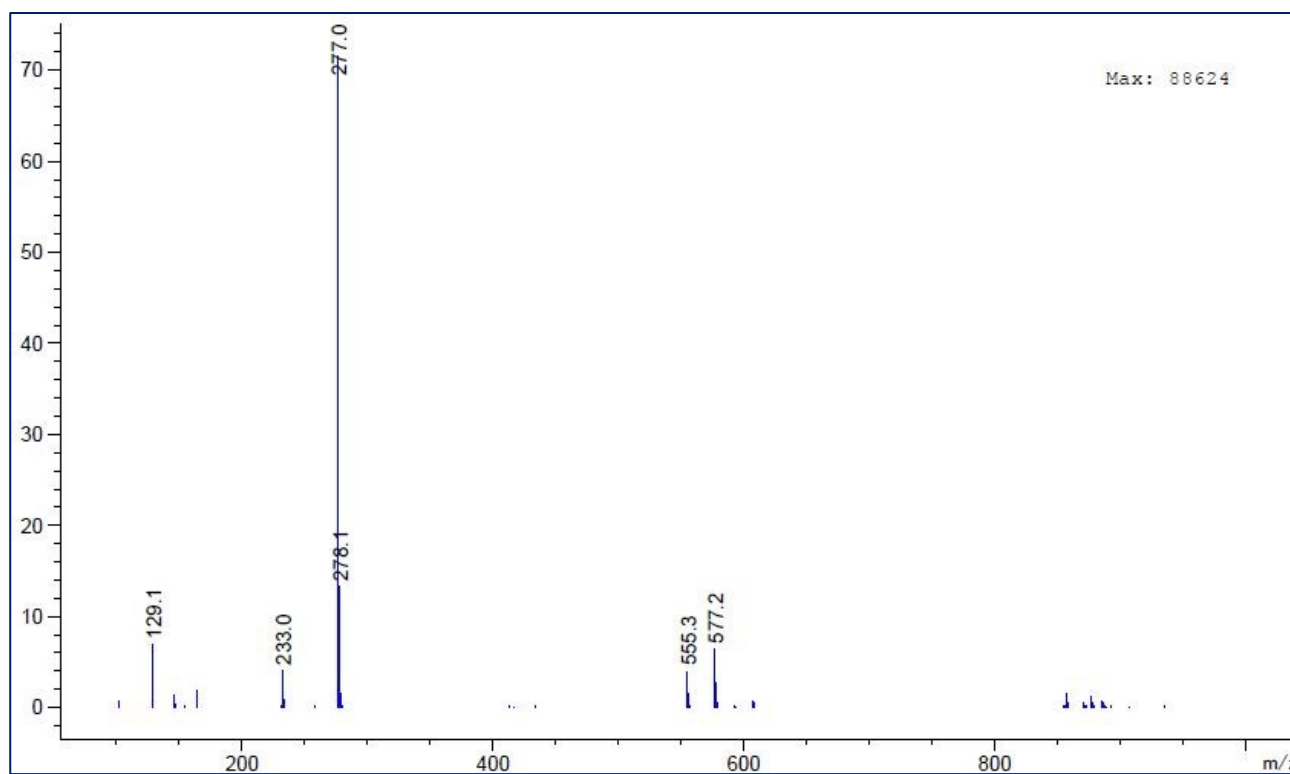
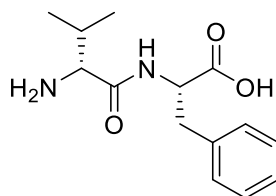


Figure 10.36. ESI-MS spectrum of L-Ile-L-Phe (negative ion mode)

10.4. Manuscript 6. “Dipeptide self-assembly into water-channels and gel biomaterial” described in Chapter 7.

D-Val-L-Phe spectroscopic data



Chemical Formula: $C_{14}H_{20}N_2O_3$

Exact Mass: 264,15

Molecular Weight: 264,33

1H NMR (400 MHz, DMSO- d_6 , TMS)

1H NMR (400 MHz, DMSO- d_6 , TMS) δ (ppm): 8.69 (d, $J = 8.4$ Hz, 1H), 7.31 – 7.15 (m, 5H), 4.59 (ddd, $J = 10.3, 8.4, 4.4$ Hz, 1H), 3.57 (d, $J = 4.6$ Hz, 1H), 3.16 (dd, $J = 13.9, 4.4$ Hz, 1H), 2.83 (dd, $J = 13.9, 10.4$ Hz, 1H), 1.94 – 1.80 (m, 1H), 0.72 (d, $J = 6.9$ Hz, 3H), 0.51 (d, $J = 7.0$ Hz, 3H).

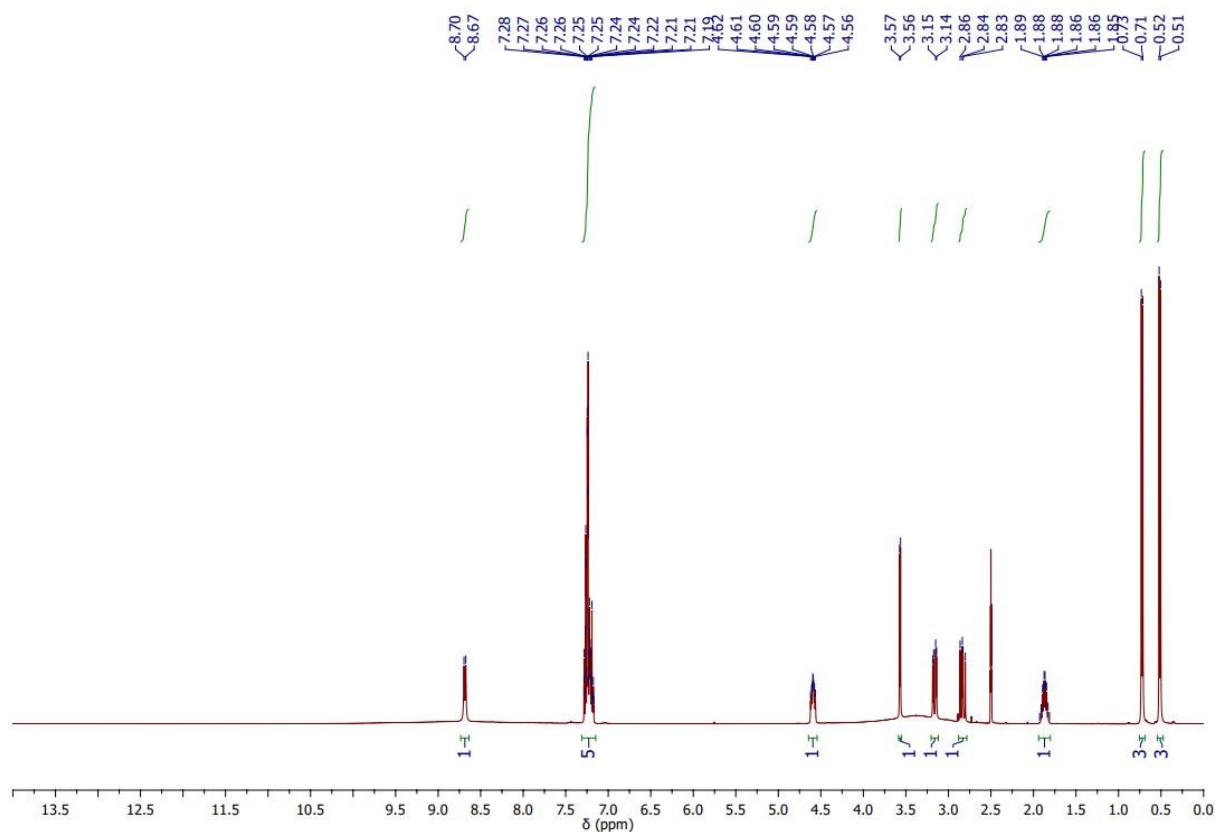


Figure 10.37. 1H -NMR spectrum of D-Val-L-Phe

^{13}C -NMR (100 MHz, DMSO- d_6 , TMS)

^{13}C NMR (100 MHz, DMSO- d_6 , TMS) δ (ppm): 172.6, 167.9 (2 x CO); 137.3, 129.1, 128.2, 126.5 (Ar); 57.3, 53.5 (2 x αC); 37.1, 29.7 (2 x βC); 18.3, 16.6 (2 x γC).

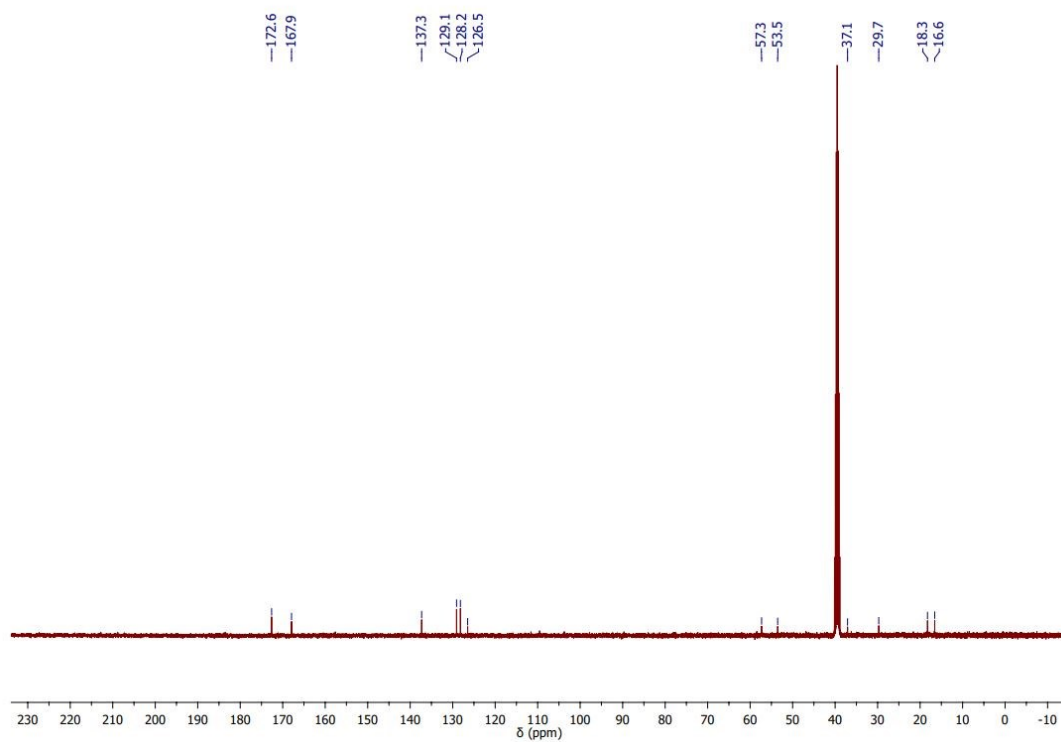


Figure 10.38. ^{13}C -NMR spectrum of D-Val-L-Phe

MS (ESI): m/z 265.1 ($M+H$)⁺, 287.1 ($M+Na$)⁺, 529.1 ($2M+Na$)⁺, 263 ($M-H$)⁻

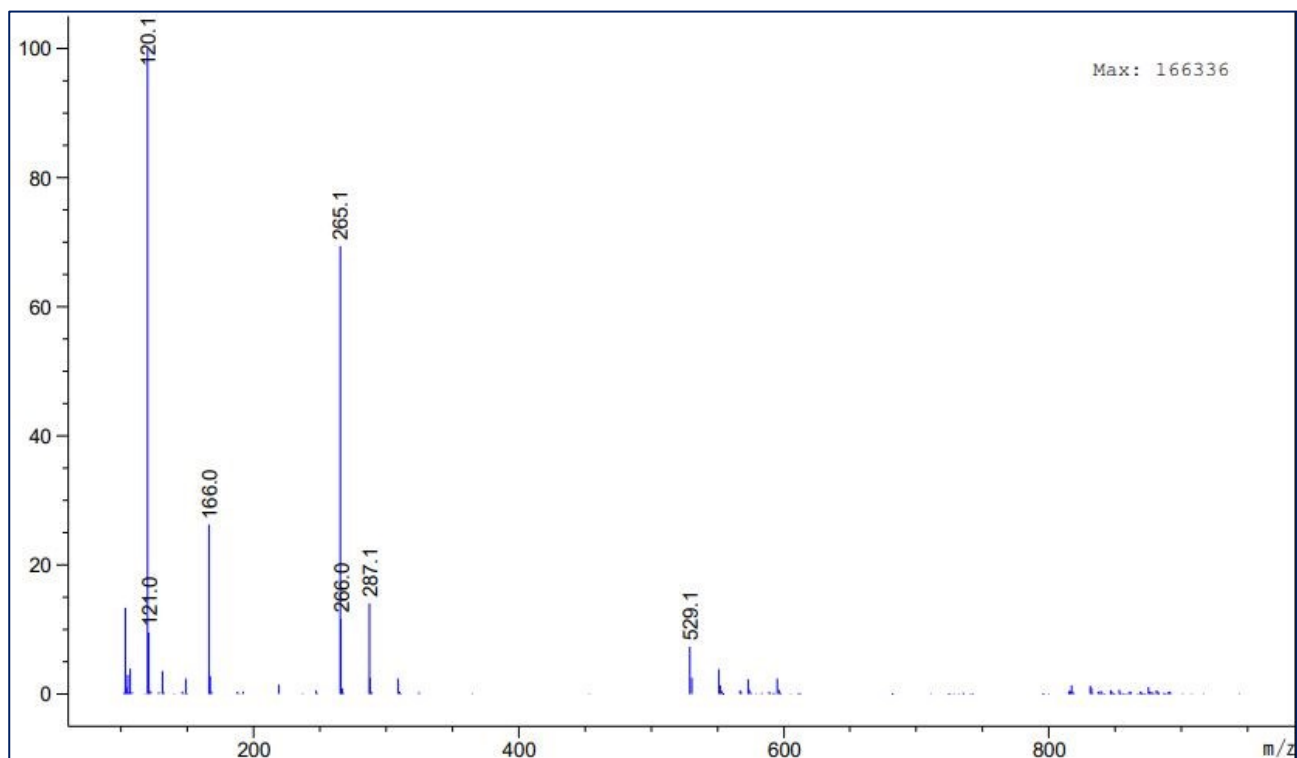


Figure 10.39. ESI-MS spectrum of D-Val-L-Phe (positive ion mode)

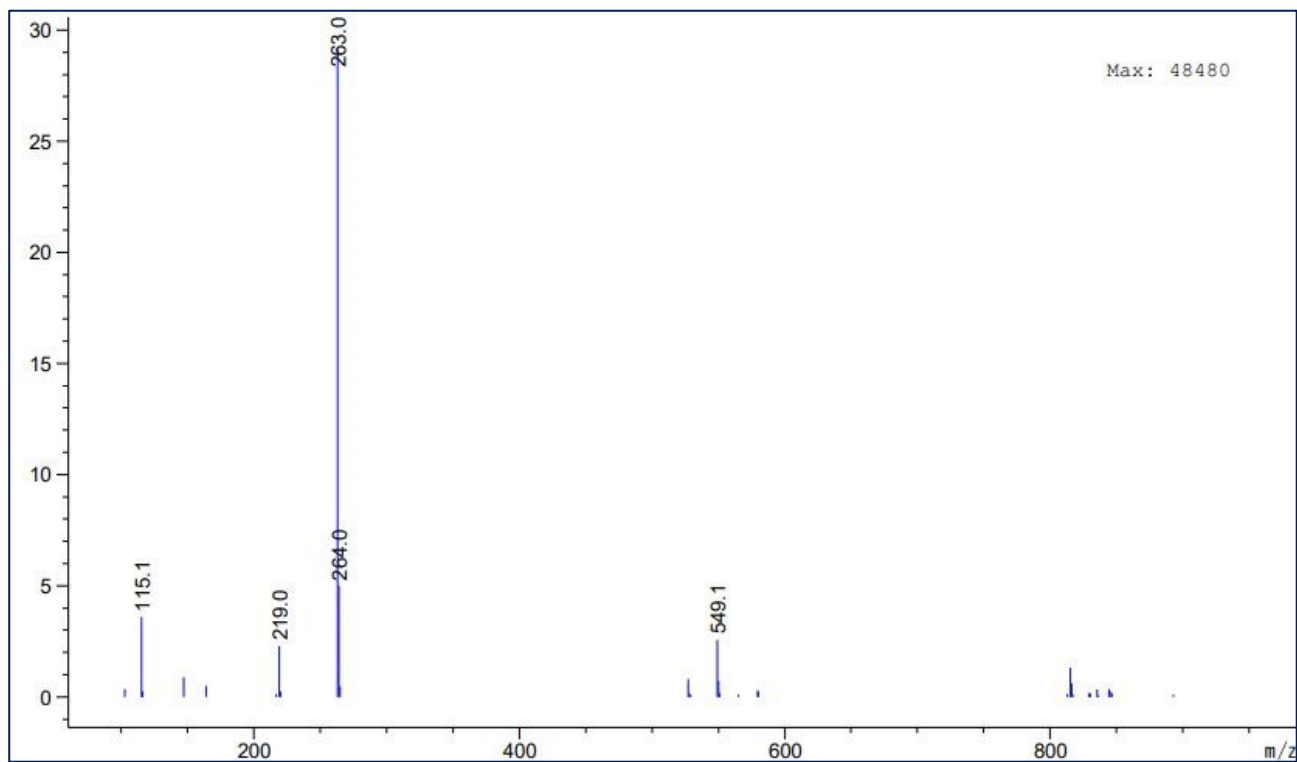
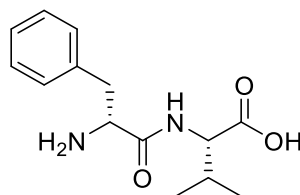


Figure 10.40. ESI-MS spectrum of D-Val-L-Phe (negative ion mode)

D-Phe-L-Val spectroscopic data

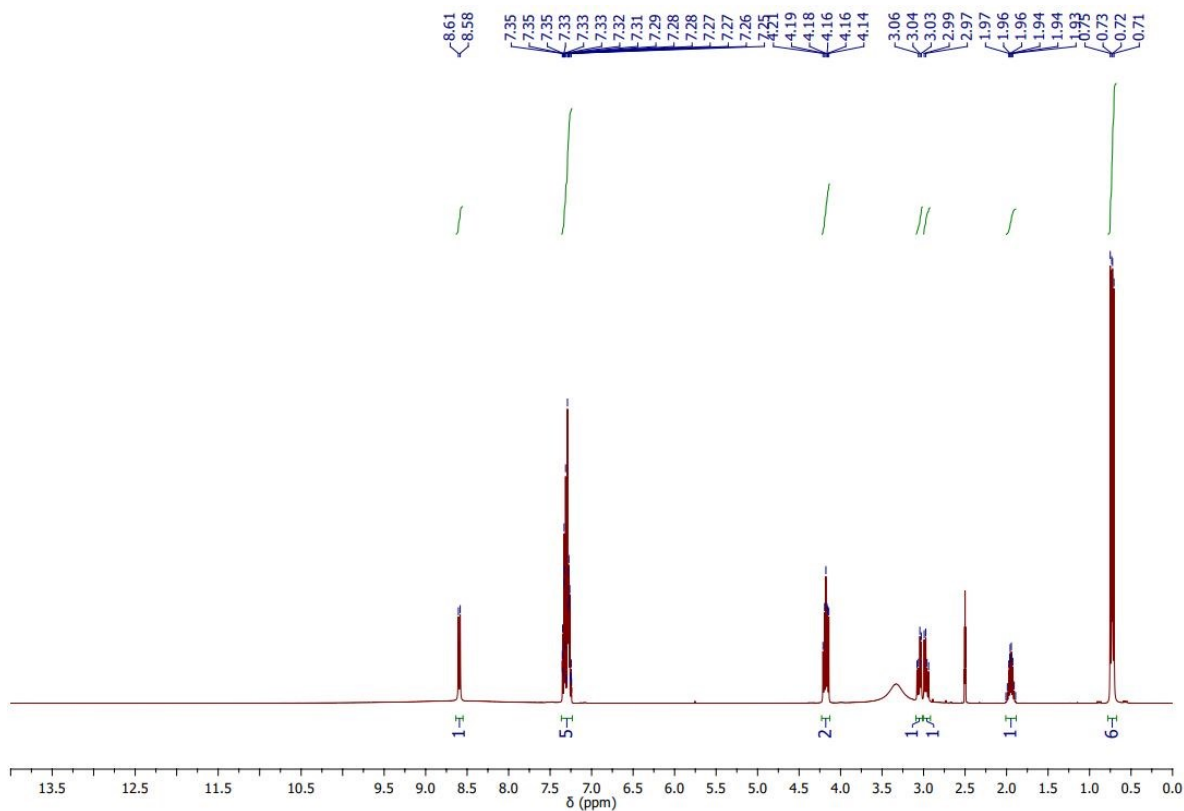
Chemical Formula: C₁₄H₂₀N₂O₃

Exact Mass: 264,15

Molecular Weight: 264,33

¹H NMR (400 MHz, DMSO-*d*₆, TMS)

¹H NMR (400 MHz, DMSO-*d*₆, TMS) δ (ppm): 8.59 (d, *J* = 8.6 Hz, 1H), 7.36 – 7.23 (m, 5H), 4.23 – 4.13 (m, 2H), 3.05 (dd, *J* = 13.8, 6.7 Hz, 1H), 2.97 (dd, *J* = 13.8, 7.9 Hz, 1H), 2.01 – 1.88 (m, 1H), 0.73 (dd, *J* = 11.1, 6.8 Hz, 6H).

Figure 10.41. ¹H-NMR spectrum of D-Phe-L-Val¹³C-NMR (100 MHz, DMSO-*d*₆, TMS)

^{13}C NMR (100 MHz, DMSO- d_6 , TMS) δ (ppm): 172.4, 168.3 (2 x CO); 134.9, 129.5, 128.5, 127.1 (Ar); 57.3, 53.2 (2 x αC); 37.6, 30.1 (2 x βC); 18.8, 17.7 (2 x γC).

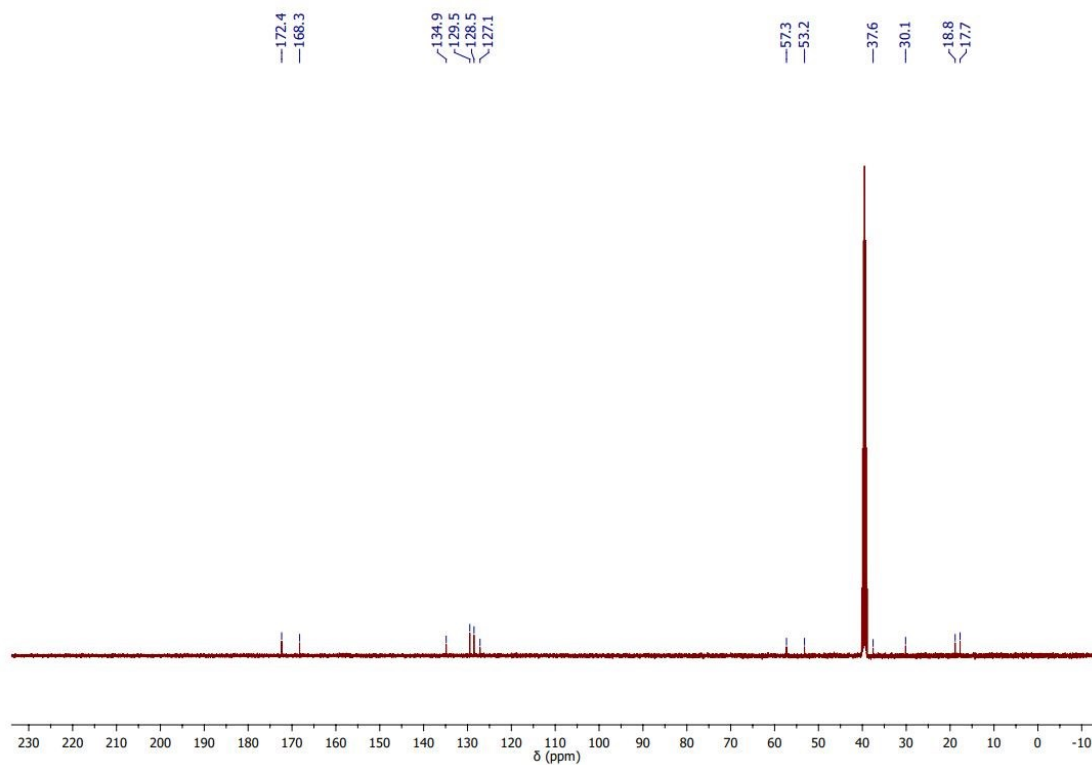


Figure 10.42. ^{13}C -NMR spectrum of D-Phe-L-Val

MS (ESI): m/z 265.1 ($\text{M}+\text{H}$) $^+$; 263 ($\text{M}-\text{H}$) $^-$

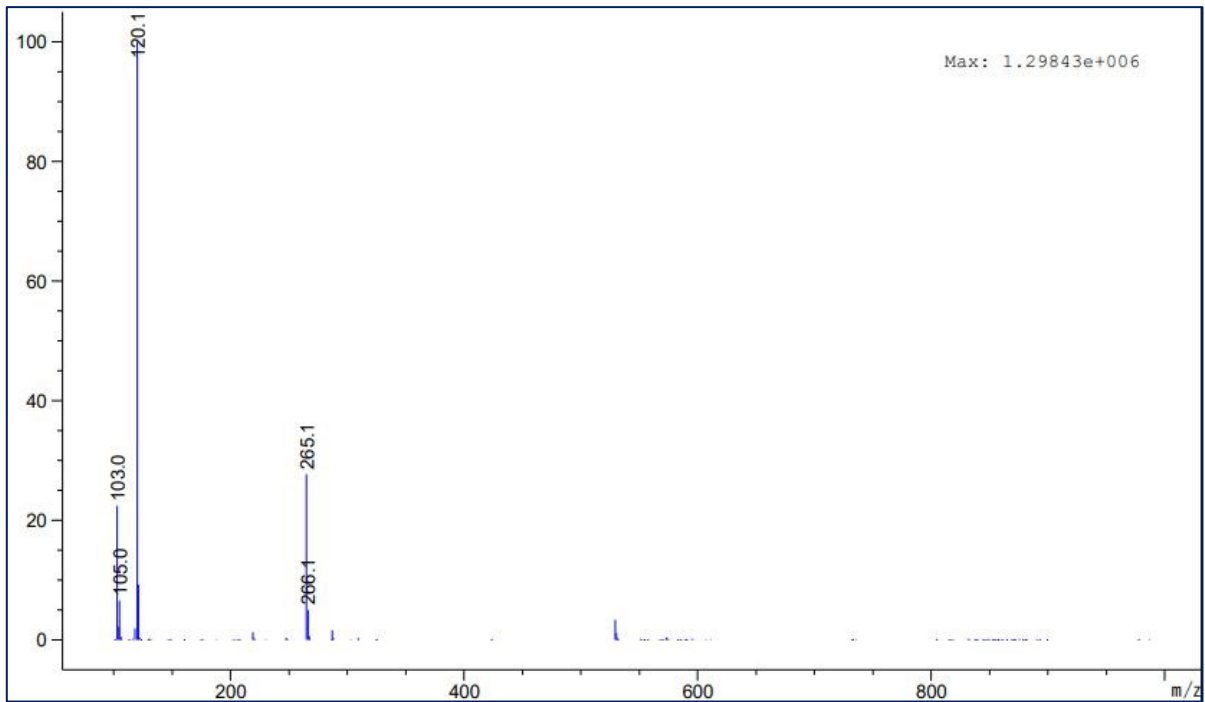


Figure 10.43. ESI-MS spectrum of D-Phe-L-Val (positive ion mode)

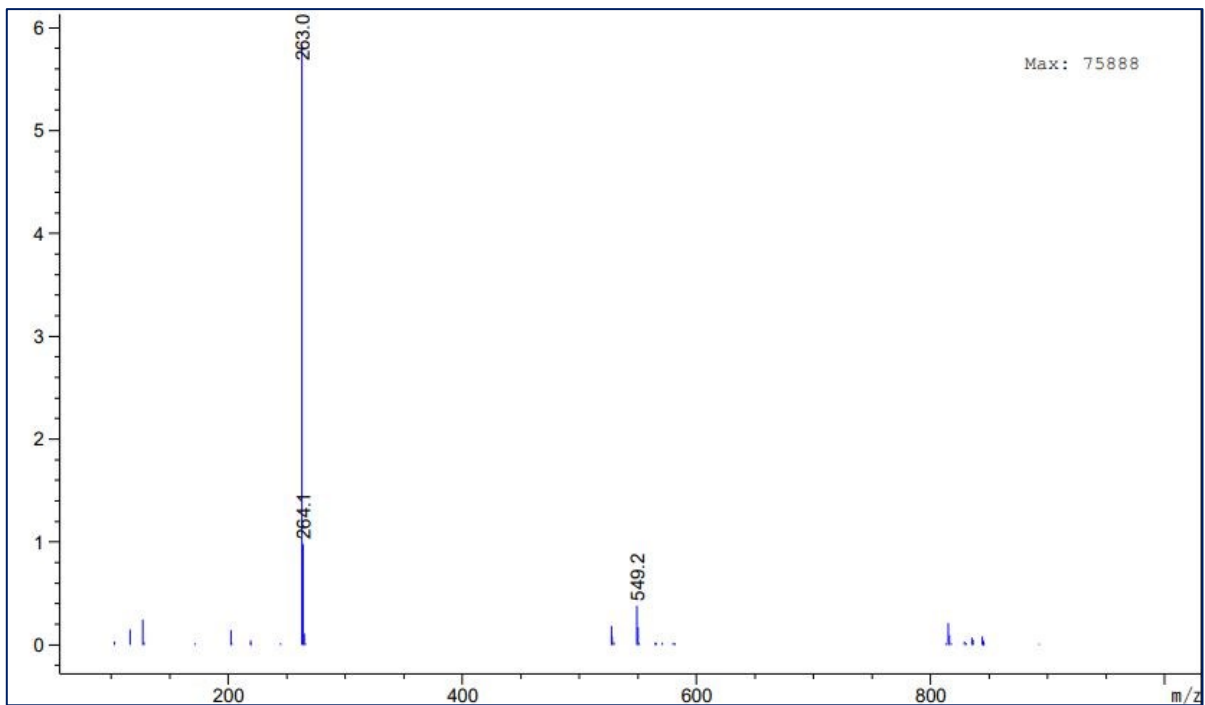


Figure 10.44. ESI-MS spectrum of D-Phe-L-Val (negative ion mode)

Acknowledgments

First and foremost, I would really like to thank my Supervisor, *Prof. Silvia Marchesan*, for her invaluable supervision, continuous support, and humanity during my PhD carrier. Her energy and positivism have encouraged me a lot throughout my academic research inspiring me during all these years. I am truly grateful to have had the opportunity to work with such a high-level supervisor. Her admirable passion for sciences and great research ideas are always able to coordinate multidisciplinary teams leading to scientific and stimulating discoveries.

I would like to express my sincere gratitude to all the contributors who have made each publication possible. I would like to acknowledge Elettra Sincrotrone Trieste (Italy) for providing access to its synchrotron radiation facilities, especially *Maurizio Polentarutti, N. Demitri and Giorgio Bais* for assistance with beamline XRD1. A great thank you to all the crystallographers such as *Prof. Rita De Zorzi and Prof. Silvano Geremia* from University of Trieste and *Consiglia Tedesco and Giovanni Pierri*, from University of Salerno, for the fruitful collaboration and all the XRD crystal data resolution. A special thanks goes to *Prof. Rita De Zorzi*, for being an irreplaceable and brilliant guide in the world of crystallography, for her patience, humanity and cordiality shown to me in every situation. Thanks to *Barbara Rossi and Maria Grazia Tortora*, for their precious assistance with the IUVS Beamline. I acknowledge the CENN Nanocenter (Slovenia) for the use of electron microscopy (TEM), especially *Dr. Slavko Kralj*, for his great collaboration, brilliant competence, and always active assistance in the acquisition of all Tem images.

Many thanks to *Prof. Alessandro Tossi*, for his kindness in always helping.

For biological experiments, I gratefully acknowledge *Dr. Sabrina Semeraro*, for her unwavering support and friendly and precious advice during all these years, *Dr. Barbara Medagli*, for her patience and generous help, *Professor Antonella Bandiera and Professor Paola D'Andrea* for training me in cell culture work, for the fruitful scientific discussions and for bringing me into the wonderful world of microscopy and biology. Additionally, I would like to thank the *Professor Mikaela Groenholm* from University of Helsinki (Finland), for her kind hospitality in her lab and for making me feel at home even if far away.

I would really like to thank all *my lab mates*, friends more than colleagues, for the cherished time spent together in the lab, for their moral support and for teaching me what it means to be a team. The former members, *Eva, Marina, Cristina, and Serena* for their valuable advice and for making me immediately feel part of the group. The current members, *Simone*, always present with a strong and unforgettable support, *Petr*, for his kindness and precious company and *Erica*, for her great energy and contagious positivism.

Thanks to all the other friends and colleagues met during my PhD, *Simone, Cristian, Marco, Maria Chiara, Claudia, Greta, and Rossella*, for their sincere friendship. Thanks to all the students, *Giuseppe, Tiziano, Lorenzo, Kevin, Veronica, Federica, Beatrice, Giovanni, and Davide* I had the opportunity to know and/or work with.

Thanks also to *Mrs. Manuela Bisiacchi, Mr. Marco Tedesco, Mr. Paolo Gambini, Mr. Renzo Crevatin and Mr. Elvio Merlach* for their kind technical assistance at University of Trieste.

In the end, but not for importance, I would like to express a special thanks to *My Family and Friends*, for their unconditionally love and huge support in everyday life, thank you for being the best and most precious part of my life.